

**Alkaline Magmatism, Water-Rock Interaction and  
Multiple Metamorphism in the Seiland Igneous  
Province, Northern Norway**



DISSERTATION

zur

Erlangung des Doktorgrades  
der Fakultät für Chemie, Pharmazie und Geowissenschaften  
der Albert-Ludwigs-Universität Freiburg im Breisgau

vorgelegt von

**Xiaoyan Li**

geboren am 18.Apr.1983 in Henan, China

2013



## **Declaration**

I. I declare that I wrote this thesis without the unauthorized help of third persons and without using any aids other than those here stated. All data and ideas which were taken directly or indirectly from other sources are marked as such. In particular, I did not take advantage of paid help from consulting services or agencies. No one received payment from me, either directly or indirectly, for work performed in connection with this dissertation.

The dissertation has never been submitted in the same or similar form to any other examination committee in Germany or abroad.

II. I am aware of the provisions described in the doctoral regulations of the Faculty of Chemistry, Pharmacy, and Earth Sciences. In particular, I know that I am not authorized to use the academic title of doctor until I have received my doctoral diploma.

Date: 28.08.2013

Signature: Xiaoyan Li



Vorsitzender des Promotionsausschusses: Professor Dr. Thorsten Koslowski

Referentin: Professor Dr. Caroline Röhr

Koreferent: Professor Dr. Kurt Bucher

Tag des Promotionsausschusses: 06.12.2013





This picture is downloaded from internet





## ACKNOWLEDGEMENTS

During the past five years, Prof. Bucher supervised me of scientific investigations in the wide scopes of geochemistry, petrology and mineralogy and manuscript writing, which made this thesis possible. I have benefited a lot from the mentoring of Kurt in the field of thermodynamic modeling using various approaches. Other than varieties of in-door works conducted at Freiburg, I have also spent many happy and exciting days during field works at Alps and northern Norway, with Kurt and other colleagues. Now, when I am about to finish the thesis, and thus my PhD study under the supervision of Prof Bucher appears to be drawing to a conclusion, my first acknowledge is to express my heartfelt thanks and deep appreciation to Kurt for all that I benefited from his supervision, as well as his great patience.

My PhD study can only go on with many supports from many colleagues. Analysis of minerals using electron microprobe is a key part of my PhD study, and I have fortunately completed longtime work in the microprobe lab thanks to the supervision by Dr. Hiltrud Müller-Sigmund for which I appreciate her so much. I also wish to thank the secretaries, Mrs Christine Höher and Karin Eckmann, as they kindly helped me on many documents in German language. Other many staffs of in our institute, as well as PhD students, have helped me in many kinds of works, such as sample preparation, microprobe use, geological excursions, scientific discussion and professional conferences, and I would like to sincerely thank many colleagues for their helps, including Prof. Dr. Reto Gieré, Dr. Fleurice Parat, Susanne Schuble, Dagmar Flemming, Angela Thiemann, Isolde Schmidt, Sigrid Hirth-Walther, Melanie Schrage, Paul Robert Keppner, and also Dr. Weisenberger Tobias, Dr. Zeng Lü, Dr. Wei Zhou, Dr. Sebastian Weber, Hoa Thi Bich Hoang, Gang Mei and etc.

My five-year PhD study at the University of Freiburg has been financially supported by the China Scholarship Council (CSC), and research expense has been provided through scientific programs granted to Prof. Kurt Bucher. I would like to express my appreciations to these funds.

At last, I want to thank my parents for their continuous understanding and supports. I also appreciate my husband Dr. Chao Zhang (who was studying petrology at University of Hannover, northern Germany) for his considerable and meticulous discussion concerning the longtime costing PhD of mine, which is now presented in this thesis.

# INTRODUCTION

The Norwegian Caledonian orogenic belt is characterized by a series of thrust sheets that are grouped into the Uppermost Allochthon representing exotic Laurentian terranes, the Upper Allochthon representing the Iapetus oceanic lithosphere, and the Lower and Middle Allochthon representing the margin of Pre-Caledonian Baltica (Andresen, 1988; Ritzmann and Faleide, 2007; Roberts and Gee, 1985; Stephens and Gee, 1985), all of which thrust eastwards onto the Precambrian crystalline basement of the Baltic shield during the Silurian continental collision (ca. 431-428 Ma at Finnmark, Kirkland et al., 2006; Kirkland et al., 2007) between Baltica and Laurentia following the early Palaeozoic closure of the Iapetus Ocean (Gee, 1975; Roberts, 2003). The development of Norwegian Caledonian orogenic belt involves a series of sequential events: the formation of Iapetus ocean crust with associated initial rifting, the production of ophiolite, the subsequent consumption of ocean crust along a destructive plate margin, and a continent-continent collision with stacking of crusts, crustal thickening and lateral nappe displacements (e.g. Andersen et al., 1991; Bucher-Nurminen, 1991; Gee et al., 2012; Osmundsen and Andersen, 1994).

The Seiland Igneous Province (SIP) now resides within and as a part of the highest nappe of the Kalak Nappe Complex (KNC) which belongs to the Middle Allochthon, occupying an area of nearly 5,000 km<sup>2</sup> on the islands of Seiland, Sørøy and Stjernøy, and on the Øksfjord Peninsula in the northern Finnmark, Norway (Fig. 1).

The Seiland igneous province has a long and complex history concerning magmatic evolution: voluminous ultramafic rocks at 829±18 Ma (Krogh and Elvevold, 1990), layered gabbroic plutons of 700±33 Ma, 604±44 Ma and 570 Ma (Daly et al., 1991; Roberts et al., 2006) and a final stage of calc-alkaline intrusions represented by alkaline pyroxenite, syenite, nepheline syenite and carbonatite at 574± 5 Ma (Roberts et al., 2010). All these various rocks are considered to represent a synorogenic (Caledonian orogenic belt) intrusive activity evolved from tholeiitic basalt, compositionally ranging from high-K calc-alkaline magmas, through alkaline olivine basalt and picrite and finally to highly differentiated alkaline magmas and carbonatite (Appleyard, 1974; Robins and Gardner, 1975; Sturt et al., 1967; Sturt et al., 1978).

In this PhD thesis, I investigated the autometamorphism in the nepheline syenite on Stjernøy island (Chapter 1), and the zeolite formation (Chapter 2) and rare stronalsite-banalsite solid solution (Chapter 3) during hydrothermal events of nepheline syenite. In addition, water samples (Chapter 4) from the nepheline syenite-carbonatite attachment were analyzed and further explained through the zeolite formation. Metamorphism

in Øksfjord Peninsula was demonstrated by multiple metamorphism (Chapter 5) in contact aureole of the Rein fjord ultramafic complex, and metamorphism of parageneses from other five locations.

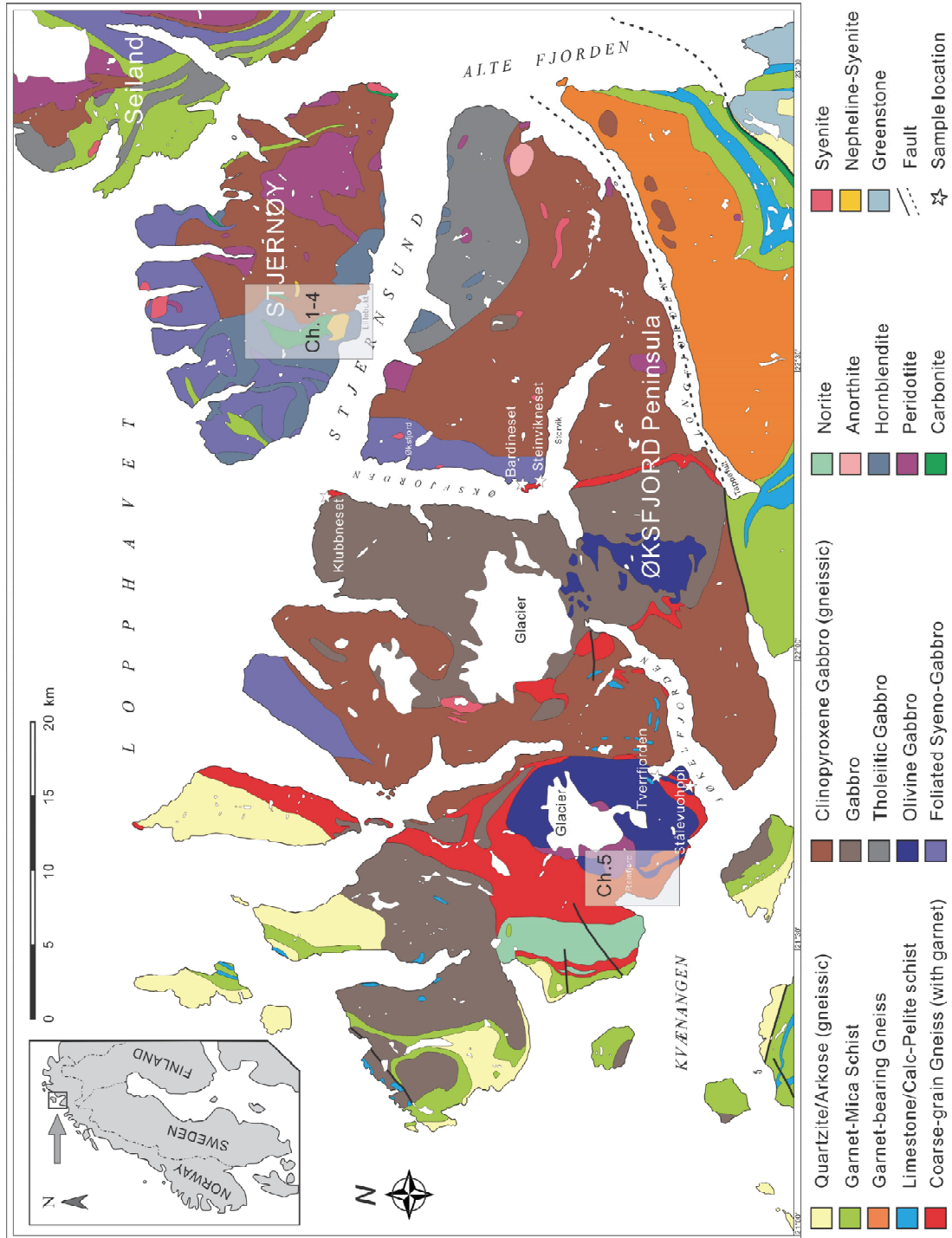


**Fig 1. Geological map of the Seiland Igneous Province, Northern Norway. Study areas for Chapter 1-4 and Chapter 5 are shown in the figure. Sampling locations for Chapter 6 are denoted as white stars.**

In Chapter 1, textures of nepheline syenite indicate a complex succession of reactions during cooling from an igneous crystallization stage to late hydrothermal events. Based on microscopic observation of primary and secondary minerals in the rock samples, the derived reactions, and the thermodynamic modeling for mineral assemblages, several conclusions concerning the evolution of nepheline syenite can be drawn: (1) Orthomagmatic stage of nepheline syenite is characteristic with assemblage of nepheline + K-feldspar + clinopyroxene + amphibole ± magnetite ± ilmenite at temperatures between ca. 500-700 °C at activity of silica being ca. 0.15-0.33. (2) Autometamorphic stage is represented by coronas of amphibole on clinopyroxene and biotite on amphibole, which are result from reactions between primary minerals and residual melt. (3) Hydrothermal stage I is impressed by pervasive natrolite transformed from nepheline and albite dissolution. The related fluid is considered as fluid expelled by crystallizing magma, which has decreasing silica activity and slightly increasing Na activity with the product of natrolite. (4) Hydrothermal stage II is dominated by infiltration of Ca-HCO<sub>3</sub> fluid from carbonatite catchment into the nepheline syenite along fractures which resulted in the generation of thomsonite by transformation from nepheline and natrolite.

In Chapter 2, I describe two hydrothermal stages in nepheline syenite. Hydrothermal stage I is impressed by pervasive natrolite transformed from nepheline and albite dissolution. The related fluid is considered as fluid expelled by crystallizing magma, which has decreasing silica activity and slightly increasing Na activity with the product of natrolite. Hydrothermal stage II is dominated by infiltration of Ca-HCO<sub>3</sub> fluid from carbonatite catchment into the nepheline syenite along fractures which resulted in the generation of thomsonite at low CO<sub>2</sub> partial pressures by transformation from nepheline and natrolite.

In Chapter 3, based on the investigation of secondary minerals from the nepheline syenite, combined with the microscopic, mineral composition and thermodynamic modeling, several conclusions concerning the formation of stronalsite-banalsite solid solution can be drawn. Stronalsite-banalsite solid solution and natrolite generated simultaneously through nepheline dissolution. The extra silica required for stronalsite-banalsite solid solution and natrolite is probably derived from dissolution of albite lamella in perthite. The fluid corresponding to formation of stronalsite-banalsite minerals is a diluted silica-poor fluid with maximal  $a_{\text{SiO}_2}$  value of  $10^{-8}$ .

In Chapter 4, I demonstrate that the water chemistry and secondary minerals are consequences of complicated water-rock interaction. Fluids from nepheline syenite is mostly dominated by NaSO<sub>4</sub> component, while fluids from carbonatite catchment Ca-HCO<sub>3</sub>. The variation among all fluids is resulted from mixing vector of NaSO<sub>4</sub> - Ca-HCO<sub>3</sub> to different extents. Albite dissolution provide the high NaSO<sub>4</sub> signature of the fluid in nepheline syenite,

the released SiO<sub>2</sub> simultaneously promote the precipitation of natrolite. Infiltration of Ca-HCO<sub>3</sub> fluid from carbonatite into the nepheline syenite along fractures has resulted in the generation of thomsonite by transformation from nepheline and natrolite, and calcite through precipitation in the middle of fluid conduit which indicates local disequilibrium between water and host rock. Thomsonite tends to be stabilized at low CO<sub>2</sub> partial pressures.

In Chapter 5, I present investigation on the contact aureole of the Reinfjord ultramafic complex, one of the largest layered peridotite and gabbro plutons in the Seiland Igneous Province. Three main stages in a chronological order could be summarized from the P-T conditions and mineral stability fields: (1) contact metamorphism at 850-900°C and 7.5-9.5 kbar; (2) uplift cooling with pressure decrease by ~3 kbar and temperature decrease by ~100°C (ends at 800°C and 6.5 kbar); (3) thrust cooling until 650°C and 10kbar. The first high temperature contact metamorphism was resulted from the Proterozoic emplacement of volumes of ultramafic rocks. The following uplift cooling corresponded to the initial rifting and extension. Sequential thrust cooling was accompanied with Caledonian crustal thinning and compression.

In Chapter 6, I offer mineralogical and thermodynamic constraints on the paragneisses from Øksfjord peninsula, and two main stages in a chronological order could be summarized from the P-T conditions and mineral stability fields of: (1) contact metamorphism at ca. 800°C and 5.5-6.5 kbar; (2) thrust cooling until 700°C and 9.5 kbar. The first high temperature contact metamorphism was deduced by the emplacement of volumes of ultramafic rocks. Sequential thrust cooling was accompanied with crustal thinning and compression.

## References

- Andersen, T.B., Jamtveit, B., Dewey, J.F. and Swensson, E., 1991. Subduction and exhumation of continental crust: major mechanisms during continent-continent collision and orogenic extensional collapse, a model based on the south Norwegian Caledonides. *Terra Nova*, 3(3): 303-310.
- Andresen, A., 1988. Caledonian terranes of Northern Norway and their characteristics. *Trabajos de geología*, 17: 103-117.
- Appleyard, E.C., 1974. Syn-orogenic igneous alkaline rocks of eastern Ontario and northern Norway. *Lithos*, 7(3): 147-169.
- Bucher-Nurminen, K., 1991. Mantle fragments in the Scandinavian caledonides. *Tectonophysics*, 190(2-4): 173-192.
- Daly, J.S., Aitchison, S.J., Cliff, R.A., Gayer, R.A. and Rice, A.H.N., 1991. Geochronological Evidence from Discordant Plutons for a Late Proterozoic Orogen in the Caledonides of

- Finmark, Northern Norway. *Journal of the Geological Society*, 148: 29-40.
- Gee, D., 1975. A tectonic model for the central part of the Scandinavian Caledonides. *American Journal of Science*, 275: 468–515.
- Gee, D.G., Janák, M., Majka, J., Robinson, P. and van Roermund, H., 2012. Subduction along and within the Baltoscandian margin during closing of the Iapetus Ocean and Baltica-Laurentia collision. *Lithosphere*.
- Kirkland, C.L., Daly, J.S., Eide, E.A. and Whitehouse, M.J., 2006. The structure and timing of lateral escape during the Scandian Orogeny: A combined strain and geochronological investigation in Finnmark, Arctic Norwegian Caledonides. *Tectonophysics*, 425(1-4): 159-189.
- Kirkland, Christopher L., Stephen Daly, J. and Whitehouse, Martin J., 2007. Provenance and Terrane Evolution of the Kalak Nappe Complex, Norwegian Caledonides: Implications for Neoproterozoic Paleogeography and Tectonics. *The Journal of Geology*, 115(1): 21-41.
- Krogh, E. and Elvevold, S., 1990. A Precambrian age for an early gabbro-monzonitic intrusive on the Øksfjord peninsula, Seiland Igneous Province, northern Norway. *Norsk Geologisk Tidsskrift*, 70(4): 267-273.
- Osmundsen, P.T. and Andersen, T.B., 1994. Caledonian Compressional and Late-Orogenic Extensional Deformation in the Staveneset Area, Sunnfjord, Western Norway. *Journal of Structural Geology*, 16(10): 1385-1401.
- Ritzmann, O. and Faleide, J.I., 2007. Caledonian basement of the western Barents Sea. *Tectonics*, 26(5): TC5014.
- Roberts, D., 2003. The Scandinavian Caledonides: event chronology, palaeogeographic settings and likely modern analogues. *Tectonophysics*, 365(1-4): 283-299.
- Roberts, D. and Gee, D.G., 1985. An introduction to the structure of the Scandinavian Caledonides. In Gee, D.G. & Sturt, B.A. (eds.) *The Caledonide orogen - Scandinavia and related areas*: 55-68.
- Roberts, R.J., Corfu, F., Torsvik, T.H., Ashwal, L.D. and Ramsay, D.M., 2006. Short-lived mafic magmatism at 560-570 Ma in the northern Norwegian Caledonides: U-Pb zircon ages from the Seiland Igneous Province. *Geological Magazine*, 143(6): 887-903.
- Roberts, R.J., Corfu, F., Torsvik, T.H., Hetherington, C.J. and Ashwal, L.D., 2010. Age of alkaline rocks in the Seiland Igneous Province, Northern Norway. *Journal of the Geological Society*, 167(1): 71-81.
- Robins, B. and Gardner, P.M., 1975. The magmatic evolution of the Seiland province, and Caledonian plate boundaries in northern Norway. *Earth and Planetary Science Letters*, 26(2): 167-178.
- Stephens, M.B. and Gee, D.G., 1985. A tectonic model for the evolution of the eugeoclinal terranes in central Scandinavian Caledonides. In Gee, D.G. & Sturt, B.A. (eds.) *The Caledonide orogen - Scandinavia and related areas*: 953-978.
- Sturt, B.A., Miller, J.A. and Fitch, F.J., 1967. The age of alkaline rocks from West Finnmark, northern Norway, and their bearing on the datings of the Caledonian orogeny. *Norsk Geologisk Tidsskrift*, 47: 255-273.
- Sturt, B.A., Pringle, I.R. and Ramsay, D.M., 1978. The Finnmarkian phase of the Caledonian Orogeny. *Journal of the Geological Society*, 135(6): 597-610.

# CURRICULUM VITAE

## XIAOYAN LI

Institut für Geowissenschaften  
Mineralogie – Geochemie  
Albertstr. 23b  
79104 Freiburg, Germany  
Email: xiaoyan.li@minpet.uni-freiburg.de  
Nationality: Chinese

## Education

2008/09 – current PhD in Petrology, Institut für Geowissenschaften, Universität Freiburg (Germany)  
2005/09 – 2008/08 Master in Petrology, Faculty of Earth Sciences, China University of Geosciences  
2001/09 – 2005/06 Bachelor in Geology, Faculty of Earth Sciences, China University of Geosciences

## Conference Abstracts

**Li Xiaoyan**, Bucher Kurt. 2012. Multiple partial melting events in the contact aureole of the Reinfjord ultramafic complex, Seiland Igneous Province, Northern Norway. European Mineralogical Conference 2012, Frankfurt.  
**Li Xiaoyan**, Bucher Kurt. 2011. The Lillebukt Alkaline Complex, Northern Norway. PERALK CARB 2011, Tübingen.

## Publications

Zhang Chao, Holtz Francois, Ma Changqian, Wolff Paul Eric, **Li Xiaoyan**. 2012. Tracing the evolution and distribution of F and Cl in plutonic systems from volatile-bearing minerals: A case study from the Liujiawa pluton (Dabie orogen, China). *Contributions to Mineralogy and Petrology*, 164(5): 859-879.

# TABLE OF CONTENTS

<b>Acknowledgements</b> .....	<b>i</b>
<b>Introduction</b> .....	<b>ii</b>
<b>Curriculum vitae</b> .....	<b>vii</b>

## **Part I     Autometamorphism of Nepheline Syenite from the Seiland**

### **Igneous Province, Northern Norway..... 1**

1. Abstract .....	2
2. Introduction .....	2
3. Geological background .....	3
4. Sample description and petrography.....	6
4.1 Sample description.....	6
4.2 Petrography.....	7
4.2.1 Samples 1145, 1147, 1148 and 1151 .....	7
4.2.3 Sample 926 .....	11
4.2.3 Textures under CL .....	12
5. Methods .....	12
5.1 Whole-rock analysis.....	12
5.2 Mineral analysis.....	12
5.3 Cathodoluminescence.....	13
6. Whole-rock geochemistry.....	13
7. Mineral composition.....	15
7.1 Clinopyroxene .....	15
7.2 Amphibole.....	16
7.3 Nepheline.....	18
7.4 Feldspar .....	19
7.5 Biotite.....	20
7.6 Fe-Ti oxides .....	21
7.7 Other minerals .....	21
8. Discussion .....	26
8.1 Evolutionary stages and related reactions .....	26
8.1.1 Orthomagmatic stage .....	26
8.1.2 Autometamorphic stage.....	26
8.1.3 Hydrothermal stage I.....	27



8.1.4 Hydrothermal stage II.....	29
8.2 Constraints on intrinsic parameters of orthomagmatic stage.....	30
8.2.1 Geochemical modeling method.....	30
8.2.2 Pressure estimation.....	30
8.2.3 Temperature and Silica activity.....	30
8.3 Fluid evolution.....	32
8.3.1 Geochemical modeling for mineral stability diagram.....	32
8.3.2 Fluid evolution derived from zeolite stability diagram.....	32
8.3.2.1 Fluid property of hydrothermal stage I.....	32
8.3.2.2 Fluid property of hydrothermal stage II.....	32
8.4 Redox reactions.....	34
9. Conclusions.....	34
References.....	35

## **Part II Zeolites in Nepheline Syenite of Seiland Igneous Province, Northern Norway..... 39**

1. Abstract.....	40
2. Introduction.....	40
3. Geological background.....	41
4. Sample description and petrography.....	43
4.1 Sample description.....	43
4.2 Petrography of host nepheline syenite.....	43
4.3 Textures related with Zeolite.....	46
5. Methods.....	46
5.1 Whole-rock analysis.....	46
5.2 Mineral analysis.....	46
5.3 Geochemical modeling for mineral stability diagram.....	47
6. Whole-rock geochemistry and mass changes.....	47
7. Mineral composition.....	49
7.1 Zeolite.....	49
7.1.1 Natrolite.....	49
7.1.2 Thomsonite.....	49
7.2 Nepheline.....	51
7.3 Feldspar.....	52
8. Discussion.....	52
8.1 Hydrothermal stage I.....	53
8.2 Hydrothermal stage II.....	54
8.3 Fluid evolution derived from zeolite stability diagram.....	56
8.3.1 Fluid property of hydrothermal stage I.....	57

8.3.2 Fluid property of hydrothermal stage II.....	58
8.3.3 Partial pressure of CO <sub>2</sub> .....	58
9. Conclusions.....	59
References.....	59

### **Part III Stronalsite-Banalsite in Nepheline Syenite of Seiland**

#### **Igneous Province, Northern Norway ..... 62**

1. Abstract .....	63
2. Introduction.....	63
3. Geological background.....	64
4. Petrography.....	66
4.1 Petrography of host nepheline syenite.....	66
4.2 Petrography related with Zeolite .....	66
4.3 Petrography related with Stronalsite-Banalsite .....	66
5. Mineral composition .....	69
5.1 Mineral analysis method .....	69
5.2 Stronalsite-Banalsite.....	69
5.3 Zeolite.....	72
5.4 Nepheline .....	73
6. Discussion.....	73
6.1 Stronalsite-Banalsite forming Reactions .....	73
6.1.1 Reactions related with Natrolite.....	73
6.1.2 Reactions related with Stronalsite-Banalsite.....	74
6.2 Formation condition .....	75
6.2.1 Geochemical modeling for mineral stability diagram.....	75
6.2.2 Formation condition derived from natrolite stability .....	75
7. Conclusions.....	77
References.....	77

### **Part IV Fluid Property and Water-Rock Interaction in the**

#### **Alkaline Complex of Seiland Igneous Province, Northern Norway . 80**

1. Abstract .....	81
2. Introduction.....	81
3. Geology and petrography.....	82

3.1 Geology of the study area.....	82
3.2 Petrography of host rocks.....	84
3.2.1 Nepheline syenite.....	85
3.2.2 Carbonatite.....	87
4. Methods.....	87
4.1 Analytical methods of water.....	87
4.2 Geochemical modeling for water.....	87
4.3 Geochemical modeling for mineral stability diagram.....	88
5. Hydrochemistry.....	88
5.1 Type A: Ca-HCO <sub>3</sub> type.....	91
5.2 Type B: Ca-Na-HCO <sub>3</sub> -SO <sub>4</sub> type.....	91
5.3 Type C: Ca-Na-HCO <sub>3</sub> -Cl type.....	91
5.4 Type D: Na-Ca-HCO <sub>3</sub> -Cl-SO <sub>4</sub> type.....	92
5.5 Type E: Na -SO <sub>4</sub> -Cl mixture type.....	92
5.6 Redox potential.....	92
5.7 Mixing vector.....	93
6. Discussions.....	94
6.1 Equilibrium temperature of waters.....	94
6.2 The saturation state of the water.....	95
6.3 Mineral stability diagrams.....	102
6.4 Partial pressure of CO <sub>2</sub> .....	103
6.5 Strontium and barium.....	107
6.6 Reactions controlling the water component.....	107
7. Conclusions.....	108
References.....	109

**Part V      Multiple metamorphism in the contact aureole of the  
Reinfjord ultramafic complex, Seiland Igneous Province, Northern  
Norway .....113**

1. Abstract.....	114
2. Introduction.....	114
3. Geological background.....	115
4. Methods.....	118
4.1 Sampling.....	118
4.2 Whole-rock analysis.....	118
4.3 Mineral analysis.....	118
4.4 Cathodoluminescence.....	118
4.5 Phase diagram modeling.....	124

5 Petrography and mineral chemistry.....	124
5.1 Textures under CL.....	124
5.2 Sample 1286 and 1290.....	126
5.3 Sample 1125 and 1291.....	128
5.4 Sample 1284 and 1289.....	128
5.5 Sample 1283.....	131
6. P-T conditions estimated by phase diagrams.....	132
6.1 Sample 1286 and 1290.....	132
6.1.1 Sample 1286.....	132
6.1.2 Sample 1290.....	132
6.2 Sample 1125 and 1291.....	135
6.2.1 Sample 1125.....	135
6.2.2 Sample 1291.....	135
6.3 Sample 1284 and 1289.....	136
6.3.1 Sample 1284.....	136
6.3.2 Sample 1289.....	136
6.4 Sample 1283.....	138
7. Metamorphic evolution.....	138
7.1 Peak metamorphic condition.....	138
7.2 Uplift cooling.....	138
7.3 Thrust cooling.....	139
8. Implications for tectonic evolution.....	140
9. Conclusions.....	141
References.....	141

**Part VI      Regional metamorphism in the paragneisses of Seiland  
Igneous Province, Northern Norway ..... 144**

1. Abstract.....	145
2. Introduction.....	145
3. Geological background and sampling.....	147
3.1 Geological background.....	147
3.2 Sampling.....	147
4. Methods.....	148
4.1 Whole-rock analysis.....	148
4.2 Mineral analysis.....	148
4.3 Cathodoluminescence.....	148
4.4 Phase diagram modeling.....	155
5 Petrography and mineral chemistry.....	155
5.1 Textures under CL.....	155

5.2 Samples from Tverrfjorden.....	156
5.2.1 Sample 1031.....	156
5.2.2 Sample 1032.....	157
5.2.3 Sample 1214.....	158
5.2.4 Sample 1215.....	158
5.3 Samples from Stålevuohppi.....	158
5.3.1 Sample 1191.....	158
5.3.2 Sample 1193.....	158
5.4 Samples from Steinvikneset.....	159
5.4.1 Sample 1041.....	159
5.4.2 Sample 1042.....	159
5.5 Samples from Bardineset.....	160
5.5.1 Sample 1271.....	160
5.5.2 Sample 1276.....	162
5.6 Sample 1240 from Klubbneset.....	162
6. P-T conditions estimated by phase diagrams.....	163
6.1 Samples from Tverrfjorden.....	163
6.1.1 Sample 1031.....	163
6.1.2 Sample 1032.....	163
6.1.3 Sample 1214.....	166
6.1.4 Sample 1215.....	166
6.2 Samples from Stålevuohppi.....	166
6.2.1 Sample 1191.....	166
6.2.2 Sample 1193.....	167
6.3 Samples from Steinvikneset.....	167
6.3.1 Sample 1041.....	167
6.3.2 Sample 1042.....	170
6.4 Samples from Bardineset.....	170
6.4.1 Sample 1271.....	170
6.4.2 Sample 1276.....	172
6.5 Sample 1240 from Klubbneset.....	172
7. Metamorphic evolution .....	175
7.1 Peak metamorphic condition.....	175
7.2 Thrust cooling.....	175
8. Implications for tectonic evolution .....	175
9. Conclusions.....	176
References.....	176

## Appendixes

Appendix A. Thin section scans.....	179
Appendix B. Photomicrographs of textures .....	193
Appendix C. Phase diagrams of P-T modeling.....	239
Appendix Tables. Mineral compositions .....	261
Table 1. Garnet.....	261
Table 2. Feldspar .....	324
Table 3. Biotite.....	353
Table 4. Pyroxene.....	367
Table 5. Muscovite .....	374
Table 6. Amphibole.....	375
Table 7. Chlorite.....	381
Table 8. Epidote .....	382
Table 9. Titanite.....	383
Table 10. Magnetite .....	385
Table 11. Hercynite.....	387
Table 12. Ilmenite.....	389
Table 13. Rutile.....	392
Table 14. Sillimanite.....	396
Table 15. Corundum .....	399
Table 16. Nepheline.....	400
Table 17. Zeolite.....	404
Table 18. Stronalsite-Banalsite.....	413

**Part I      Autometamorphism of Nepheline  
Syenite from the Seiland Igneous Province,  
Northern Norway**

## 1. Abstract

Peralkaline igneous rocks crystallize from volatile-rich melts, from which residual fluids cause autometamorphism during cooling. Textures of nepheline syenite from the Seiland Igneous Province (Northern Norway) indicate a complex succession of reactions during cooling from an igneous crystallization stage to late hydrothermal events. Based on microscopic observation of primary and secondary minerals in the rock samples, the derived reactions, and the thermodynamic modeling for mineral assemblages, several conclusions concerning the evolution of nepheline syenite can be drawn: (1) Orthomagmatic stage of nepheline syenite is characteristic with assemblage of nepheline + K-feldspar + clinopyroxene + amphibole  $\pm$  magnetite  $\pm$  ilmenite at temperatures between ca. 500-700 °C at activity of silica being ca. 0.15-0.33. (2) Autometamorphic stage is represented by coronas of amphibole on clinopyroxene and biotite on amphibole, which are result from reactions between primary minerals and residual melt. (3) Hydrothermal stage I is impressed by pervasive natrolite transformed from nepheline and albite dissolution. The related fluid is considered as fluid expelled by crystallizing magma, which has decreasing silica activity and slightly increasing Na activity with the product of natrolite. (4) Hydrothermal stage II is dominated by infiltration of Ca-HCO<sub>3</sub> fluid from carbonatite catchment into the nepheline syenite along fractures which resulted in the generation of thomsonite by transformation from nepheline and natrolite.

## 2. Introduction

The magmatic evolution of silica undersaturated alkaline rocks, which represent some of the most highly differentiated magmatic rocks, has received considerable interest due to their metasomatized mantle origin (e.g. Markl et al., 2010; Marks et al., 2008), their fluid-rich character (e.g. Krumrei et al., 2007; Sørensen, 1980), the associated autometamorphism and the extensive connected metasomatic alteration of country rocks (e.g. Mitchell and Liferovich, 2006; Schönenberger et al., 2006). Representative studies of alkaline complexes worldwide, such as Ilímaussaq and Motzfeldt complex in South Greenland (e.g. Finch et al., 2001; Konnerup-Madsen, 2001; Markl, 2001; Marks et al., 2007), Khibina and Lovozero complex of Kola Peninsula (e.g. Beeskow et al., 2006; Korobeinikov et al., 2000; Potter et al., 2004), Tamazeght complex in Morocco (Marks et al., 2008; Schilling et al., 2009), and Strange lake complex in Quebec-Labrad (Boily and Williams-Jones, 1994; Salvi and Williams-Jones, 1997), have improved our understanding of the nature and origin of alkaline rocks.

Agpaitic and miaskitic nepheline syenites are two common types among all kinds of



silica undersaturated peralkaline rocks investigated. The agpaitic nepheline syenite is characterized by chlorine and fluorine-rich volatiles and the presence of complex Na-Zr silicates like eudialyte and rinkite (Sørensen, 1980; Sørensen, 1992; Sørensen, 1997). Miaskitic nepheline syenite contains common minerals like zircon, limenite and titanite. Both types have a broad magmatic crystallization interval from 950°C until 500°C (e.g. Marks and Markl, 2003; Sørensen, 1997). Parameters (e.g. T,  $fO_2$ ,  $aSiO_2$ , fluid) controlling the sequence of mineral assemblages during agpaitic and miaskitic magma evolution have been derived from studies of mineral composition, fluid inclusion, isotope data and phase diagram (e.g. Fall et al., 2007; Mann et al., 2006; Markl and Baumgartner, 2002; Schilling et al., 2009; Schönenberger et al., 2008; Schönenberger and Markl, 2008). For instance, fluid-solid REDOX reactions transform reduced miaskitic rocks ( $\Delta FMQ = -1$ , Fe<sup>2+</sup>-rich, arfvedsonite, zircon) to more oxidized ( $\Delta FMQ = +5$  or even above HM, Fe<sup>3+</sup>-rich, aegirine, eudialyte) agpaitic assemblages with decreasing temperature and an overall increase of Na (+K) in the melt. The associated C-H-S-O fluid is methane-rich in reduced miaskitic melts and CO<sub>2</sub>-rich in oxidized agpaitic melts (Schönenberger et al., 2008).

Generally, the evolution of agpaitic and miaskitic nepheline syenite along the cooling path can be divided into four stages: (1) orthomagmatic stage with primary igneous crystallization of minerals, (2) late magmatic stage represented by reactions between residual melt and crystallizing minerals, (3) post magmatic stage characterized by replacement of primary minerals with fluid expelled by melt, and (4) late hydrothermal alteration related to infiltration of external fluids (e.g. Berger et al., 2009; Graser and Markl, 2008; Marks and Markl, 2003; Marks et al., 2007; Schilling et al., 2009).

In this study, we present the magmatic and fluid evolution history from the orthomagmatic to the late hydrothermal alteration stages of the miaskitic nepheline syenite from the Seiland Igneous Province (SIP) of Finnmark, Northern Norway. Detailed texture analysis permits to derive a sequence of reactions, which allows quantifying the redox processes and the local reactions during autometamorphism of the syenite during cooling.

### 3. Geological background

The Seiland igneous province occupies an area of nearly 5,000 km<sup>2</sup> on the islands of Seiland, Sørøy and Stjernøy, and on the Øksfjord Peninsula in the northern Finnmark, Norway (Fig. 1). The province is located within the Kalak nappe complex of the Norwegian Caledonian orogenic belt, which has thrust eastwards onto the Precambrian crystalline basement of the Baltic shield during the Silurian continental collision (ca. 431-428 Ma at Finnmark, Kirkland et al., 2006; Kirkland et al., 2007) between Baltica and Laurentia following the early Palaeozoic closure of the

Iapetus Ocean (Gee, 1975; Roberts, 2003). The Seiland igneous province has a long and complex history concerning magmatic evolution: voluminous ultramafic rocks at  $829\pm 18$  Ma (Krogh and Elvevold, 1990), layered gabbroic plutons of  $700\pm 33$  Ma,  $604\pm 44$  Ma and 570 Ma (Daly et al., 1991; Roberts et al., 2006) and a final stage of calc-alkaline intrusions represented by alkaline pyroxenite, syenite, nepheline syenite and carbonatite at  $574\pm 5$  Ma (Roberts et al., 2010). All these various rocks are considered to represent a synorogenic (Caledonian orogenic belt) intrusive activity evolved from tholeiitic basalt, compositionally ranging from high-K calc-alkaline magmas, through alkaline olivine basalt and picrite and finally to highly differentiated alkaline magmas and carbonatite (Appleyard, 1974; Robins and Gardner, 1975; Sturt et al., 1967; Sturt et al., 1978).

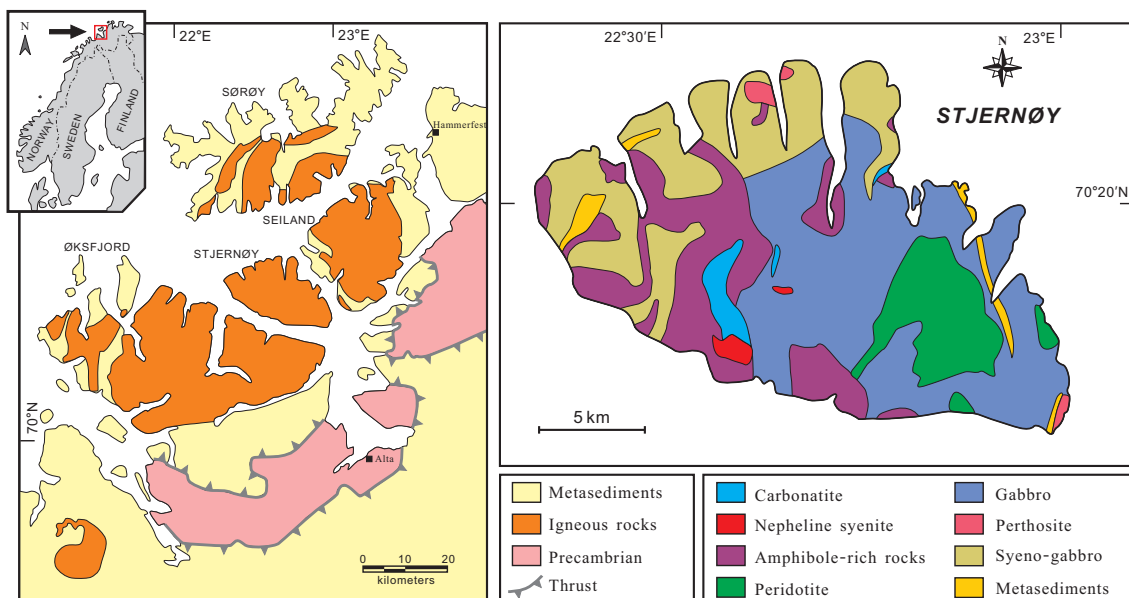


**Fig. 1 (a) Geological sketch of the Seiland Igneous Province, Northern Norway modified after Robins and Gardner (1975). (b) Simplified geological map of the Stjernøy Island.**

The Lillebukt alkaline complex (Fig. 2), on Stjernøy Island, is enclosed in the ultramafic and mafic rocks of peridotite, pyroxenite, gabbro and hornblendite (Heier, 1961; Oosterom, 1963). The boundary is blurred and thus the relationship between the alkaline complex and the hosting rocks is unclear. The alkaline complex is composed of syenite, nepheline syenite, and carbonatite, all of which have been intruded by late mafic and syenite dikes, and pegmatites (Pedersen et al.,

1989; Robins and Tysseland, 1980). The silico-carbonatite of the Lillebukt alkaline complex is closely related to the nepheline syenite and contains abundant amphibole, biotite and apatite in the silicate-rich layers (Robins and Tysseland, 1983; Strand, 1980). It has been suggested that the carbonatite represents the latest igneous activity of the Caledonian orogeny (Robins and Gardner, 1975). The nepheline syenite has been mined by North Cape Minerals in an open pit on Nabberen (earlier in an underground mine inside Nabberen) and the raw material is processed at the Lillebukt plant. The fine powdered nepheline - K-feldspar mixture is shipped from the small port to customers in the ceramics and glass industry worldwide.

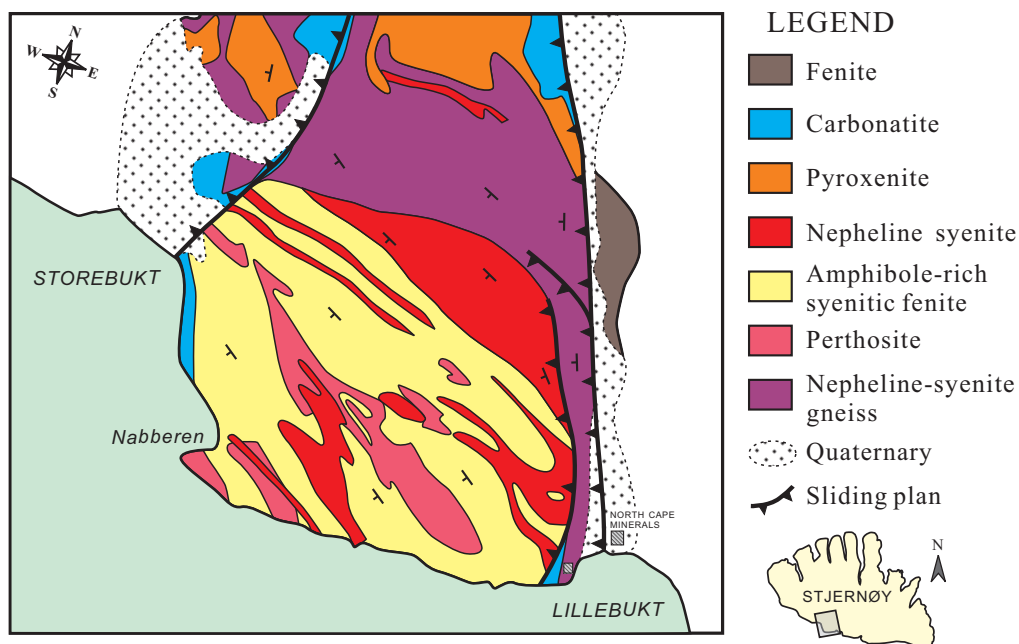


**Fig. 2 Detailed geological map of Lillebukt alkaline complex on the Stjernøy Island.**

The Nabberen nepheline syenite body is a lens-shaped stock located in the north of the summit of Nabberen (Fig. 2), which occupies an area of  $1700 \times 300 \text{ m}^2$  (Geis, 1979). It is a miaskitic nepheline syenite characterized by high concentration of alkalis, Ba and Sr, and depletion of REE, Y, Nb, Sc, Zr, U, and Th (Heier, 1964; Heier and Taylor, 1962; Heier, 1966; Robins and Tysseland, 1980). The surrounding gabbros have been fenitized, probably by the low-density fluid expelled from the volatile-rich alkaline magmas which now crystallized as nepheline syenite and carbonatite (Appleyard, 1980; Kjøsnes, 1980; Robins, 1984; Robins and Tysseland, 1980; Robins and Tysseland, 1983). Hydrothermal assemblages including zeolites (natrolite) and clay minerals (palygorskite, a magnesium clay mineral) have been observed in the

Lillebukt mine, and they were regarded as products of post-tectonic low-temperature reactions with groundwater (Geis, 1979; Holdridge, 1962; Salter and Appleyard, 1974).

## 4. Sample description and petrography

### 4.1 Sample description

During extended field work 2003 and 2009 a large number of samples and field data (structures, textures) have been collected from the old mine tunnels, the open pit and from natural outcrops including samples from the carbonatite. We selected five representative rock samples from that collection for detailed investigation. All samples are from the Nabberen nepheline syenite mine. Specifically, samples 1145, 1147 and 1148 are from the underground tunnels, sample 1151 from the open pit of the Nabberen summit and sample 926 from a core from an exploration borehole. All the samples are massive and have no preferred orientation of minerals.

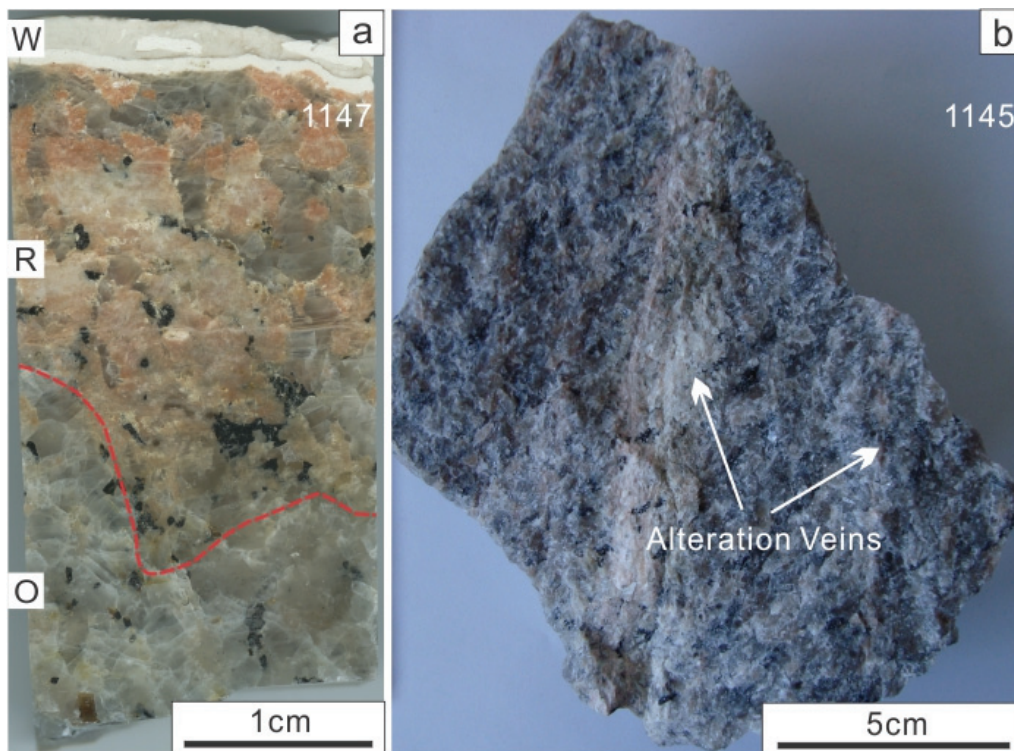


**Fig. 3 (a) Nepheline syenite sample 1147 which illustrating alteration phenomenon. O: Original part; R: Reaction zone; W: White vein. (b) Nepheline syenite sample 1145 with fine alteration seams.**

In samples 1147, 1148 and 1151, white reaction veins are generally less than 1 cm in width and can be clearly identified (Fig. 3). Wide veins (up to 5 mm) are accompanied by bilateral reaction zones (up to 2 cm). These bilateral reaction zones display a reddish color distinctive from the white veins and the gray original nepheline syenite (Fig. 3a). In addition, there are numerous irregular fine seams (less than 1 mm wide) which can be identified under careful observation by their indistinct white color and occasionally reddish reaction speckles along the seams (Fig. 3b). These tiny seams cut each other and form a network over the whole sample. The white alteration veins are entirely composed of fine-grained brown-grey zeolite aggregates. The rock matrix of nepheline syenite is mainly composed of potassium feldspar (40 %), nepheline (35 %), amphibole (10 %) and clinopyroxene (5 %), with accessory albite, biotite, apatite, titanite, magnetite, ilmenite, calcite and zeolite. There is no difference in mineral constituents between rock matrix and reaction zones, except more intense alteration of nepheline in the latter.

Sample 926 has a clear dark gray color, and is thus considered to be formed without significant alteration. Therefore, the alteration degree of our samples can be simply arranged as 1148, 1147, 1151, 1145 and 926 from high to low.

## 4.2 Petrography

### 4.2.1 *Samples 1145, 1147, 1148 and 1151*

Light green clinopyroxene occurs as prismatic crystals (up to 1 cm) with irregular grain boundaries and inclusions of apatite. Most amphiboles appear as dark green coronas around or thin rims along clinopyroxene (Fig. 4a-d). Fine vermiform amphibole crystals coarsening outward forming the corona (Fig. 4d). There are also amphibole rims around calcite crystals adjacent to the clinopyroxene (Fig. 4d). A few amphibole crystals also show prismatic crystals. Potassium feldspar and nepheline are large anhedral to subhedral crystals, which coexist with each other in textural equilibrium, indicative of approximately contemporaneous crystallization. Tiny anhedral apatite crystals are distributed sporadic in the matrix and as inclusions in clinopyroxene and amphibole (Fig. 4d). Titanite occurs as euhedral crystals or rims around magnetite and ilmenite (Fig. 4e). Minor hercynite crystals are present close to the margin of the magnetite rimmed by titanite (Fig. 4e). Rare biotite crystals are found together with ilmenite and magnetite (Fig. 4f).

Potassium feldspars show widespread perthite textures with albite as blade or drop shaped lamellae. The site of albite lamellae has become cavity likely due to dissolution (Fig. 5a). Nepheline crystals are speckled or replaced by fine-grained zeolite and diaspore (Fig. 5b). In the

white veins within nepheline syenite, mixture of fine-grained natrolite and thomsonite occurs as rounded spots with diameter of ca. 0.5 mm (Fig. 5c). Calcite-rich veins in the nepheline syenite are accompanied with natrolite, thomsonite and Sr-rich thomsonite (Fig. 5d). Natrolite grains are overgrown by thomsonite locally in all samples (Fig. 5e). Stronalsite-banalsite solid solution minerals are present in nepheline grains which are enriched in fissures (Fig. 5b).

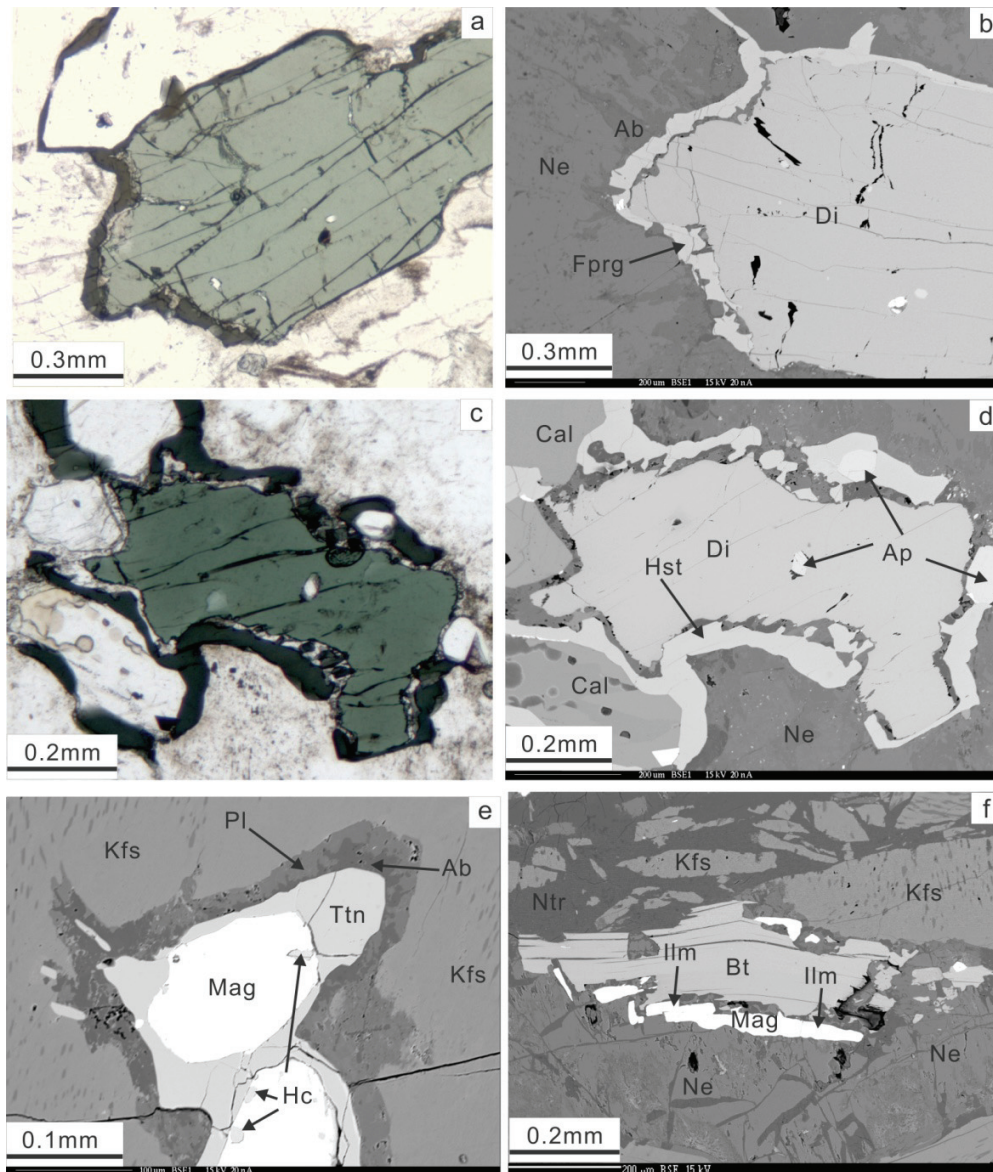


**Fig. 4** Photomicrographs (under plane-polarized light) and BSE images of mineral textures in nepheline syenite samples. See text for explanations.

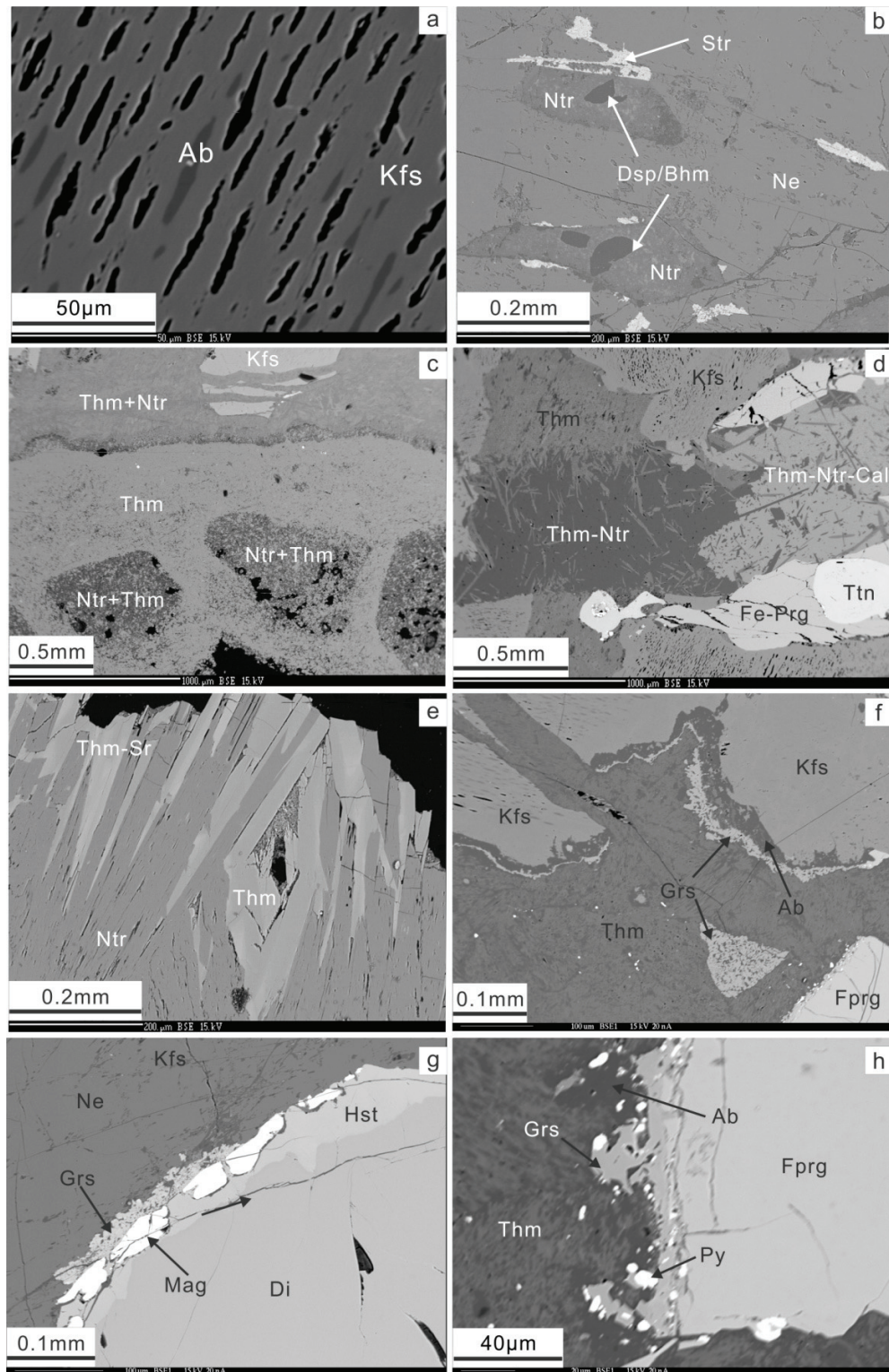


**Fig. 5** BSE images showing various secondary mineral textures. See text for explanations.

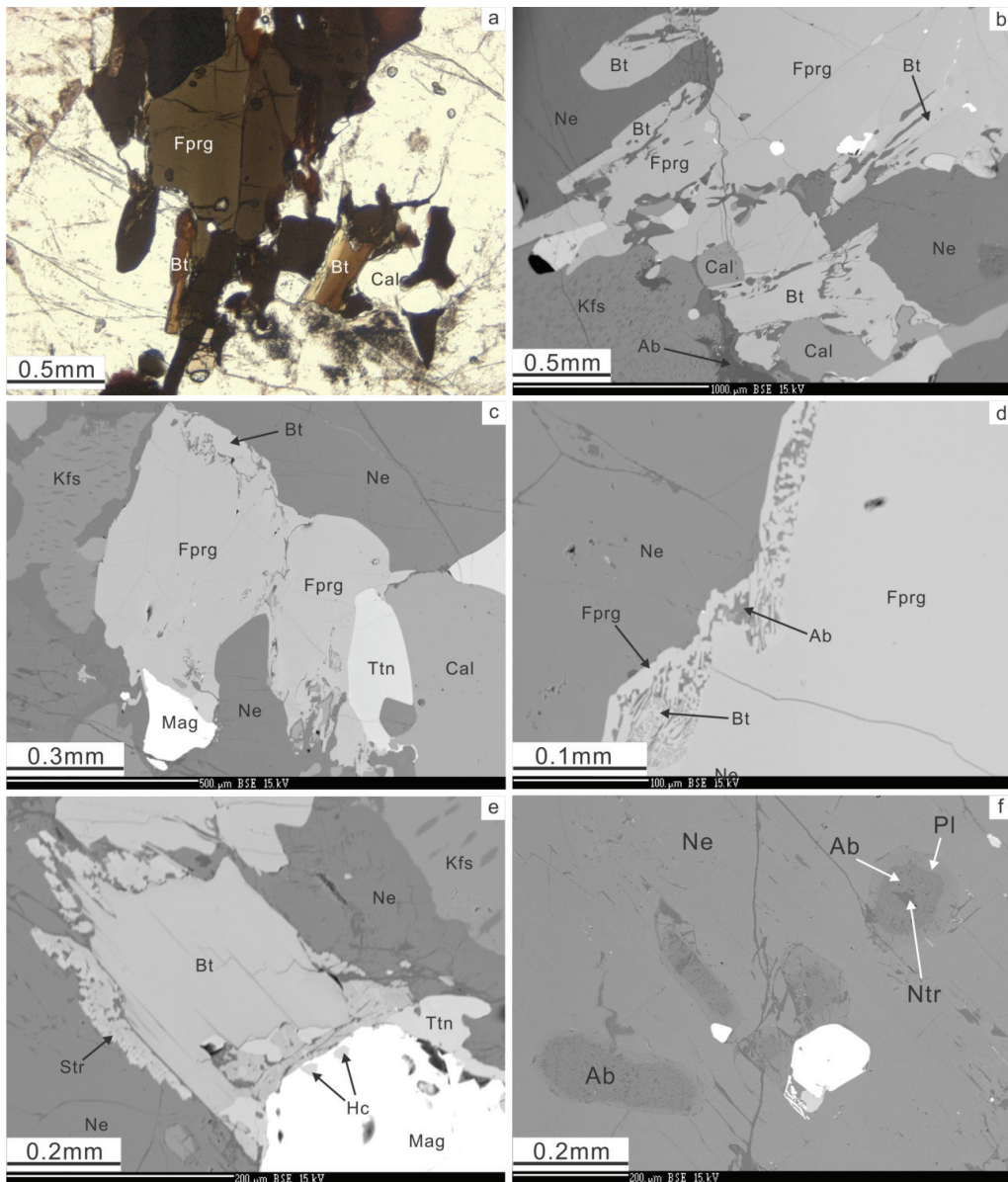


**Fig. 6 Photomicrographs (under plane-polarized light) and BSE images of mineral textures in sample 926. See text for explanations.**

Three special mineral assemblages can be observed that involve garnet: grossular-albite between zeolite vein and potassium feldspar (Fig. 5f); grossular-magnetite pairs between nepheline and clinopyroxene (Fig. 5g), and grossular-pyrite pairs attached to amphibole crystals (Fig. 5h).



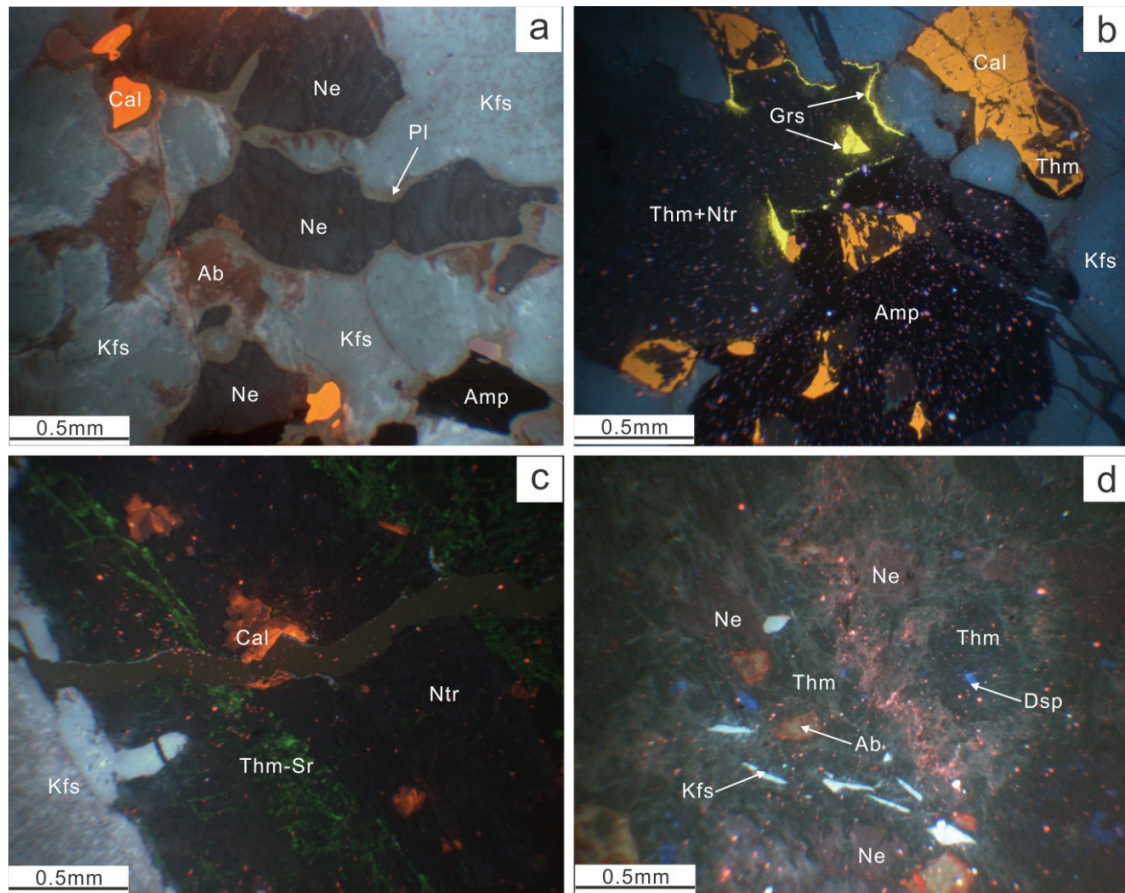


**Fig. 7** Cathodoluminescence (CL) images of mineral textures. See text for explanations.

#### 4.2.3 Sample 926

In contrast to the nepheline syenite samples described above, sample 926 contains amphibole as a dominant mafic mineral phase whereas pyroxene is absent. The amphiboles are euhedral or subhedral grains with a long axis varying from 0.5 to 2 mm, and sometimes form aggregates (Fig. 6a). In addition, amphibole grains are commonly replaced by needle-like biotite crystals (Fig. 6b), thin biotite rims (Fig. 6c), or vermiform intergrowth of biotite and albite (Fig. 6d). A few isolated biotite crystals are locally rimmed by stronalsite aggregates (Fig. 6e). Some magnetite grains can be rimmed by titanite together with minor hercynite (Fig. 6e), and enclose tiny apatite and amphibole inclusions.

### ***4.2.3 Textures under CL***

As revealed by cathodoluminescence (CL) images (Fig. 7), Fe-rich minerals such as clinopyroxene, amphibole and Fe-Ti oxides are dark black in color, K-feldspar shows light to deep grayed blue, and nepheline shows deep blue in color. Albite occurs as interstitial phases between K-feldspar and nepheline, showing a brown red CL color. Plagioclase occurs only as overgrowth (rim) around nepheline with dark gray CL color (Fig. 7a). Grossular, which occurs as rims between K-feldspar and thomsonite-natrolite aggregate, shows a clear bright yellow CL color (Fig. 7b). Calcite shows a remarked bright orange CL color; at some locations, calcite grains are partly corroded and replaced by thomsonite which is black in CL color (Fig. 7b). Another type of Sr-rich thomsonite which is greenish in CL color has been observed, and its textural features have been described above (Fig. 7c). Spotty diaspore shows indigo blue, occurring as tiny inclusions within thomsonite (Fig. 7d).

## **5. Methods**

### **5.1 Whole-rock analysis**

The composition of the rock samples was analyzed at the Institute of Geosciences, University of Freiburg. A Philips 2404 X-ray fluorescence spectrometer was used with element specific acceleration voltage 30 kV and current 40 nA, with fused beads for major elements and powder pellets for minor elements, respectively. Loss on ignition (LOI) was determined to complete the XRF analyses, and total Fe is reported as Fe<sub>2</sub>O<sub>3</sub>tot. FeO contents are analyzed by titrimetry method using KMnO<sub>4</sub> and 40% HF.

### **5.2 Mineral analysis**

Mineral analyses were performed by electron beam microanalysis using wavelength-dispersive spectrometry (WDS) of a digital CAMECA SX100 electron microprobe at the Institute of Geosciences, University of Freiburg. During analyses an accelerating voltage of 15 kV and a current of 20 nA were used. Beam diameter was 0.5 μm (for feldspar, sometimes 5 μm). We used the stoichiometric method of Droop (1987) to estimate the ferrous and ferric iron contents in clinopyroxene, amphibole and garnet. With regard to amphibole, the basis of 23 oxygen and 16 cations (including Ca, Na and K on a fully filled A site) were used to obtain the stoichiometric formula.

### 5.3 Cathodoluminescence

Cathodoluminescence (CL) images were obtained by ELM-3R luminoscope at the Institute of Geosciences, University of Freiburg with an accelerating voltage of 12 kV and beam current of 0.8 mA. All the CL images were captured by Leica DC500 camera with exposure time of 60s.

## 6. Whole-rock geochemistry

Whole-rock major and trace element compositions are given in Table 1. Following the sample description above, samples 1147, 1148 and 1151 analyses have been performed on both the original unaltered rock (O) and the reaction zones (R), while from sample 1145 only original rock (O) and from sample 926 the bulk rock has been analyzed. All samples have relatively high aluminum and alkali concentrations, which are the typical character of alkaline rocks.

Samples 1147 and 1148 have similar element ratio variation trends from original to reaction zone:  $\text{Na}_2\text{O}/\text{K}_2\text{O}$  molar ratio decreases from 1.31 to 1.02 and from 1.35 to 1.06, respectively. Corresponding  $\text{Fe}^{2+}/\text{Fe}^{3+}$  ratio decrease from 1.22 to 1.16 and from 1.30 to 1.09, respectively (Table 1). In contrast, sample 1151 has an opposite variation trend of  $\text{Na}_2\text{O}/\text{K}_2\text{O}$  molar ratio from 1.32 to 1.16 and of  $\text{Fe}^{2+}/\text{Fe}^{3+}$  ratio from 0.78 to 0.86 (Table 1). In addition, sample 1145O has the highest  $\text{Na}_2\text{O}/\text{K}_2\text{O}$  molar ratio of 1.47 and the highest  $\text{Fe}^{2+}/\text{Fe}^{3+}$  ratio of 1.67, while sample 926 has medium values of the two ratios, i.e. 1.20 and 1.15, respectively (Table 1). The peralkalinity index (= molar  $(\text{Na}_2\text{O}+\text{K}_2\text{O})/\text{Al}_2\text{O}_3$ ) for original zones of all samples have a similar value about 0.91, and decrease to 0.66 for reaction zones (Table 1). Compared to original rocks, the CaO content is raised in the reaction zones of samples 1147 and 1148. LOI is significantly increased in all reaction zones.

All the samples have relatively high concentrations of Ba and Sr, and low contents of Sc, U, Th, Pb, Ta and Hf, which reflecting the miaskitic character of the alkaline rocks. The trace element data are consistent with earlier data obtained in this area (Appleyard, 1974; Heier, 1964; Heier, 1965). Compared to the original rock matrix, Sr and Ba are markedly enriched in the reaction zones, while S is depleted and Cl strongly depleted. Other elements do not show significant changes in the reaction zones.

Table 1 Major and trace element compositions and CIPW of nepheline syenite samples.

Sample	1145 O	1147 O	1147 R	1148 O	1148 R	1151 O	1151 R	Kb926
Oxide (wt%)								
SiO <sub>2</sub>	54.36	53.87	53.57	53.84	53.62	53.31	54.29	54.02
TiO <sub>2</sub>	0.27	0.35	0.38	0.35	0.40	0.50	0.50	0.33
Al <sub>2</sub> O <sub>3</sub>	24.07	24.00	23.02	24.16	23.11	23.11	22.81	22.60
Fe <sub>2</sub> O <sub>3</sub> tot	1.85	2.24	2.42	2.12	2.25	2.95	2.75	2.40
MnO	0.03	0.05	0.05	0.04	0.05	0.06	0.06	0.05
MgO	0.04	0.08	0.12	0.07	0.13	0.14	0.17	0.16
CaO	1.52	1.79	4.11	1.70	4.33	2.69	2.64	2.16
Na <sub>2</sub> O	7.82	7.46	4.78	7.68	4.78	7.32	6.09	6.84
K <sub>2</sub> O	8.06	8.66	7.14	8.66	6.90	8.43	7.95	8.65
P <sub>2</sub> O <sub>5</sub>	0.03	0.04	0.05	0.04	0.05	0.06	0.07	0.05
LOI	1.50	1.01	4.42	0.81	4.68	1.08	2.42	1.48
SUM	99.55	99.55	100.06	99.47	100.30	99.65	99.75	98.74
FeO*	1.10	1.14	1.22	1.08	1.07	1.24	1.24	1.27
Fe <sub>2</sub> O <sub>3</sub> calc	0.63	0.97	1.06	0.92	1.06	1.57	1.37	0.99
H <sub>2</sub> O	1.40	0.85	4.97	0.53	5.37	0.38	2.74	0.82
CO <sub>2</sub>	0.59	0.53	0.13	0.49	0.08	0.93	0.20	1.03
Na <sub>2</sub> O/ K <sub>2</sub> O	1.47	1.31	1.02	1.35	1.05	1.32	1.16	1.20
(Na <sub>2</sub> O+ K <sub>2</sub> O) / Al <sub>2</sub> O <sub>3</sub>	0.90	0.90	0.68	0.91	0.66	0.92	0.82	0.91
Trace element (ppm)								
Cl	10	44	2	40	—	17	—	26
S	96	156	77	125	63	154	69	155
Sc	1	—	2	1	3	2	1	—
V	23	23	28	25	27	35	38	34
Cr	10	55	38	8	4	94	21	5
Co	—	1	—	—	—	1	—	4
Ni	5	6	6	5	5	6	5	6
Zn	13	13	16	14	16	16	16	27
Sr	2331	2712	3480	2606	3373	2488	3324	2911
Ba	1858	1809	1984	1745	1961	1515	1655	1624
Rb	103	114	92	113	91	117	108	131
U	2	3	2	2	1	2	2	3
Th	1	—	—	—	—	1	1	—
Ga	15	15	12	16	11	16	14	16
Pb	1	2	1	1	1	1	0	2
Nb	32	47	52	45	62	68	80	29
Ta	2	1	1	1	—	1	—	4
Y	12	14	18	13	18	16	20	5
Zr	27	36	43	35	45	52	59	33
Hf	4	4	4	3	4	4	4	4
CIPW (wt%)								
Plagioclase	18.08	13.61		12.64		13.81		16.48
Orthoclase	48.34	51.71		51.65		50.11		52.06
Nepheline	28.58	30.06		31.53		29.19		25.16
Corundum	1.18	0.44		0.28		0.00		0.58
Diopside	—	—		—		1.27		—
Wollastonite	—	—		—		0.09		—
Olivine	0.95	0.77		0.69		—		1.10
Ilmenite	0.51	0.66		0.66		0.95		0.65
Magnetite	0.93	1.42		1.35		2.29		1.46
Apatite	0.07	0.09		0.09		0.14		0.12
Calcite	1.36	1.23		1.11		2.14		2.39

Fe<sub>2</sub>O<sub>3</sub>\*: total Fe; FeO: ferrous iron data obtained by wet chemical method; —: under detection limit

## 7. Mineral composition

### 7.1 Clinopyroxene

Pyroxene is of nearly uniform diopside composition (Morimoto, 1988) with an average stoichiometry of  $Wo_{50}En_{32}Fs_{18}$  (Fig. 8).  $TiO_2$  ranges between 1.28 wt. % and 2.0 wt. %. Calculated  $Fe^{3+}$  is approximately 0.3 p.f.u.,  $Fe^{2+}$  is 0.16 - 0.25 p.f.u., and thus the  $Fe^{2+}/Fe^{3+}$  ratio (0.51-0.85) is low and a characteristic of all pyroxenes (Table 2).

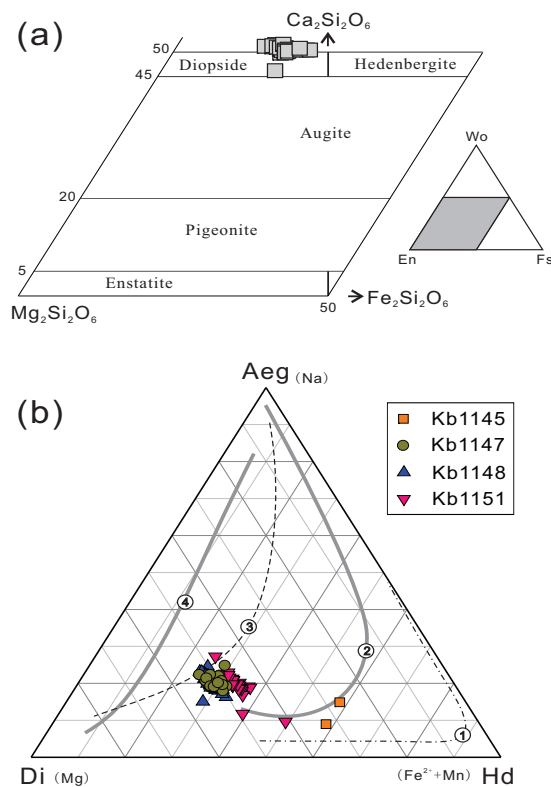


Fig. 8 (a) Nomenclature diagram for clinopyroxene (after Morimoto, 1988). (b) Compositional variations of the clinopyroxene in the system Aeg-Di-Hd. Clinopyroxene trend ① is from Ilímaussaq alkaline complex (Marks and Markl, 2001) ; Clinopyroxene trend ② is from Coldwell alkaline complex (Mitchell and Platt, 1982); Clinopyroxene trend ③ is from Lovozero alkaline complex (Korobeynikov and Laaioki, 1994) ; Clinopyroxene trend ④ is from Katzenbuckel volcano (Mann et al., 2006).

Table 2 Representative microprobe analyses of clinopyroxene.

Sample Point	1145B Cpx023	1147A Cpx68	1147A Cpx114	1148A Cpx010	1148B Cpx022	1151 Cpx008
Wt%						
SiO <sub>2</sub>	48.11	46.401	46.927	46.77	46.37	47.23
TiO <sub>2</sub>	1.62	1.868	1.284	1.57	1.76	1.4
Al <sub>2</sub> O <sub>3</sub>	6.92	7.818	6.409	7	7.72	9.84
Fe <sub>total</sub>	15.46	14.897	15.029	15.48	15.19	15.52
MnO	0.49	0.529	0.726	0.71	0.57	0.58
MgO	7.14	6.458	7.029	6.58	6.43	5.04
CaO	16.74	18.797	18.999	18.99	19.21	17.88
Na <sub>2</sub> O	3.83	3.203	3.141	3.03	2.96	4.51
K <sub>2</sub> O	0.02	0.023	0.014	0	0	0.02
Total	100.330	99.994	99.558	100.130	100.210	102.040
Cations						
Si	1.801	1.752	1.778	1.769	1.752	1.736
Ti	0.046	0.053	0.037	0.045	0.050	0.039
Al <sup>(IV)</sup>	0.199	0.248	0.222	0.231	0.248	0.264
Al <sup>(VI)</sup>	0.106	0.100	0.064	0.081	0.095	0.163
Fe <sup>3+</sup>	0.281	0.277	0.316	0.284	0.270	0.345
Fe <sup>2+</sup>	0.203	0.193	0.160	0.206	0.210	0.132
Mn	0.016	0.017	0.023	0.023	0.018	0.018
Mg	0.398	0.364	0.397	0.371	0.362	0.276
Ca	0.671	0.760	0.771	0.769	0.778	0.704
Na	0.278	0.234	0.231	0.222	0.217	0.321
K	0.001	0.001	0.001	0.000	0.000	0.001
Total	4.000	4.000	4.000	4.000	4.000	4.000
X <sub>Fe</sub>	0.35	0.37	0.32	0.38	0.39	0.35
endmembers						
Jadeite (Jd)	10.62	10.00	6.42	8.06	9.54	16.26
Aegirine(Aeg)	17.18	13.45	16.66	14.16	12.14	15.88
Diopside (Di)	39.84	36.35	39.70	37.09	36.21	27.62
Hedenbergite (Hd)	21.88	20.99	18.35	22.86	22.85	14.97
Enstatite (En)	0.00	0.00	0.00	0.00	0.00	0.00
Ferrosilite (Fs)	0.00	0.00	0.00	0.00	0.00	0.00

## 7.2 Amphibole

Amphiboles in all nepheline syenite samples are Ca and Al-rich hastingsites and ferro-pargasites (Leake et al., 1997) (Fig. 9a, Table 3). Fe<sup>3+</sup> in hastingsite varies from 0.456 to 1.013 p.f.u., and Al<sup>VI</sup> changes from 0.404 to 0.655 p.f.u. In ferro-pargasite, however, the corresponding changes are 0.066-0.766 p.f.u. and 0.398-1.074 p.f.u. Average F and Cl contents in hastingsite and ferro-pargasite are 0.039 and 0.050, 0.056 and 0.041, respectively.

The  $\text{Al}_2\text{O}_3$  and  $\text{TiO}_2$  content of amphiboles varies in hastingsite, from 13.88 to 16.42 wt.% and from 0.732 to 3.320 wt.%, respectively, in ferro-pargasite, from 14.04 to 18.04 wt.% and from 0.96 to 3.63 wt.%, respectively (Fig. 9b).

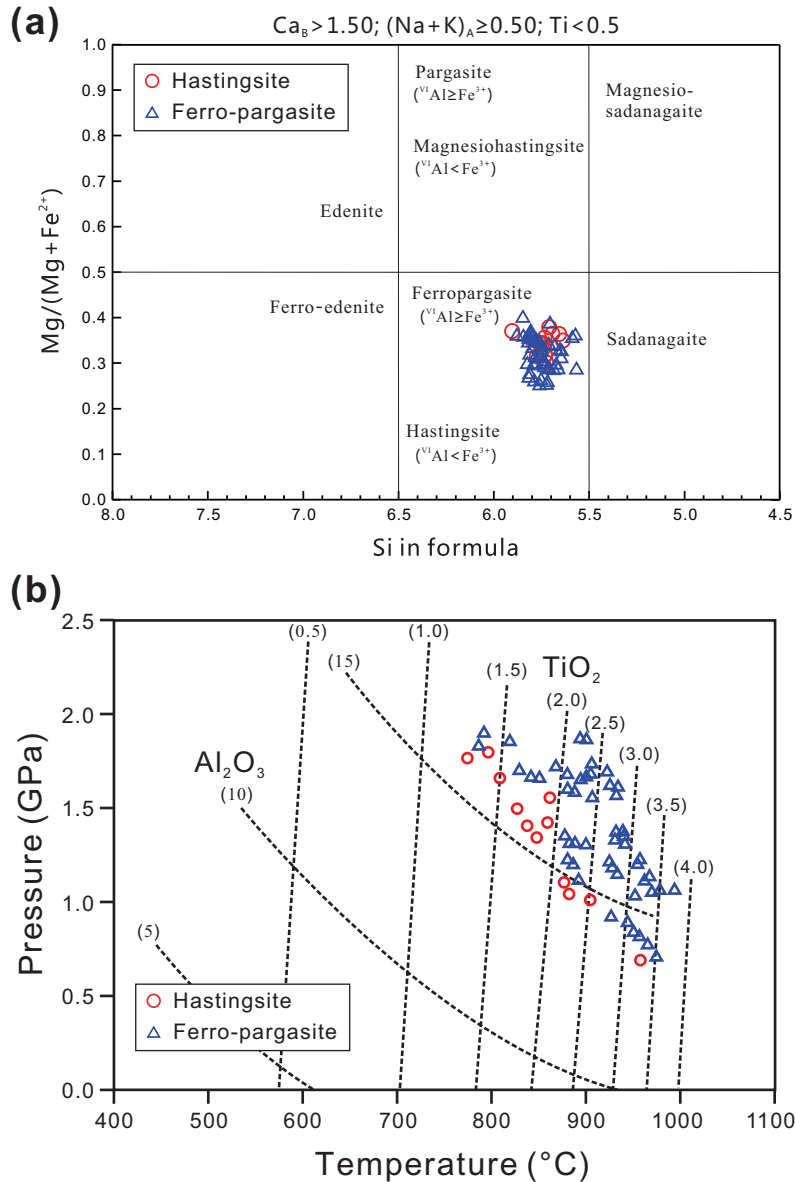


**Fig. 9 (a) Classification diagram for calcium amphibole (after Leake et al., 1997). (b) Semiquantitative P-T estimates by amphibole  $\text{TiO}_2$  and  $\text{Al}_2\text{O}_3$  contents (after Ernst and Liu, 1998).**

Table 3 Representative microprobe analyses of amphibole.

Sample Point	1145A Amp018	1145B Amp018	1145C Amp001	1147A Amp011	1147B Amp002	1148A Amp061	1148B Amp020	1151 Amp032	Kb926 Amp006
Comment									
SiO <sub>2</sub>	38.42	37.99	37.49	37.446	36.471	37.480	37.1	36.68	37.22
TiO <sub>2</sub>	3.03	2.89	3.34	1.655	1.404	1.370	2.27	1.61	2.84
Al <sub>2</sub> O <sub>3</sub>	14.79	15.22	14.19	15.614	16.446	16.190	15.33	15.77	16.66
FeO <sub>total</sub>	20.82	21.85	21.38	22.484	22.808	22.410	23.46	23.43	19.43
MnO	0.53	0.56	0.6	1.043	0.886	0.840	0.96	0.82	0.7
MgO	6.33	5.6	5.91	5.181	4.260	4.440	4.06	4.39	4.97
CaO	9.75	9.61	9.79	9.828	9.677	9.680	9.88	9.53	9.33
Na <sub>2</sub> O	2.97	3.07	3.17	2.928	3.076	2.840	2.94	2.81	3.17
K <sub>2</sub> O	2.13	2.39	2.27	2.586	2.698	2.520	2.59	2.72	2.48
F	0.12	0.16	0.13	0.045	0.083	0.070	0.09	0.08	0.17
Cl	0.16	0.18	0.17	0.202	0.225	0.270	0.18	0.11	0.08
-O=F+Cl	0.09	0.11	0.09	0.06	0.09	0.09	0.08	0.06	0.09
H <sub>2</sub> O <sub>calc</sub>	1.87	1.84	1.83	1.88	1.82	1.83	1.83	1.86	1.82
Total <sub>calc</sub>	100.56	100.92	99.88	100.58	99.46	99.51	100.35	99.56	98.55
Cations									
Si	5.847	5.797	5.807	5.761	5.706	5.824	5.786	5.724	5.812
Ti	0.347	0.332	0.389	0.192	0.165	0.160	0.266	0.189	0.334
Al <sup>(IV)</sup>	2.153	2.203	2.193	2.239	2.294	2.176	2.214	2.276	2.188
Al <sup>(VI)</sup>	0.499	0.534	0.398	0.592	0.739	0.789	0.603	0.624	0.877
Fe <sup>3+</sup>	0.491	0.490	0.366	0.644	0.507	0.489	0.372	0.696	0.066
Fe <sup>2+</sup>	2.158	2.298	2.403	2.249	2.477	2.423	2.687	2.361	2.471
Mn	0.068	0.072	0.079	0.136	0.117	0.111	0.127	0.108	0.093
Mg	1.436	1.274	1.365	1.188	0.994	1.028	0.944	1.021	1.157
Ca	1.590	1.571	1.625	1.620	1.622	1.612	1.651	1.593	1.561
Na	0.876	0.908	0.952	0.873	0.933	0.856	0.889	0.850	0.960
K	0.414	0.465	0.449	0.508	0.539	0.500	0.515	0.541	0.494
Total	15.880	15.945	16.025	16.001	16.094	15.967	16.055	15.985	16.015
Volatiles									
F	0.058	0.077	0.064	0.022	0.041	0.034	0.044	0.039	0.084
Cl	0.041	0.047	0.045	0.053	0.060	0.071	0.048	0.029	0.021
OH	1.901	1.876	1.892	1.925	1.899	1.894	1.908	1.931	1.895

### 7.3 Nepheline

Representative nepheline compositions are given in Table 4. For all nepheline syenite samples, nepheline varies in composition between  $\text{Ne}_{80}\text{Ks}_{20}\text{Qtz}_1$  and  $\text{Ne}_{77}\text{Ks}_{18}\text{Qtz}_4$  without systematic differences. These Qtz-poor (from 1.22 to 4.22 mol %) and Ne-rich compositions are typical features of nepheline grains and common in large slowly-cooled plutonic bodies (Marks et al., 2008). The Na/K ratio in nepheline ranges from 3.63 to 4.33, with an average value of 3.95. All nepheline compositions are plotted below the line of 500°C on the nepheline-kalsilite-silica (Ne–Ks–Qz) diagram (Hamilton, 1961; Hamilton and Mackenzie, 1960). This indicates that nepheline has gained a chemical re-equilibration at near 500°C (Fall et al., 2007).

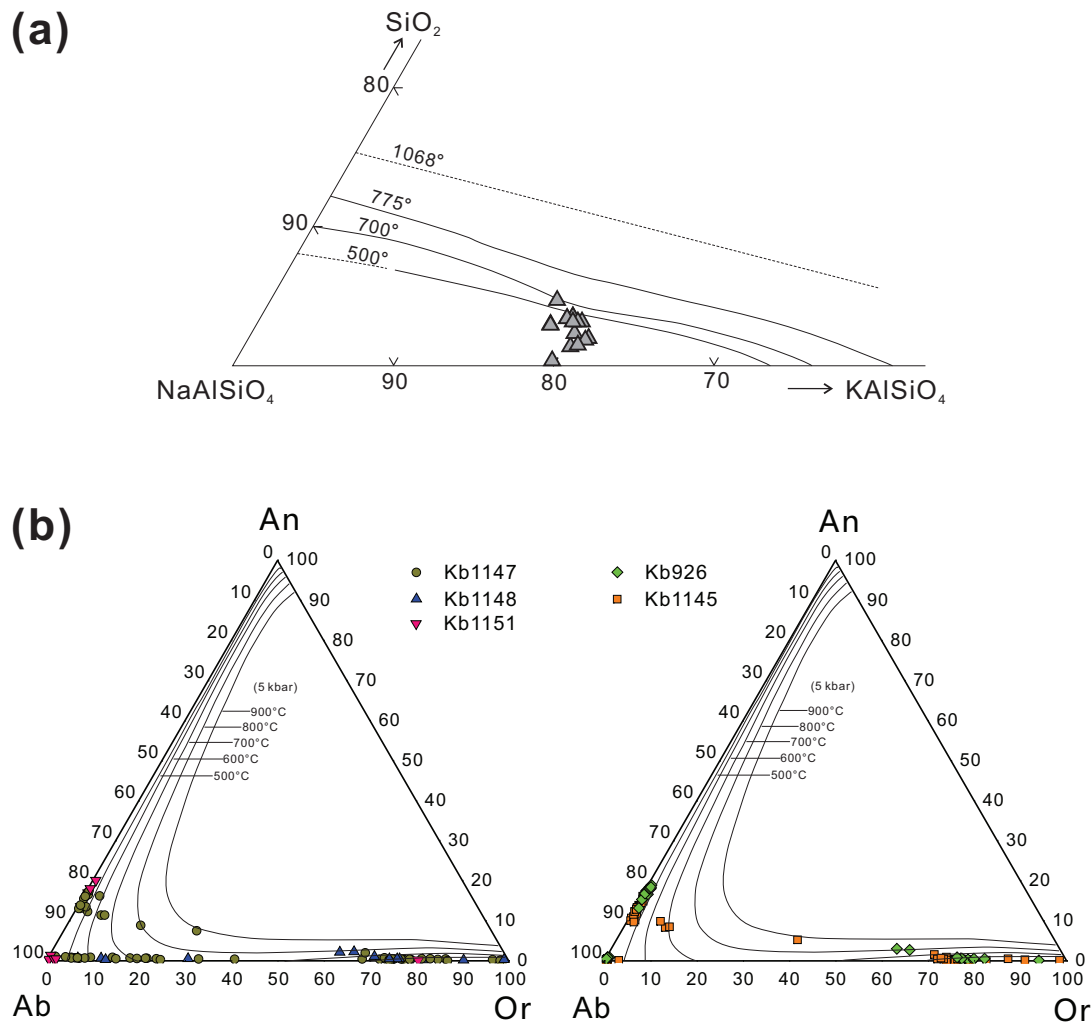


Table 4 Representative microprobe analyses of nepheline.

Sample	1145A	1145B	1145C	1147A	1147B	1148A	1148B	1151	Kb926
Point	Ne 031	Ne 087	Ne 037	Ne 015	Ne 039	Ne 021	Ne 026	Ne 027	Ne 005
SiO <sub>2</sub>	42.978	43.79	43.48	42.57	42.91	42.8	43.36	42.51	42.885
Al <sub>2</sub> O <sub>3</sub>	34.432	34.54	34.53	35.32	35.05	34.46	34.58	34.37	34.691
FeOtotal	0.061	0.08	0.14	0.09	0.06	0.1	0.11	0.09	0.103
MnO	0	0	0	0	0.03	0	0	0.01	0
MgO	0.003	0.01	0.01	0.01	0	0.02	0	0	0.008
SrO	0.021	0.02	0.35	0	0.07	0	0.02	0.02	0
BaO	0.013	0.04	0	0	0.02	0.01	0.01	0.04	0.008
CaO	0.611	0.62	0.56	0.94	0.72	0.74	1.04	1.38	0.922
Na <sub>2</sub> O	16.168	16.93	16.78	15.91	16.69	16.76	15.96	16.9	16.032
K <sub>2</sub> O	6.149	6.33	6.28	5.74	6.49	6.24	5.64	5.26	6.398
Total	100.436	102.360	102.130	100.580	102.040	101.130	100.720	100.580	101.047
Cations									
Si	4.113	4.124	4.110	4.059	4.062	4.083	4.125	4.069	4.088
Al	3.884	3.834	3.847	3.969	3.910	3.875	3.877	3.878	3.897
Fe <sup>3+</sup>	0.005	0.006	0.011	0.007	0.005	0.008	0.009	0.007	0.008
Mn	0.000	0.000	0.000	0.000	0.002	0.000	0.000	0.001	0.000
Mg	0.000	0.001	0.001	0.001	0.000	0.003	0.000	0.000	0.001
Sr	0.001	0.001	0.019	0.000	0.004	0.000	0.001	0.001	0.000
Ba	0.000	0.001	0.000	0.000	0.001	0.000	0.000	0.002	0.000
Ca	0.063	0.063	0.057	0.096	0.073	0.076	0.106	0.142	0.094
Na	3.000	3.091	3.075	2.941	3.063	3.100	2.944	3.137	2.963
K	0.751	0.760	0.757	0.698	0.784	0.760	0.684	0.642	0.778
Total	11.818	11.882	11.877	11.772	11.904	11.905	11.746	11.878	11.830
Endmembers									
An	1.55	1.50	1.38	2.49	1.81	1.84	2.66	3.49	2.35
Ne	74.26	74.27	74.84	76.32	75.75	75.57	73.89	77.28	73.87
Ks	18.58	18.27	18.43	18.12	19.38	18.51	17.18	15.83	19.40
Q	5.61	5.95	5.35	3.07	3.06	4.07	6.27	3.41	4.38

## 7.4 Feldspar

Representative feldspar compositions are listed in Table 5. Most alkali feldspar shows a perthitic structure formed by subsolvus exsolution developing Na- and K-rich lamellae (Fig. 5a). While, the composition derived from multiple lamellas using wide electron beam (diameter 5  $\mu$ m) show two main composition groups without An component: Ab<sub>15-30</sub> and Or<sub>65-86</sub>, depending on the volume ratio of exsolved lamellae and matrix under the corresponding beam. In addition, there is some ternary feldspar with scattered composition such as An<sub>8</sub>Ab<sub>64</sub>Or<sub>29</sub> and An<sub>11</sub>Ab<sub>81</sub>Or<sub>7</sub>, suggesting high crystallization temperatures of 900°C references (Fig.10b). The feldspar doubling ribbons (Fig. 7a) are pure albite or oligoclase (average Ab<sub>83</sub>An<sub>17</sub>).



**Fig. 10 (a) Nepheline-kalsilite-silica (Ne-Ks-Qz) diagram for nepheline (after Hamilton, 1961). (b) Feldspar ternary composition diagram with isotherms (after Fuhrman and Lindsley, 1988).**

## 7.5 Biotite

Table 6 lists the composition of biotite. They have surprisingly variable contents of MgO (7–11.24 wt. %) and  $\text{TiO}_2$  (3.44–6.24 wt. %), as well as Mg# (=Mg/(Mg+Fe), 0.54–1.08) and  $\text{Fe}^{2+}/\text{Fe}^{3+}$  ratio (0.45–0.76) (Fig. 11a). Calculation based on stoichiometry suggests no octahedral Al for all biotite. Biotite contains very small amounts of halogens, F and Cl.

Table 5 Representative microprobe analyses of feldspar.

Sample	1145A	1145A	1145B	1145C	1147A	1147A	1148A	1148B	1151	Kb926	Kb926
Point	Kfs 001	Pl 033	Kfs 005	Pl 031	Kfs 016	pl 021	Kfs 045	Kfs 032	Pl 070	kfs 002	Pl 026
SiO <sub>2</sub>	62.044	64.772	64.113	65.19	64.76	63.5	64.23	62.66	63.74	64.843	65.064
Al <sub>2</sub> O <sub>3</sub>	18.512	22.623	19.356	21.58	19.07	22.36	19.46	17.81	22.92	19.094	22.533
FeO <sub>total</sub>	0.043	0.002	0.034	0.14	0.04	0.05	0.02	0.04	0.39	0.026	0.039
MnO	0	0.002	0.02	0.01	0.02	0	0.02	0.02	0	0	0
MgO	0.008	0	0	0	0	0	0	0.01	0	0.013	0.016
SrO	0.363	0.373	0.683	0.45	0.57	0.5	0.8	0	0.44	0.401	0.428
BaO	0.544	0	0.629	0	0.66	0.02	0.46	0.06	0	0.329	0
CaO	0.03	2.917	0.03	2.43	0.06	3.46	0.21	0.06	3.73	0.11	2.916
Na <sub>2</sub> O	1.843	10.058	2.551	10.68	2.93	10.38	3.18	0.09	9.99	2.162	10.483
K <sub>2</sub> O	13.378	0.133	12.575	0.14	12.48	0.07	11.95	16.2	0.1	13.242	0.167
Total	96.765	100.880	99.991	100.620	100.590	100.340	100.330	96.950	101.310	100.220	101.646
Cations											
Si	2.961	2.836	2.953	2.865	2.965	2.811	2.945	2.995	2.794	2.972	2.834
Al	1.041	1.167	1.051	1.118	1.029	1.167	1.052	1.003	1.184	1.032	1.157
Fe <sup>3+</sup>	0.002	0.000	0.001	0.005	0.002	0.002	0.001	0.002	0.014	0.001	0.001
Mn	0.000	0.000	0.001	0.000	0.001	0.000	0.001	0.001	0.000	0.000	0.000
Mg	0.001	0.000	0.000	0.000	0.000	0.000	0.000	0.001	0.000	0.001	0.001
Sr	0.010	0.009	0.018	0.011	0.015	0.013	0.021	0.000	0.011	0.011	0.011
Ba	0.010	0.000	0.011	0.000	0.012	0.000	0.008	0.001	0.000	0.006	0.000
Ca	0.002	0.137	0.001	0.114	0.003	0.164	0.010	0.003	0.175	0.005	0.136
Na	0.171	0.854	0.228	0.910	0.260	0.891	0.283	0.008	0.849	0.192	0.885
K	0.814	0.007	0.739	0.008	0.729	0.004	0.699	0.988	0.006	0.774	0.009
Total	5.011	5.011	5.004	5.032	5.015	5.052	5.020	5.001	5.034	4.995	5.034
Endmembers											
Sr-feldspar	1.00	0.94	1.83	1.10	1.49	1.20	2.08	0.00	1.07	1.08	1.04
Ba-feldspar	1.01	0.00	1.14	0.00	1.16	0.03	0.81	0.11	0.00	0.60	0.00
An	0.15	13.58	0.15	10.96	0.29	15.31	1.01	0.31	16.83	0.55	13.07
Ab	16.94	84.74	22.83	87.19	25.53	83.10	27.67	0.83	81.56	19.44	85.00
Or	80.90	0.74	74.05	0.75	71.54	0.37	68.43	98.75	0.54	78.34	0.89

## 7.6 Fe-Ti oxides

Representative compositions of magnetite, hercynite and ilmenite are summarized in Table 7. TiO<sub>2</sub> content of magnetite and hercynite varies in 0.39-1.24 wt. % and 0.05-0.40 wt. %, respectively. MnO content is distinctive for the three kinds of minerals: 0.34-0.90 wt. % for magnetite, 2.13-3.72 wt. % for hercynite, and 4.59-15.32 wt. % for ilmenite. Magnetite and ilmenite both contain a small amount of MgO (<0.2 wt %). The ZnO content of hercynite is very high: 6 wt. % in sample 926, and 10-15 wt. % in the other samples. All the three kinds of minerals have no significant variation in the Fe-Ti oxide diagram (Fig. 11b).

## 7.7 Other minerals

Zeolites are rich in Na, and the main species are natrolite and thomsonite. Representative compositions are listed in Table 8. Titanite contains 0.2-0.4 wt. % fluorine. Garnet in all nepheline syenite samples is pure grossular (Fig. 7a-c). Composition variations of the banalsite-stronalsite solid solution deviate from the simple mixing of the two endmembers. Carbonate minerals consist of calcite exclusively with trace Fe and Mg abundances.

Table 6 Representative microprobe analyses of biotite.

Sample	1145B	1145C	Kb926	Kb926	Kb926	Kb926
Point	Bt 076	Bt 063	bt 041	bt 045	bt 049	bt 050
SiO <sub>2</sub>	34.87	36.03	34.58	34.39	33.86	34.01
TiO <sub>2</sub>	0	0	4.61	4.88	4.32	4.61
Al <sub>2</sub> O <sub>3</sub>	16.47	18.69	17.06	16.8	17.12	17.12
FeO <sub>total</sub>	20.99	20.43	22.4	22.21	21.03	21.05
MnO	0.21	0.16	0.7	0.66	0.75	0.65
MgO	10.31	5.08	8.11	7.93	8.57	8.52
CaO	0.05	9.3	0.02	0.01	0.12	0.12
Na <sub>2</sub> O	0.26	3.31	0.18	0.21	0.23	0.31
K <sub>2</sub> O	9.23	2.57	9.48	9.23	9.1	9.22
F	0	0	0.12	0.11	0.11	0.17
Cl	0.06	0.1	0.04	0.03	0.03	0.03
-O=F+Cl	0.01	0.02	0.06	0.05	0.05	0.08
H <sub>2</sub> O <sub>calc</sub>	4.26	4.37	4.30	4.27	4.24	4.24
Total <sub>calc</sub>	96.63	99.91	101.39	100.54	99.29	99.77
Cations						
Si	2.448	2.460	2.372	2.383	2.359	2.357
Ti	0.000	0.000	0.238	0.254	0.226	0.240
Al <sup>(IV)</sup>	1.363	1.504	1.379	1.372	1.406	1.398
Al <sup>(VI)</sup>	0.000	0.000	0.000	0.000	0.000	0.000
Cr	0.000	0.000	0.001	0.001	0.000	0.000
Fe <sup>3+</sup>	1.232	1.167	1.285	1.287	1.225	1.220
Fe <sup>2+</sup>	0.000	0.000	0.000	0.000	0.000	0.000
Mn	0.012	0.009	0.041	0.039	0.044	0.038
Mg	1.079	0.517	0.829	0.819	0.890	0.880
Ca	0.004	0.680	0.001	0.001	0.009	0.009
Na	0.035	0.438	0.024	0.028	0.031	0.042
K	0.827	0.224	0.830	0.816	0.809	0.815
Total	7.000	7.000	7.000	7.000	7.000	7.000
Volatiles						
F	0.000	0.000	0.026	0.024	0.024	0.037
Cl	0.007	0.012	0.005	0.004	0.004	0.004
OH	1.993	1.988	1.969	1.972	1.972	1.959
X <sub>Mg</sub>	0.467	0.307	0.392	0.389	0.421	0.419

Table 7 Representative microprobe analyses of Fe-Ti oxides.

Sample Point	1145A Mag 012	1147A Mag93	Kb926 Mag 040	1147B her 003	1147B her 004	1145A ilm 011	1147B ilm 009	Kb926 ilm 018
	Magnetite			Hercynite		Ilmenite		
SiO <sub>2</sub>	0.01	0.028	0	0.49	0.21	0.02	0	0.02
TiO <sub>2</sub>	0.37	1.221	0.24	0.4	0.07	50.88	51.11	51.04
Al <sub>2</sub> O <sub>3</sub>	0.54	0.805	1	57.11	56.83	0	0	0
Cr <sub>2</sub> O <sub>3</sub>	0	0.000	0	0.03	0	0	0.01	0
FeO <sub>total</sub>	91.32	91.211	89.89	25.74	22.68	41.67	38.29	31.32
MnO	0.11	0.785	0.42	3.72	2.68	5.92	9.14	15.52
MgO	0.04	0.041	0.03	2.77	2.55	0.54	0.52	0.22
CaO	0	0.035	0.02	0.08	0.05	0.01	0	0.15
NiO	0.07	0	0.02	0.03	0	0	0	0.04
ZnO	0	0	0	10.71	15.12	0	0.09	0.07
V <sub>2</sub> O <sub>3</sub>	0	0	0	0	0	0	0	0
Total	92.460	94.126	91.620	101.080	100.190	99.040	99.160	98.380
Cations								
Si	0.000	0.001	0.000	0.014	0.006	0.001	0.000	0.001
Ti	0.011	0.035	0.007	0.009	0.002	0.969	0.973	0.980
Al	0.025	0.036	0.046	1.924	1.942	0.000	0.000	0.000
Cr	0.000	0.000	0.000	0.001	0.000	0.000	0.000	0.000
Fe <sup>3+</sup>	1.953	1.892	1.940	0.030	0.043	0.060	0.055	0.038
Fe <sup>2+</sup>	1.003	1.007	0.990	0.585	0.507	0.822	0.755	0.631
Mn	0.004	0.025	0.014	0.090	0.066	0.127	0.196	0.336
Mg	0.002	0.002	0.002	0.118	0.110	0.020	0.020	0.008
Ca	0.000	0.001	0.001	0.002	0.002	0.000	0.000	0.004
Ni	0.002	0.000	0.001	0.001	0.000	0.000	0.000	0.001
Zn	0.000	0.000	0.000	0.226	0.323	0.000	0.002	0.001
V	0.000	0.000	0.000	0.000	0.000	0.000	0.000	0.000
Endmembers								
Usp	1.09	3.56	0.72					
Mt	98.91	96.44	99.28					

Table 8 Representative microprobe analyses of zeolite.

Sample	1145A	1145A	1145B	1147A	1147B	1148A	1151
Point	Zeo 006	Zeo 021	Zeo 019	Zeo 033	Zeo 016	Zeo 027	Zeo 014
SiO <sub>2</sub>	48.485	37.155	41.477	46.66	42.01	37.11	37.08
Al <sub>2</sub> O <sub>3</sub>	28.33	30.14	30.202	27	30.98	30.64	29.68
FeO <sub>total</sub>	0.026	0.011	0	0.03	0.05	0.11	0.03
MnO	0.025	0.019	0.004	0.02	0	0.02	0.03
MgO	0.005	0	0	0	0	0	0
SrO	0.027	3.327	0.273	0.08	0.1	0.14	3.78
BaO	0	0	0	0	0.06	0	0
CaO	0.488	11.315	9.19	0.05	9.24	13.32	11.06
Na <sub>2</sub> O	15.334	4.168	7.937	16.4	7.98	3.04	3.99
K <sub>2</sub> O	0.029	0.022	0.021	0.08	0.01	0.03	0.01
Total	92.749	86.157	89.104	90.320	90.430	84.410	85.660
Cations							
Si	23.864	20.397	21.538	23.752	21.464	20.354	20.513
Al	16.434	19.500	18.483	16.199	18.655	19.806	19.351
Fe <sup>3+</sup>	0.011	0.005	0.000	0.013	0.021	0.050	0.014
Mn	0.010	0.009	0.002	0.009	0.000	0.009	0.014
Mg	0.004	0.000	0.000	0.000	0.000	0.000	0.000
Sr	0.008	1.059	0.082	0.024	0.030	0.045	1.213
Ba	0.000	0.000	0.000	0.000	0.012	0.000	0.000
Ca	0.257	6.655	5.113	0.027	5.058	7.828	6.556
Na	14.633	4.436	7.991	16.186	7.905	3.233	4.280
K	0.018	0.015	0.014	0.052	0.007	0.021	0.007
Total	55.239	52.077	53.223	56.261	53.153	51.345	51.948
E%	8.267	-1.887	0.479	-0.787	3.119	4.519	-2.311
T <sub>Si</sub>	0.592	0.511	0.538	0.595	0.535	0.507	0.515
Si/Al	1.452	1.046	1.165	1.466	1.151	1.028	1.060
Ca/(Ca+Na)	0.017	0.600	0.390	0.002	0.390	0.708	0.605

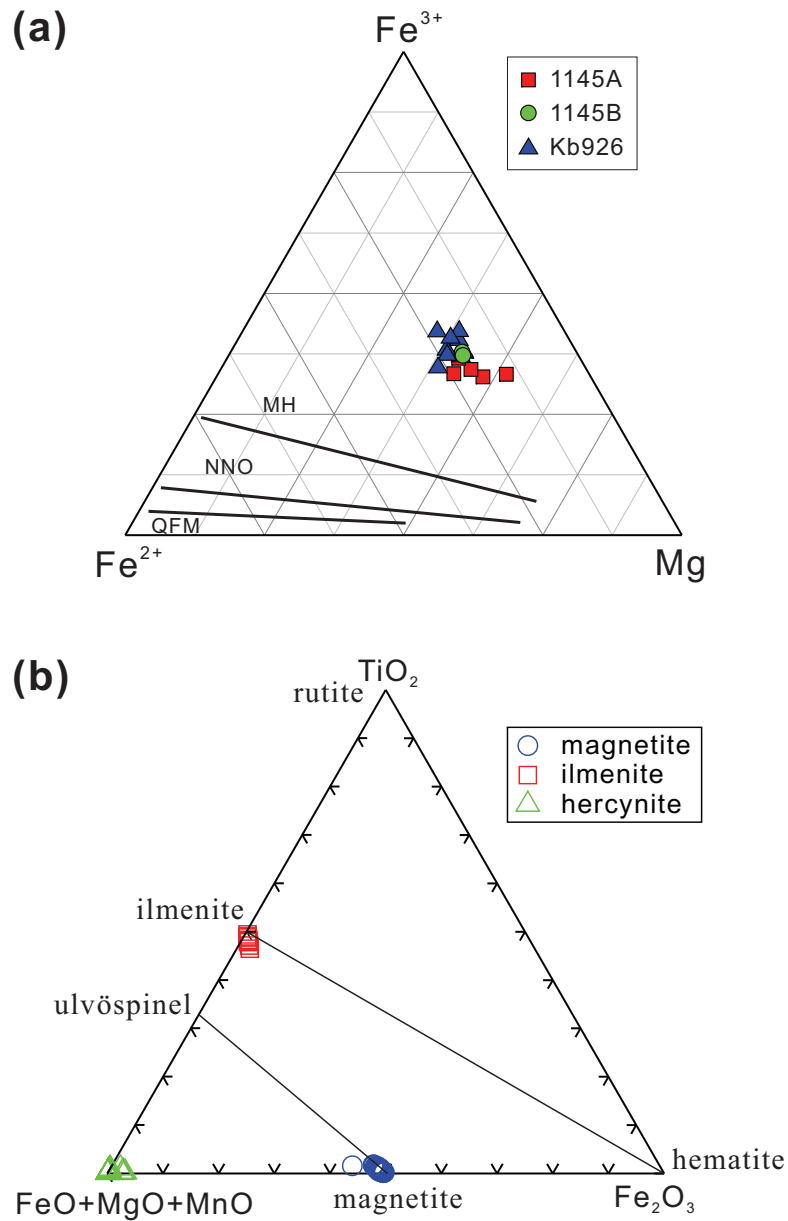


Fig. 11 (a) Composition plots of biotite in terms of Fe<sup>2+</sup>-Fe<sup>3+</sup>-Mg with lines represent oxygen fugacity buffers (after Wones and Eugster, 1965). MH: magnetite-hematite, NNO: nickel-nickel oxide, QFM: quartz-fayalite-magnetite. (b) Nomenclature diagram for Fe-Ti oxides.

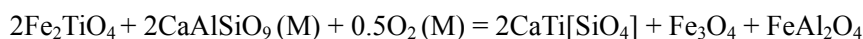
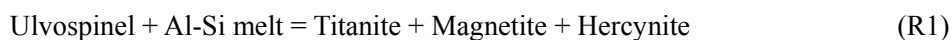
## 8. Discussion

### 8.1 Evolutionary stages and related reactions

#### 8.1.1 Orthomagmatic stage

The prime felsic minerals defining the igneous assemblage are nepheline and K-feldspar. Kfs probably reached the solidus surface first, but Kfs and Ne co-precipitated from the liquid for most parts of the liquid line of descent. Diopside and ferro-paragsite occur as large prismatic crystals in most samples, but diopside is absent from sample 926 (Figs. 4 & 6). Cpx and ferro-paragsite are the primary ferromagnesian minerals which crystallized from the parent alkaline magma, similar to the Dismal nepheline syenite from Antarctica (Worley and Cooper, 1995). The crystallization hierarchy of the two Fe-Mg minerals will be discussed in detail below.

An exclusive mineral assemblage forming clusters of magnetite, ilmenite, hercynite and titanite is found either surrounded by nepheline and feldspar (Fig. 4e and Fig. 6e) or is enclosed in large ferro-paragsite crystals. The textures indicate that the titanite-forming reaction progressed in an early melt-present stage. The simplified reaction can be written as:

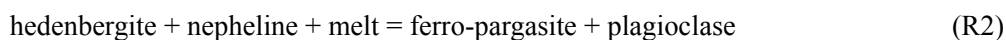


The formation of titanite together with magnetite and hercynite implies a decrease of oxygen fugacity during subsolidus cooling.

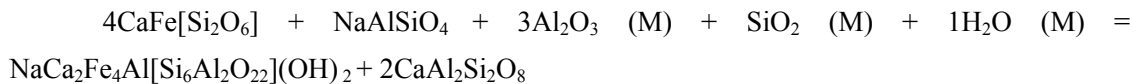
Euhedral crystals of calcite (Fig. 7a) or irregular inclusions in ferro-paragsite may also represent an early phase crystallized in the orthomagmatic stage.

#### 8.1.2 Autometamorphic stage

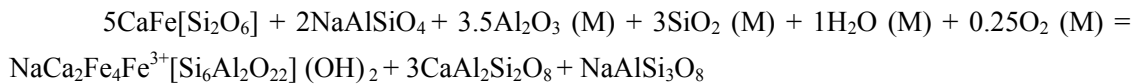
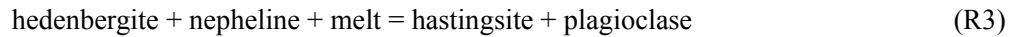
Hastingsite and ferro-paragsite rims on diopside (Fig. 5a-d) and biotite rims on ferro-paragsite (Fig. 7a-d) indicate that subsolidus reactions between a residual interstitial volatile-rich melt (M) and primary minerals took place during slow cooling of the nepheline syenite body. Here we use simple hedenbergite endmember of pyroxene and the stoichiometric formula of amphibole to deduce the following reactions:







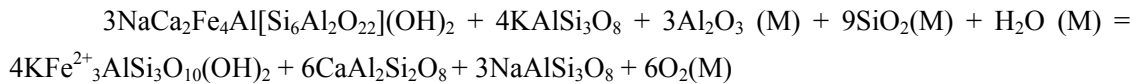
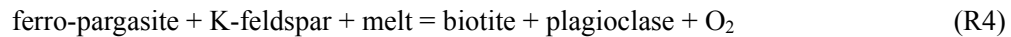
and



The reactions above transform nepheline to plagioclase (Ca-Na solid solution).

Thermobarometry based on the  $\text{Al}_2\text{O}_3$  and  $\text{TiO}_2$  contents of the amphiboles in nepheline syenite reveals  $P$ - $T$  conditions of 0.5-2.0 GPa and 700-1000°C (Ernst and Liu, 1998) (Fig. 9b). This result indicates a broad  $P$ - $T$  range for the amphibole-forming reactions.

In addition, the biotite rims on ferro-pargasite in sample 926 suggest that the mica formed by the reaction:



The simple reaction:



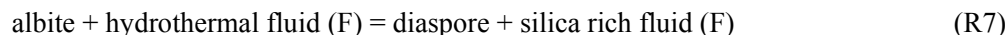
describes the process adequately and explains the textures where albite replaces nepheline along grain boundaries (Fig. 7a). The dissolved silica migrates along grain boundaries and originates probably from the local reactions of Kfs to Bt and Cpx to Amp transformation. Albite is thus a side product of reactions of R2, R3 and R4.

### 8.1.3 Hydrothermal stage I

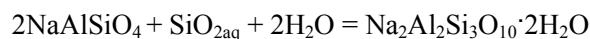
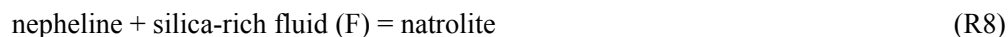
The hydrothermal stage I is characterized by natrolite formation, the related mineral assemblages and textures are shown in Fig. 5a-h. Hydrothermal veins are mainly composed of zeolite (and calcite) (Fig. 5c-d), the principal reaction of the hydrothermal stage is the nepheline - zeolite transformation, which can be written as:



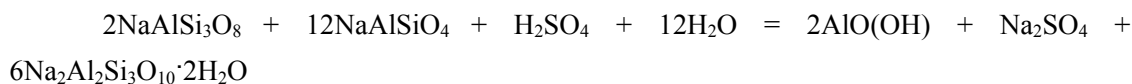
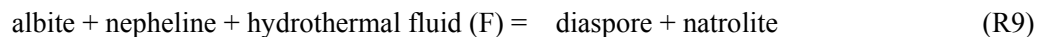
The dissolved aqueous silica necessary for the zeolitization is likely to result from internal dissolution of the albite lamella in perthite. Albite dissolution have been observed in nepheline syenite (Fig. 5a), the corresponding reaction could be described by the following reaction:



The reaction consumes  $\text{H}_2\text{SO}_4$  component from fluid and release silica and thenardite component to the fluid. Simultaneously, diaspore precipitated in the in situ locality or other place (Fig. 5b). The released  $\text{SiO}_2$  will increase the silica activity of the fluid, which thus destabilized nepheline by reactions like these:



The above nepheline dissolution reaction is accompanied by precipitation of natrolite (Fig. 5b). The process consumes the silica derived from R7. The combined reaction is:

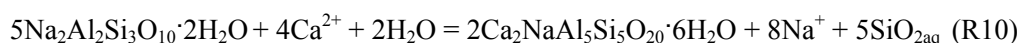


This could explain the co-occurrence of natrolite and diaspore which replace nepheline (Fig. 5b). The reaction would increase the Na activity of the fluid. This arbitrary reaction also would maintain constant silica activity, only if all the silica released by R7 is totally consumed by R2, which however can hardly be fulfilled in a real case.

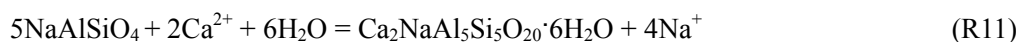
Therefore the increase of Silica and  $\text{Na}^+$  activities of fluid together as a result of R7 will further promote the stabilization of natrolite through the reaction R8. As a result of reaction R8 and precipitation of natrolite, silica activity would be compensated partly but still tends to increase. Thus the initial fluid of nepheline syenite catchment would have a  $\text{Na}_2\text{SO}_4$  -rich signature.

### 8.1.4 Hydrothermal stage II

Large amount of Ca-HCO<sub>3</sub> fluid from carbonatite catchment probably have infiltrated into nepheline syenite along faults or fractures and mixed with the initial fluid of nepheline syenite. The mixed fluid would increase Ca activity at constant SiO<sub>2</sub> activity. Fluid will cross the natrolite field and enter the thomsonite stability field. Thomsonite which overgrowth on natrolite (Fig. 5e) and co-precipitated with calcite (Fig. 5d) could be explained by this mixed fluid. The corresponding reaction is:



The reaction R10 would consume the Ca<sup>2+</sup> and release Na<sup>+</sup> with the precipitation of thomsonite. The direct alteration of nepheline to thomsonite could be described by reaction:

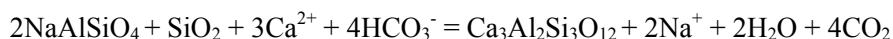
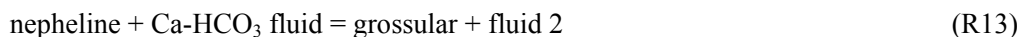


The transportation of Ca-HCO<sub>3</sub> fluid along fractures in nepheline syenite will precipitate thomsonite on the fracture wall when contact with nepheline or natrolite (Fig. 5d), and precipitate calcite in the middle of fluid conduit through reaction:



The precipitation of calcite in this case emphasizes the importance of local disequilibrium in the water-rock system.

The formation of grossular mostly as rims around other minerals (Fig. 5f-h) may result from infiltration of Ca-HCO<sub>3</sub> fluid from carbonatite catchment. Note that the amount of grossular is very small and the reaction occurred probably at the same stage as thomsonite. A possible possibly reaction could be:

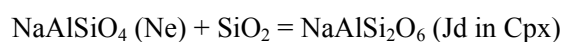
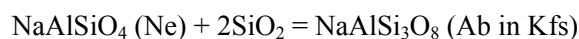


In addition, minor grossular can be observed in the vicinity of hastingsite and magnetite (Fig. 5g), and also in the vicinity of ferro-paragsite and pyrite (Fig. 5h), which are likely related to local reactions at different redox conditions. That is, magnetite and grossular are generated at an oxidizing condition through dissolution of hastingsite involving the participation of fluid; in contrast, pyrite and grossular are generated at a reducing condition.

## 8.2 Constraints on intrinsic parameters of orthomagmatic stage

### 8.2.1 Geochemical modeling method

Nepheline and K-feldspar mineral equilibrium is a common buffer used in silica deficient rocks (Powell, 1978), when they coexist with clinopyroxene, the jadeite component could also be used to construct equilibria for sodium component of each minerals .



Mineral equilibria diagrams were calculated using Theriak-Domino software (de Capitani and Brown, 1987; de Capitani and Petrakakis, 2010) with the database of Berman (1988). For the activity calculation, the on-site mixing model was used for nepheline, the solution model of Fuhrman and Lindsley (1988) was used for feldspar, and the model of Green et al. (2007) for clinopyroxene.

### 8.2.2 Pressure estimation

There is no reliable pressure estimate for the emplacement of nepheline syenite because of lacking of mineral pairs. Pressures of 8-10 kbar has been obtained for the nepheline syenite in Lillebukt alkaline complex by various Al in amphibole barometers (Arzamastsev et al., 2002). Contact metamorphism in Øksfjord area indicates an intrusive pressure of 5-6.5 kbar for gabbroic rocks (Elvevold et al., 1994). The common orthopyroxene coronas developed between olivine and plagioclase grains during the cooling of ultramafic rocks of Seiland igneous province illustrate pressure range of 8-10 kbar at reasonable temperature (Gardner and Robins, 1974). In order to keep accordance with the pressure range of the major mafic rocks in Seiland igneous province, we prefer to use 10 kbar as a plausible pressure for nepheline syenite in the phase diagram calculation.

### 8.2.3 Temperature and Silica activity

As stated before, the feldspar compositions infer a broad range of generation temperatures of 500-900°C (Fig. 10b). However, much lower temperatures are estimated from nepheline compositions, which are lower 700 °C but mostly below 500 °C (Fig. 10a).

Nepheline with the highest amounts of excess silica, which record the highest temperature (Hamilton, 1961), was used in phase diagram calculation to constrain the early magmatic crystallization condition. The compositions of clinopyroxene core and the integrated K-feldspar were assumed to represent the original composition that in equilibrium with the high temperature nepheline.

The phase diagram shown in Fig. 12 demonstrates that the equilibrium involving nepheline, K-feldspar and diopside, which are defined by analyzed mineral compositions, can be achieved at temperatures between ca. 500-700 °C at activity of silica being ca. 0.15-0.33. This temperature estimate is similar to that yielded from nepheline composition as shown in Fig. 10a.

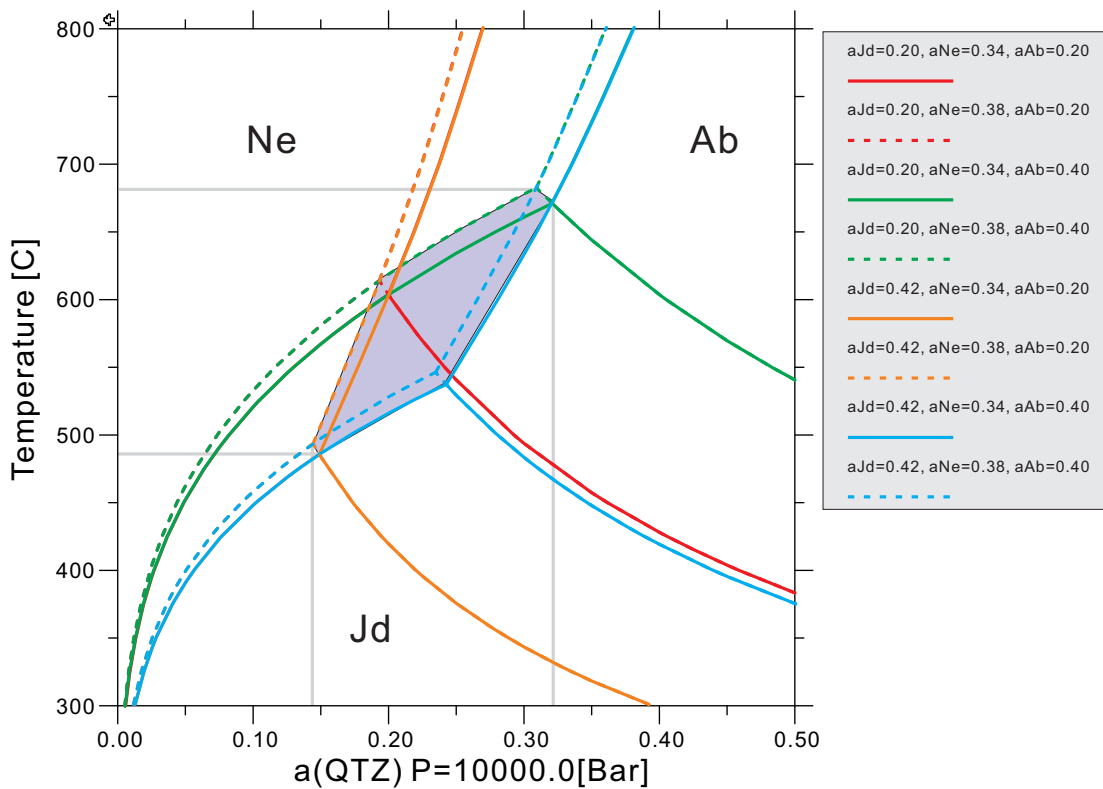


**Fig. 12 Mineral equilibrium diagrams constrained by orthomagmatic mineral compositions. See text for explanations.**

## 8.3 Fluid evolution

### 8.3.1 Geochemical modeling for mineral stability diagram

Mineral stability fields represented in activity-activity diagrams were calculated with the TWQ program (Lieberman and Petrakakis, 1991) using mineral database of JUN92 (Berman, 1988) and aqueous database of HKF81 (Helgeson et al., 1981). The utilized thermodynamic data in this study for most zeolite group minerals (heulandite, laumontite, stilbite and wairakite) are derived from Frey et al. (1991). As a rare case, the data of analcite is derived from the database of Holland and Powell (2011). Notably, in order to maintain the internal consistency of database, the thermodynamic data for thomsonite, natrolite and mesolite (which are not available in the commonly used database, e.g. JUN92) are constructed by integrating other thermodynamic data of reaction-related minerals. For example, considering the reaction  $[1 \text{ Nat} + 1 \text{ Qtz} + 2 \text{ Ky} = 2 \text{ Pg}]$ , the thermodynamic data of natrolite (Nat) can be induced from the other three minerals.

### 8.3.2 Fluid evolution derived from zeolite stability diagram

As described before, two stages of hydrothermal events, which are characterized by natrolite and thomsonite formation respectively, have been identified in the nepheline syenite. All dominating reactions involve chemical components of the fluid phase. The fluid of stage I is considered as fluid expelled by crystallizing magma, while the fluid of stage II is dominated by infiltration of Ca-HCO<sub>3</sub> fluid from carbonatite catchment.

#### 8.3.2.1 Fluid property of hydrothermal stage I

According to reaction R8, The transformation of nepheline to natrolite is mainly controlled by the activity of nepheline, and activities of water and silica in the fluid. As shown in Fig. 13a, for nepheline activity of 0.34 and silica activity of 0.15 which defined by orthomagmatic mineral assemblages, the lowest logaH<sub>2</sub>O value of -4 is needed for natrolite formation. With processing of natrolite formation, the silica activity of fluid will decrease gradually due to consumption of silica by natrolite. The decreasing silica activity will then require increasing water activity for producing natrolite (Fig. 13a). Comparing the topology of phase diagram for pure nepheline and nepheline with activity 0.34 (Fig. 13b), the activity of nepheline does not play a significant role as that of water and silica in zeolite formation.

#### 8.3.2.2 Fluid property of hydrothermal stage II

Mineral stability diagrams in the system Ca-Na-Si-Al-O-H have been constructed at 1 bar, 25°C and 100°C. The topology and the field size of the diagrams don't change with pressure, but

change remarkably with temperature. Stability fields of natrolite and thomsonite decrease gradually at elevated temperature (Fig. 13c-d) and finally disappear at ca. 200°C.

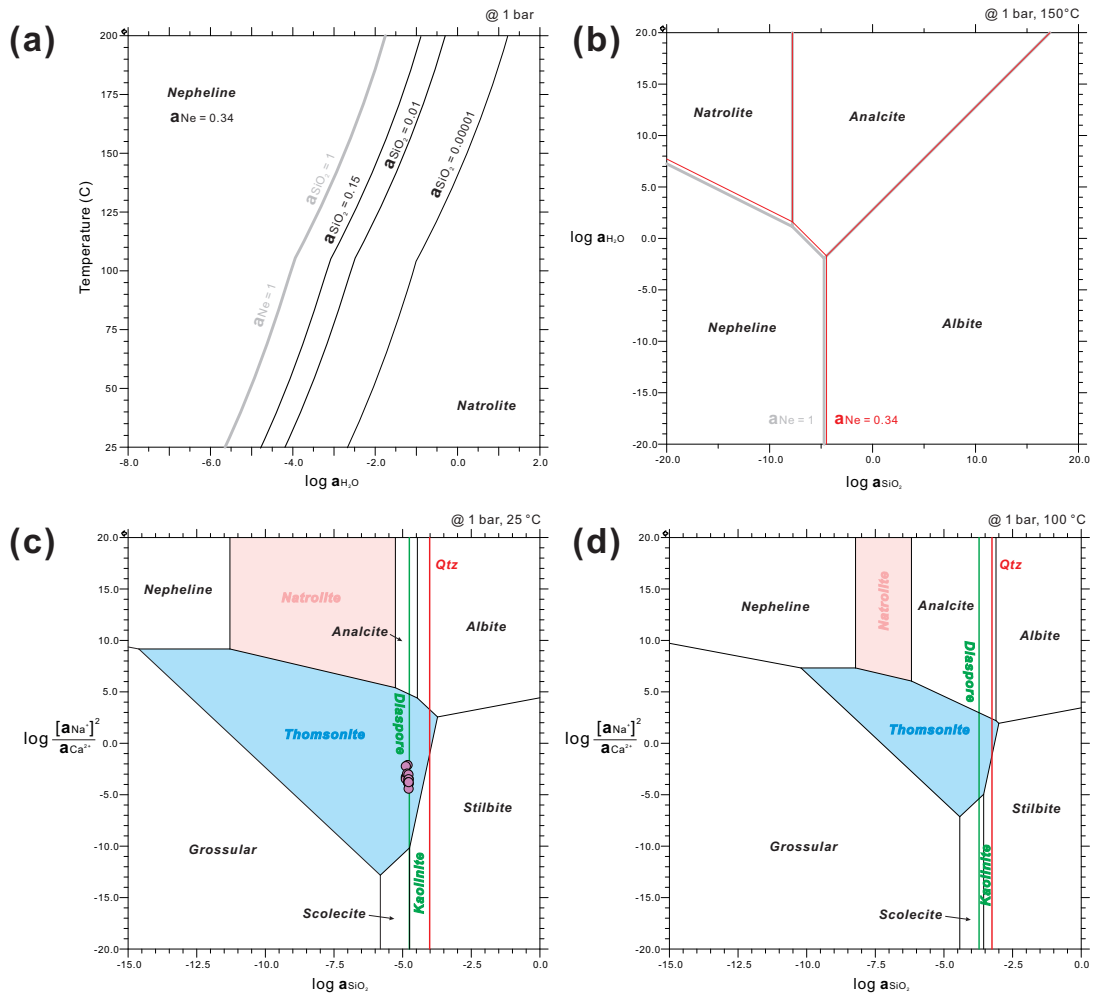


**Fig. 13** Mineral stability diagrams for natrolite and thomsonite at 1 bar. See text for explanations.

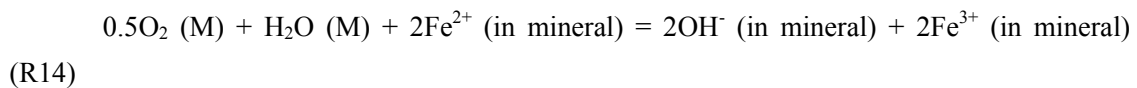
As shown in Fig. 13c, all the water compositions sampled from nepheline syenite catchment (Holger, 2010) are plotted in the stability field of thomsonite, and very close to the boundary of diaspore stability. This modeled stability field is well consistent with the microscopic observations that thomsonite is present as a major phase coexisting with a very small amount of diaspore (Fig. 7d). As indicated by the modeled phase diagram as a function of varying activities

of  $\text{Na}^+$ ,  $\text{Ca}^{2+}$  and  $\text{SiO}_2$  in the fluid, the texture of thomsonite can be reasonably interpreted as a reaction consequence of nepheline with decreasing activity of  $\text{Na}^+$ , but also probably with increasing activity of  $\text{Ca}^{2+}$ . For the decrease of the activity of  $\text{Na}^+$ , it could be a result of generation of natrolite which largely consumes  $\text{Na}^+$  in the fluid. It is well demonstrated from the occurrence of natrolite and thomsonite at different locations or at the same sites, which indicate that the activities of  $\text{Na}^+$  and  $\text{Ca}^{2+}$  in the fluids are close to the boundary condition between natrolite and thomsonite in the phase diagram (Fig. 13c).

## 8.4 Redox reactions

In magmatic evolution, regardless of the composition of parent magma, oxygen activity of the melt plays a key role in controlling the sequences of mineral assemblages (Carmichael and Ghiorso, 1990). Other parameters such as silica activity,  $\text{H}_2\text{O}$  activity and fluid composition also control the final reaction path in a complex manner. In the orthomagmatic, subsolidus and hydrothermal stages, all dominating reactions involve chemical components in the melt or fluid phase. Fluid species play a key role in crystallization and differentiation during subsolidus evolution of the syenite, and the fluid phase is needed to be described in the C-H-O system.

$\text{O}_2$  participates in reactions as a reactant (R3) or a product (R4). Oxygen in the system exists either as  $\text{H}_2\text{O}$  or as  $\text{OH}^-$  in the melt (Markl et al. 2010). And it affects the redox state of melt by the following simplified reaction:



This hastingsite-forming reaction could consume  $\text{O}_2$  in the melt and decrease the oxygen fugacity and then could make residual melt to a more reduction state. Similarly, the reverse of the biotite-forming reaction has an opposite evolution and effect. Since R14 is a simplified model reaction that represents R3, and the opposite of R4, the formation of hastingsite drives the melt to a more reduced state, while, the formation of biotite drives to a more oxidized melt state.

## 9. Conclusions

Based on microscopic observation of primary and secondary minerals in the rock samples, the derived reactions, and the thermodynamic modeling for mineral assemblages, several conclusions concerning the evolution of nepheline syenite can be drawn below:

Orthomagmatic stage of nepheline syenite is characteristic with assemblage of nepheline



+ K-feldspar + clinopyroxene + amphibole  $\pm$  magnetite  $\pm$  ilmenite at temperatures between ca. 500-700 °C at activity of silica being ca. 0.15-0.33.

Autometamorphic stage is represented by coronas of amphibole on clinopyroxene and biotite on amphibole, which are result from reactions between primary minerals and residual melt.

Hydrothermal stage I is impressed by pervasive natrolite transformed from nepheline and albite dissolution. The related fluid is considered as fluid expelled by crystallizing magma, which has decreasing silica activity and slightly increasing Na activity with the product of natrolite.

Hydrothermal stage II is dominated by infiltration of Ca-HCO<sub>3</sub> fluid from carbonatite catchment into the nepheline syenite along fractures which resulted in the generation of thomsonite by transformation from nepheline and natrolite.

## References

- Appleyard, E.C., 1974. Syn-orogenic igneous alkaline rocks of eastern Ontario and northern Norway. *Lithos*, 7(3): 147-169.
- Appleyard, E.C., 1980. Mass balance computations in metasomatism: Metagabbro/nepheline syenite pegmatite interaction in northern Norway. *Contributions to Mineralogy and Petrology*, 73(2): 131-144.
- Arzamastsev, A.A., Arzamastseva, L.V. and Kuzmin, S.V., 2002. Mineral associations in rocks of the Lillebukt syenite-carbonatite intrusion (North Norway) as indicators of its forming conditions. *Proceedings of the Russian Mineralogical Society*, 131(1): 47-63.
- Beeskov, B., Treloar, P.J., Rankin, A.H., Vennemann, T.W. and Spangenberg, J., 2006. A reassessment of models for hydrocarbon generation in the Khibiny nepheline syenite complex, Kola Peninsula, Russia. *Lithos*, 91(1-4): 1-18.
- Berger, J., Ennih, N., Mercier, J.-C.C., Liegeois, J.-P. and Demaiffe, D., 2009. The role of fractional crystallization and late-stage peralkaline melt segregation in the mineralogical evolution of Cenozoic nephelinites/phonolites from Saghro (SE Morocco). *Mineralogical Magazine*, 73(1): 59-82.
- Berman, R., 1988. Internally-consistent thermodynamic data for minerals in the system Na<sub>2</sub>O-K<sub>2</sub>O-CaO-MgO-FeO-Fe<sub>2</sub>O<sub>3</sub>-Al<sub>2</sub>O<sub>3</sub>-SiO<sub>2</sub>-TiO<sub>2</sub>-H<sub>2</sub>O-CO<sub>2</sub>. *Journal of Petrology*, 29(2): 445.
- Boily, M. and Williams-Jones, A.E., 1994. The role of magmatic and hydrothermal processes in the chemical evolution of the Strange Lake plutonic complex, Québec-Labrador. *Contributions to Mineralogy and Petrology*, 118(1): 33-47.
- Carmichael, I. and Ghiorso, M., 1990. The effect of oxygen fugacity on the redox state of natural liquids and their crystallizing phases. *Reviews in Mineralogy and Geochemistry*, 24(1): 191-212.
- Daly, J.S., Aitchison, S.J., Cliff, R.A., Gayer, R.A. and Rice, A.H.N., 1991. Geochronological Evidence from Discordant Plutons for a Late Proterozoic Orogen in the Caledonides of Finnmark, Northern Norway. *Journal of the Geological Society*, 148: 29-40.
- de Capitani, C. and Brown, T., 1987. The computation of chemical equilibrium in complex systems containing non-ideal solutions. *Geochimica Et Cosmochimica Acta*, 51(10): 2639-2652.
- de Capitani, C. and Petrakakis, K., 2010. The computation of equilibrium assemblage diagrams with Theriak/Domino software. *American Mineralogist*, 95(7): 1006-1016.
- Droop, G., 1987. A general equation for estimating Fe<sup>3+</sup> concentrations in ferromagnesian silicates and

- oxides from microprobe analyses, using stoichiometric criteria. *Mineralogical Magazine*, 51(361): 431-435.
- Elvevold, S., Reginiussen, H., Krogh, E.J. and Bjorklund, F., 1994. Reworking of Deep-Seated Gabbros and Associated Contact Metamorphosed Paragneisses in the South-Eastern Part of the Seiland Igneous Province, Northern Norway. *Journal of Metamorphic Geology*, 12(4): 539-556.
- Ernst, W.G. and Liu, J., 1998. Experimental phase-equilibrium study of Al- and Ti-contents of calcic amphibole in MORB; a semiquantitative thermobarometer. *American Mineralogist*, 83(9-10): 952-969.
- Fall, A., Bodnar, R.J., Szabó, C. and Pál-Molnár, E., 2007. Fluid evolution in the nepheline syenites of the Ditrau Alkaline Massif, Transylvania, Romania. *Lithos*, 95(3-4): 331-345.
- Finch, A.A., Goodenough, K.M., Salmon, H.M. and Andersen, T., 2001. The petrology and petrogenesis of the North Motzfeldt Centre, Gardar Province, South Greenland. *Mineralogical Magazine*, 65(6): 759-774.
- Frey, M., Capitani, C.D. and Liou, J.G., 1991. A new petrogenetic grid for low-grade metabasites. *Journal of Metamorphic Geology*, 9(4): 497-509.
- Fuhrman, M.L. and Lindsley, D.H., 1988. Ternary-feldspar modeling and thermometry. *American Mineralogist*, 73(3-4): 201-215.
- Gardner, P.M. and Robins, B., 1974. The olivine-plagioclase reaction: Geological evidence from the seiland petrographic province, northern Norway. *Contributions to Mineralogy and Petrology*, 44(2): 149-156.
- Gee, D., 1975. A tectonic model for the central part of the Scandinavian Caledonides. *American Journal of Science*, 275: 468-515.
- Geis, H.P., 1979. Nepheline syenite on Stjernøy, Northern Norway. *Economic Geology*, 74(5): 1286-1295.
- Graser, G. and Markl, G., 2008. Ca-rich Ilvaite-Epidote-Hydrogarnet Endoskarns: a Record of Late-Magmatic Fluid Influx into the Persodic Ilimaussaq Complex, South Greenland. *Journal of Petrology*, 49(2): 239-265.
- Green, E., Holland, T. and Powell, R., 2007. An order-disorder model for omphacitic pyroxenes in the system jadeite-diopside-hedenbergite-acmite, with applications to eclogitic rocks. *American Mineralogist*, 92(7): 1181-1189.
- Hamilton, D.L., 1961. Nephelines as Crystallization Temperature Indicators. *The Journal of Geology*, 69(3): 321-329.
- Hamilton, D.L. and Mackenzie, W.S., 1960. Nepheline Solid Solution in the System NaAlSi<sub>3</sub>O<sub>8</sub>-KAlSi<sub>3</sub>O<sub>8</sub>-SiO<sub>2</sub>. *Journal of Petrology*, 1(1): 56-72.
- Heier, K., 1961. Layered gabbro, hornblende, carbonatite and nepheline syenite on Stjernøy, North Norway. *Norsk Geologisk Tidsskrift*, 41: 109-155.
- Heier, K., 1964. Geochemistry of the nepheline syenite on Stjernøy, North Norway. *Norsk Geologisk Tidsskrift*, 44: 205-216.
- Heier, K., 1965. A geochemical comparison of the Blue Mountain (Ontario, Canada) and Stjernøy (Finnmark, north Norway) nepheline syenites. *Norsk Geologisk Tidsskrift*, 45: 41-52.
- Heier, K. and Taylor, S., 1962. A note on the U, Th and K contents in the nepheline syenite on Stjernøy, north Noeway. *Norsk Geologisk Tidsskrift*, 42: 287-292.
- Heier, K.S., 1966. Some Crystallo-chemical Relations of Nephelines and Feldspars on Stjernøy, North Norway. *Journal of Petrology*, 7(1): 95-113.
- Helgeson, H.C., Kirkham, D.H. and Flowers, G.C., 1981. Theoretical prediction of the thermodynamic behavior of aqueous electrolytes by high pressures and temperatures; IV, Calculation of activity coefficients, osmotic coefficients, and apparent molal and standard and relative partial molal properties to 600 degrees C and 5kb. *American Journal of Science*, 281(10): 1249-1516.
- Holdridge, D., 1962. A clay mineral from Stjernøy, Norway. *Clay Minerals*, 5(27): 26-30.
- Holger, T., 2010. The chemical composition of surface waters from the Seiland Igneous Province, Northern Norway. Master Thesis, University of Freiburg, Freiburg, 164 pp.
- Holland, T.J.B. and Powell, R., 2011. An improved and extended internally consistent thermodynamic dataset for phases of petrological interest, involving a new equation of state for solids. *Journal of Metamorphic Geology*, 29(3): 333-383.
- Kirkland, C.L., Daly, J.S., Eide, E.A. and Whitehouse, M.J., 2006. The structure and timing of lateral escape during the Scandian Orogeny: A combined strain and geochronological investigation in Finnmark, Arctic Norwegian Caledonides. *Tectonophysics*, 425(1-4): 159-189.

- Kirkland, Christopher L., Stephen Daly, J. and Whitehouse, Martin J., 2007. Provenance and Terrane Evolution of the Kalak Nappe Complex, Norwegian Caledonides: Implications for Neoproterozoic Paleogeography and Tectonics. *The Journal of Geology*, 115(1): 21-41.
- Kjøsnes, K., 1980. Fertilization of layered mafic rocks in the Lillebukt alkaline complex, Stjernøy, Norway. *Lithos*, 13(2): 215-215.
- Konnerup-Madsen, J., 2001. A review of the composition and evolution of hydrocarbon gases during solidification of the Ilimaussaq alkaline complex, South Greenland. *Geology of Greenland Survey Bulletin*, 190: 159-166.
- Korobeinikov, A.N., Laajoki, K. and Gehör, S., 2000. Nepheline-bearing alkali feldspar syenite (pulaskite) in the Khibina pluton, Kola Peninsula, NW Russia: petrological investigation. *Journal of Asian Earth Sciences*, 18(2): 205-212.
- Korobeynikov, A. and Laajoki, K., 1994. Petrological Aspects of the Evolution of Clinopyroxene Composition in the Intrusive Rocks of the Lovozero Alkali Massif. *Geochemistry International*, 31(3): 69-76.
- Krogh, E. and Elvevold, S., 1990. A Precambrian age for an early gabbro-monzonitic intrusive on the ksfjord peninsula, Seiland Igneous Province, northern Norway. *Norsk Geologisk Tidsskrift*, 70(4): 267-273.
- Krumrei, T.V., Pernicka, E., Kaliwoda, M. and Markl, G., 2007. Volatiles in a peralkaline system: Abiogenic hydrocarbons and F-Cl-Br systematics in the naujaite of the Ilimaussaq intrusion, South Greenland. *Lithos*, 95(3-4): 298-314.
- Leake, B.E. et al., 1997. Nomenclature of amphiboles; report of the Subcommittee on Amphiboles of the International Mineralogical Association Commission on New Minerals and Mineral Names. *European Journal of Mineralogy*, 9(3): 623-651.
- Lieberman, J. and Petrakakis, K., 1991. TWEEQU thermobarometry; analysis of uncertainties and applications to granulites from western Alaska and Austria. *The Canadian Mineralogist*, 29(4): 857-887.
- Mann, U., Marks, M. and Markl, G., 2006. Influence of oxygen fugacity on mineral compositions in peralkaline melts: The Katzenbuckel volcano, Southwest Germany. *Lithos*, 91(1-4): 262-285.
- Markl, G., 2001. A new type of silicate liquid immiscibility in peralkaline nepheline syenites (lujavrites) of the Ilimaussaq complex, South Greenland. *Contributions to Mineralogy and Petrology*, 141(4): 458-472.
- Markl, G. and Baumgartner, L., 2002. pH changes in peralkaline late-magmatic fluids. *Contributions to Mineralogy and Petrology*, 144(3): 331-346.
- Markl, G., Marks, M.A.W. and Frost, B.R., 2010. On the Controls of Oxygen Fugacity in the Generation and Crystallization of Peralkaline Melts. *Journal of Petrology*, 51(9): 1831-1847.
- Marks, M. and Markl, G., 2001. Fractionation and Assimilation Processes in the Alkaline Augite Syenite Unit of the Ilimaussaq Intrusion, South Greenland, as Deduced from Phase Equilibria. *Journal of Petrology*, 42(10): 1947-1969.
- Marks, M. and Markl, G., 2003. Ilimaussaq 'en miniature': closed-system fractionation in an agpaitic dyke rock from the Gardar Province, South Greenland (contribution to the mineralogy of Ilimaussaq no. 117). *Mineralogical Magazine*, 67(5): 893-919.
- Marks, M., Schilling, J., Coulson, I., Wenzel, T. and Markl, G., 2008. The alkaline-peralkaline Tamazeght complex, High Atlas mountains, Morocco: Mineral chemistry and petrological constraints for derivation from a compositionally heterogeneous mantle source. *Journal of Petrology*, 49(6): 1097.
- Marks, M.A.W., Rudnick, R.L., McCammon, C., Vennemann, T. and Markl, G., 2007. Arrested kinetic Li isotope fractionation at the margin of the Ilimaussaq complex, South Greenland: Evidence for open-system processes during final cooling of peralkaline igneous rocks. *Chemical Geology*, 246(3-4): 207-230.
- Mitchell, R.H. and Liferovich, R.P., 2006. Subsolidus deuteric/hydrothermal alteration of eudialyte in lujavrite from the Pilansberg alkaline complex, South Africa. *Lithos*, 91(1-4): 352-372.
- Mitchell, R.H. and Platt, R.G., 1982. Mineralogy and Petrology of Nepheline Syenites from the Coldwell Alkaline Complex, Ontario, Canada. *Journal of Petrology*, 23(2): 186-214.
- Morimoto, N., 1988. Nomenclature of pyroxenes. *Mineralogy and Petrology*, 39(1): 55-76.
- Oosterom, M., 1963. The ultramafites and layered gabbro sequences in the granulite facies rocks on Stjernøy (Finmark, Norway). *Leidse Geol Mededelingen*, 28: 177-296.
- Pedersen, R., Dunning, G. and Robins, B., 1989. U-Pb ages of nepheline syenite pegmatites from the

- Seiland Magmatic Province, N. Norway. The Caledonide Geology of Scandinavia: 3-8.
- Potter, J., Rankin, A.H. and Treloar, P.J., 2004. Abiogenic Fischer-Tropsch synthesis of hydrocarbons in alkaline igneous rocks; fluid inclusion, textural and isotopic evidence from the Lovozero complex, N.W. Russia. *Lithos*, 75(3-4): 311-330.
- Powell, M., 1978. The crystallisation history of the Igdlarfígssalik nepheline syenite intrusion, Greenland. *Lithos*, 11(2): 99-120.
- Roberts, D., 2003. The Scandinavian Caledonides: event chronology, palaeogeographic settings and likely modern analogues. *Tectonophysics*, 365(1-4): 283-299.
- Roberts, R.J., Corfu, F., Torsvik, T.H., Ashwal, L.D. and Ramsay, D.M., 2006. Short-lived mafic magmatism at 560-570 Ma in the northern Norwegian Caledonides: U-Pb zircon ages from the Seiland Igneous Province. *Geological Magazine*, 143(6): 887-903.
- Roberts, R.J., Corfu, F., Torsvik, T.H., Hetherington, C.J. and Ashwal, L.D., 2010. Age of alkaline rocks in the Seiland Igneous Province, Northern Norway. *Journal of the Geological Society*, 167(1): 71-81.
- Robins, B., 1984. Petrography and petrogenesis of nephelinized metagabbros from Finnmark, Northern Norway. *Contributions to Mineralogy and Petrology*, 86(2): 170-177.
- Robins, B. and Gardner, P.M., 1975. The magmatic evolution of the Seiland province, and Caledonian plate boundaries in northern Norway. *Earth and Planetary Science Letters*, 26(2): 167-178.
- Robins, B. and Tysseland, M., 1980. Fertilization of mafic cumulates by the Pollen carbonatite, Finnmark, Norway. *Lithos*, 13(2): 220-220.
- Robins, B. and Tysseland, M., 1983. The geology, geochemistry and origin of ultrabasic fenites associated with the Pollen Carbonatite (Finnmark, Norway). *Chemical Geology*, 40(1-2): 65-95.
- Salter, D.L. and Appleyard, E.C., 1974. An occurrence of vein palygorskite from the nepheline syenite of Lillebukt, Stjernøy, northern Norway. *Norsk Geologisk Tidsskrift*, 54: 329-336.
- Salvi, S. and Williams-Jones, A.E., 1997. Fischer-Tropsch synthesis of hydrocarbons during sub-solidus alteration of the Strange Lake peralkaline granite, Quebec/Labrador, Canada. *Geochimica Et Cosmochimica Acta*, 61(1): 83-99.
- Schilling, J., Marks, M.A.W., Wenzel, T. and Markl, G., 2009. Reconstruction of magmatic to subsolidus processes in an agpaitic system using eudialyte textures and composition: A case study from tamazeght, morocco. *Canadian Mineralogist*, 47(2): 351-365.
- Schönenberger, J., Köhler, J. and Markl, G., 2008. REE systematics of fluorides, calcite and siderite in peralkaline plutonic rocks from the Gardar Province, South Greenland. *Chemical Geology*, 247(1-2): 16-35.
- Schönenberger, J. and Markl, G., 2008. The Magmatic and Fluid Evolution of the Motzfeldt Intrusion in South Greenland: Insights into the Formation of Agpaitic and Miaskitic Rocks. *Journal of Petrology*, 49(9): 1549-1577.
- Schönenberger, J., Marks, M., Wagner, T. and Markl, G., 2006. Fluid-rock interaction in autoliths of agpaitic nepheline syenites in the Ilimaussaq intrusion, South Greenland. *Lithos*, 91(1-4): 331-351.
- Sørensen, H., 1980. On the role of volatile components in the evolution of alkaline igneous rocks. *Lithos*, 13(2): 221-222.
- Sørensen, H., 1992. Agpaitic nepheline syenites: a potential source of rare elements. *Applied Geochemistry*, 7(5): 417-427.
- Sørensen, H., 1997. The agpaitic rocks - an overview. *Mineralogical Magazine*, 61(4): 485-498.
- Strand, T., 1980. The chemistry of the Lillebukt carbonatite, Stjernøy, Norway. *Lithos*, 13(2): 223-223.
- Sturt, B.A., Miller, J.A. and Fitch, F.J., 1967. The age of alkaline rocks from West Finnmark, northern Norway, and their bearing on the datings of the Caledonian orogeny. *Norsk Geologisk Tidsskrift*, 47: 255-273.
- Sturt, B.A., Pringle, I.R. and Ramsay, D.M., 1978. The Finnmarkian phase of the Caledonian Orogeny. *Journal of the Geological Society*, 135(6): 597-610.
- Wones, D. and Eugster, H., 1965. Stability of biotite: experiment, theory and application. *American Mineralogist*, 50(9): 1228-1272.
- Worley, B.A. and Cooper, A.F., 1995. Mineralogy of the Dismal Nepheline Syenite, Southern Victoria Land, Antarctica. *Lithos*, 35(1-2): 109-128.

## **Part II Zeolites in Nepheline Syenite of Seiland Igneous Province, Northern Norway**

## 1. Abstract

Based on microscopic observation of secondary minerals in the rock samples, the derived reactions, and the thermodynamic modeling for mineral assemblages, two hydrothermal stages of nepheline syenite can be identified. Hydrothermal stage I is impressed by pervasive natrolite transformed from nepheline and albite dissolution. The related fluid is considered as fluid expelled by crystallizing magma, which has decreasing silica activity and slightly increasing Na activity with the product of natrolite. Hydrothermal stage II is dominated by infiltration of Ca-HCO<sub>3</sub> fluid from carbonatite catchment into the nepheline syenite along fractures which resulted in the generation of thomsonite at low CO<sub>2</sub> partial pressures by transformation from nepheline and natrolite.

## 2. Introduction

Infiltration of aqueous fluid into the silicate rocks along fractures commonly causes water-rock interaction process due to the disequilibrium between minerals and exotic fluid (e.g. Bucher and Stober, 2010; Giggenbach, 1981; Nordstrom et al., 1989). This disequilibrium is a function of both intensive variables (e.g. pressure, temperature, chemical potential and oxidation potential) and extensive ones (e.g. mass and volume of the fluid). The interaction process is generally associated with the dissolution of primary minerals and the precipitation of secondary minerals. Water-rock interaction process has been widely investigated for rock types from many case studies. For the upper continental crust which is predominantly composed of granite and gneiss, the interaction processes involve breakdown of primary plagioclase and biotite and the formation of Ca-zeolite minerals and chlorites (Weisenberger and Bucher, 2010; Weisenberger and Bucher, 2011). Hydrothermal fluids in volcanic field composed of basalt usually precipitate phyllosilicate and various zeolites at the expense of feldspar and glass (de'Gennaro et al., 2000; Kousehlar et al., 2012; Passaglia and Vezzalini, 1985; Weisenberger and Selbekk, 2009; Weisenberger and Spürgin, 2009). Zeolite species in low grade metamorphism which involve extensive fluid are also widely investigated (e.g. Frey et al., 1991; Neuhoff et al., 1999; Schmidt et al., 1997). The dominating zeolite minerals among most studies are Ca-zeolite like chabazite, heulandite, laumontite and stilbite, which all belong to high and middle silica zeolite group (Deer et al., 2004). Although hydrothermal processes which can stabilize zeolite minerals (e.g. natrolite) and dissolve feldspathoid have been demonstrated in various alkaline complexes (e.g. Marks et al., 2009; Schilling et al., 2009; Schilling et al., 2011), the formation condition and associated fluid responsible for Na-zeolite are inadequately interpreted.

In this study, I investigated the zeolite species, dominating by natrolite and thomsonite, in nepheline syenite of the Seiland igneous province of northern Norway, by means of texture observation, mineral composition and thermodynamic modeling method. The results show that two hydrothermal stages with distinct fluid chemistry are responsible for the natrolite and thomsonite formation.

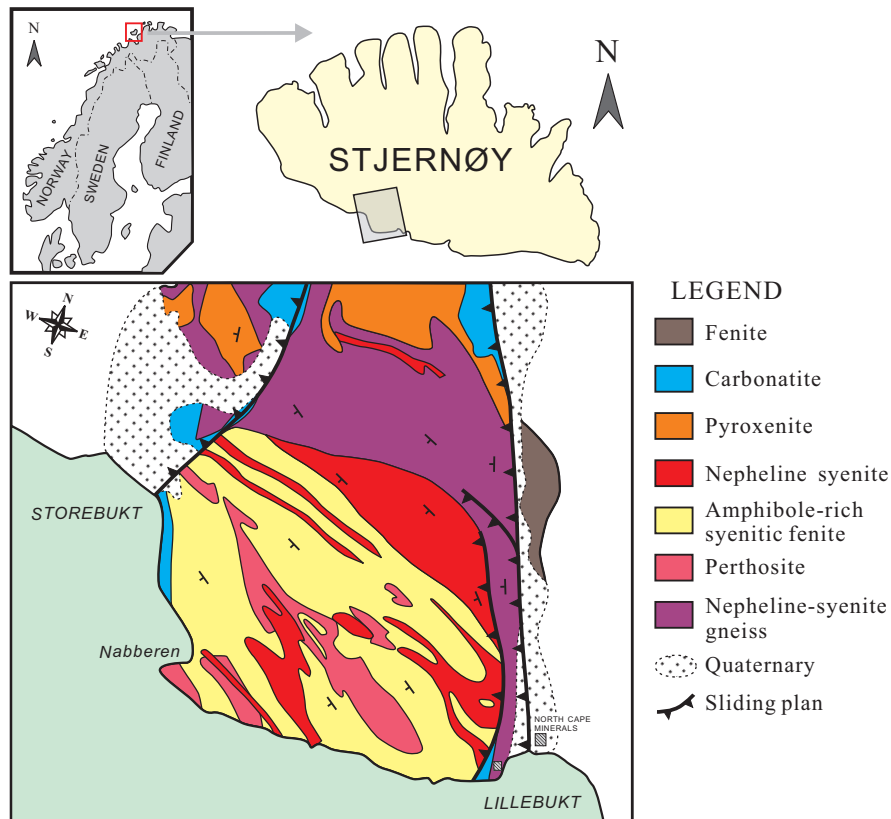


Fig. 1 Geological map of Lillebukt alkaline complex on the Stjernøy Island.

### 3. Geological background

The Seiland igneous province occupies an area of nearly 5,000 km<sup>2</sup> on the islands of Seiland, Sørøy and Stjernøy, and on the Øksfjord Peninsula in the northern Finnmark, Norway (Fig. 1). The province is located within the Kalak nappe complex of the Norwegian Caledonian orogenic belt, which has thrust eastwards onto the Precambrian crystalline basement of the Baltic shield during the Silurian continental collision (ca. 431-428 Ma at Finnmark, Kirkland et al., 2006;

Kirkland et al., 2007) between Baltica and Laurentia following the early Palaeozoic closure of the Iapetus Ocean (Gee, 1975; Roberts, 2003). The Seiland igneous province has a long and complex history concerning magmatic evolution: voluminous ultramafic rocks at  $829 \pm 18$  Ma (Krogh and Elvevold, 1990), layered gabbroic plutons of  $700 \pm 33$  Ma,  $604 \pm 44$  Ma and 570 Ma (Daly et al., 1991; Roberts et al., 2006) and a final stage of calc-alkaline intrusions represented by alkaline pyroxenite, syenite, nepheline syenite and carbonatite at  $574 \pm 5$  Ma (Roberts et al., 2010). All these various rocks are considered to represent a synorogenic (Caledonian orogenic belt) intrusive activity evolved from tholeiitic basalt, compositionally ranging from high-K calc-alkaline magmas, through alkaline olivine basalt and picrite and finally to highly differentiated alkaline magmas and carbonatite (Appleyard, 1974; Robins and Gardner, 1975; Sturt et al., 1967; Sturt et al., 1978).

The Lillebukt alkaline complex (Fig. 1), on Stjernøy Island, is enclosed in the ultramafic and mafic rocks of peridotite, pyroxenite, gabbro and hornblendite (Heier, 1961; Oosterom, 1963). The boundary is blurred and thus the relationship between the alkaline complex and the hosting rocks is unclear. The alkaline complex is composed of syenite, nepheline syenite, and carbonatite, all of which have been intruded by late mafic and syenite dikes, and pegmatites (Pedersen et al., 1989; Robins and Tysseland, 1980). The silico-carbonatite of the Lillebukt alkaline complex is closely related to the nepheline syenite and contains abundant amphibole, biotite and apatite in the silicate-rich layers (Robins and Tysseland, 1983; Strand, 1980). It has been suggested that the carbonatite represents the latest igneous activity of the Caledonian orogeny (Robins and Gardner, 1975). The nepheline syenite has been mined by North Cape Minerals in an open pit on Nabberen (earlier in an underground mine inside Nabberen) and the raw material is processed at the Lillebukt plant. The fine powdered nepheline - K-feldspar mixture is shipped from the small port to customers in the ceramics and glass industry worldwide.

The Nabberen nepheline syenite body is a lens-shaped stock located in the north of the summit of Nabberen (Fig. 1), which occupies an area of  $1700 \times 300$  m<sup>2</sup> (Geis, 1979). It is a miaskitic nepheline syenite characterized by high concentration of alkalis, Ba and Sr, and depletion of REE, Y, Nb, Sc, Zr, U, and Th (Heier, 1964; Heier and Taylor, 1962; Heier, 1966; Robins and Tysseland, 1980). The surrounding gabbros have been fenitized, probably by the low-density fluid expelled from the volatile-rich alkaline magmas which now crystallized as nepheline syenite and carbonatite (Appleyard, 1980; Kjøsnes, 1980; Robins, 1984; Robins and Tysseland, 1980; Robins and Tysseland, 1983). Hydrothermal assemblages including zeolites (natrolite) and clay minerals (palygorskite, a magnesium clay mineral) have been observed in the Lillebukt mine, and they were regarded as products of post-tectonic low-temperature reactions



with groundwater (Geis, 1979; Holdridge, 1962; Salter and Appleyard, 1974).

## 4. Sample description and petrography

### 4.1 Sample description

During extended field work 2003 and 2009 a large number of samples and field data (structures, textures) have been collected from the old mine tunnels, the open pit and from natural outcrops including samples from the carbonatite. We selected five representative rock samples from that collection for detailed investigation. All samples are from the Nabberen nepheline syenite mine. Specifically, samples 1145, 1147 and 1148 are from the underground tunnels, sample 1151 from the open pit of the Nabberen summit and sample 926 from a core from an exploration borehole. All the samples are massive and have no preferred orientation of minerals.

In samples 1147, 1148 and 1151, white reaction veins are generally less than 1 cm in width and can be clearly identified (Fig. 2). Wide veins (up to 5 mm) are accompanied by bilateral reaction zones (up to 2 cm). These bilateral reaction zones display a reddish color distinctive from the white veins and the gray original nepheline syenite (Fig. 2a). In addition, there are numerous irregular fine seams (less than 1 mm wide) which can be identified under careful observation by their indistinct white color and occasionally reddish reaction speckles along the seams (Fig. 2b). These tiny seams cut each other and form a network over the whole sample. The white alteration veins are entirely composed of fine-grained brown-grey zeolite aggregates. There is no significant difference in mineral constituents between rock matrix and reaction zones, except more intense alteration of nepheline in the latter.

Sample 926 has a clear dark gray color, and is thus considered to be formed without significant alteration. Therefore, the alteration degree of our samples can be simply arranged as 1148, 1147, 1151, 1145 and 926 from high to low.

### 4.2 Petrography of host nepheline syenite

The rock matrix of nepheline syenite is mainly composed of potassium feldspar (40 %), nepheline (35 %), amphibole (10 %) and clinopyroxene (5 %), with accessory albite, biotite, apatite, titanite, magnetite, ilmenite, calcite and zeolite. Light green clinopyroxene occurs as prismatic crystals (up to 1 cm) with irregular grain boundaries and inclusions of apatite. Most amphiboles appear as dark green coronas around or thin rims along clinopyroxene. Fine vermiform amphibole crystals coarsening outward forming the corona. There are also amphibole

rims around calcite crystals adjacent to the clinopyroxene. A few amphibole crystals also show prismatic crystals. Potassium feldspar and nepheline are large anhedral to subhedral crystals, which coexist with each other in textural equilibrium, indicative of approximately contemporaneous crystallization. Tiny anhedral apatite crystals are distributed sporadic in the matrix and as inclusions in clinopyroxene and amphibole. Titanite occurs as euhedral crystals or rims around magnetite and ilmenite. Minor hercynite crystals are present close to the margin of the magnetite rimmed by titanite. Rare biotite crystals are found together with ilmenite and magnetite.

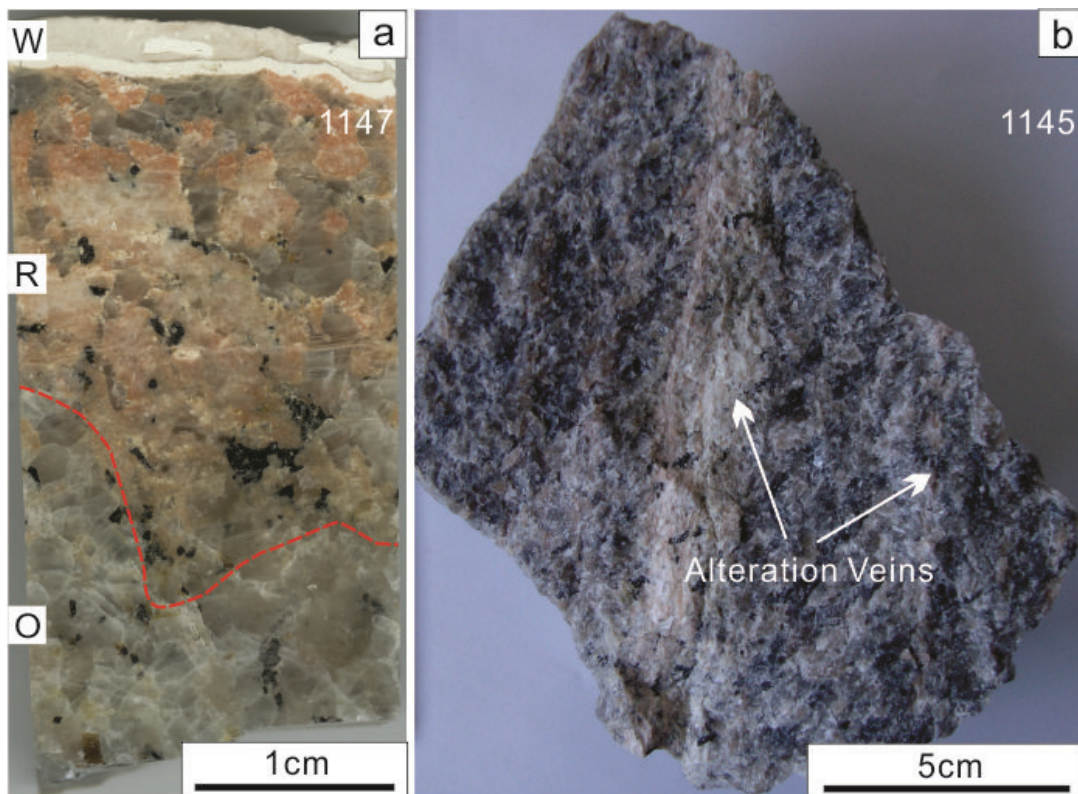


**Fig. 2 (a) Nepheline syenite sample 1147 which illustrating alteration phenomenon. O: Original part; R: Reaction zone; W: White vein. (b) Nepheline syenite sample 1145 with fine alteration seams.**

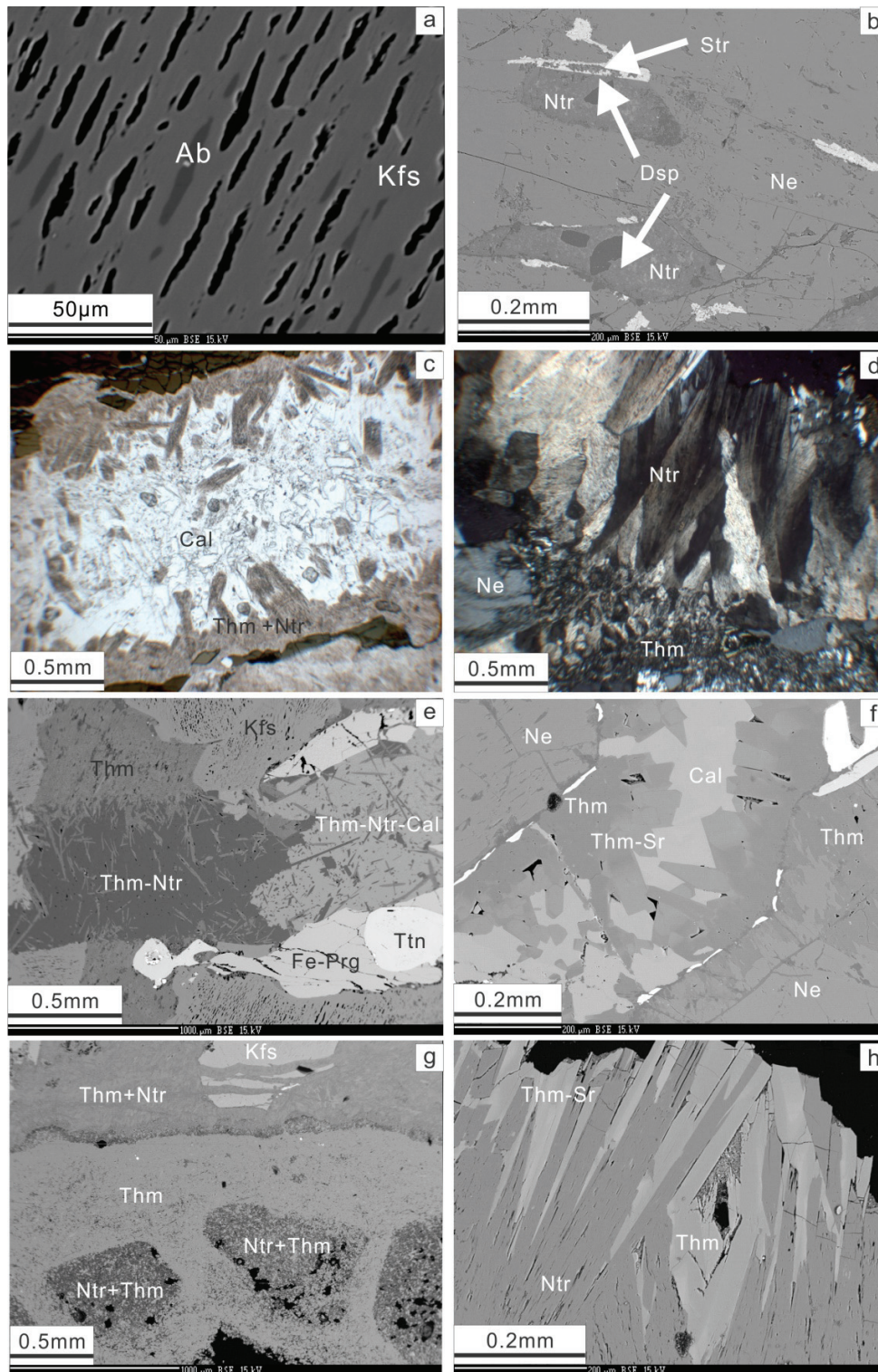


**Fig. 3 Photomicrographs (under plane-polarized light) and BSE images showing various secondary mineral textures. See text for explanations.**

### 4.3 Textures related with Zeolite

Potassium feldspars show widespread perthite textures with albite as blade or drop shaped lamellae. The site of albite lamellae has become cavity likely due to dissolution (Fig. 3c). Nepheline crystals are speckled or replaced by fine-grained zeolite and diaspore (Fig. 3d). Stronalsite-banalsite solid solution minerals are present in nepheline grains which are enriched in fissures (Fig. 3d). Natrolite crystals are blade-shaped with brown color under thin section, while thomsonite are usually clear and form aggregate together (Fig. 3c and Fig. 3d). Calcite-rich veins in the nepheline syenite are accompanied with natrolite, thomsonite and Sr-rich thomsonite (Fig. 3e and Fig. 3f). Calcite crystals usually precipitated in the center of the vein with small inclusions of natrolite and thomsonite (Fig. 3e), thomsonite precipitated on the wall of the vein and infiltrated into nepheline (Fig. 3f). Strontium-rich thomsonite are presented adjacent to calcite. In the white veins within nepheline syenite, mixture of fine-grained natrolite and thomsonite occurs as rounded spots with diameter of ca. 0.5 mm (Fig. 3g). Natrolite grains are overgrown by thomsonite locally in all samples (Fig. 3h).

## 5. Methods

### 5.1 Whole-rock analysis

The composition of the rock samples was analyzed at the Institute of Geosciences, University of Freiburg. A Philips 2404 X-ray fluorescence spectrometer was used with element specific acceleration voltage 30 kV and current 40 nA, with fused beads for major elements and powder pellets for minor elements, respectively. Loss on ignition (LOI) was determined to complete the XRF analyses, and total Fe is reported as  $\text{Fe}_2\text{O}_{3\text{tot}}$ . FeO contents are analyzed by titrimetry method using  $\text{KMnO}_4$  and 40% HF.

### 5.2 Mineral analysis

Mineral analyses were performed by electron beam microanalysis using wavelength-dispersive spectrometry (WDS) of a digital CAMECA SX100 electron microprobe at the Institute of Geosciences, University of Freiburg. During analyses an accelerating voltage of 15 kV and a current of 20 nA were used. Beam diameter was 0.5  $\mu\text{m}$  (for feldspar, sometimes 5  $\mu\text{m}$ ).

### 5.3 Geochemical modeling for mineral stability diagram

Mineral stability fields represented in activity-activity diagrams were calculated with the TWQ program (Lieberman and Petrakakis, 1991) using mineral database of JUN92 (Berman, 1988) and aqueous database of HKF81 (Helgeson et al., 1981). The utilized thermodynamic data in this study for most zeolite group minerals (heulandite, laumontite, stilbite and wairakite) are derived from Frey et al. (1991). As a rare case, the data of analcite is derived from the database of Holland and Powell (2011). Notably, in order to maintain the internal consistency of database, the thermodynamic data for thomsonite, natrolite and mesolite (which are not available in the commonly used database, e.g. JUN92) are constructed by integrating other thermodynamic data of reaction-related minerals (Table 1). Calcite saturation condition and corresponding partial pressure of CO<sub>2</sub> gas were calculated by SUPCRT92 program (Johnson et al., 1992) with dprons92 database (Helgeson et al., 1981).

Table 1 Thermodynamic data of zeolite minerals additionally inserted to JUN92 database.

Mineral	Formula	Reactions used	G <sup>0</sup> [J]	H <sup>0</sup> [J]	S <sup>0</sup> [J/K]	V <sup>0</sup> [J/bar]	K1	K4	K3	K8
Natrolite	Na <sub>2</sub> Al <sub>2</sub> Si <sub>6</sub> O <sub>10</sub> ·2H <sub>2</sub> O	1Nat + 1Qtz + 2Ky = 2Pg	-5318700.00	-5720700.00	359.73	16.97	549.76	1297.49	-56882572.00	9734949744.00
Thomsonite	Ca <sub>2</sub> NaAl <sub>5</sub> Si <sub>6</sub> O <sub>20</sub> ·6H <sub>2</sub> O	2Lw + 2Pg - 2Ky - Ab = Thm	-11553866.00	-12509689.06	624.48	33.99	1693.48	-13023.40	-52536430.00	10856994928.00
Mesolite	Na <sub>2</sub> Ca <sub>2</sub> Al <sub>6</sub> Si <sub>6</sub> O <sub>30</sub> ·8H <sub>2</sub> O	4Lw + 2Ab - 2An - Qtz = Mes	-16573905.00	-17937739.31	923.70	51.37	2743.21	-30114.64	-12238968.00	5685975808.00

## 6. Whole-rock geochemistry and mass changes

Whole-rock major and trace element compositions are given in Table 2. Following the sample description above, samples 1147, 1148 and 1151 analyses have been performed on both the original unaltered rock (O) and the reaction zones (R), while from sample 1145 only original rock (O) and from sample 926 the bulk rock has been analyzed.

All samples have relatively high aluminum and alkali concentrations, which are the typical character of alkaline rocks. The high concentrations of Ba and Sr, and low contents of Sc, U, Th, Pb, Ta and Hf reflect the miaskitic character of the alkaline rocks. The trace element data are consistent with earlier data obtained in this area (Appleyard, 1974; Heier, 1964; Heier, 1965).

The mass balance calculation on samples 1147, 1148 and 1151 are constructed by GEOISO program (Coelho, 2006). Each element mass of alteration part was compared to its mass in the original rock (Fig. 4). TiO<sub>2</sub> is regarded as inert oxide due to the absence of titanite and other Ti-bearing minerals in the alteration vein. Isocon diagrams showing constant mass (CM), constant volume (CV) and Isocon lines are presented in Fig. 4a. Element and oxide which above the isocon lines are mass enriched, in contrast, element and oxide below the isocon lines are depleted.

All three samples have similar element depletion and enrichment future with various absolute extents (Fig. 4b). The alteration zone is strongly enriched in H<sub>2</sub>O, Ca and Sr, and weakly enriched in Mg and P. The depleted elements are CO<sub>2</sub>, Na, K, Al and Si during alteration. Nobly, Ba is enriched in alteration part of sample 1151, but depleted in that of sample 1147 and 1148. The enrichment of H<sub>2</sub>O, Ca and Sr is clearly evidenced by the formation of thomsonite, Sr-rich thomsonite and calcite (Fig. 3f).

Table 2 Major and trace element compositions of nepheline syenite samples.

Sample	1145 O	1147 O	1147 R	1148 O	1148 R	1151 O	1151 R	Kb926
Oxide (wt%)								
SiO <sub>2</sub>	54.36	53.87	53.57	53.84	53.62	53.31	54.29	54.02
TiO <sub>2</sub>	0.27	0.35	0.38	0.35	0.40	0.50	0.50	0.33
Al <sub>2</sub> O <sub>3</sub>	24.07	24.00	23.02	24.16	23.11	23.11	22.81	22.60
Fe <sub>2</sub> O <sub>3</sub> tot	1.85	2.24	2.42	2.12	2.25	2.95	2.75	2.40
MnO	0.03	0.05	0.05	0.04	0.05	0.06	0.06	0.05
MgO	0.04	0.08	0.12	0.07	0.13	0.14	0.17	0.16
CaO	1.52	1.79	4.11	1.70	4.33	2.69	2.64	2.16
Na <sub>2</sub> O	7.82	7.46	4.78	7.68	4.78	7.32	6.09	6.84
K <sub>2</sub> O	8.06	8.66	7.14	8.66	6.90	8.43	7.95	8.65
P <sub>2</sub> O <sub>5</sub>	0.03	0.04	0.05	0.04	0.05	0.06	0.07	0.05
LOI	1.50	1.01	4.42	0.81	4.68	1.08	2.42	1.48
SUM	99.55	99.55	100.06	99.47	100.30	99.65	99.75	98.74
FeO*	1.10	1.14	1.22	1.08	1.07	1.24	1.24	1.27
Fe <sub>2</sub> O <sub>3</sub> calc	0.63	0.97	1.06	0.92	1.06	1.57	1.37	0.99
H <sub>2</sub> O	1.40	0.85	4.97	0.53	5.37	0.38	2.74	0.82
CO <sub>2</sub>	0.59	0.53	0.13	0.49	0.08	0.93	0.20	1.03
Na <sub>2</sub> O/ K <sub>2</sub> O	1.47	1.31	1.02	1.35	1.05	1.32	1.16	1.20
(Na <sub>2</sub> O+ K <sub>2</sub> O) / Al <sub>2</sub> O <sub>3</sub>	0.90	0.90	0.68	0.91	0.66	0.92	0.82	0.91
Trace element (ppm)								
Cl	10	44	2	40	—	17	—	26
S	96	156	77	125	63	154	69	155
Sc	1	—	2	1	3	2	1	—
V	23	23	28	25	27	35	38	34
Cr	10	55	38	8	4	94	21	5
Co	—	1	—	—	—	1	—	4
Ni	5	6	6	5	5	6	5	6
Zn	13	13	16	14	16	16	16	27
Sr	2331	2712	3480	2606	3373	2488	3324	2911
Ba	1858	1809	1984	1745	1961	1515	1655	1624
Rb	103	114	92	113	91	117	108	131
U	2	3	2	2	1	2	2	3
Th	1	—	—	—	—	1	1	—
Ga	15	15	12	16	11	16	14	16
Pb	1	2	1	1	1	1	0	2
Nb	32	47	52	45	62	68	80	29
Ta	2	1	1	1	—	1	—	4
Y	12	14	18	13	18	16	20	5
Zr	27	36	43	35	45	52	59	33
Hf	4	4	4	3	4	4	4	4

Fe<sub>2</sub>O<sub>3</sub>\*: total Fe; FeO: ferrous iron data obtained by wet chemical method; —: under detection limit

Table 3 Representative microprobe analyses of zeolite

Sample Point	1145A	1145B	1145C	Kb926	1145A	1145B	1147A	1148A	1148B	1151	Kb926	1151	1151	
	Zeo 006	Zeo 041	Zeo 036	Zeo 037	Zeo 009	Zeo 040	Zeo 063	Zeo 003	Zeo 002	Zeo 050	Zeo 043	Zeo 013	Zeo 014	
	Ntr		Ntr		Thm		Thm		Thm		Sr-Thm		Sr-Thm	
SiO <sub>2</sub>	48.485	47.359	45.87	48.146	38.219	40.483	37.96	37.25	37.82	37.39	53.144	40.25	37.08	
Al <sub>2</sub> O <sub>3</sub>	28.33	28.879	26.45	27.795	30.407	30.126	30.84	31.59	30.87	30.75	20.675	29.28	29.68	
FeOtotal	0.026	0.019	0.03	0.099	0.08	0.039	0.04	0.04	0.02	0.08	0.173	0.03	0.03	
MnO	0.025	0	0	0	0.03	0.003	0.01	0	0.02	0.01	0.05	0.02	0.03	
MgO	0.005	0.002	0	0	0.022	0.005	0.01	0.08	0	0.01	0	0	0	
SrO	0.027	0.089	0.16	0.03	3.189	0.963	0.42	1.22	0.23	0.93	0.549	2.51	3.78	
BaO	0	0	0	0	0	0	0.03	0.12	0.02	0	0	0.01	0	
CaO	0.488	1.483	1.46	0.056	10.951	10.34	11.95	12.39	12.79	12.27	3.288	10.41	11.06	
Na <sub>2</sub> O	15.334	14.62	13.05	15.871	4.64	6.444	4.42	3.41	4.55	4.47	9.41	4.69	3.99	
K <sub>2</sub> O	0.029	0.023	0.17	0.029	0.181	0.038	0.04	0.13	0.02	0.04	0.079	0.02	0.01	
Total	92.749	92.474	87.190	92.026	87.719	88.441	85.720	86.230	86.340	85.950	87.368	87.220	85.660	
Cations per 80 oxygens														
Si	23.864	23.441	23.992	23.918	20.583	21.280	20.535	20.144	20.371	20.305	27.234	21.540	20.513	
Al	16.434	16.847	16.305	16.274	19.300	18.664	19.663	20.134	19.597	19.682	12.487	18.467	19.351	
Fe <sup>3+</sup>	0.011	0.008	0.013	0.041	0.036	0.017	0.018	0.018	0.009	0.036	0.074	0.013	0.014	
Mn	0.010	0.000	0.000	0.000	0.014	0.001	0.005	0.000	0.009	0.005	0.022	0.009	0.014	
Mg	0.004	0.001	0.000	0.000	0.018	0.004	0.008	0.064	0.000	0.008	0.000	0.000	0.000	
Sr	0.008	0.026	0.049	0.009	0.996	0.294	0.132	0.383	0.072	0.293	0.163	0.779	1.213	
Ba	0.000	0.000	0.000	0.000	0.000	0.000	0.006	0.025	0.004	0.000	0.000	0.002	0.000	
Ca	0.257	0.786	0.818	0.030	6.319	5.824	6.926	7.179	7.381	7.140	1.805	5.969	6.556	
Na	14.633	14.030	13.234	15.287	4.845	6.568	4.636	3.575	4.752	4.707	9.350	4.866	4.280	
K	0.018	0.015	0.113	0.018	0.124	0.025	0.028	0.090	0.014	0.028	0.052	0.014	0.007	
Total	55.239	55.154	54.523	55.577	52.234	52.676	51.956	51.613	52.209	52.203	51.186	51.660	51.948	
E%	8.267	7.546	8.203	6.064	-1.521	-0.819	4.635	6.241	-0.378	0.522	-5.826	0.549	-2.311	
T <sub>Si</sub>	0.592	0.582	0.595	0.595	0.516	0.533	0.511	0.500	0.510	0.508	0.686	0.538	0.515	
Si/Al	1.452	1.391	1.471	1.470	1.066	1.140	1.044	1.001	1.040	1.032	2.181	1.166	1.060	

E% = -10% -10%, acceptable according to Passaglia (1970)

E% = 100\*(Al - (Na +K) + 2\*(Mg + Ca + Sr + Ba))/(Na + K) + 2\* (Mg + Ca + Sr + Ba)

T<sub>Si</sub> = Si/(Si+Al)

## 7. Mineral composition

### 7.1 Zeolite

Zeolites are rich in Na, and the main species are natrolite and thomsonite. Representative compositions are listed in Table 3 and illustrated in Fig. 5. The acceptable zeolite analysis have E% between -10% to 10% according to the method of Passaglia (1970).

#### 7.1.1 Natrolite

The framework cation of natrolite is almost entirely Na, which is close to the stoichiometric formula. The extra-framework cations are Ca, K, and Sr. K and Sr in natrolite are below 0.02 pfu, while Ca is widely scattered up to ca. 1.4 pfu. The Si/(Si+Al) ratio slightly varies between 1.3 to 1.5.

#### 7.1.2 Thomsonite

Thomsonite compositions have wide range of Na and Ca contents. The Ca/Na ratios of thomsonite vary from 0.5 to 2.2. The substitution of Ca to Na is accompanied with Si-Al substitution. Thus Si/Al ratios vary from 1 to 1.2 correspondingly. Sr content is widely scattered up to ca. 1 pfu. Several extreme Sr-rich thomsonite have highest Sr values up to 1.8 pfu. K in thomsonite is below 0.5 pfu.





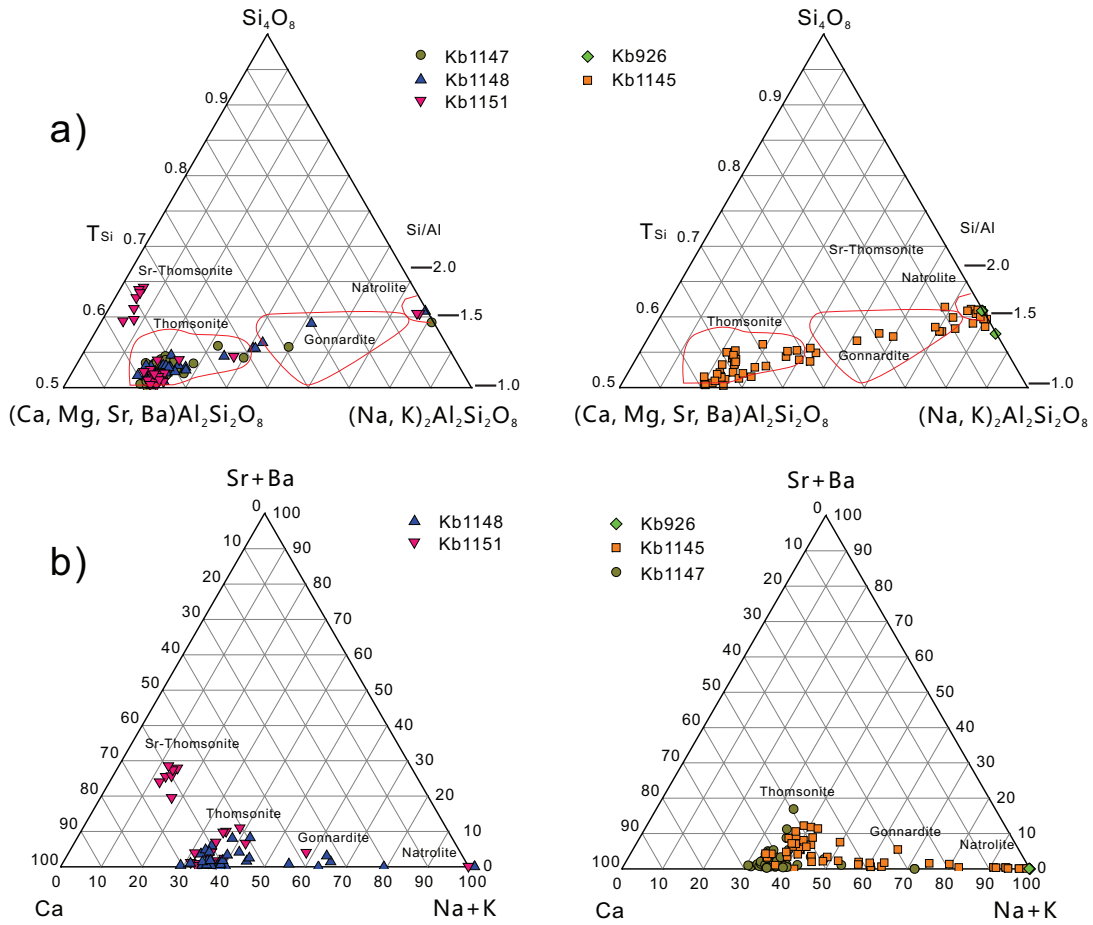


**Fig. 5** Compositional plots of zeolite minerals.

## 7.2 Nepheline

Representative nepheline compositions are given in Table 4. For all nepheline syenite samples, nepheline varies in composition between  $\text{Ne}_{80}\text{Ks}_{20}\text{Qtz}_1$  and  $\text{Ne}_{77}\text{Ks}_{18}\text{Qtz}_4$  without systematic differences. These Qtz-poor (from 1.22 to 4.22 mol %) and Ne-rich compositions are typical features of nepheline grains and common in large slowly-cooled plutonic bodies (Marks et al., 2008). The Na/K ratio in nepheline ranges from 3.63 to 4.33, with an average value of 3.95. All nepheline compositions are plotted below the line of 500°C on the nepheline-kalsilite-silica (Ne–Ks–Qz) diagram (Hamilton, 1961; Hamilton and Mackenzie, 1960). This indicates that nepheline has gained a chemical re-equilibration at near 500°C (Fall et al., 2007).

Table 4 Representative microprobe analyses of nepheline and feldspar.

Sample Point	1145A Ne 031	1147A Ne 015	1148A Ne 021	1151 Ne 027	Kb926 Ne 005	1145A Kfs 001	1145A Pl 033	1147A Kfs 016	1151 Pl 070	Kb926 kfs 002	Kb926 Pl 026
	Nepheline					Feldspar					
SiO <sub>2</sub>	42.978	42.57	42.8	42.51	42.885	62.044	64.772	64.76	63.74	64.843	65.064
Al <sub>2</sub> O <sub>3</sub>	34.432	35.32	34.46	34.37	34.691	18.512	22.623	19.07	22.92	19.094	22.533
FeO <sub>total</sub>	0.061	0.09	0.1	0.09	0.103	0.043	0.002	0.04	0.39	0.026	0.039
MnO	0	0	0	0.01	0	0	0.002	0.02	0	0	0
MgO	0.003	0.01	0.02	0	0.008	0.008	0	0	0	0.013	0.016
SrO	0.021	0	0	0.02	0	0.363	0.373	0.57	0.44	0.401	0.428
BaO	0.013	0	0.01	0.04	0.008	0.544	0	0.66	0	0.329	0
CaO	0.611	0.94	0.74	1.38	0.922	0.03	2.917	0.06	3.73	0.11	2.916
Na <sub>2</sub> O	16.168	15.91	16.76	16.9	16.032	1.843	10.058	2.93	9.99	2.162	10.483
K <sub>2</sub> O	6.149	5.74	6.24	5.26	6.398	13.378	0.133	12.48	0.1	13.242	0.167
Total	100.436	100.580	101.130	100.580	101.047	96.765	100.880	100.590	101.310	100.220	101.646
	Cations per 16 oxygens					Cations per 8 oxygens					
Si	4.113	4.059	4.083	4.069	4.088	2.961	2.836	2.965	2.794	2.972	2.834
Al	3.884	3.969	3.875	3.878	3.897	1.041	1.167	1.029	1.184	1.032	1.157
Fe <sup>3+</sup>	0.005	0.007	0.008	0.007	0.008	0.002	0.000	0.002	0.014	0.001	0.001
Mn	0.000	0.000	0.000	0.001	0.000	0.000	0.000	0.001	0.000	0.000	0.000
Mg	0.000	0.001	0.003	0.000	0.001	0.001	0.000	0.000	0.000	0.001	0.001
Sr	0.001	0.000	0.000	0.001	0.000	0.010	0.009	0.015	0.011	0.011	0.011
Ba	0.000	0.000	0.000	0.002	0.000	0.010	0.000	0.012	0.000	0.006	0.000
Ca	0.063	0.096	0.076	0.142	0.094	0.002	0.137	0.003	0.175	0.005	0.136
Na	3.000	2.941	3.100	3.137	2.963	0.171	0.854	0.260	0.849	0.192	0.885
K	0.751	0.698	0.760	0.642	0.778	0.814	0.007	0.729	0.006	0.774	0.009
Total	11.818	11.772	11.905	11.878	11.830	5.011	5.011	5.015	5.034	4.995	5.034

### 7.3 Feldspar

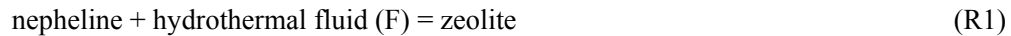
Representative feldspar compositions are listed in Table 4. Most alkali feldspar shows a perthitic structure formed by subsolvus exsolution developing Na- and K-rich lamellae. While, the composition derived from multiple lamellas using wide electron beam (diameter 5  $\mu\text{m}$ ) show two main composition groups without An component: Ab<sub>15-30</sub> and Or<sub>65-86</sub>, depending on the volume ratio of exsolved lamellae and matrix under the corresponding beam. In addition, there is some ternary feldspar with scattered composition such as An<sub>8</sub>Ab<sub>64</sub>Or<sub>29</sub> and An<sub>11</sub>Ab<sub>81</sub>Or<sub>7</sub>, suggesting high crystallization temperatures of 900°C references. The feldspar doubling ribbons are pure albite or oligoclase (average Ab<sub>83</sub>An<sub>17</sub>).

## 8. Discussion

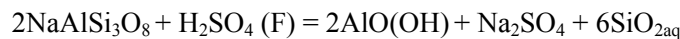
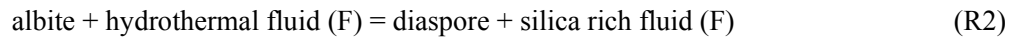
Based on microscopic observation of primary and secondary minerals in the rock samples, the derived reactions, and the thermodynamic modeling for mineral assemblages, several conclusions concerning the evolution of nepheline syenite can be drawn: (1) Orthomagmatic stage of nepheline syenite is characteristic with assemblage of nepheline + K-feldspar + clinopyroxene + amphibole  $\pm$  magnetite  $\pm$  ilmenite at temperatures between ca. 500-700 °C at activity of silica being ca. 0.15-0.33. (2) Autometamorphic stage is represented by coronas of amphibole on clinopyroxene and biotite on amphibole, which are result from reactions between primary minerals and residual melt. Two stages of hydrothermal events, which are characterized by natrolite and thomsonite formation respectively, could be identified in this paper.

## 8.1 Hydrothermal stage I

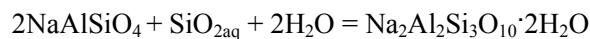
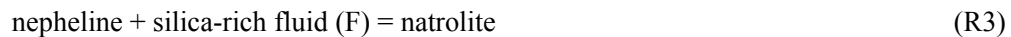
The hydrothermal stage I is characterized by natrolite formation, the related mineral assemblages and textures are shown in Fig. 3a-h. Hydrothermal veins are mainly composed of zeolite (and calcite) (Fig. 3a-h), the principal reaction of the hydrothermal stage is the nepheline - zeolite transformation, which can be written as:



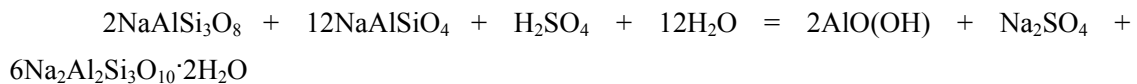
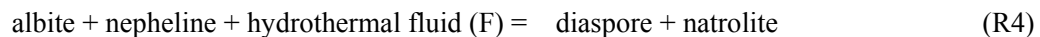
The dissolved aqueous silica necessary for the zeolitization is likely to result from internal dissolution of the albite lamella in perthite. Albite dissolution have been observed in nepheline syenite (Fig. 3a), the corresponding reaction could be described by the following reaction:



The reaction consumes  $\text{H}_2\text{SO}_4$  component from fluid and release silica and thenardite component to the fluid. Simultaneously, diaspore precipitated in the in situ locality or other place (Fig. 3b). The released  $\text{SiO}_2$  will increase the silica activity of the fluid, which thus destabilized nepheline by reactions like these:



The above nepheline dissolution reaction is accompanied by precipitation of natrolite (Fig. 3b). The process consumes the silica derived from R3. The combined reaction is:

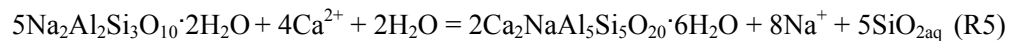


This could explain the co-occurrence of natrolite and diaspore which replace nepheline (Fig. 3b). The reaction would increase the Na activity of the fluid. This arbitrary reaction also would maintain constant silica activity, only if all the silica released by R2 is totally consumed by R3, which however can hardly be fulfilled in a real case.

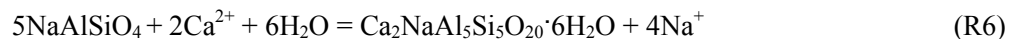
Therefore the increase of Silica and  $\text{Na}^+$  activities of fluid together as a result of R2 will further promote the stabilization of natrolite through the reaction R3. As a result of reaction R4 and precipitation of natrolite, silica activity would be compensated partly but still tends to increase. Thus the initial fluid of nepheline syenite catchment would have a  $\text{Na}_2\text{SO}_4$  -rich signature.

## 8.2 Hydrothermal stage II

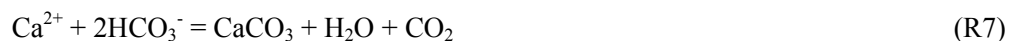
Large amount of  $\text{Ca-HCO}_3$  fluid from carbonatite catchment probably have infiltrated into nepheline syenite along faults or fractures and mixed with the initial fluid of nepheline syenite. The mixed fluid would increase Ca activity at constant  $\text{SiO}_2$  activity. Fluid will cross the natrolite field and enter the thomsonite stability field. Thomsonite which overgrowth on natrolite (Fig. 3h) and co-precipitated with calcite (Fig. 3f) could be explained by this mixed fluid. The corresponding reaction is:



The reaction R10 would consume the  $\text{Ca}^{2+}$  and release  $\text{Na}^+$  with the precipitation of thomsonite. The direct alteration of nepheline to thomsonite could be described by reaction:



The transportation of  $\text{Ca-HCO}_3$  fluid along fractures in nepheline syenite will precipitate thomsonite on the fracture wall when contact with nepheline or natrolite (Fig. 3f), and precipitate calcite in the middle of fluid conduit through reaction:



The precipitation of calcite in this case emphasizes the importance of local disequilibrium in the water-rock system.

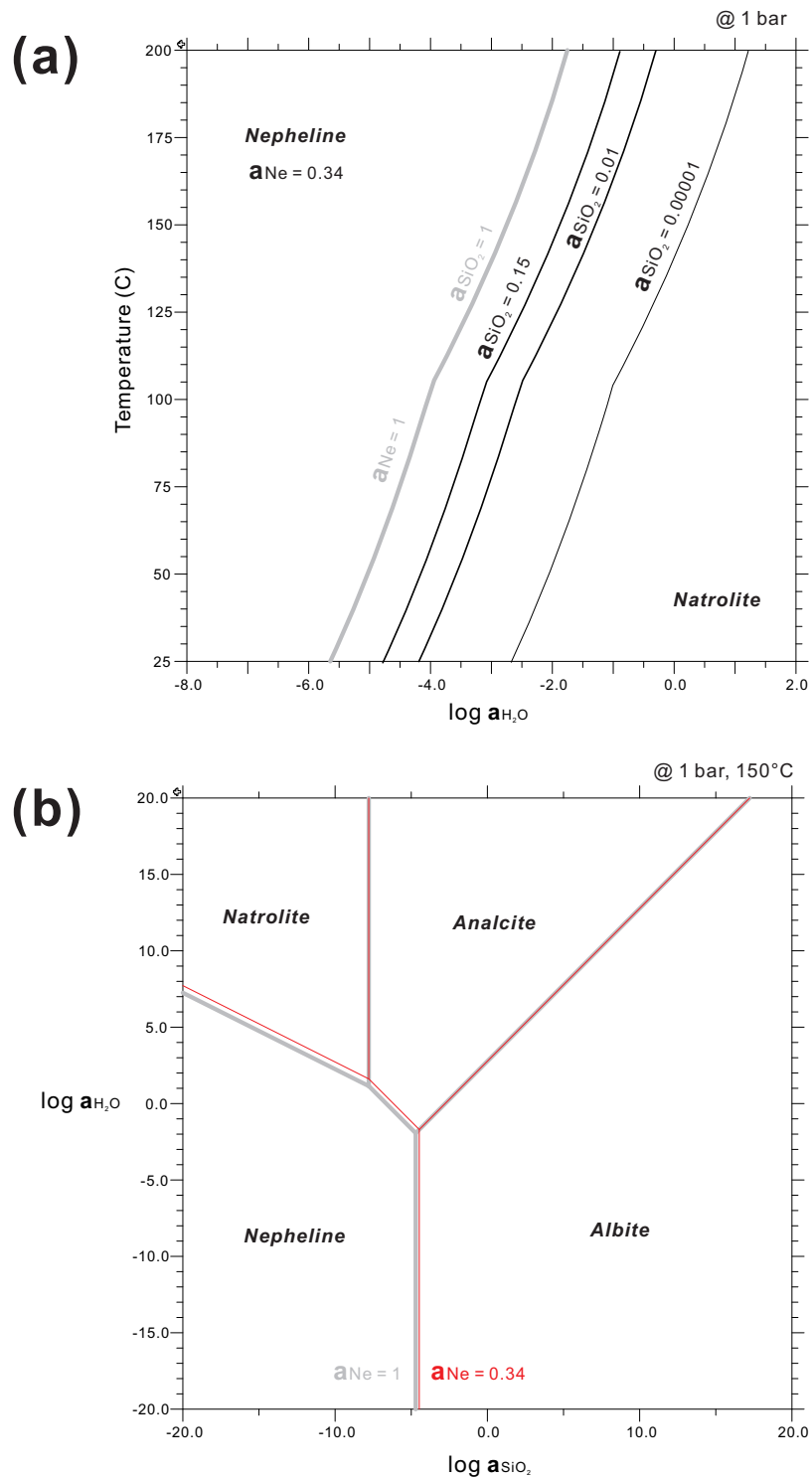
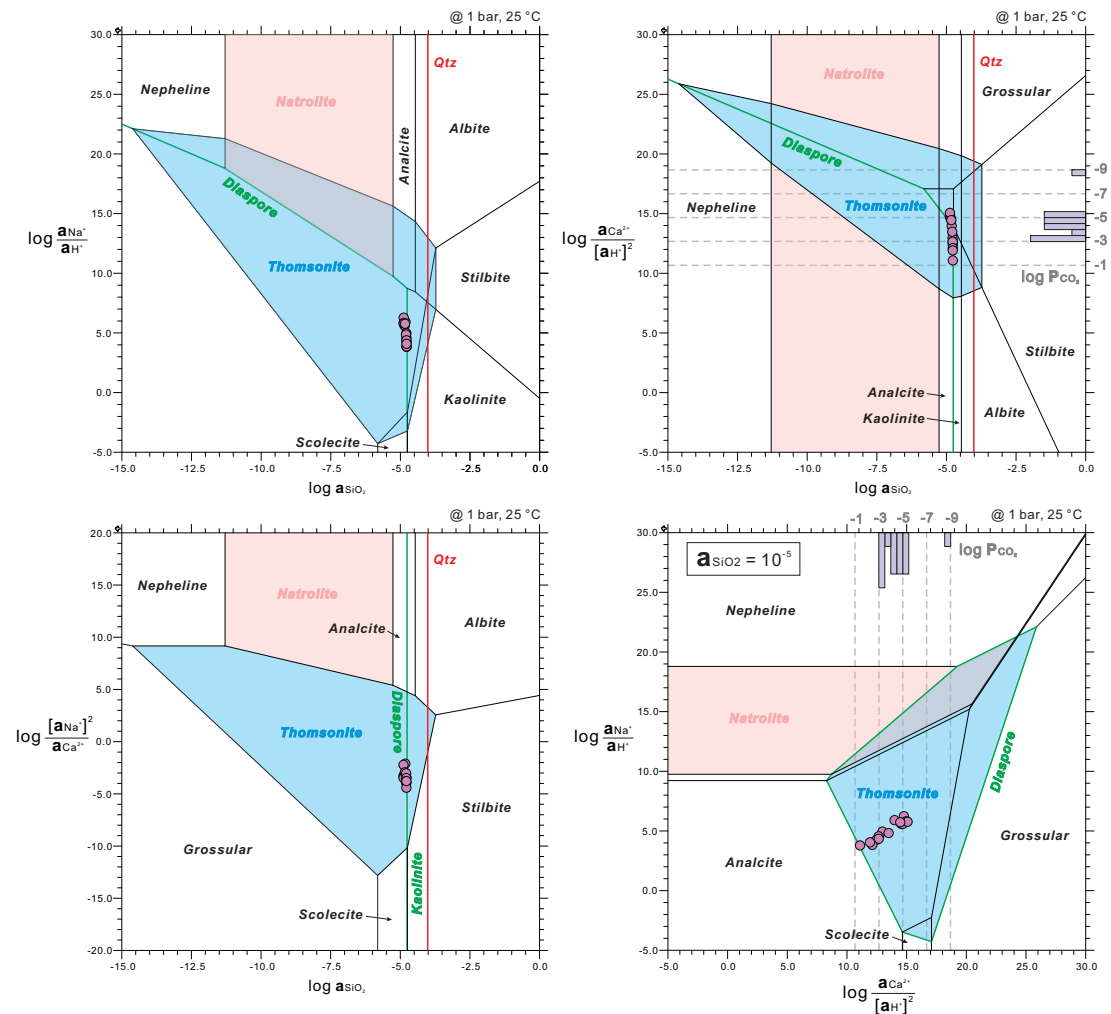


Fig. 6 Mineral stability diagrams for natrolite at 1 bar. See text for explanations.

### 8.3 Fluid evolution derived from zeolite stability diagram

Mineral stability diagrams in the system Ca-Na-Si-Al-O-H have been constructed at 1 bar and 25°C, which is regarded as equilibrium temperature of water. The topology and the field size of the diagrams do not change with pressure, but change remarkably with temperature. Stability fields of natrolite and thomsonite decrease gradually at elevated temperature (Fig. 7 and Fig. 8) and finally disappear at ca. 150°C.



**Fig. 7 Mineral stability diagrams for thomsonite at 1 bar and 25°C. See text for explanations.**

As described before, two stages of hydrothermal events, which are characterized by natrolite and thomsonite formation respectively, have been identified in the nepheline syenite. All

dominating reactions involve chemical components of the fluid phase. The fluid of stage I is considered as fluid expelled by crystallizing magma, while the fluid of stage II is dominated by infiltration of Ca-HCO<sub>3</sub> fluid from carbonatite catchment.

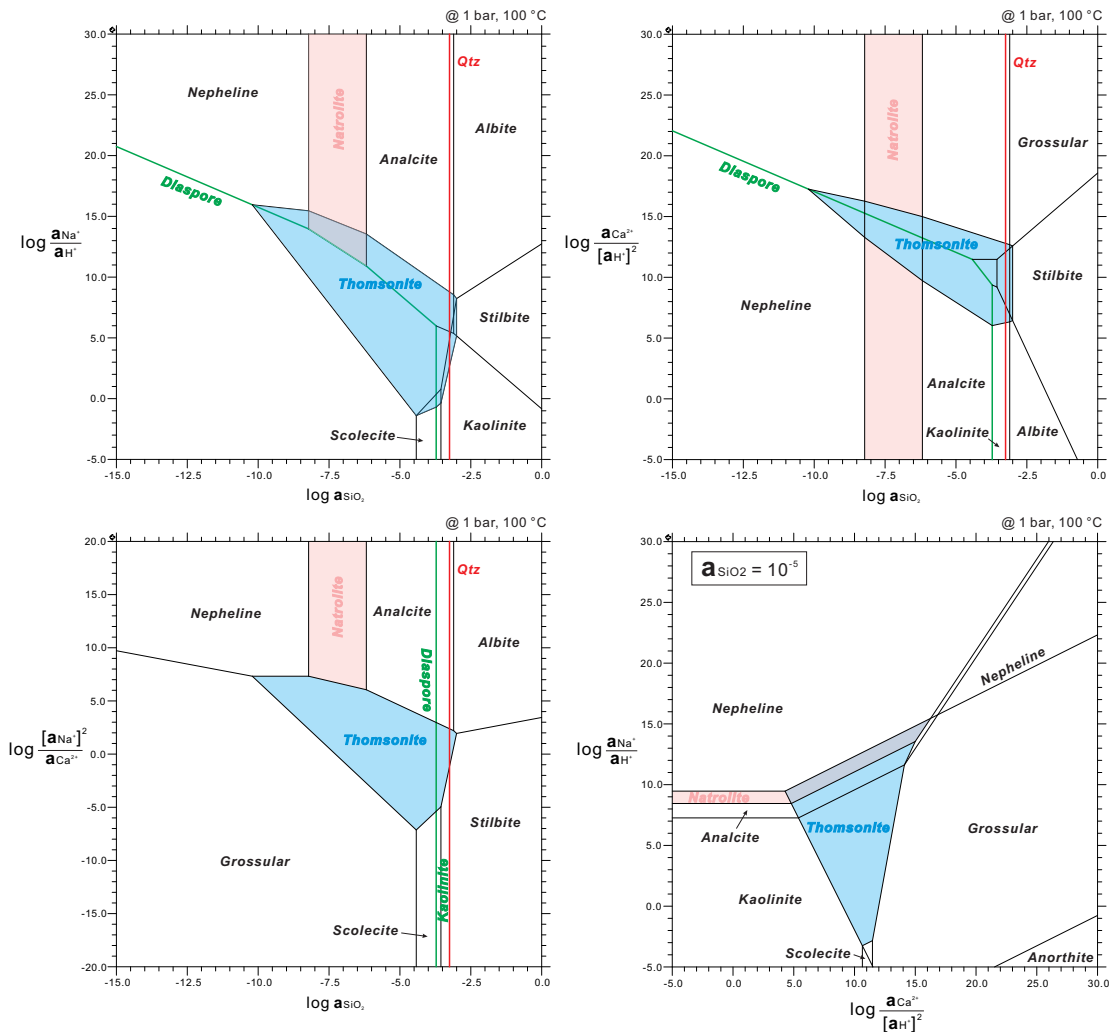


**Fig. 8** Mineral stability diagrams for thomsonite at 1 bar and 100 °C. See text for explanations.

### 8.3.1 Fluid property of hydrothermal stage I

According to reaction R3, The transformation of nepheline to natrolite is mainly controlled by the activity of nepheline, and activities of water and silica in the fluid. As shown in Fig. 6a, for nepheline activity of 0.34 and silica activity of 0.15 which defined by orthomagmatic

mineral assemblages, the lowest  $\log a_{\text{H}_2\text{O}}$  value of -4 is needed for natrolite formation. With processing of natrolite formation, the silica activity of fluid will decrease gradually due to consumption of silica by natrolite. The decreasing silica activity will then require increasing water activity for producing natrolite (Fig. 6a). Comparing the topology of phase diagram for pure nepheline and nepheline with activity 0.34 (Fig. 6b), the activity of nepheline does not play a significant role as that of water and silica in zeolite formation.

### **8.3.2 Fluid property of hydrothermal stage II**

As shown in Fig. 6, all the water compositions sampled from nepheline syenite catchment (Holger, 2010) are plotted in the stability field of thomsonite, and very close to the boundary of diaspore stability. This modeled stability field is well consistent with the microscopic observations that thomsonite is present as a major phase coexisting with a very small amount of diaspore. As indicated by the modeled phase diagram as a function of varying activities of  $\text{Na}^+$ ,  $\text{Ca}^{2+}$  and  $\text{SiO}_2$  in the fluid, the texture of thomsonite can be reasonably interpreted as a reaction consequence of nepheline with decreasing activity of  $\text{Na}^+$ , but also probably with increasing activity of  $\text{Ca}^{2+}$ . For the decrease of the activity of  $\text{Na}^+$ , it could be a result of generation of natrolite which largely consumes  $\text{Na}^+$  in the fluid. It is well demonstrated from the occurrence of natrolite and thomsonite at different locations or at the same sites, which indicate that the activities of  $\text{Na}^+$  and  $\text{Ca}^{2+}$  in the fluids are close to the boundary condition between natrolite and thomsonite in the phase diagram (Fig. 6).

### **8.3.3 Partial pressure of $\text{CO}_2$**

Corresponding partial pressure of  $\text{CO}_2$  based on calcite dissolution reaction, ratios of  $\text{Ca}^{2+}$  concentration and pH are also presented in Fig. 6. Sample points plotted in the activity-activity diagram fall into  $\log P_{\text{CO}_2}$  range of -1 to -6.

Calcite and thomsonite are stable phases coexisting with each, as observed from the nepheline syenite samples. The relation of their coexisting is also demonstrated by the modeling result that they are corresponding to similar values of  $\log a_{\text{Ca}^{2+}/[\text{a}_{\text{H}^+}]^2}$  (mostly 10~15), which requires low activity of  $\text{CO}_2$  in fluid ( $\log P_{\text{CO}_2}$  range of -1 to -6, Fig. 6). The low activity of  $\text{CO}_2$  in fluid for the stabilization of zeolite has also been revealed by the study of Weisenberger and Bucher (2010).



## 9. Conclusions

Based on microscopic observation of secondary minerals in the rock samples, the derived reactions, and the thermodynamic modeling for mineral assemblages, several conclusions concerning the hydrothermal evolution of nepheline syenite can be drawn below:

Hydrothermal stage I is impressed by pervasive natrolite transformed from nepheline and albite dissolution. The related fluid is considered as fluid expelled by crystallizing magma, which has decreasing silica activity and slightly increasing Na activity with the product of natrolite.

Hydrothermal stage II is dominated by infiltration of Ca-HCO<sub>3</sub> fluid from carbonatite catchment into the nepheline syenite along fractures which resulted in the generation of thomsonite at low CO<sub>2</sub> partial pressures by transformation from nepheline and natrolite.

## References

- Appleyard, E.C., 1974. Syn-orogenic igneous alkaline rocks of eastern Ontario and northern Norway. *Lithos*, 7(3): 147-169.
- Appleyard, E.C., 1980. Mass balance computations in metasomatism: Metagabbro/nepheline syenite pegmatite interaction in northern Norway. *Contributions to Mineralogy and Petrology*, 73(2): 131-144.
- Berman, R., 1988. Internally-consistent thermodynamic data for minerals in the system Na<sub>2</sub>O-K<sub>2</sub>O-CaO-MgO-FeO-Fe<sub>2</sub>O<sub>3</sub>-Al<sub>2</sub>O<sub>3</sub>-SiO<sub>2</sub>-TiO<sub>2</sub>-H<sub>2</sub>O-CO<sub>2</sub>. *Journal of Petrology*, 29(2): 445.
- Bucher, K. and Stober, I., 2010. Fluids in the upper continental crust. *Geofluids*, 10(1-2): 241-253.
- Coelho, J., 2006. GEOISO--A Windows(TM) program to calculate and plot mass balances and volume changes occurring in a wide variety of geologic processes. *Computers & Geosciences*, 32(9): 1523-1528.
- Daly, J.S., Aitchison, S.J., Cliff, R.A., Gayer, R.A. and Rice, A.H.N., 1991. Geochronological Evidence from Discordant Plutons for a Late Proterozoic Orogen in the Caledonides of Finnmark, Northern Norway. *Journal of the Geological Society*, 148: 29-40.
- de'Gennaro, M., Cappelletti, P., Langella, A., Perrotta, A. and Scarpati, C., 2000. Genesis of zeolites in the Neapolitan Yellow Tuff: geological, volcanological and mineralogical evidence. *Contributions to Mineralogy and Petrology*, 139(1): 17-35.
- Deer, W.A., Howie, R.A., Zussman, J. and Wise, W.S., 2004. *Framework Silicates: Silica Minerals, Feldspathoids and the Zeolites*. Geological Society.
- Fall, A., Bodnar, R.J., Szabó, C. and Pál-Molnár, E., 2007. Fluid evolution in the nepheline syenites of the Ditrau Alkaline Massif, Transylvania, Romania. *Lithos*, 95(3-4): 331-345.
- Frey, M., Capitani, C.D. and Liou, J.G., 1991. A new petrogenetic grid for low-grade metabasites. *Journal of Metamorphic Geology*, 9(4): 497-509.
- Gee, D., 1975. A tectonic model for the central part of the Scandinavian Caledonides. *American Journal of Science*, 275: 468-515.
- Geis, H.P., 1979. Nepheline syenite on Stjernøy, Northern Norway. *Economic Geology*, 74(5): 1286-1295.
- Giggenbach, W.F., 1981. Geothermal mineral equilibria. *Geochimica et Cosmochimica Acta*, 45(3): 393-410.
- Hamilton, D.L., 1961. Nephelines as Crystallization Temperature Indicators. *The Journal of Geology*, 69(3): 321-329.
- Hamilton, D.L. and Mackenzie, W.S., 1960. Nepheline Solid Solution in the System NaAlSiO<sub>4</sub>-KAlSiO<sub>4</sub>-SiO<sub>2</sub>. *Journal of Petrology*, 1(1): 56-72.

- Heier, K., 1961. Layered gabbro, hornblende, carbonatite and nepheline syenite on Stjernøy, North Norway. *Norsk Geologisk Tidsskrift*, 41: 109-155.
- Heier, K., 1964. Geochemistry of the nepheline syenite on Stjernøy, North Norway. *Norsk Geologisk Tidsskrift*, 44: 205-216.
- Heier, K., 1965. A geochemical comparison of the Blue Mountain (Ontario, Canada) and Stjernøy (Finnmark, north Norway) nepheline syenites. *Norsk Geologisk Tidsskrift*, 45: 41-52.
- Heier, K. and Taylor, S., 1962. A note on the U, Th and K contents in the nepheline syenite on Stjernøy, north Noeway. *Norsk Geologisk Tidsskrift*, 42: 287-292.
- Heier, K.S., 1966. Some Crystallo-chemical Relations of Nephelines and Feldspars on Stjernøy, North Norway. *Journal of Petrology*, 7(1): 95-113.
- Helgeson, H.C., Kirkham, D.H. and Flowers, G.C., 1981. Theoretical prediction of the thermodynamic behavior of aqueous electrolytes by high pressures and temperatures; IV, Calculation of activity coefficients, osmotic coefficients, and apparent molal and standard and relative partial molal properties to 600 degrees C and 5kb. *American Journal of Science*, 281(10): 1249-1516.
- Holdridge, D., 1962. A clay mineral from Stjernøy, Norway. *Clay Minerals*, 5(27): 26-30.
- Holger, T., 2010. The chemical composition of surface waters from the Seiland Igneous Province, Northern Norway. Master Thesis, University of Freiburg, Freiburg, 164 pp.
- Holland, T.J.B. and Powell, R., 2011. An improved and extended internally consistent thermodynamic dataset for phases of petrological interest, involving a new equation of state for solids. *Journal of Metamorphic Geology*, 29(3): 333-383.
- Johnson, J.W., Oelkers, E.H. and Helgeson, H.C., 1992. SUPCRT92: A software package for calculating the standard molal thermodynamic properties of minerals, gases, aqueous species, and reactions from 1 to 5000 bar and 0 to 1000°C. *Computers & Geosciences*, 18(7): 899-947.
- Kirkland, C.L., Daly, J.S., Eide, E.A. and Whitehouse, M.J., 2006. The structure and timing of lateral escape during the Scandian Orogeny: A combined strain and geochronological investigation in Finnmark, Arctic Norwegian Caledonides. *Tectonophysics*, 425(1-4): 159-189.
- Kirkland, Christopher L., Stephen Daly, J. and Whitehouse, Martin J., 2007. Provenance and Terrane Evolution of the Kalak Nappe Complex, Norwegian Caledonides: Implications for Neoproterozoic Paleogeography and Tectonics. *The Journal of Geology*, 115(1): 21-41.
- Kjøsnes, K., 1980. Fertilization of layered mafic rocks in the Lillebukt alkaline complex, Stjernøy, Norway. *Lithos*, 13(2): 215-215.
- Kousehlar, M., Weisenberger, T.B., Tutti, F. and Mirnejad, H., 2012. Fluid control on low-temperature mineral formation in volcanic rocks of Kahrizak, Iran. *Geofluids: no-no*.
- Krogh, E. and Elvevold, S., 1990. A Precambrian age for an early gabbro-monzonitic intrusive on the ksfjord peninsula, Seiland Igneous Province, northern Norway. *Norsk Geologisk Tidsskrift*, 70(4): 267-273.
- Lieberman, J. and Petrakakis, K., 1991. TWEEQU thermobarometry; analysis of uncertainties and applications to granulites from western Alaska and Austria. *The Canadian Mineralogist*, 29(4): 857-887.
- Marks, M., Neukirchen, F., Vennemann, T. and Markl, G., 2009. Textural, chemical, and isotopic effects of late-magmatic carbonatitic fluids in the carbonatite-syenite Tamazeght complex, High Atlas Mountains, Morocco. *Mineralogy and Petrology*, 97(1): 23-42.
- Marks, M., Schilling, J., Coulson, I., Wenzel, T. and Markl, G., 2008. The alkaline-peralkaline Tamazeght complex, High Atlas mountains, Morocco: Mineral chemistry and petrological constraints for derivation from a compositionally heterogeneous mantle source. *Journal of Petrology*, 49(6): 1097.
- Neuhoff, P.S., FRIDRIKSSON, T.I., RISSON, S.N.A. and Bird, D.K., 1999. Porosity evolution and mineral paragenesis during low-grade metamorphism of basaltic lavas at Teigarhorn, eastern Iceland. *American Journal of Science*, 94305: 2115.
- Nordstrom, D.K., Ball, J.W., Donahoe, R.J. and Whittemore, D., 1989. Groundwater chemistry and water-rock interactions at Stripa. *Geochimica et Cosmochimica Acta*, 53(8): 1727-1740.
- Oosterom, M., 1963. The ultramafites and layered gabbro sequences in the granulite facies rocks on Stjernøy (Finnmark, Norway). *Leidse Geol Mededelingen*, 28: 177-296.
- Passaglia, E., 1970. The crystal chemistry of chabazites. *American Mineralogist*, 55: 1278@C1301.
- Passaglia, E. and Vezzalini, G., 1985. Crystal chemistry of diagenetic zeolites in volcanoclastic deposits of Italy. *Contributions to Mineralogy and Petrology*, 90(2): 190-198.
- Pedersen, R., Dunning, G. and Robins, B., 1989. U-Pb ages of nepheline syenite pegmatites from the

- Seiland Magmatic Province, N. Norway. The Caledonide Geology of Scandinavia: 3-8.
- Roberts, D., 2003. The Scandinavian Caledonides: event chronology, palaeogeographic settings and likely modern analogues. *Tectonophysics*, 365(1-4): 283-299.
- Roberts, R.J., Corfu, F., Torsvik, T.H., Ashwal, L.D. and Ramsay, D.M., 2006. Short-lived mafic magmatism at 560-570 Ma in the northern Norwegian Caledonides: U-Pb zircon ages from the Seiland Igneous Province. *Geological Magazine*, 143(6): 887-903.
- Roberts, R.J., Corfu, F., Torsvik, T.H., Hetherington, C.J. and Ashwal, L.D., 2010. Age of alkaline rocks in the Seiland Igneous Province, Northern Norway. *Journal of the Geological Society*, 167(1): 71-81.
- Robins, B., 1984. Petrography and petrogenesis of nephelinized metagabbros from Finnmark, Northern Norway. *Contributions to Mineralogy and Petrology*, 86(2): 170-177.
- Robins, B. and Gardner, P.M., 1975. The magmatic evolution of the Seiland province, and Caledonian plate boundaries in northern Norway. *Earth and Planetary Science Letters*, 26(2): 167-178.
- Robins, B. and Tysseland, M., 1980. Fenitization of mafic cumulates by the Pollen carbonatite, Finnmark, Norway. *Lithos*, 13(2): 220-220.
- Robins, B. and Tysseland, M., 1983. The geology, geochemistry and origin of ultrabasic fenites associated with the Pollen Carbonatite (Finnmark, Norway). *Chemical Geology*, 40(1-2): 65-95.
- Salter, D.L. and Appleyard, E.C., 1974. An occurrence of vein palygorskite from the nepheline syenite of Lillebukt, Stjernøy, northern Norway. *Norsk Geologisk Tidsskrift*, 54: 329-336.
- Schilling, J., Marks, M.A.W., Wenzel, T. and Markl, G., 2009. Reconstruction of magmatic to subsolidus processes in an apgaitic system using eudialyte textures and composition: A case study from tamazeght, morocco. *Canadian Mineralogist*, 47(2): 351-365.
- Schilling, J. et al., 2011. The Magmatic to Hydrothermal Evolution of the Intrusive Mont Saint-Hilaire Complex: Insights into the Late-stage Evolution of Peralkaline Rocks. *Journal of Petrology*, 52(11): 2147-2185.
- Schmidt, D., Schmidt, S., Mullis, J., Ferreira Mählmann, R. and Frey, M., 1997. Very low grade metamorphism of the Taveyanne formation of western Switzerland. *Contributions to Mineralogy and Petrology*, 129(4): 385-403.
- Strand, T., 1980. The chemistry of the Lillebukt carbonatite, Stjernøy, Norway. *Lithos*, 13(2): 223-223.
- Sturt, B.A., Miller, J.A. and Fitch, F.J., 1967. The age of alkaline rocks from West Finnmark, northern Norway, and their bearing on the datings of the Caledonian orogeny. *Norsk Geologisk Tidsskrift*, 47: 255-273.
- Sturt, B.A., Pringle, I.R. and Ramsay, D.M., 1978. The Finnmarkian phase of the Caledonian Orogeny. *Journal of the Geological Society*, 135(6): 597-610.
- Weisenberger, T. and Bucher, K., 2010. Zeolites in fissures of granites and gneisses of the Central Alps. *Journal of Metamorphic Geology*, 28(8): 825-847.
- Weisenberger, T. and Bucher, K., 2011. Mass transfer and porosity evolution during low temperature water-rock interaction in gneisses of the simano nappe: Arvigo, Val Calanca, Swiss Alps. *Contributions to Mineralogy and Petrology*, 162(1): 61-81.
- Weisenberger, T. and Selbekk, R., 2009. Multi-stage zeolite facies mineralization in the Hvalfjörður area, Iceland. *International Journal of Earth Sciences*, 98(5): 985-999.
- Weisenberger, T. and Spürgin, S., 2009. Zeolites in alkaline rocks of the Kaiserstuhl volcanic complex, SW Germany - New microprobe investigation and the relationship of zeolite mineralogy to the host rock. *Geologica Belgica*, 12(1-2): 75-91.

**Part III Stronalsite-Banalsite in Nepheline  
Syenite of Seiland Igneous Province,  
Northern Norway**

## 1. Abstract

Based on the investigation of secondary minerals from the alkaline rock in the Seiland igneous province of northern Norway, combined with the microscopic, mineral composition and thermodynamic modeling, several conclusions concerning the formation of stronalsite-banalsite solid solution can be drawn. Stronalsite-banalsite solid solution and natrolite generated simultaneously through nepheline dissolution. The extra silica required for stronalsite-banalsite solid solution and natrolite is probably derived from dissolution of albite lamella in perthite. The fluid corresponding to formation of stronalsite-banalsite minerals is a diluted silica-poor fluid with maximal  $a_{\text{SiO}_2}$  value of  $10^{-8}$ .

## 2. Introduction

Stronalsite-banalsite are Sr and Ba-rich tectosilicates which are rare in normal geological environments, but only have been observed in metasomatized ultramafic rocks (e.g. Hori et al., 1987; Kobayashi et al., 1987; Liferovich et al., 2006; Shi et al., 2012). However, the compositions of stronalsite and banalsite are not always reported at cases their occurrences are described. The complete solid solution  $(\text{Ba}_{1-x}\text{Sr}_x)\text{Na}_2\text{Al}_4\text{SiO}_4\text{O}_{16}$  was first documented from the description of Koneva in 1996 (see the review of Liferovich et al. (2006)), which occurs as a minor phase in feldspar-zeolite veins cutting alkaline pyroxenites at the contact with nepheline syenite. Recently, Liferovich et al. (2006) offered a good review of literature data as well as newly analyzed mineral compositions of stronalsite-banalsite, and discussed thoroughly the paragenesis and compositional variation of stronalsite-banalsite solid solution series from five new occurrences in nepheline syenite and ultramafic alkaline rocks. It has been revealed that the topological similarity of the structures of stronalsite and banalsite results in the complete  $(\text{Ba}_{1-x}\text{Sr}_x)\text{Na}_2\text{Al}_4\text{SiO}_4\text{O}_{16}$  solid solution. The origin of stronalsite and banalsite is usually associated with the post-magmatic conversion of nepheline to analcime. However, the condition of this process is poorly understood, but has been only inferred from other co-existing minerals. For example, the formation condition of analcime estimated by Marks and Markl (2003) has been utilized by Liferovich et al. (2006) to constrain the temperature (below 300°C) and  $\text{H}_2\text{O}$  activity (0.5-1) for stronalsite-banalsite solution.

In this study, I investigated the textural and chemical variations of stronalsite-banalsite in nepheline syenite of the Seiland igneous province of northern Norway. Reactions associated with stronalsite-banalsite and thermodynamic modeling of co-existing natrolite, have been established to demonstrate the paragenesis of stronalsite-banalsite solid solution.

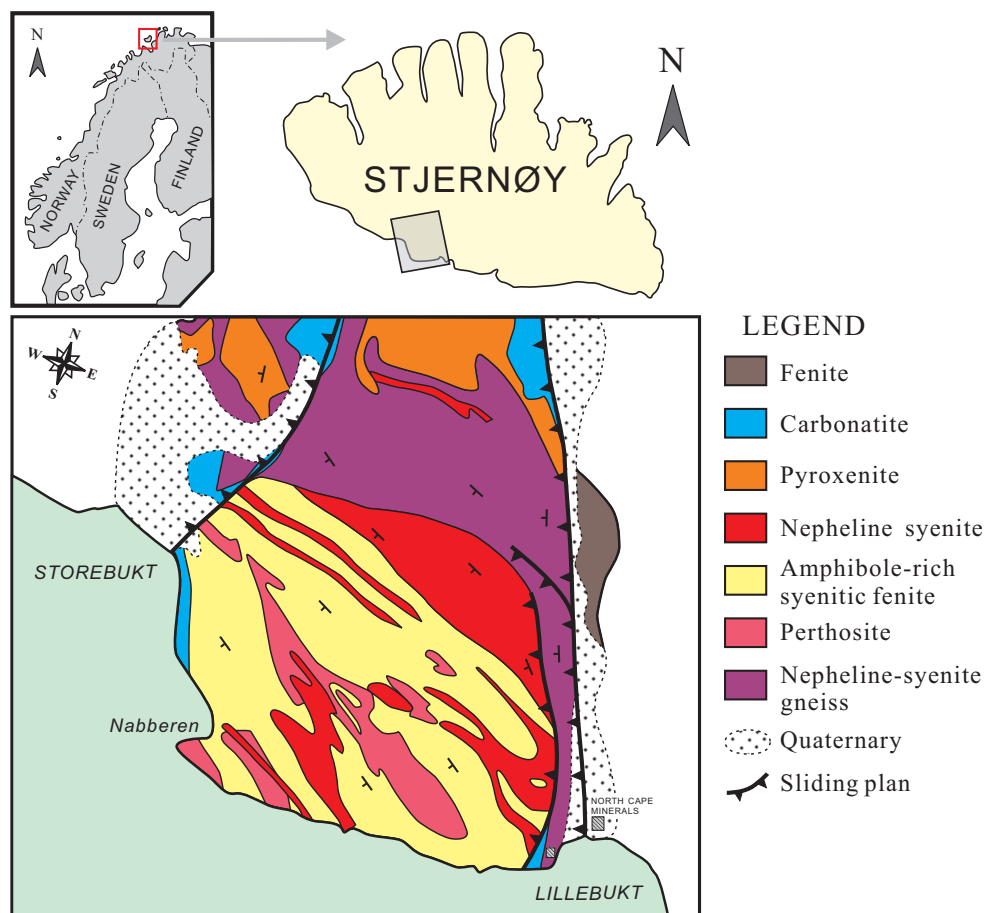


**Fig. 1 Geological map of Lillebukt alkaline complex on the Stjernøy Island.**

### 3. Geological background

The Seiland igneous province occupies an area of nearly 5,000 km<sup>2</sup> on the islands of Seiland, Sørøy and Stjernøy, and on the Øksfjord Peninsula in the northern Finnmark, Norway (Fig. 1). The province is located within the Kalak nappe complex of the Norwegian Caledonian orogenic belt, which has thrust eastwards onto the Precambrian crystalline basement of the Baltic shield during the Silurian continental collision (ca. 431-428 Ma at Finnmark, Kirkland et al., 2006; Kirkland et al., 2007) between Baltica and Laurentia following the early Palaeozoic closure of the Iapetus Ocean (Gee, 1975; Roberts, 2003). The Seiland igneous province has a long and complex history concerning magmatic evolution: voluminous ultramafic rocks at 829±18 Ma (Krogh and Elvevold, 1990), layered gabbroic plutons of 700±33 Ma, 604±44 Ma and 570 Ma (Daly et al.,

1991; Roberts et al., 2006) and a final stage of calc-alkaline intrusions represented by alkaline pyroxenite, syenite, nepheline syenite and carbonatite at  $574 \pm 5$  Ma (Roberts et al., 2010). All these various rocks are considered to represent a synorogenic (Caledonian orogenic belt) intrusive activity evolved from tholeiitic basalt, compositionally ranging from high-K calc-alkaline magmas, through alkaline olivine basalt and picrite and finally to highly differentiated alkaline magmas and carbonatite (Appleyard, 1974; Robins and Gardner, 1975; Sturt et al., 1967; Sturt et al., 1978).

The Lillebukt alkaline complex (Fig. 1), on Stjernøy Island, is enclosed in the ultramafic and mafic rocks of peridotite, pyroxenite, gabbro and hornblendite (Heier, 1961; Oosterom, 1963). The boundary is blurred and thus the relationship between the alkaline complex and the hosting rocks is unclear. The alkaline complex is composed of syenite, nepheline syenite, and carbonatite, all of which have been intruded by late mafic and syenite dikes, and pegmatites (Pedersen et al., 1989; Robins and Tysseland, 1980). The silico-carbonatite of the Lillebukt alkaline complex is closely related to the nepheline syenite and contains abundant amphibole, biotite and apatite in the silicate-rich layers (Robins and Tysseland, 1983; Strand, 1980). It has been suggested that the carbonatite represents the latest igneous activity of the Caledonian orogeny (Robins and Gardner, 1975). The nepheline syenite has been mined by North Cape Minerals in an open pit on Nabberen (earlier in an underground mine inside Nabberen) and the raw material is processed at the Lillebukt plant. The fine powdered nepheline - K-feldspar mixture is shipped from the small port to customers in the ceramics and glass industry worldwide.

The Nabberen nepheline syenite body is a lens-shaped stock located in the north of the summit of Nabberen (Fig. 1), which occupies an area of  $1700 \times 300$  m<sup>2</sup> (Geis, 1979). It is a miaskitic nepheline syenite characterized by high concentration of alkalis, Ba and Sr, and depletion of REE, Y, Nb, Sc, Zr, U, and Th (Heier, 1964; Heier and Taylor, 1962; Heier, 1966; Robins and Tysseland, 1980). The surrounding gabbros have been fenitized, probably by the low-density fluid expelled from the volatile-rich alkaline magmas which now crystallized as nepheline syenite and carbonatite (Appleyard, 1980; Kjøsnes, 1980; Robins, 1984; Robins and Tysseland, 1980; Robins and Tysseland, 1983). Hydrothermal assemblages including zeolites (natrolite) and clay minerals (palygorskite, a magnesium clay mineral) have been observed in the Lillebukt mine, and they were regarded as products of post-tectonic low-temperature reactions with groundwater (Geis, 1979; Holdridge, 1962; Salter and Appleyard, 1974).

## 4. Petrography

### 4.1 Petrography of host nepheline syenite

Nepheline syenite on Nabberen, from which water samples were collected, is massive and has no preferred orientation of minerals. White hydrothermal veins can be clearly identified in nepheline syenite. Wide veins (up to 5 mm) are accompanied by bilateral reaction zones (up to 2 cm). These bilateral reaction zones display a reddish color distinctive from the white veins and the gray original nepheline syenite. In addition, there are numerous irregular fine seams (less than 1 mm wide) which can be identified under careful observation by their indistinct white color and occasionally reddish reaction speckles along the seams. These tiny seams cut each other and form a network over the whole sample. The white alteration veins are entirely composed of fine-grained brown-grey zeolite aggregates. The rock matrix of nepheline syenite is mainly composed of potassium feldspar (40 %), nepheline (35 %), amphibole (10 %) and clinopyroxene (5 %), with accessory albite, biotite, apatite, titanite, magnetite, ilmenite, calcite and zeolite. There is no difference in mineral constituents between rock matrix and reaction zones, except more intense alteration of nepheline in the latter.

### 4.2 Petrography related with Zeolite

Potassium feldspars show widespread perthite textures with albite as blade or drop shaped lamellae. The site of albite lamellae has become cavity likely due to dissolution. Nepheline crystals are speckled or replaced by fine-grained zeolite and diaspore. In the white veins within nepheline syenite, mixture of fine-grained natrolite and thomsonite occurs as rounded spots with diameter of ca. 0.5 mm. Calcite-rich veins in the nepheline syenite are accompanied with natrolite, thomsonite and Sr-rich thomsonite. Natrolite grains are overgrown by thomsonite locally in all samples.

### 4.3 Petrography related with Stronalsite-Banalsite

Stronalsite-banalsite solid solution minerals usually grow together with secondary albite or natrolite along grain boundaries between nepheline and K-feldspar (Fig. 2a), or between ilmenite and K-feldspar (Fig. 2b). Nepheline crystals are speckled by fine-grained natrolite aggregate, diaspore and stronalsite-banalsite (Fig. 2c-d). Skeletal stronalsite-banalsite minerals are situated along fissures in nepheline grains, which are fulfilled by natrolite (Fig. 2e-h). Compositional variations of stronalsite-banalsite minerals could be observed under BSE images due to the variations of Ba and Sr contents. Both high contents of Sr and Ba will cause brighter



color under BSE images. The brighter parts are speckle or film-shaped (Fig. 2e-g), without clear zoning. Therefore, no systematical chemical variation for stronalsite-banalsite solid solution could be observed for a single crystal grain.

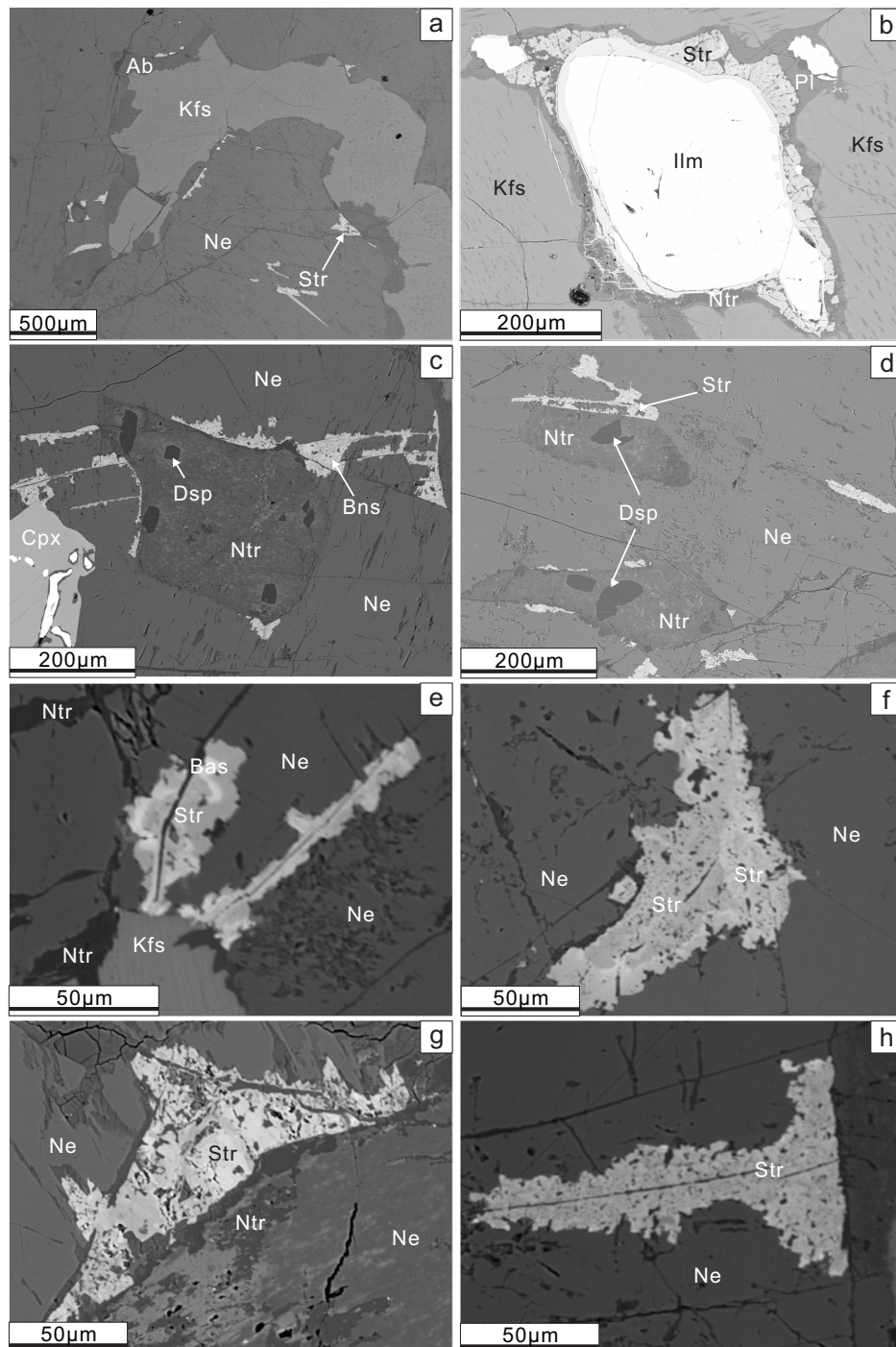


**Fig. 2** BSE images showing various secondary mineral textures. See text for explanations.

Table 1 Representative microprobe analyses of stronalsite-banalsite mineral.

Sample Point	1145A	1145B	1145B	1147A	1147A	1147B	1147B	1147B	1147B	1148A	1148B	1148B	1148B	1151	1151	1151	Kb926	Kb926	
Str	039	065	066	002	006	046	059	036	022	023	023	022	023	064	066	023	Str	Str	
Wt%																			
SiO <sub>2</sub>	39.821	40.6	40.12	38.84	39.87	38.15	38.83	38.7	38.76	41.32	41.32	38.76	41.32	38.71	39.2	40.967	40.523	40.523	40.523
Al <sub>2</sub> O <sub>3</sub>	33.673	33.15	32.95	32.64	33.19	32.77	32.24	32.76	33.13	32.89	32.89	33.13	32.89	33.39	34.14	32.651	33.094	33.094	33.094
FeOtotal	0.325	0.07	0.08	0.31	0.08	0.11	0.26	0.02	0.03	0.04	0.04	0.03	0.04	0.3	0.16	0.034	0.145	0.145	0.145
MnO	0.021	0.03	0	0	0.03	0	0	0	0	0	0	0	0	0	0	0	0.004	0.004	0.004
MgO	0.001	0.01	0	0	0	0.01	0	0	0.01	0	0	0.01	0	0.01	0	0.001	0	0	0
SrO	14.505	10.99	9.46	11.74	8.14	5.75	6.09	11.54	7.32	7.33	7.33	7.32	7.33	10.61	12.85	7.367	8.645	8.645	8.645
BaO	2.829	5.17	5.85	6.04	7.26	13.06	12.61	5.79	9.71	7.59	7.59	9.71	7.59	5.35	1.69	6.558	6.426	6.426	6.426
CaO	0.408	0.72	1.05	0.12	1.43	1.11	0.16	0.29	1.5	0.91	0.91	1.5	0.91	1.41	2	1.205	1.245	1.245	1.245
Na <sub>2</sub> O	10.351	11.03	10.73	10.67	10.79	10.54	10.69	10.77	10.37	10.54	10.54	10.37	10.54	10.58	10.66	10.723	10.443	10.443	10.443
K <sub>2</sub> O	0	0.14	0.11	0.12	0.09	0.04	0.16	0.1	0.02	0.16	0.16	0.02	0.16	0.02	0.05	0.065	0.07	0.07	0.07
Total	101.934	101.910	100.350	100.480	100.880	101.540	101.040	99.970	100.850	100.780	100.780	100.850	100.780	100.380	100.750	99.571	100.595	100.595	100.595
Cations per 16 oxygens																			
Si	3.996	4.064	4.065	4.000	4.034	3.958	4.035	3.992	3.979	4.149	4.149	3.979	4.149	3.951	3.932	4.142	4.085	4.085	4.085
Al	3.982	3.910	3.934	3.962	3.958	4.007	3.948	3.983	4.009	3.892	3.892	4.009	3.892	4.017	4.036	3.891	3.932	3.932	3.932
Fe	0.027	0.006	0.007	0.027	0.007	0.010	0.023	0.002	0.003	0.003	0.003	0.003	0.003	0.026	0.013	0.003	0.012	0.012	0.012
Mn	0.002	0.003	0.000	0.000	0.003	0.000	0.000	0.000	0.000	0.000	0.000	0.000	0.000	0.000	0.000	0.000	0.000	0.000	0.000
Mg	0.000	0.001	0.000	0.000	0.000	0.002	0.000	0.000	0.002	0.000	0.000	0.002	0.000	0.002	0.000	0.000	0.000	0.000	0.000
Sr	0.844	0.638	0.556	0.701	0.478	0.346	0.367	0.690	0.436	0.427	0.427	0.436	0.427	0.628	0.747	0.432	0.505	0.505	0.505
Ba	0.111	0.203	0.232	0.244	0.288	0.531	0.513	0.234	0.391	0.299	0.299	0.391	0.299	0.214	0.066	0.260	0.254	0.254	0.254
Ca	0.044	0.077	0.114	0.013	0.155	0.123	0.018	0.032	0.165	0.098	0.098	0.165	0.098	0.154	0.215	0.131	0.134	0.134	0.134
Na	2.014	2.140	2.108	2.130	2.117	2.120	2.154	2.154	2.064	2.052	2.052	2.064	2.052	2.094	2.073	2.102	2.041	2.041	2.041
K	0.000	0.018	0.014	0.016	0.012	0.005	0.021	0.013	0.003	0.020	0.020	0.003	0.020	0.003	0.006	0.008	0.009	0.009	0.009
Total	11.020	11.060	11.029	11.092	11.051	11.101	11.079	11.100	11.050	10.941	10.941	11.050	10.941	11.088	11.090	10.968	10.974	10.974	10.974

## 5. Mineral composition

### 5.1 Mineral analysis method

Mineral analyses were performed by electron beam microanalysis using wavelength-dispersive spectrometry (WDS) of a digital CAMECA SX100 electron microprobe at the Institute of Geosciences, University of Freiburg. During analyses an accelerating voltage of 15 kV and a current of 20 nA were used. Beam diameter was 0.5  $\mu\text{m}$  (for feldspar, sometimes 5  $\mu\text{m}$ ). Standard minerals for Sr and Ba elements are celestine ( $\text{SrSO}_4$ ) and barite ( $\text{BaSO}_4$ ) respectively.

### 5.2 Stronalsite-Banalsite

Representative stronalsite-banalsite compositions are presented in Table 1 and Fig. 3. The SrO contents vary widely from 2.2 wt% to 16.5 wt%, which correspond to 0.13 apfu to 0.97 apfu in structure. The contents of BaO have a wider range between 0.24 wt% and 19.43 wt% with corresponding Ba of 0.01 apfu to 0.8 apfu in structure. The contents of  $\text{Na}_2\text{O}$  have a limited range of 9.36 wt% to 11.15 wt% and 1.81 to 2.21 apfu in the Na site of structure. The beyond over 2 is possibly due to analytical error for sodium. The stronalsite-banalsite contains CaO up to 2.83 wt% and  $\text{K}_2\text{O}$  up to 0.24 wt%. Trace amount of FeO, MnO and MgO could be detected in the stronalsite-banalsite.

The majority compositions of stronalsite-banalsite solid solutions are plotted into stronalsite field with few points in banalsite field (Fig. 3). The points of Sr versus Ba deviate from the 1:1 line, which indicate a incomplete substitution of Sr by Ba in A site of  $(\text{Ba}_{1-x}\text{Sr}_x)\text{Na}_2\text{Al}_4\text{SiO}_4\text{O}_{16}$ . The complimentary of Ca with Sr is possibly the extra substitution vector: Sr or Ba  $\leftrightarrow$  Ca, indicating a full solution as  $(\text{Ba}_x\text{Sr}_y\text{Ca}_{1-x-y})\text{Na}_2\text{Al}_4\text{SiO}_4\text{O}_{16}$ .

Table 2 Representative microprobe analyses of zeolite

Sample	1145A	1145B	1145C	Kb926	1145A	1147A	1148A
Point	Zeo 006	Zeo 041	Zeo 036	Zeo 037	Zeo 009	Zeo 063	Zeo 003
Wt%	Ntr	Ntr	Ntr	Ntr	Thm	Thm	Thm
SiO <sub>2</sub>	48.485	47.359	45.87	48.146	38.219	37.96	37.25
Al <sub>2</sub> O <sub>3</sub>	28.33	28.879	26.45	27.795	30.407	30.84	31.59
FeOtotal	0.026	0.019	0.03	0.099	0.08	0.04	0.04
MnO	0.025	0	0	0	0.03	0.01	0
MgO	0.005	0.002	0	0	0.022	0.01	0.08
SrO	0.027	0.089	0.16	0.03	3.189	0.42	1.22
BaO	0	0	0	0	0	0.03	0.12
CaO	0.488	1.483	1.46	0.056	10.951	11.95	12.39
Na <sub>2</sub> O	15.334	14.62	13.05	15.871	4.64	4.42	3.41
K <sub>2</sub> O	0.029	0.023	0.17	0.029	0.181	0.04	0.13
Total	92.749	92.474	87.190	92.026	87.719	85.720	86.230
Cations per 80 oxygens							
Si	23.864	23.441	23.992	23.918	20.583	20.535	20.144
Al	16.434	16.847	16.305	16.274	19.300	19.663	20.134
Fe <sup>3+</sup>	0.011	0.008	0.013	0.041	0.036	0.018	0.018
Mn	0.010	0.000	0.000	0.000	0.014	0.005	0.000
Mg	0.004	0.001	0.000	0.000	0.018	0.008	0.064
Sr	0.008	0.026	0.049	0.009	0.996	0.132	0.383
Ba	0.000	0.000	0.000	0.000	0.000	0.006	0.025
Ca	0.257	0.786	0.818	0.030	6.319	6.926	7.179
Na	14.633	14.030	13.234	15.287	4.845	4.636	3.575
K	0.018	0.015	0.113	0.018	0.124	0.028	0.090
Total	55.239	55.154	54.523	55.577	52.234	51.956	51.613
E%	8.267	7.546	8.203	6.064	-1.521	4.635	6.241
T <sub>si</sub>	0.592	0.582	0.595	0.595	0.516	0.511	0.500
Si/Al	1.452	1.391	1.471	1.470	1.066	1.044	1.001

E% = -10% -10%, acceptable according to Passaglia (1970)

$E\% = 100 * ((Al - (Na + K) + 2 * (Mg + Ca + Sr + Ba)) / (Na + K) + 2 * (Mg + Ca + Sr + Ba))$

$T_{si} = Si / (Si + Al)$

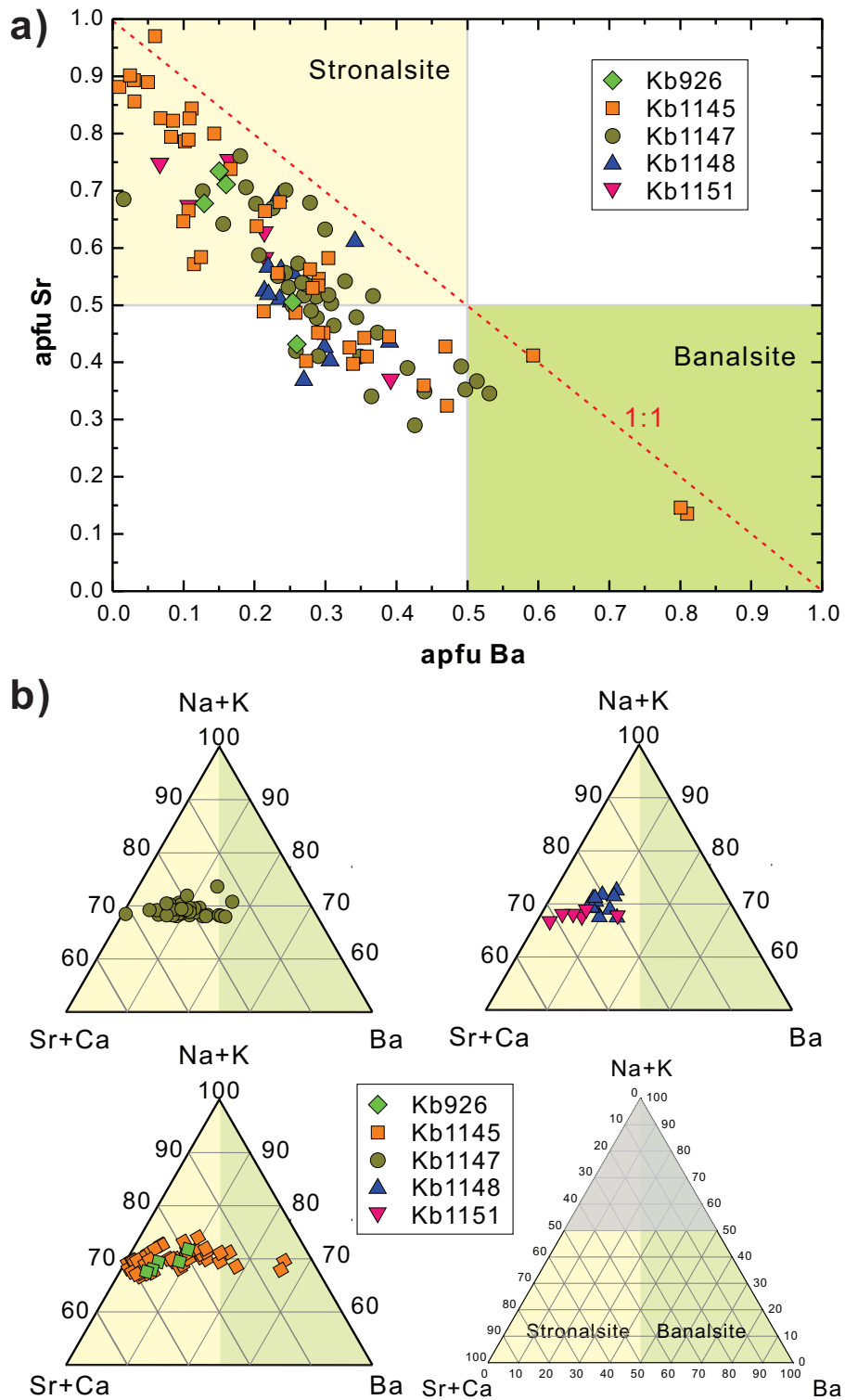


**Fig. 3 Compositional plots of stronalsite-banalsite minerals.**

### 5.3 Zeolite

Zeolites are rich in Na, and the main species are natrolite and thomsonite. Representative compositions are listed in Table 2. The acceptable zeolite analysis have E% between -10% to 10% according to the method of Passaglia (1970). The framework cation of natrolite is almost entirely Na, which is close to the stoichiometric formula. The extra-framework cations are Ca, K, and Sr. K and Sr in natrolite are below 0.02 pfu, while Ca is widely scattered up to ca. 1.4 pfu. The Si/(Si+Al) ratio slightly varies between 1.3 to 1.5. Thomsonite compositions have wide range of Na and Ca contents. The Ca/Na ratios of thomsonite vary from 0.5 to 2.2. The substitution of Ca to Na is accompanied with Si-Al substitution.

Table 3 Representative microprobe analyses of nepheline.

Sample Point	1145A Ne 031	1147A Ne 015	1148A Ne 021	1151 Ne 027	Kb926 Ne 005
Wt%					
SiO <sub>2</sub>	42.978	42.57	42.8	42.51	42.885
Al <sub>2</sub> O <sub>3</sub>	34.432	35.32	34.46	34.37	34.691
FeO <sub>total</sub>	0.061	0.09	0.1	0.09	0.103
MnO	0	0	0	0.01	0
MgO	0.003	0.01	0.02	0	0.008
SrO	0.021	0	0	0.02	0
BaO	0.013	0	0.01	0.04	0.008
CaO	0.611	0.94	0.74	1.38	0.922
Na <sub>2</sub> O	16.168	15.91	16.76	16.9	16.032
K <sub>2</sub> O	6.149	5.74	6.24	5.26	6.398
Total	100.436	100.580	101.130	100.580	101.047
Cations per 16 oxygens					
Si	4.113	4.059	4.083	4.069	4.088
Al	3.884	3.969	3.875	3.878	3.897
Fe <sup>3+</sup>	0.005	0.007	0.008	0.007	0.008
Mn	0.000	0.000	0.000	0.001	0.000
Mg	0.000	0.001	0.003	0.000	0.001
Sr	0.001	0.000	0.000	0.001	0.000
Ba	0.000	0.000	0.000	0.002	0.000
Ca	0.063	0.096	0.076	0.142	0.094
Na	3.000	2.941	3.100	3.137	2.963
K	0.751	0.698	0.760	0.642	0.778
Total	11.818	11.772	11.905	11.878	11.830

## 5.4 Nepheline

Representative nepheline compositions are given in Table 3. For all nepheline syenite samples, nepheline varies in composition between  $\text{Ne}_{80}\text{Ks}_{20}\text{Qtz}_1$  and  $\text{Ne}_{77}\text{Ks}_{18}\text{Qtz}_4$  without systematic differences. These Qtz-poor (from 1.22 to 4.22 mol %) and Ne-rich compositions are typical features of nepheline grains and common in large slowly-cooled plutonic bodies (Marks et al., 2008). The Na/K ratio in nepheline ranges from 3.63 to 4.33, with an average value of 3.95. All nepheline compositions are plotted below the line of 500°C on the nepheline-kalsilite-silica (Ne–Ks–Qz) diagram (Hamilton, 1961; Hamilton and Mackenzie, 1960). This indicates that nepheline has gained a chemical re-equilibration at near 500°C (Fall et al., 2007).

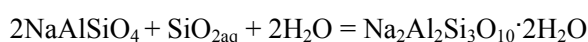
## 6. Discussion

### 6.1 Stronalsite-Banalsite forming Reactions

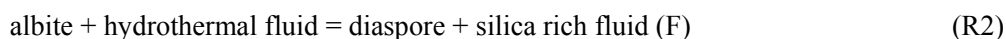
As described above, stronalsite-banalsite solid solutions are closely related with the transformation of nepheline to natrolite. The elements Sr and Ba in the structure of stronalsite-banalsite solid solutions are probably derived from nepheline dissolution. Thus stronalsite-banalsite forming reactions are accompanied portions of the natrolite forming reaction.

#### 6.1.1 Reactions related with Natrolite

The principal reaction of the nepheline - zeolite transformation can be written as:

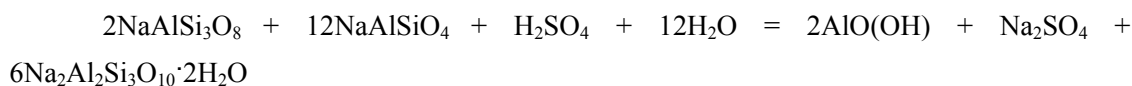
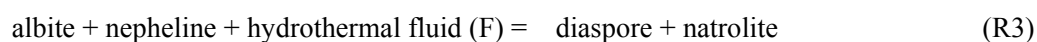


The dissolved aqueous silica necessary for the zeolitization is likely to result from internal dissolution of the albite lamella in perthite. Albite dissolution has been observed in nepheline syenite, the corresponding reaction could be described by the following reaction:



The reaction consumes  $\text{H}_2\text{SO}_4$  component from fluid and release silica and thenardite component to the fluid. Simultaneously, diaspore precipitated in the in situ locality or other place. The released  $\text{SiO}_2$  will increase the silica activity of the fluid, which thus destabilized nepheline.

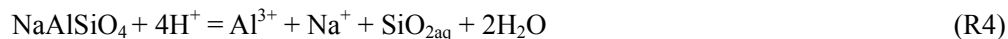
The combined reaction is:



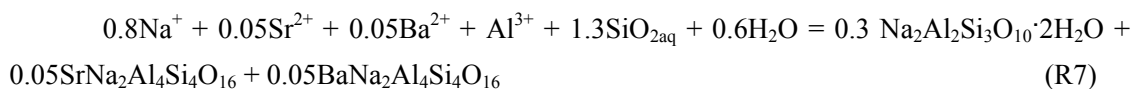
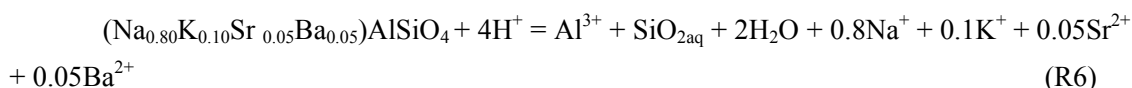
This could explain the co-occurrence of natrolite and diaspore which replace nepheline (Fig. 2a and Fig. 2b). The reaction would increase the Na activity of the fluid. This arbitrary reaction also would maintain constant silica activity, only if all the silica released by R2 is totally consumed by R1, which however can hardly be fulfilled in a real case. Therefore the increase of Silica and  $\text{Na}^+$  activities of fluid together as a result of R2 will further promote the stabilization of natrolite through the reaction R1. As a result of reaction R1 and precipitation of natrolite, silica activity would be compensated partly but still tends to increase.

### 6.1.2 Reactions related with Stronalsite-Banalsite

The reaction R1 of natrolite formation could be divided into two reactions of nepheline dissolution and natrolite formation.



A complex nepheline dissolution reaction concerning the real nepheline compositions could be established:



Reactions R6 and reaction R7 illustrate the dissolution of real nepheline and the formation of natrolite and stronalsite-banalsite solid solution. This is clearly proved by the co-existence of natrolite and stronalsite-banalsite minerals which replacing nepheline (Fig. 2d). The relative small amount stronalsite-banalsite minerals compared with pervasive natrolite also demonstrate this reaction process. Compositional variations of stronalsite-banalsite minerals are controlled by local fluid chemistry and the primary nepheline composition.



$K^+$  released from nepheline dissolution could precipitate as secondary K-feldspar or enter the framework of natrolite, or stay in the fluid due to the undersaturation state with respect to other K-bearing minerals. Excess silica (compared with that released from R6) required for reaction R7 probably derived from R2 which liberate sufficient silica with few amount of albite dissolution.

## 6.2 Formation condition

As discussed before, stronalsite-banalsite minerals and natrolite generated simultaneously through reaction R7, thus their formation conditions are similar. Therefore the conditions of stronalsite-banalsite minerals could be derived indirectly from natrolite stability due to lacking of thermodynamic data for stronalsite-banalsite minerals.

### 6.2.1 Geochemical modeling for mineral stability diagram

Mineral stability fields represented in activity-activity diagrams were calculated with the TWQ program (Lieberman and Petrakakis, 1991) using mineral database of JUN92 (Berman, 1988) and aqueous database of HKF81 (Helgeson et al., 1981). The data of analcite is derived from the database of Holland and Powell (2011). Notably, in order to maintain the internal consistency of database, the thermodynamic data for natrolite (which are not available in the commonly used database, e.g. JUN92) is constructed by integrating other thermodynamic data of reaction-related minerals. For example, considering the reaction  $[1 \text{ Nat} + 1 \text{ Qtz} + 2 \text{ Ky} = 2 \text{ Pg}]$ , the thermodynamic data of natrolite (Nat) can be induced from the other three minerals.

### 6.2.2 Formation condition derived from natrolite stability

According to reaction R1, The transformation of nepheline to natrolite is mainly controlled by the activity of nepheline, and activities of water and silica in the fluid. As shown in Fig. 4a, for nepheline activity of 0.34 and silica activity of 0.15 which defined by orthomagmatic mineral assemblages, the lowest  $\log a_{H_2O}$  value of -4 is needed for natrolite formation. With processing of natrolite formation, the silica activity of fluid will decrease gradually due to consumption of silica by natrolite. The decreasing silica activity will then require increasing water activity for producing natrolite (Fig. 4a). Comparing the topology of phase diagram for pure nepheline and nepheline with activity 0.34 (Fig. 4b), the activity of nepheline does not play a significant role as that of water and silica in zeolite formation. At 1 bar and 150 °C which are assumed to be the equilibrium condition, the boundaries of natrolite stability field are constrained by  $\log a_{SiO_2}$  of -8 and  $\log a_{H_2O}$  of 2.

Therefore the fluid corresponding to formation of stronalsite-banalsite minerals is a diluted silica-poor fluid with maximal  $a_{\text{SiO}_2}$  value of  $10^{-8}$ .

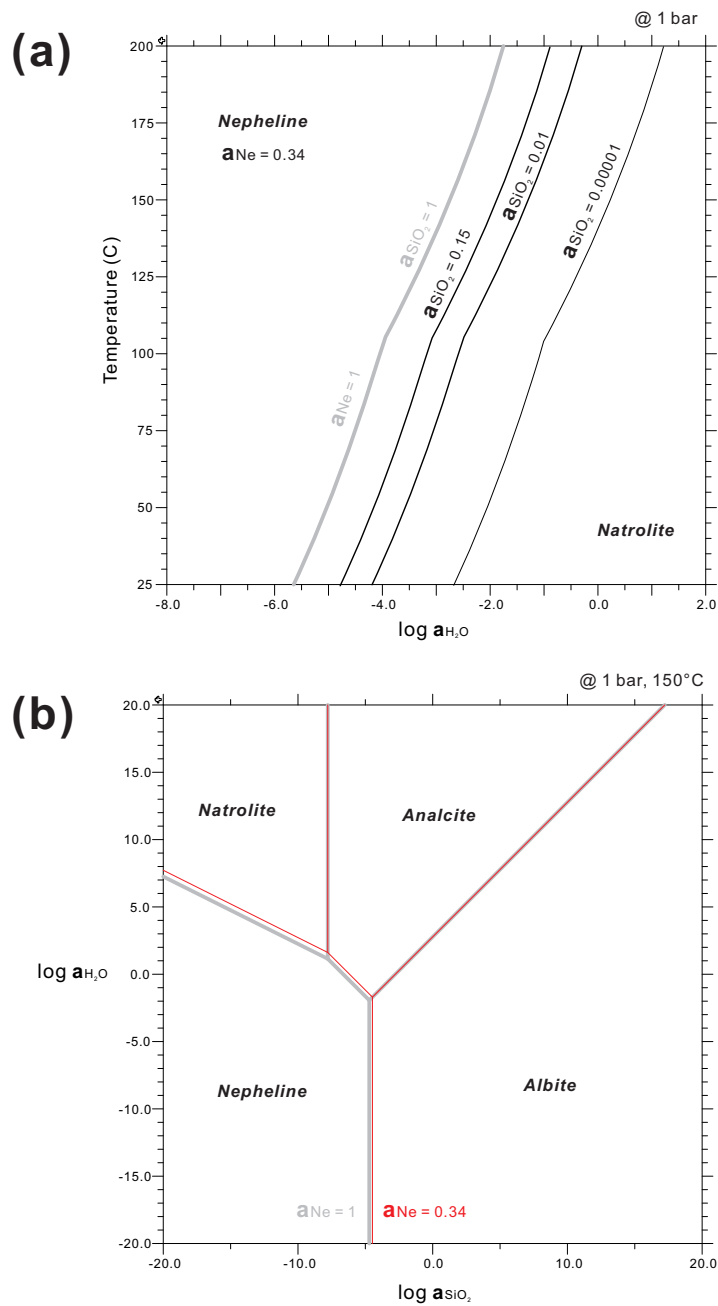


Fig. 4 Mineral stability diagrams for natrolite at 1 bar. See text for explanations.

## 7. Conclusions

Based on the investigation of secondary minerals from alkaline rock in the Seiland igneous province of northern Norway, combined with the microscopic, mineral composition and thermodynamic modeling, several conclusions concerning the formation of stronalsite-banalsite solid solution can be drawn below:

- (1) Stronalsite-banalsite solid solution and natrolite generated simultaneously through nepheline dissolution.
- (2) The extra silica required for stronalsite-banalsite solid solution and natrolite is probably derived from dissolution of albite lamella in perthite.
- (3) The fluid corresponding to formation of stronalsite-banalsite minerals is a diluted silica-poor fluid with maximal  $a_{\text{SiO}_2}$  value of  $10^{-8}$ .

## References

- Appleyard, E.C., 1974. Syn-orogenic igneous alkaline rocks of eastern Ontario and northern Norway. *Lithos*, 7(3): 147-169.
- Appleyard, E.C., 1980. Mass balance computations in metasomatism: Metagabbro/nepheline syenite pegmatite interaction in northern Norway. *Contributions to Mineralogy and Petrology*, 73(2): 131-144.
- Berman, R., 1988. Internally-consistent thermodynamic data for minerals in the system Na<sub>2</sub>O-K<sub>2</sub>O-CaO-MgO-FeO-Fe<sub>2</sub>O<sub>3</sub>-Al<sub>2</sub>O<sub>3</sub>-SiO<sub>2</sub>-TiO<sub>2</sub>-H<sub>2</sub>O-CO<sub>2</sub>. *Journal of Petrology*, 29(2): 445.
- Daly, J.S., Aitchison, S.J., Cliff, R.A., Gayer, R.A. and Rice, A.H.N., 1991. Geochronological Evidence from Discordant Plutons for a Late Proterozoic Orogen in the Caledonides of Finnmark, Northern Norway. *Journal of the Geological Society*, 148: 29-40.
- Fall, A., Bodnar, R.J., Szabó, C. and Pál-Molnár, E., 2007. Fluid evolution in the nepheline syenites of the Ditrau Alkaline Massif, Transylvania, Romania. *Lithos*, 95(3-4): 331-345.
- Gee, D., 1975. A tectonic model for the central part of the Scandinavian Caledonides. *American Journal of Science*, 275: 468-515.
- Geis, H.P., 1979. Nepheline syenite on Stjernøy, Northern Norway. *Economic Geology*, 74(5): 1286-1295.
- Hamilton, D.L., 1961. Nephelines as Crystallization Temperature Indicators. *The Journal of Geology*, 69(3): 321-329.
- Hamilton, D.L. and Mackenzie, W.S., 1960. Nepheline Solid Solution in the System NaAlSi<sub>3</sub>O<sub>8</sub>-KAlSi<sub>3</sub>O<sub>8</sub>-SiO<sub>2</sub>. *Journal of Petrology*, 1(1): 56-72.
- Heier, K., 1961. Layered gabbro, hornblende, carbonatite and nepheline syenite on Stjernøy, North Norway. *Norsk Geologisk Tidsskrift*, 41: 109-155.
- Heier, K., 1964. Geochemistry of the nepheline syenite on Stjernøy, North Norway. *Norsk Geologisk Tidsskrift*, 44: 205-216.
- Heier, K. and Taylor, S., 1962. A note on the U, Th and K contents in the nepheline syenite on Stjernøy, north Noeway. *Norsk Geologisk Tidsskrift*, 42: 287-292.
- Heier, K.S., 1966. Some Crystallo-chemical Relations of Nephelines and Feldspars on Stjernøy, North Norway. *Journal of Petrology*, 7(1): 95-113.
- Helgeson, H.C., Kirkham, D.H. and Flowers, G.C., 1981. Theoretical prediction of the thermodynamic behavior of aqueous electrolytes by high pressures and temperatures; IV, Calculation of activity

- coefficients, osmotic coefficients, and apparent molal and standard and relative partial molal properties to 600 degrees C and 5kb. *American Journal of Science*, 281(10): 1249-1516.
- Holdridge, D., 1962. A clay mineral from Stjernøy, Norway. *Clay Minerals*, 5(27): 26-30.
- Holland, T.J.B. and Powell, R., 2011. An improved and extended internally consistent thermodynamic dataset for phases of petrological interest, involving a new equation of state for solids. *Journal of Metamorphic Geology*, 29(3): 333-383.
- Hori, H., Nakai, I., Nagashima, K., Matsubara, S. and Kato, A., 1987. Stronalsite, SrNa<sub>2</sub>Al<sub>4</sub>Si<sub>4</sub>O<sub>16</sub>, a new mineral from Rendai, Kochi City, Japan. *Mineralogical Journal*, 13(6): 368-375.
- Kirkland, C.L., Daly, J.S., Eide, E.A. and Whitehouse, M.J., 2006. The structure and timing of lateral escape during the Scandian Orogeny: A combined strain and geochronological investigation in Finnmark, Arctic Norwegian Caledonides. *Tectonophysics*, 425(1-4): 159-189.
- Kirkland, Christopher L., Stephen Daly, J. and Whitehouse, Martin J., 2007. Provenance and Terrane Evolution of the Kalak Nappe Complex, Norwegian Caledonides: Implications for Neoproterozoic Paleogeography and Tectonics. *The Journal of Geology*, 115(1): 21-41.
- Kjøsnes, K., 1980. Fenitization of layered mafic rocks in the Lillebukt alkaline complex, Stjernøy, Norway. *Lithos*, 13(2): 215-215.
- Kobayashi, S., Miyake, H. and Shoji, T., 1987. A Jadeite Rock from Oosa-cho, Okayama Prefecture, Southwestern Japan. *Mineralogical Journal*, 13(6): 314-327.
- Krogh, E. and Elvevold, S., 1990. A Precambrian age for an early gabbro-monzonitic intrusive on the ksfjord peninsula, Seiland Igneous Province, northern Norway. *Norsk Geologisk Tidsskrift*, 70(4): 267-273.
- Lieberman, J. and Petrakakis, K., 1991. TWEEQU thermobarometry; analysis of uncertainties and applications to granulites from western Alaska and Austria. *The Canadian Mineralogist*, 29(4): 857-887.
- Liferovich, R.P., Mitchell, R.H., Zozulya, D.R. and Shpachenko, A.K., 2006. Paragenesis and composition of Banasite, Stronalsite, and their solid solution in nepheline syenite and ultramafic alkaline rocks. *Can Mineral*, 44(4): 929-942.
- Marks, M. and Markl, G., 2003. Ilimaussaq 'en miniature': closed-system fractionation in an agpaitic dyke rock from the Gardar Province, South Greenland (contribution to the mineralogy of Ilimaussaq no. 117). *Mineralogical Magazine*, 67(5): 893-919.
- Marks, M., Schilling, J., Coulson, I., Wenzel, T. and Markl, G., 2008. The alkaline-peralkaline Tamazeght complex, High Atlas mountains, Morocco: Mineral chemistry and petrological constraints for derivation from a compositionally heterogeneous mantle source. *Journal of Petrology*, 49(6): 1097.
- Oosterom, M., 1963. The ultramafites and layered gabbro sequences in the granulite facies rocks on Stjernøy (Finnmark, Norway). *Leidse Geol Mededelingen*, 28: 177-296.
- Passaglia, E., 1970. The crystal chemistry of chabazites. *American Mineralogist*, 55: 1278-1301.
- Pedersen, R., Dunning, G. and Robins, B., 1989. U-Pb ages of nepheline syenite pegmatites from the Seiland Magmatic Province, N. Norway. *The Caledonide Geology of Scandinavia*: 3-8.
- Roberts, D., 2003. The Scandinavian Caledonides: event chronology, palaeogeographic settings and likely modern analogues. *Tectonophysics*, 365(1-4): 283-299.
- Roberts, R.J., Corfu, F., Torsvik, T.H., Ashwal, L.D. and Ramsay, D.M., 2006. Short-lived mafic magmatism at 560-570 Ma in the northern Norwegian Caledonides: U-Pb zircon ages from the Seiland Igneous Province. *Geological Magazine*, 143(6): 887-903.
- Roberts, R.J., Corfu, F., Torsvik, T.H., Hetherington, C.J. and Ashwal, L.D., 2010. Age of alkaline rocks in the Seiland Igneous Province, Northern Norway. *Journal of the Geological Society*, 167(1): 71-81.
- Robins, B., 1984. Petrography and petrogenesis of nephelinized metagabbros from Finnmark, Northern Norway. *Contributions to Mineralogy and Petrology*, 86(2): 170-177.
- Robins, B. and Gardner, P.M., 1975. The magmatic evolution of the Seiland province, and Caledonian plate boundaries in northern Norway. *Earth and Planetary Science Letters*, 26(2): 167-178.
- Robins, B. and Tysseland, M., 1980. Fenitization of mafic cumulates by the Pollen carbonatite, Finnmark, Norway. *Lithos*, 13(2): 220-220.
- Robins, B. and Tysseland, M., 1983. The geology, geochemistry and origin of ultrabasic fenites associated with the Pollen Carbonatite (Finnmark, Norway). *Chemical Geology*, 40(1-2): 65-95.
- Salter, D.L. and Appleyard, E.C., 1974. An occurrence of vein palygorskite from the nepheline syenite of Lillebukt, Stjernøy, northern Norway. *Norsk Geologisk Tidsskrift*, 54: 329-336.
- Shi, G. et al., 2012. Mineralogy of jadeitite and related rocks from Myanmar: a review with new data.

- European Journal of Mineralogy, 24(2): 345-370.
- Strand, T., 1980. The chemistry of the Lillebukt carbonatite, Stjernøy, Norway. *Lithos*, 13(2): 223-223.
- Sturt, B.A., Miller, J.A. and Fitch, F.J., 1967. The age of alkaline rocks from West Finnmark, northern Norway, and their bearing on the datings of the Caledonian orogeny. *Norsk Geologisk Tidsskrift*, 47: 255-273.
- Sturt, B.A., Pringle, I.R. and Ramsay, D.M., 1978. The Finnmarkian phase of the Caledonian Orogeny. *Journal of the Geological Society*, 135(6): 597-610.

**Part IV Fluid Property and Water-Rock  
Interaction in the Alkaline Complex of Seiland  
Igneous Province, Northern Norway**

## 1. Abstract

Based on the investigation of the water chemistry from alkaline rock in the Seiland igneous province of northern Norway, combined with the microscopic observation of secondary minerals in the rock samples and thermodynamic modeling for water and mineral assemblages, it has been demonstrated that the water chemistry and secondary minerals are consequences of complicated water-rock interaction. Fluids from nepheline syenite are mostly dominated by  $\text{NaSO}_4$  component, while fluids from carbonatite catchment  $\text{Ca-HCO}_3$ . The variation among all fluids is resulted from mixing vector of  $\text{NaSO}_4$  -  $\text{Ca-HCO}_3$  to different extents. Albite dissolution provides the high  $\text{NaSO}_4$  signature of the fluid in nepheline syenite, the released  $\text{SiO}_2$  simultaneously promotes the precipitation of natrolite. Infiltration of  $\text{Ca-HCO}_3$  fluid from carbonatite into the nepheline syenite along fractures has resulted in the generation of thomsonite by transformation from nepheline and natrolite, and precipitation of calcite in the middle of fluid conduit, which both indicate local disequilibrium between water and host rock. Thomsonite tends to be stabilized at low  $\text{CO}_2$  partial pressure.

## 2. Introduction

Infiltration of aqueous fluid into the silicate rocks along fractures commonly causes water-rock interaction process due to the disequilibrium between minerals and exotic fluid (e.g. Bucher and Stober, 2010; Giggenbach, 1981; Nordstrom et al., 1989). This disequilibrium is a function of both intensive variables (e.g. pressure, temperature, chemical potential and oxidation potential) and extensive ones (e.g. mass and volume of the fluid). The interaction process is generally associated with the dissolution of primary minerals and the precipitation of secondary minerals. Consequently, fluid composition changes gradually with the reaction process undergoing until reaching equilibrium with the rock or depart from the host rock. Thus the whole host rock could be regarded as a solid buffer for the fluid, and meanwhile the fluid chemistry controls the alteration of the host rock. Therefore, fluid from a particular rock reservoir has specific characteristics, and vice versa.

Water-rock interaction process has been widely investigated for various water types and rock types from many case studies. For the upper continental crust which is predominantly composed of granite and gneiss, fluids are generally dominated by  $\text{Ca-Na-HCO}_3$  at surface and contain increasing amounts of alkalis, sulfate and chloride at greater depths (Bucher and Stober, 2010). The interaction processes in granite and gneiss involve breakdown of primary plagioclase and biotite and the formation of Ca-zeolite minerals and chlorites (Weisenberger and Bucher,

2010; Weisenberger and Bucher, 2011). Hot spring from granite reservoir which is dominated by Na-SO<sub>4</sub>-Cl is oversaturated with respect to Ca-zeolite minerals (Bucher et al., 2009). Hydrothermal fluids in volcanic field composed of basalt usually precipitate phyllosilicate and various zeolites at the expense of feldspar and olivine (Kousehlar et al., 2012; Weisenberger and Selbekk, 2009). Fluid in mafic reservoir rocks like amphibolites and gabbros is NaCl-CaCl<sub>2</sub> rich (Stober and Bucher, 2005). Hydrothermal processes which can stabilize zeolite minerals (e.g. natrolite and analcite) and dissolve feldspathoid have been demonstrated in various alkaline complexes (e.g. Marks et al., 2009; Schilling et al., 2009; Schilling et al., 2011).

Chlorine and fluorine concentrations are strongly controlled by the fluorite and halite crystals in the rock matrix or on grain boundaries (Bucher and Stober, 2010; Seelig and Bucher, 2010). In addition, other rock-forming minerals which contain minor Cl and/or F incorporated in the crystal structure can also supply these elements to some extent during water-rock interaction, such as muscovite, biotite, amphibole and apatite, etc (Marks et al., 2012; Zhu and Sverjensky, 1991; Zhu and Sverjensky, 1992). Sulfate in fluid usually originates from the oxidation of sulfide minerals, most commonly pyrite and pyrrhotite (Bucher et al., 2012). The corresponding reduction reaction is usually related to the production of elementary carbon or methane (Bucher et al., 2012). This oxidation-reduction process would potentially change the redox condition of the water-rock system.

In this study, I investigated the water chemistry from alkaline rock (nepheline syenite and carbonatite) catchments, in the Seiland igneous province of northern Norway, by means of microscopic observation of secondary minerals in the rock samples and thermodynamic modeling for both the water and mineral assemblages. The results show that the water chemistry can be well explained by water-rock interaction and fluid mixing.

## **3. Geology and petrography**

### **3.1 Geology of the study area**

The Seiland igneous province occupies an area of nearly 5,000 km<sup>2</sup> on the islands of Seiland, Sørøy and Stjernøy, and on the Øksfjord Peninsula in the northern Finnmark, Norway (Fig. 1). The province is located within the Kalak nappe complex of the Norwegian Caledonian orogenic belt, which has thrust eastwards onto the Precambrian crystalline basement of the Baltic shield during the Silurian continental collision (ca. 431-428 Ma at Finnmark, Kirkland et al., 2006; Kirkland et al., 2007) between Baltica and Laurentia following the early Palaeozoic closure of the Iapetus Ocean (Gee, 1975; Roberts, 2003). The Seiland igneous province has a long and complex



history concerning magmatic evolution: voluminous ultramafic rocks at  $829 \pm 18$  Ma (Krogh and Elvevold, 1990), layered gabbroic plutons of  $700 \pm 33$  Ma,  $604 \pm 44$  Ma and 570 Ma (Daly et al., 1991; Roberts et al., 2006) and a final stage of calc-alkaline intrusions represented by alkaline pyroxenite, syenite, nepheline syenite and carbonatite at  $574 \pm 5$  Ma (Roberts et al., 2010). All these various rocks are considered to represent a synorogenic (Caledonian orogenic belt) intrusive activity evolved from tholeiitic basalt, compositionally ranging from high-K calc-alkaline magmas, through alkaline olivine basalt and picrite and finally to highly differentiated alkaline magmas and carbonatite (Appleyard, 1974; Robins and Gardner, 1975; Sturt et al., 1967; Sturt et al., 1978).

The Lillebukt alkaline complex (Fig. 1), on Stjernøy Island, is enclosed in the ultramafic and mafic rocks of peridotite, pyroxenite, gabbro and hornblendite (Heier, 1961; Oosterom, 1963). The boundary is blurred and thus the relationship between the alkaline complex and the hosting rocks is unclear. The alkaline complex is composed of syenite, nepheline syenite, and carbonatite, all of which have been intruded by late mafic and syenite dikes, and pegmatites (Pedersen et al., 1989; Robins and Tysseland, 1980). The silico-carbonatite of the Lillebukt alkaline complex is closely related to the nepheline syenite and contains abundant amphibole, biotite and apatite in the silicate-rich layers (Robins and Tysseland, 1983; Strand, 1980). It has been suggested that the carbonatite represents the latest igneous activity of the Caledonian orogeny (Robins and Gardner, 1975). The nepheline syenite has been mined by North Cape Minerals in an open pit on Nabberen (earlier in an underground mine inside Nabberen) and the raw material is processed at the Lillebukt plant. The fine powdered nepheline - K-feldspar mixture is shipped from the small port to customers in the ceramics and glass industry worldwide.

The Nabberen nepheline syenite body is a lens-shaped stock located in the north of the summit of Nabberen (Fig. 1), which occupies an area of  $1700 \times 300$  m<sup>2</sup> (Geis, 1979). It is a miaskitic nepheline syenite characterized by high concentration of alkalis, Ba and Sr, and depletion of REE, Y, Nb, Sc, Zr, U, and Th (Heier, 1964; Heier and Taylor, 1962; Heier, 1966; Robins and Tysseland, 1980). The surrounding gabbros have been fenitized, probably by the low-density fluid expelled from the volatile-rich alkaline magmas which now crystallized as nepheline syenite and carbonatite (Appleyard, 1980; Kjøsnes, 1980; Robins, 1984; Robins and Tysseland, 1980; Robins and Tysseland, 1983). Hydrothermal assemblages including zeolites (natrolite) and clay minerals (palygorskite, a magnesium clay mineral) have been observed in the Lillebukt mine, and they were regarded as products of post-tectonic low-temperature reactions with groundwater (Geis, 1979; Holdridge, 1962; Salter and Appleyard, 1974).

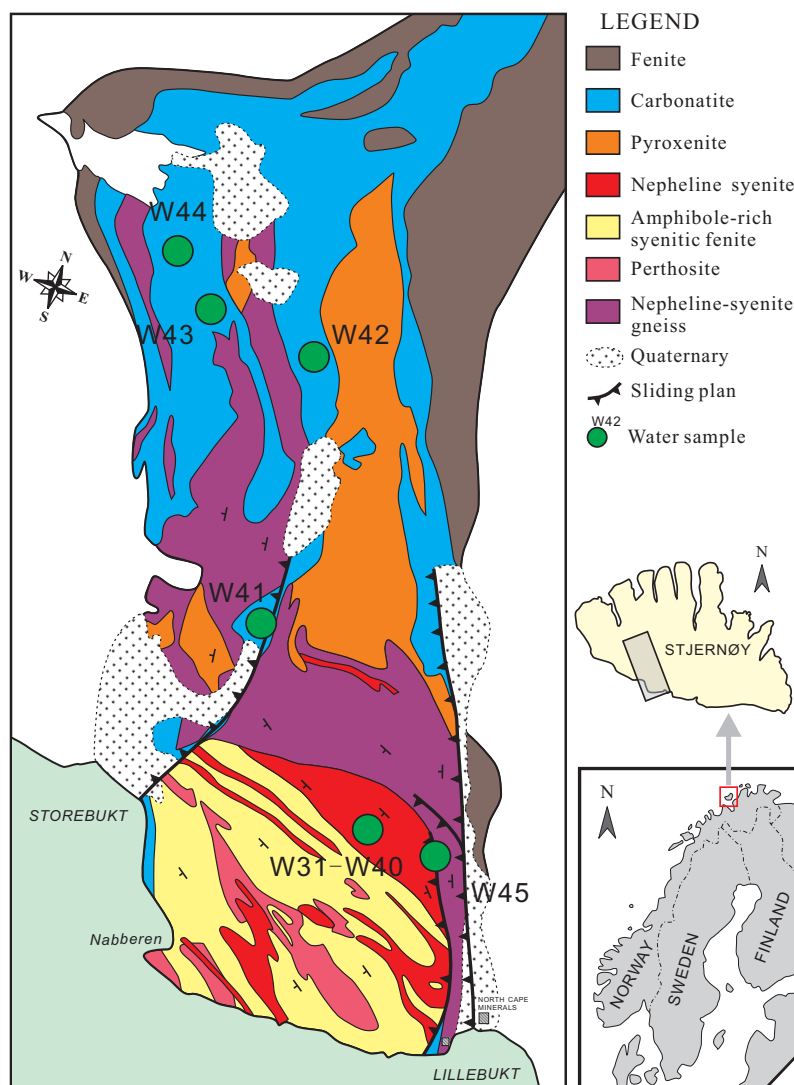


**Fig. 1 Geological map of Lillebukta alkaline complex, Seiland igneous province, Northern Norway, showing the sampling locations.**

### 3.2 Petrography of host rocks

Water samples of W31-W40, sampled by means of borehole, fissure, dripping and creek, have been collected from nepheline syenite catchment (Fig. 1 and Table 1). Others samples of W42-W44 were collected from creeks of carbonatite catchment. Samples of W41 and W45 are both collected near one fault separating nepheline syenite from gneiss and carbonatite.

### 3.2.1 *Nepheline syenite*

Nepheline syenite on Nabberen, from which water samples were collected, is massive and has no preferred orientation of minerals. White hydrothermal veins can be clearly identified in nepheline syenite. Wide veins (up to 5 mm) are accompanied by bilateral reaction zones (up to 2 cm). These bilateral reaction zones display a reddish color distinctive from the white veins and the gray original nepheline syenite. In addition, there are numerous irregular fine seams (less than 1 mm wide) which can be identified under careful observation by their indistinct white color and occasionally reddish reaction speckles along the seams. These tiny seams cut each other and form a network over the whole sample. The white alteration veins are entirely composed of fine-grained brown-grey zeolite aggregates. The rock matrix of nepheline syenite is mainly composed of potassium feldspar (40 %), nepheline (35 %), amphibole (10 %) and clinopyroxene (5 %), with accessory albite, biotite, apatite, titanite, magnetite, ilmenite, calcite and zeolite. There is no difference in mineral constituents between rock matrix and reaction zones, except more intense alteration of nepheline in the latter.

Light green clinopyroxene occurs as prismatic crystals (up to 1 cm) with irregular grain boundaries and inclusions of apatite. Most amphiboles appear as dark green coronas around or thin rims along clinopyroxene. Fine vermiform amphibole crystals coarsening outward forming the corona. There are also amphibole rims around calcite crystals adjacent to the clinopyroxene. A few amphibole crystals also show prismatic crystals. Potassium feldspar and nepheline are large anhedral to subhedral crystals, which coexist with each other in textural equilibrium, indicative of approximately contemporaneous crystallization. Tiny anhedral apatite crystals are distributed sporadic in the matrix and as inclusions in clinopyroxene and amphibole (Fig. 2a). Titanite occurs as euhedral crystals or rims around magnetite and ilmenite. Minor hercynite crystals are present close to the margin of the magnetite rimmed by titanite. Rare biotite crystals are found together with ilmenite and magnetite.

Potassium feldspars show widespread perthite textures with albite as blade or drop shaped lamellae. The site of albite lamellae has become cavity likely due to dissolution (Fig. 2b). Nepheline crystals are speckled or replaced by fine-grained zeolite and diaspore (Fig. 2c). In the white veins within nepheline syenite, mixture of fine-grained natrolite and thomsonite occurs as rounded spots with diameter of ca. 0.5 mm (Fig. 2d). Calcite-rich veins in the nepheline syenite are accompanied with natrolite, thomsonite and Sr-rich thomsonite (Fig. 2a and Fig. 2e). Natrolite grains are overgrown by thomsonite locally in all samples (Fig. 2f). Stronalsite-banalsite solid solution minerals are present in nepheline grains which are enriched in fissures (Fig. 2g). Hydrogrossular form narrow rims around natrolite, surrounded by K-feldspar (Fig. 2h) or other

minerals (figure not shown here).

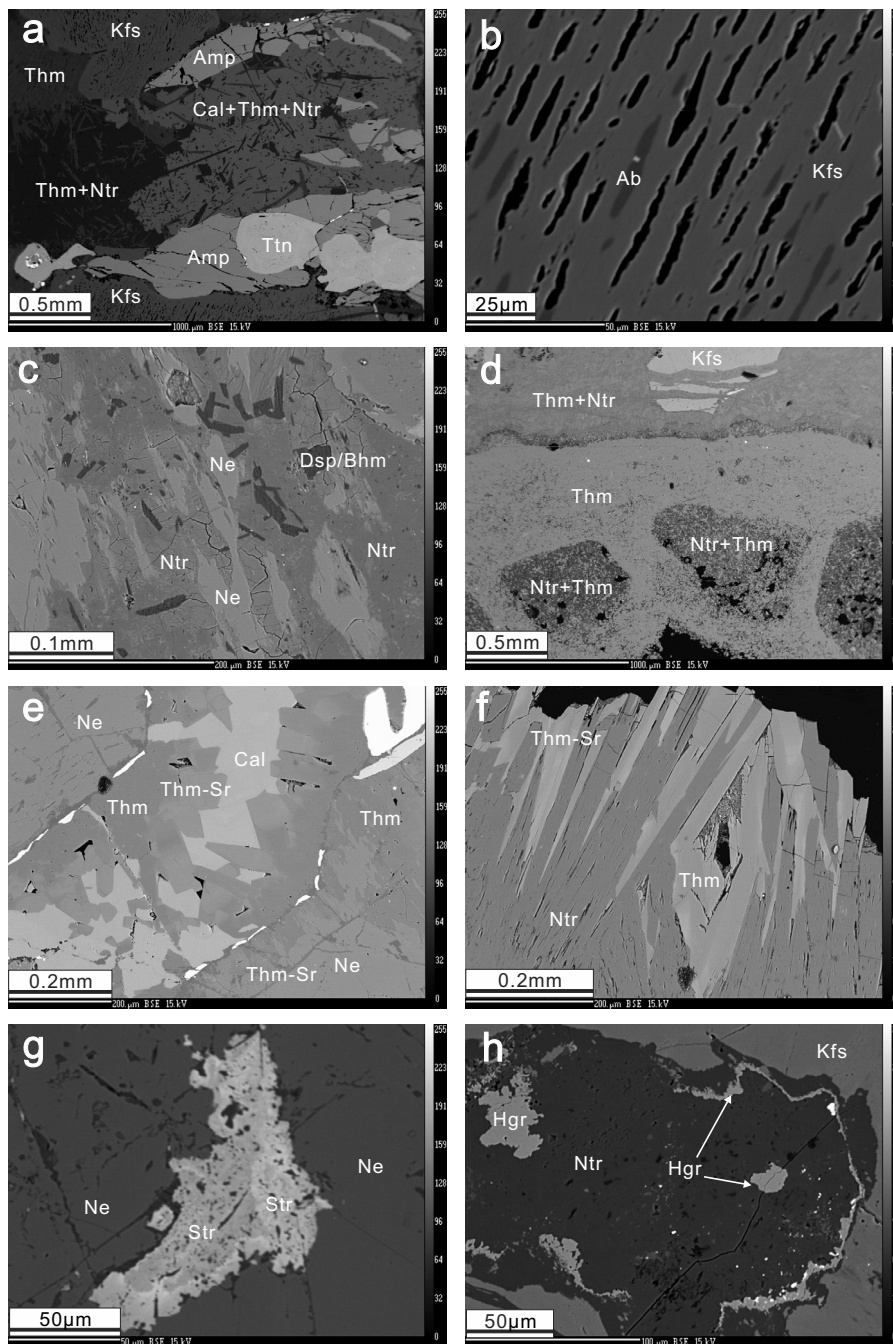


**Fig. 2** BSE images for microscopic textures of secondary minerals. See text for explanations.

### **3.2.2 Carbonatite**

The petrography of carbonatite described here is after the studies of Natalie (2010) and Heier (1961). The carbonatite contains abundant calcite, apatite, hornblende and biotite, as well as nepheline and albite to a less extent. Biotite is featured by high BaO, up to ~2 wt% in the core and up to ~4 wt% in the rim respectively. The core and rim of biotite with different BaO content might refer to fluid-induced enrichment. Apatite is compositionally fluorapatite and hydroxylapatite, highly depleted in chlorine. Calcite and apatite contain moderately abundant Sr. The transition from nepheline to natrolite has been also observed in carbonatite, which is quite similar to the phenomenon observed in nepheline syenite described above. Calcite dissolution can be clearly observed at outcrops and in thin sections.

## **4. Methods**

### **4.1 Analytical methods of water**

Temperature, pH, redox potential and electric conductivity were measured in situ during field sampling. Chemical analyses were performed in the laboratory of the institute of Mineralogy and Geochemistry at University of Freiburg. Cations and anions were analyzed by Ion Chromatography (Dionex 120). Carbonate and bicarbonate were determined by titration with 0.1mol/L HCl.

Detection limit for K, Na, and Mg is 0.02 mg/L; detection limit of Ca, Sr, F, Br and NO<sub>3</sub> is 0.05 mg/L; detection limit for Cl and SO<sub>4</sub> is 0.5 mg/L and 0.8 mg/l respectively. Notably, SiO<sub>2</sub> of the measured samples were not detectable, and thus it is assumed that the real SiO<sub>2</sub> contents are slightly lower than the detection limit of ~1 mg/L. In the following modeling involving SiO<sub>2</sub> content, the value of 1 mg/L is applied for all samples.

### **4.2 Geochemical modeling for water**

The saturation state of the waters was calculated with the Phreeqc version 2.18 with llnl database (Parkhurst and Appelo, 1999). Additional thermodynamic data of minerals have been inserted to that database (Table 2). Thermodynamic data of sodalite (Komada et al., 1995), celsian and Sr-feldspar (Chernyshova et al., 1991) were used to calculate equilibrium constant (logK) of corresponding dissolution reaction. The dissolution reaction for Ca-stilbite, Ca-heulandite, F-muscovite and F-biotite were derived from Seelig and Bucher (2010) and based on thermodynamic data from literature (Frey et al., 1991; Zhu and Sverjensky, 1991). The

thermodynamic data of thomsonite, natrolite, banalsite and stronalsite, which have been observed in nepheline syenite sample, were constructed by integrating other thermodynamic data of reaction-related minerals (see Section 4.3).

### 4.3 Geochemical modeling for mineral stability diagram

Mineral stability fields represented in activity-activity diagrams were calculated with the TWQ program (Lieberman and Petrakakis, 1991) using mineral database of JUN92 (Berman, 1988) and aqueous database of HKF81 (Helgeson et al., 1981). The utilized thermodynamic data in this study for most zeolite group minerals (heulandite, laumontite, stilbite and wairakite) are derived from Frey et al. (1991). As a rare case, the data of analcite is derived from the database of Holland and Powell (2011). Notably, in order to maintain the internal consistency of database, the thermodynamic data for thomsonite, natrolite and mesolite (which are not available in the commonly used database, e.g. JUN92) are constructed by integrating other thermodynamic data of reaction-related minerals. For example, considering the reaction  $[1 \text{ Nat} + 1 \text{ Qtz} + 2 \text{ Ky} = 2 \text{ Pg}]$ , the thermodynamic data of natrolite (Nat) can be induced from the other three minerals.

Calcite saturation condition and corresponding partial pressure of CO<sub>2</sub> gas were calculated by SUPCRT92 program (Johnson et al., 1992) with dprons92 database (Helgeson et al., 1981).

## 5. Hydrochemistry

Chemical analyses of water samples from nepheline syenite-carbonatite catchment are presented in Table 1 and Fig. 3. The field temperatures were measured to be at ca. 20°C and 11°C, which were caused by normal temperature undulating during two field trips. The pH of waters varies from 7.48 to 9.36, among which six water samples from nepheline syenite pit have pH above 9. The electrical conductivity has a total range of 55.8-155.8 μS/cm.

Magnesium in all water samples is remarkably low (around 0.5mg/L). Potassium has a limited range of 0.45-1.86 mg/L. Strontium concentrations are measured to be 0.09-1.21 mg/L. Remarkable NO<sub>3</sub> component (17.44 mg/L) in water samples are regarded as biological product which will not be considered in the following discussion. Chloride concentration has a large range of 3.23-10.52 mg/L, whereas bromide could only be detected in 4 samples with concentrations of ~0.03 mg/L, and the resultant mass ratio of Cl/Br varies from 183 to 351. The total dissolved solids (TDS) vary from 41.52 to 118.24 mg/L which indicates low degree of mineralization. All the water samples are chemically dominated by calcium, sodium, bicarbonate,

sulfate and chloride, which could be generally regarded as Ca-Na-HCO<sub>3</sub> type. They are further divided into five subgroups based on composition and origin (Fig. 3), which are discussed in detail below.

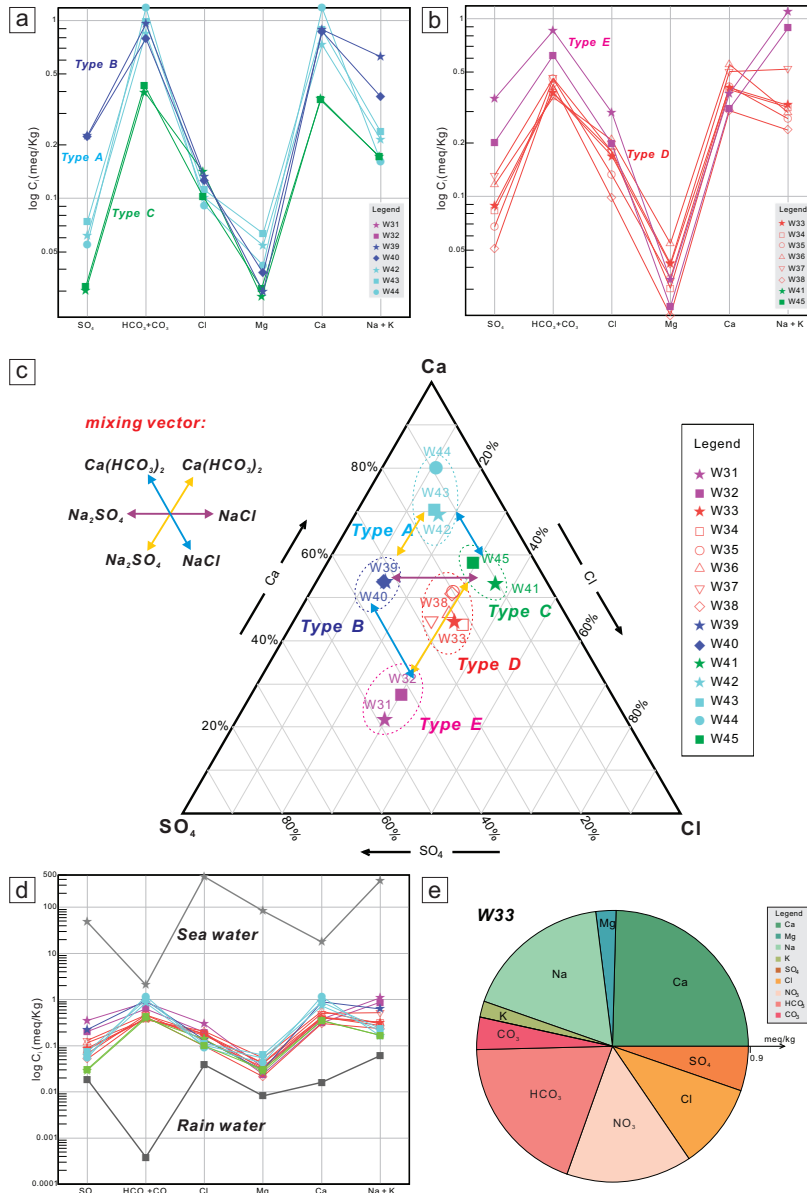


**Fig. 3** Diagrams show water geochemistry. (a) schoeller diagram for type A, type B and type C; (b) schoeller diagram for type D and type E; (c) Ca-SO<sub>4</sub>-Cl triangle diagram shows mixing vectors; (d) schoeller diagram for seawater and rain; (e) piper diagram shows water constitute of sample W33.

Sample	W31	W32	W33	W34	W35	W36	W37	W38	W39	W40	W41	W42	W43	W44	W45
Geology of Catchment	Nepheline -Syenite	Nepheline -Syenite	Nepheline -Syenite	Nepheline -Syenite	Nepheline -Syenite	Nepheline -Syenite	Nepheline -Syenite	Nepheline -Syenite	Nepheline -Syenite	Nepheline -Syenite	Nepheline -Syenite	Carbonatite	Carbonatite	Carbonatite	Nepheline-Syenite some Carb.
water type	fissure water	big borehole	fissure water	dripping water	borehole	borehole	borehole	dripping water	creek	creek	spring	creek	creek	creek	creek
Temperatur	(°C)	20.3	19.8	19.1	19.3	19.9	21.4	20.6	21.2	21.1	12.5	11.5	10.8	10.7	11.4
pH		8.91	9.34	9.36	9.16	9.21	9.36	9.07	8.21	8.05	8.65	7.97	8.05	7.72	7.87
Eh	(mV)	-40.0	-69.0	-69.0	-58.0	-59.0	-61.0	-43.0	5.0	14.0	-20.0	16.0	9.0	22.0	16.0
EC	(µS/cm)	155.8	105.8	87.4	83.2	73.9	99.8	99.7	146.0	130.0	60.4	99.4	113.4	131.6	55.8
Ca	(mg/L)	7.58	6.24	8.16	7.99	8.35	11.08	10.09	17.8	17.35	7.11	14.58	17.7	23.45	6.96
Mg	(mg/L)	0.41	0.29	0.5	0.37	0.42	0.65	0.51	0.26	0.46	0.33	0.66	0.77	0.51	0.37
Na	(mg/L)	24.57	19.46	6.73	6.7	5.7	6.25	11.15	13.28	7.77	3.58	4.41	4.82	3.12	3.6
K	(mg/L)	1.06	1.4	1.24	0.96	1.0	0.92	1.28	1.86	1.33	0.45	0.86	1.04	1.0	0.44
Sr	(mg/L)	0.34	-	-	-	-	-	-	0.33	0.43	-	0.42	0.65	1.21	0.09
Alk (CO3)	(mg/L)	3.0	4.8	3.0	1.8	1.8	3.3	1.5	-	-	0.9	-	-	-	-
Alk (HCO3)	(mg/L)	47.6	29.9	18.31	20.14	24.41	16.78	25.32	56.58	49.82	22.58	53.09	61.02	75.66	26.54
SO4	(mg/L)	17.01	9.67	4.26	3.98	3.24	5.58	6.29	10.77	10.61	1.42	2.96	3.55	2.64	1.5
Cl	(mg/L)	10.52	6.97	5.99	6.32	4.69	7.33	6.32	4.67	4.44	4.9	3.58	3.94	3.23	3.54
NO3	(mg/L)	0.8	1.57	15.34	12.56	6.26	17.44	15.09	10.59	7.24	0.25	0.09	0.12	0.7	-
F	(mg/L)	0.02	-	-	-	-	-	-	-	-	-	-	-	-	-
Br	(mg/L)	0.03	-	0.03	-	-	0.04	0.02	-	-	-	-	-	-	-
TDS	(mg/L)	112.94	80.3	63.56	60.82	55.87	69.38	77.57	118.24	98.45	41.52	80.65	93.61	111.52	43.04
EN	(meq/L)	0.98	6.28	7.91	6.80	2.43	4.61	2.17	2.09	0.88	2.03	1.42	0.44	0.13	1.66
C/Br	mass ratio	350.67	0.0	199.67	-	-	183.25	316.0	-	-	-	-	-	-	-
T <sup>a</sup>	(°C)	154	190	276	250	270	253	229	270	248	237	282	263	342	235
T <sup>b</sup>	(°C)	149	180	266	239	261	242	217	260	236	226	273	285	339	223
T <sup>c</sup>	(°C)	37	45	29	23	22	17	30	22	32	4	9	11	-	4
CO <sub>2</sub>	Bar	10 <sup>-4.23</sup>	10 <sup>-4.85</sup>	10 <sup>-5.98</sup>	10 <sup>-6.42</sup>	10 <sup>-4.83</sup>	10 <sup>-5.10</sup>	10 <sup>-4.67</sup>	10 <sup>-3.07</sup>	10 <sup>-3.46</sup>	10 <sup>-3.38</sup>	10 <sup>-3.32</sup>	10 <sup>-4.28</sup>	10 <sup>-3.93</sup>	10 <sup>-3.52</sup>

Eh:Redoxpotential; EC: electrical conductivity; TDS: total dissolved solids; EN: Electrical Neutrality

<sup>a</sup>based on Na-K thermometer of Fournier (1977);

<sup>b</sup>based on Na-K thermometer of Dan (2002);

<sup>c</sup>based on Na-K-Ca thermometer of Fournier (1977);

**Table 1 Chemical compositions of water from Nepheline syenite-carbonatite catchment of Lillibukt alkaline complex, Seiland Igneous Province**



## 5.1 Type A: Ca-HCO<sub>3</sub> type

Water samples (W42, W43, and W44) from carbonatite catchment are compositionally similar (Fig. 3a). The pH varies from 7.72 to 8.05. The composition of the water is dominated by Ca and HCO<sub>3</sub>: Ca is from 14.58 to 23.45 mg/L and HCO<sub>3</sub> from 53.09 to 75.66 mg/L. The TDS variation is mainly caused by the Ca-(HCO<sub>3</sub>) phase, varying between 80.65 and 111.52 mg/L correspondingly (Fig. 4b). There is also minor amount of Cl (3.23-3.94mg/L) and Na (3.12-4.82mg/L), which show a positive correlation (Fig. 4c). Strontium and potassium are very low, generally below 1 mg/L.

This water type is mainly controlled by Ca-(HCO<sub>3</sub>) component which probably derived from calcite dissolution in the carbonatite rocks.

## 5.2 Type B: Ca-Na-HCO<sub>3</sub>-SO<sub>4</sub> type

Samples W39 and W40 are creek waters collected from nepheline syenite catchment. The pH values are ca. 8. The dominant components are Ca, Na, HCO<sub>3</sub> and SO<sub>4</sub>. These two samples have similar Cl, Ca and SO<sub>4</sub> contents (about 4.5 mg/L, 18.0 mg/L and 11.0 mg/L, respectively). Na and HCO<sub>3</sub> contents are different in the two samples, with both higher Na (13.28 mg/L) and HCO<sub>3</sub> (58.58 mg/L) in W39 than those in W40 (Na 7.77 mg/L, HCO<sub>3</sub> 48.82 mg/L). The difference in TDS of these two samples is possibly caused by the difference in Na-(SO<sub>4</sub>) phase, which varies from 118.24 to 98.45 mg/L accordingly. Compared to Type A, Na and SO<sub>4</sub> concentrations in Type B increase remarkably (Fig. 3a). The absolute TDS values in Type B are slightly lower than that in Type A.

This water type is mainly controlled by Ca-(HCO<sub>3</sub>), Na-(HCO<sub>3</sub>) and Na-SO<sub>4</sub> components.

## 5.3 Type C: Ca-Na-HCO<sub>3</sub>-Cl type

Water samples W41 and W45 have pH values of 7.97 and 7.87. These two samples have similar chemical compositions. Their TDS values are about 42 mg/L. The concentrations of Ca, Na, HCO<sub>3</sub>, and SO<sub>4</sub> are about 7 mg/L, 3.6 mg/L, 24 mg/L and 1.5 mg/L, respectively. Cl concentrations of the two samples are slightly different with 4.9 mg/L in W41 and 3.54 mg/L in sample W45.

This water type is basically controlled by Ca-(HCO<sub>3</sub>) and NaCl components.

## 5.4 Type D: Na-Ca-HCO<sub>3</sub>-Cl-SO<sub>4</sub> type

Six samples (W33-W38) from nepheline syenite catchment have similar chemical compositions. These samples have low TDS ranging from 41.52 to 77.57 mg/L. Their pH value is nearly constant at 8.0. The composition of the water is dominated by Ca, Na, HCO<sub>3</sub>, Cl and SO<sub>4</sub>. Ca concentration varies from 6.09 to 10.09 mg/L and HCO<sub>3</sub> from 16.78 to 28.07 mg/L. Concentration variations of Cl (3.46-7.33mg/L), SO<sub>4</sub> (1.42-6.29mg/L), CO<sub>3</sub> (0.9-3.3 mg/L) and Na (3.58-11.15mg/L) have been detected.

This water type is basically controlled by Ca-(HCO<sub>3</sub>), Na-(SO<sub>4</sub>) and NaCl components.

## 5.5 Type E: Na -SO<sub>4</sub>-Cl mixture type

Sample W31 is fissure water from Nepheline syenite catchment. The pH value is 8.91. This sample has a relative high TDS of 112.94 mg/L and the highest Na and SO<sub>4</sub> contents (24.57 mg/L and 47.60 mg/L) compared to other types. The contents of Ca, HCO<sub>3</sub> and Cl are relatively low, which are 7.58 mg/L, 17.01 mg/L, and 10.52 mg/L respectively.

Sample W32 is collected from a big borehole of Nepheline syenite mine. The pH value is 9.34. It has a very similar relative component proportions among Ca, Na, Cl, HCO<sub>3</sub> and SO<sub>4</sub> with that of sample W31, but absolute amounts of these components are clearly different. The contents of Ca, HCO<sub>3</sub> and Cl are 6.24 mg/L, 9.67 mg/L, and 6.97 mg/L respectively. Na content is 19.46 mg/L and SO<sub>4</sub> concentration is 29.90 mg/L. The TDS is 80.30 mg/L.

The TDS difference of these two samples is mainly controlled by Na-(SO<sub>4</sub>) component. Compared with type D, W31 and W32 have higher proportions of Na and SO<sub>4</sub>.

This water type is controlled by mixtures of Na-(SO<sub>4</sub>) and NaCl components.

## 5.6 Redox potential

The redox potential in fluid is described by values of Eh in this study. According to the grouping stated above, different types generally show distinguishable value ranges of Eh and SO<sub>4</sub> concentration (Fig. 4a). Group A is characterized by high Eh (9~22 mV) and low SO<sub>4</sub> (2.6~3.5 mg/L); group B has high Eh (5~14 mV) but moderately high SO<sub>4</sub> (~11 mg/L); group C has a broad range of Eh (-20~16) but very low SO<sub>4</sub> (~1.5 mg/L); group D is featured by both low Eh (-69~-43 mV) and SO<sub>4</sub> (3.24~6.29 mg/L); group E has low Eh (-69~-40 mV) and broadly high SO<sub>4</sub> (10~17 mg/L).

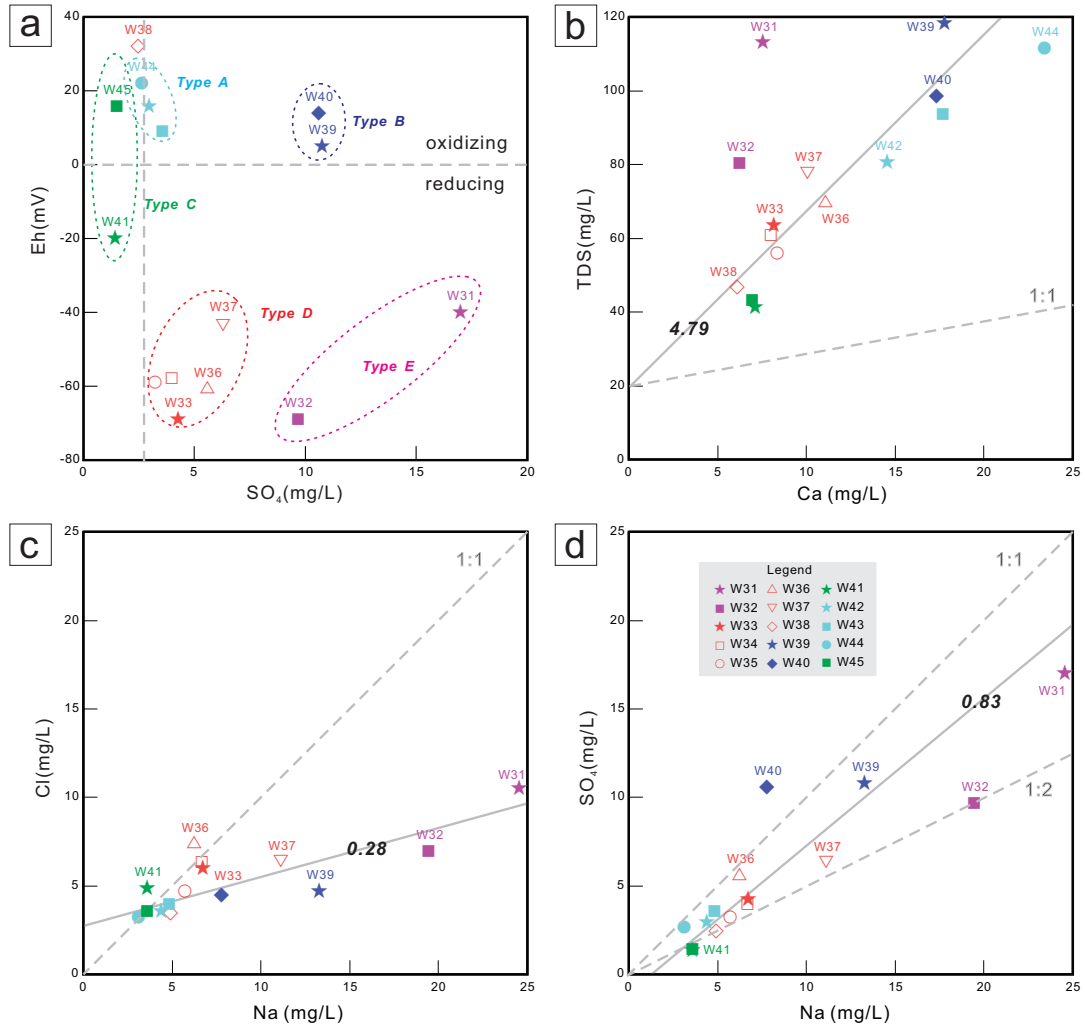


**Fig. 4** Binary diagrams of various water components. (a) Eh vs. SO<sub>4</sub>; (b) TDS (total solid solutions) vs. Ca; (c) Cl vs. Na; (d) SO<sub>4</sub> vs. Na.

As shown above, the redox potential indicated by Eh has no systematical relationship with SO<sub>4</sub> concentration. The nature of host rock might hold a primary control of the Eh values of fluids; for example, nepheline syenite generally corresponds to a highly reduced condition in the environment fluids (e.g. Marks and Markl, 2001; Marks et al., 2003; Powell, 1978).

## 5.7 Mixing vector

Mixing vectors are observable between the five types described above, which can explain fully the generation of the chemical variations. As shown in Fig. 3c schematically, three main mixing vectors are constructed, namely Na<sub>2</sub>SO<sub>4</sub>-NaCl, Na<sub>2</sub>SO<sub>4</sub>-Ca(HCO<sub>3</sub>)<sub>2</sub> and NaCl-Ca(HCO<sub>3</sub>)<sub>2</sub>.

Notably, the mixing vector of  $\text{Na}_2\text{SO}_4\text{-NaCl}$  is not as large as that of  $\text{Na}_2\text{SO}_4\text{-Ca}(\text{HCO}_3)_2$  and  $\text{NaCl-Ca}(\text{HCO}_3)_2$ ; in another word, the water compounds are largely controlled by mixing between  $\text{Na}_2\text{SO}_4$  and  $\text{Ca}(\text{HCO}_3)_2$  or  $\text{NaCl-Ca}(\text{HCO}_3)_2$ , but mixing between  $\text{Na}_2\text{SO}_4$  and  $\text{NaCl}$  is much less functional. Furthermore, as shown by the covariations of Na versus Cl (Fig. 4c) and Na versus  $\text{SO}_4$  (Fig. 4d), the variation of Na is more strongly dominated by  $\text{Na}_2\text{SO}_4$  but less by  $\text{NaCl}$ , which suggests that  $\text{Na}_2\text{SO}_4\text{-Ca}(\text{HCO}_3)_2$  is the most dominant mixing vector in the fluid system.

## 6. Discussions

### 6.1 Equilibrium temperature of waters

Equilibrium temperature here is the temperature at which the water last equilibrated with its environment. This could be estimated from chemical composition by using the popular water geothermometers (Karingithi, 2009). Silica geothermometer (Fournier and Potter, 1982) is excluded due to that silica phases (quartz/chalcedony/amorphous silica) are lacking but nepheline is present. The available water geothermometers are Na-K thermometer and Na-K-Ca thermometer based on the chemical analyses (Fournier, 1977; Fournier and Truesdell, 1973). Estimated temperatures are presented in Table 1. Results from Na-K geothermometer and Na-K-Ca thermometer show a remarkable discrepancy of hot versus cold.

Temperatures calculated by Na-K thermometer from Fournier (1977) range within 154-342°C. Temperatures calculated by Na-K thermometer of Can (2002) yield a range of 149-339 °C. Results from these two thermometer are in good agreement with each other. Particularly, W44 has the highest value near 340 °C and W31 the lowest of 150 °C; other samples have temperature >230 °C. The results from the Fournier thermometer are generally higher than that yielded from the Can thermometer by ca. 10 °C for all samples.

In contrast, Na-K-Ca geothermometer (Fournier, 1977) yields distinct cold environment of 4-45°C. The temperatures distribute regularly: Type A from carbonatite catchment has the temperature of 10°C; Type B has temperature of 20-32°C; Type C shows the lowest temperature of 4°C; Type D from nepheline syenite catchment has a moderate temperature range of 17-30°C; Type E hold the highest temperatures between 37°C and 45°C.

As Na-K geothermometer is based on equilibrium between albite and K-feldspar (Fournier, 1977), the temperatures calculated by this thermometer possibly show the temperature at which the exsolution lamellae of albite in perthite being dissolved (Fig. 2b). At this time, the exsolved albite and the host K-feldspar contacted and interacted with hot fluid, although albite

nearby the fluid micro-conduit dissolved in the fluid, the whole buffer system could still be regarded as in equilibrium. Thus albite-K-feldspar-fluid equilibrium displays hot environment with an average temperature of 260°C.

Na-K-Ca geothermometer include cation exchange reaction between Na-K feldspar and calcium bearing minerals (e.g., plagioclase and calcite) (Fournier, 1977). In the nepheline syenite, secondary calcite and zeolite vein (Fig. 2a and Fig. 2e), thin oligoclase rim and the survival nepheline and perthite constitute the buffer system for fluid. Therefore, the Na-K-Ca geothermometer is corresponding to the condition at which pervasive zeolite is generated. At the time of sampling, it was observed that zeolite veins were growing at the discharge point of nepheline syenite mine, which is an evidence of this explanation. This cold condition of 25°C is consistent with the in situ temperature (20°C) at the discharge point. The lowest temperature 4-10°C in water type A and C, which are related with carbonatite, possibly indicate the condition of calcite dissolution.

Therefore, the average 25°C could be regarded as an equilibrium temperature at which the water equilibrated with nepheline syenite complex.

## 6.2 The saturation state of the water

The saturation state of the water with respect to lots of minerals have been calculated and presented in Table 3 and Fig. 5.

All the water samples are undersaturated with feldspar components of albite, anorthite, K-feldspar, celsian and banalsite. For waters with detectable strontium concentration, Sr-feldspar is undersaturated, while stronalsite is oversaturated with moderate saturation index (5.86-7.92) coinciding with its existence in nepheline syenite. Quartz, amorphous silica and chalcedony are slightly undersaturated with saturation index varying from -0.75 to -2.14. Nepheline components are moderate undersaturated which is consistent with nepheline dissolution phenomena in the nepheline syenite.

All the samples are moderately undersaturated with respect to most zeolite group minerals of heulandite, stilbite, Ca-heulandite, laumontite, wairakite, and mordenite. These zeolites belong to intermediate or high silica zeolites with Si/Al ratios larger than 2 (Deer et al., 2004). Their saturation index varies between -1.28 and -8.49, conversely with the co-variation of the Si/Al ratio within ca. 2-5. In addition, Ca-stilbite, which has Si/Al ratio of 3.5, is weakly oversaturated (low SI of 0.03-1.02) for samples excluding W32 and W33. Since Ca-stilbite hasn't

been observed under thin sections, this weak oversaturation is probably due to the unverified thermodynamic data.

For low silica zeolites ( $Si/Al < 1.5$ ), scolecite is slightly undersaturated with saturation index range of -0.59 to -1.43, while natrolite is remarkably undersaturated with saturation index between -5.97 and -7.69. Thomsonite is strongly oversaturated with high saturation index ( $SI = 9.46 \sim 10.82$ ). The undersaturation of natrolite conflicts with the pervasive occurrence of natrolite, but the oversaturation of thomsonite conforms to the existence of thomsonite in nepheline syenite. Thus this feature perhaps indicates sequent formation processes for natrolite and thomsonite, and testifies distinct formation environments. The temperature  $25^{\circ}\text{C}$  used in modeling is not the one at which natrolite formed. Mesolite is only weakly oversaturated ( $SI = 0.03 \sim 0.32$ ) in samples W31, W39, W40 and W43, and is slightly undersaturated ( $SI = -0.01$  to  $-0.31$ ) for other samples.

Sulphate minerals including anhydrite, gypsum, barite and celestite are moderately undersaturated ( $SI$  from -1.06 to -5.19) for all waters. Waters from nepheline syenite catchment are oversaturated with calcite ( $SI = 0.02 \sim 0.24$ ), but waters related with carbonatite are undersaturated with calcite ( $SI = -0.12$  to  $-1.60$ ). This result is consistent with the presence of calcite vein in nepheline syenite and the dissolution of calcite in carbonatite. Aragonite and dolomite is undersaturated in waters from carbonatite catchment, but oversaturated ( $SI = 0.10 \sim 0.67$  and  $1.44 \sim 1.76$ ) in waters from nepheline syenite catchment. All samples excluding W38 are oversaturated with respect to witherite. Strontianite is slightly undersaturated (W39, W40, W42, W45) and oversaturated (W31, W43 and W44).

Halite and fluorite are remarkably undersaturated in all water samples. Gibbsite and diaspore are both oversaturated for waters related with carbonatite. For waters from nepheline syenite catchment, Gibbsite is undersaturated in all samples, but diaspore is weakly oversaturated in 5 samples. The observation of diaspore in nepheline syenite coincides with the saturation. The saturation indexes of illite saturation index vary between -1.09 to -3.34 which indicate its undersaturation in all samples. Kaolinite is oversaturated in waters from carbonatite catchment, but undersaturated in waters from nepheline syenite catchment. This opposite distribution of saturation indexes for kaolinite and diaspore probably demonstrates the higher silica concentration in waters from carbonatite and the lower silica in that of nepheline syenite.

Cl-bearing sodalite has the lowest saturation index of -35.89 to -43.98 that coincides with the absence of sodalite in nepheline syenite. Analcite, grossular and celadonite are undersaturated for all samples with saturation index of -2.99 to -3.71, -7.44 to -13.24 and -0.96 to -4.77 respectively. Sample W31, which has the detectable fluorine, is oversaturated with respect to F-biotite and undersaturated to F-muscovite. The stabilization of biotite and the absence of muscovite in nepheline syenite support this calculation result.

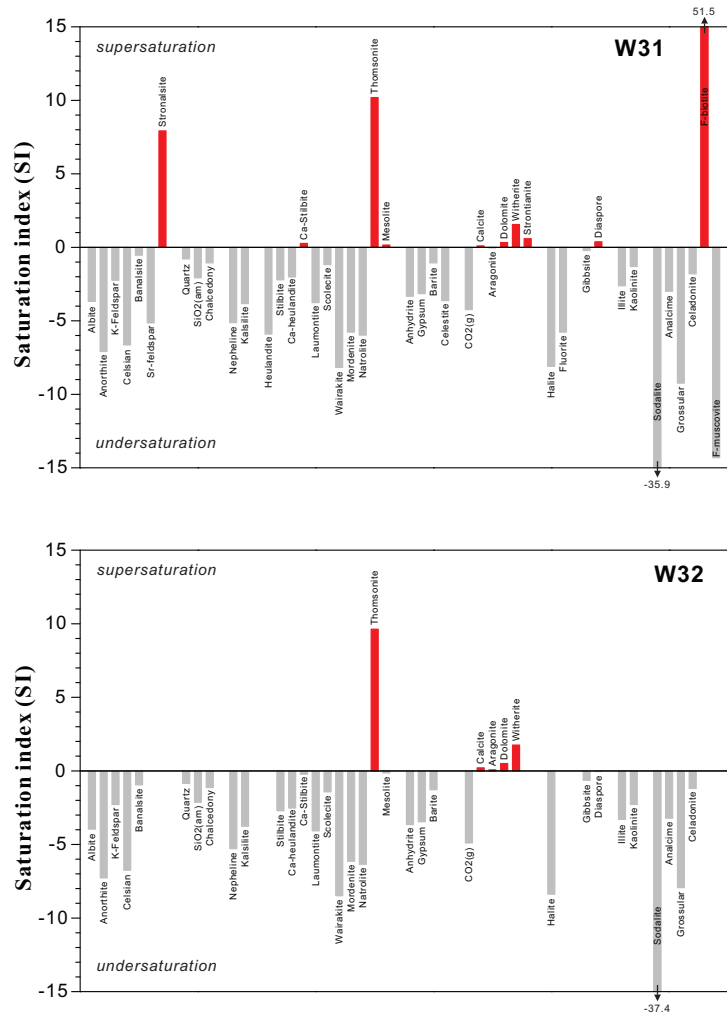


Fig. 5 Saturation index of different samples. See text for detailed explanations.

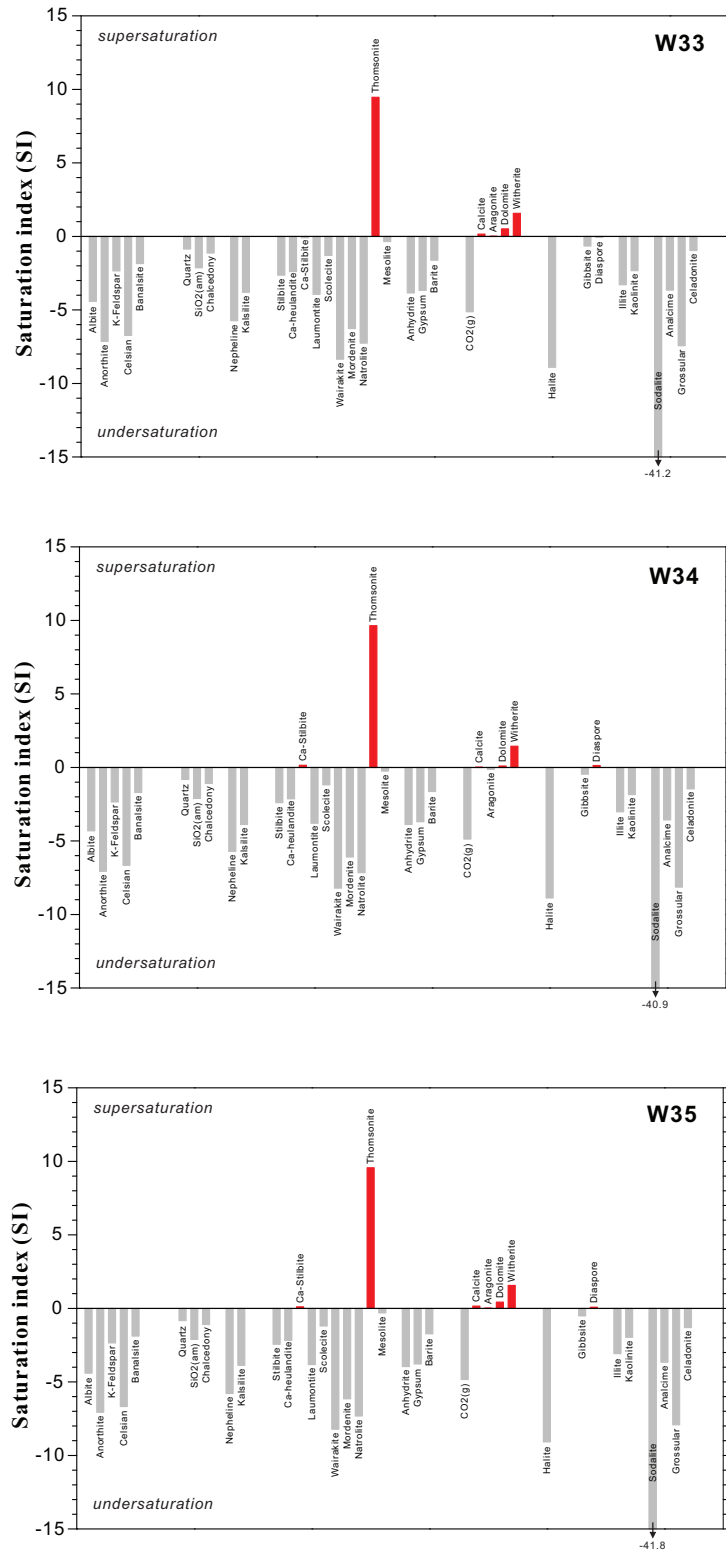


Fig. 5 (continued) Saturation index of different samples.



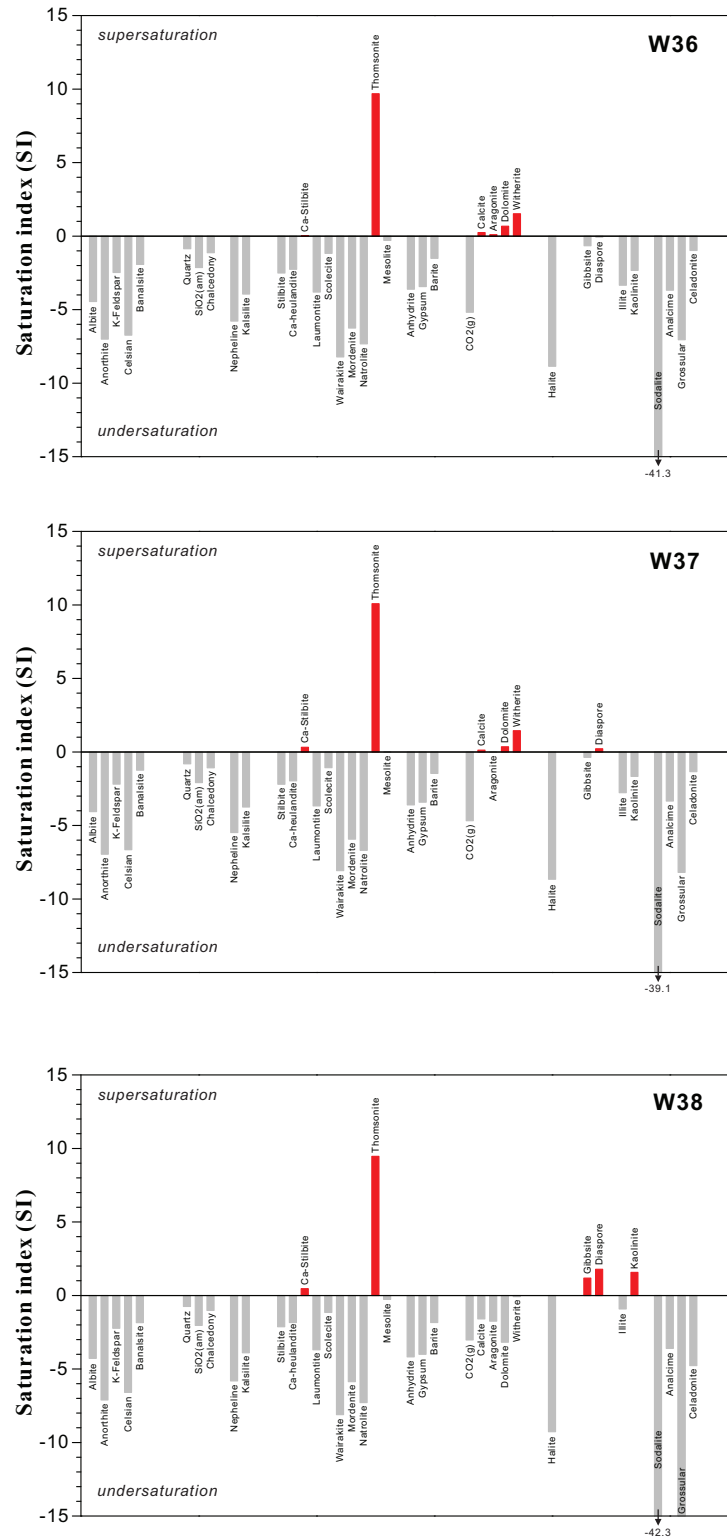


Fig. 5 (continued) Saturation index of different samples.

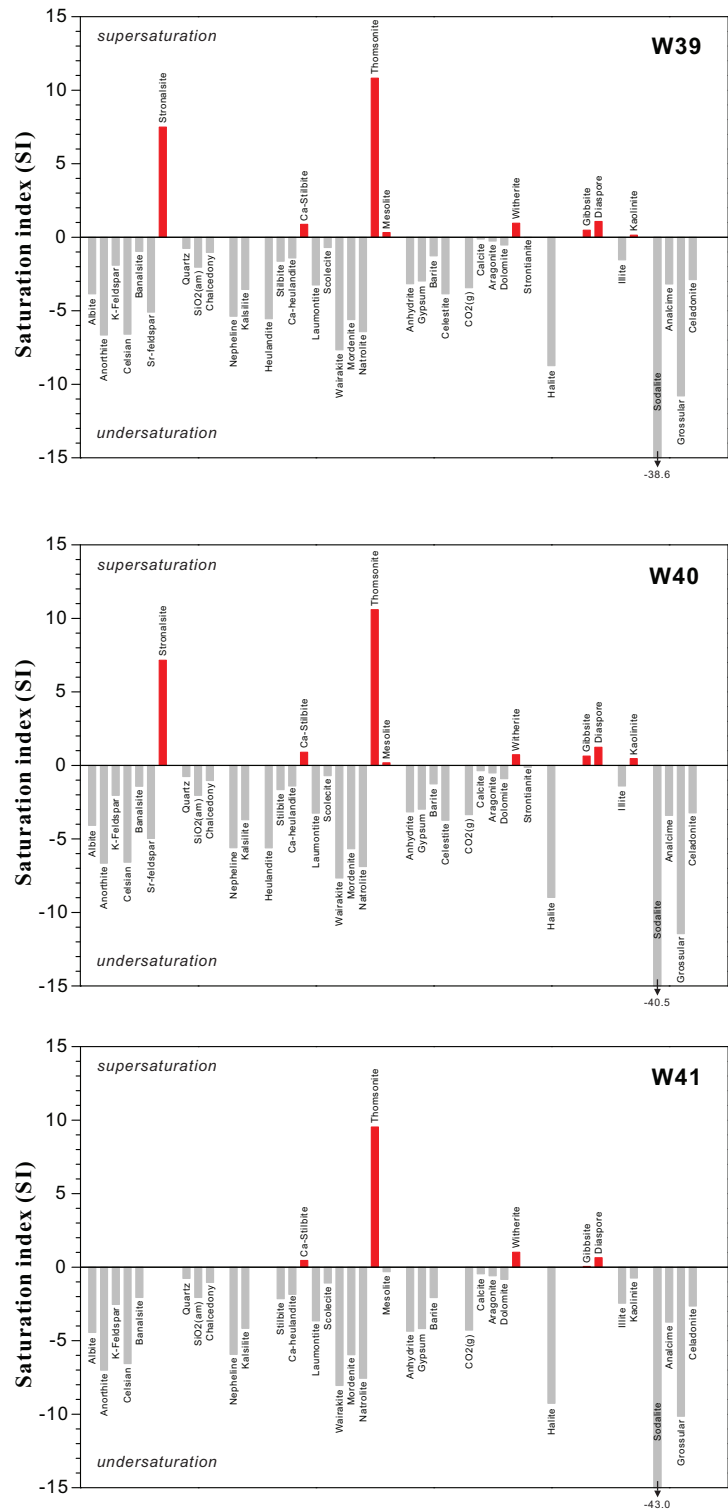


Fig. 5 (continued) Saturation index of different samples.

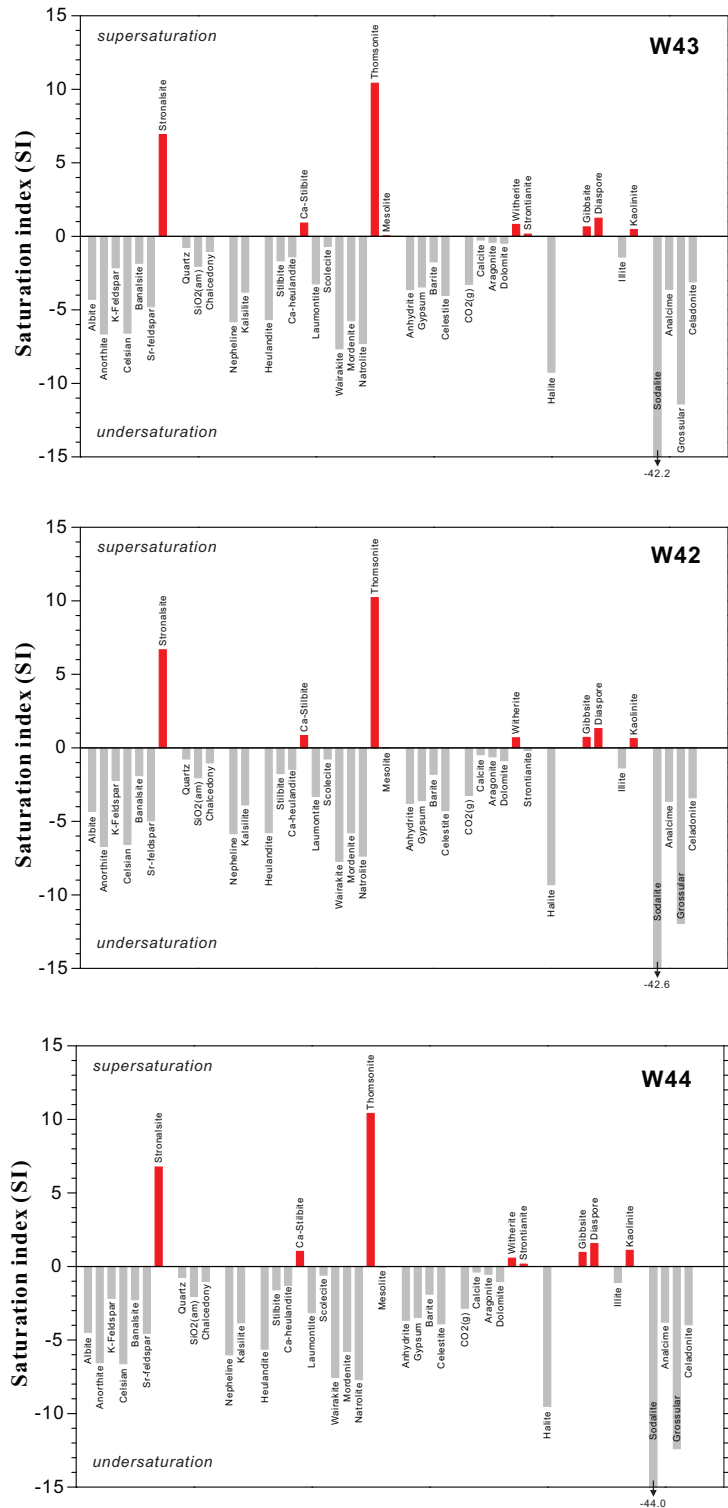


Fig. 5 (continued) Saturation index of different samples.

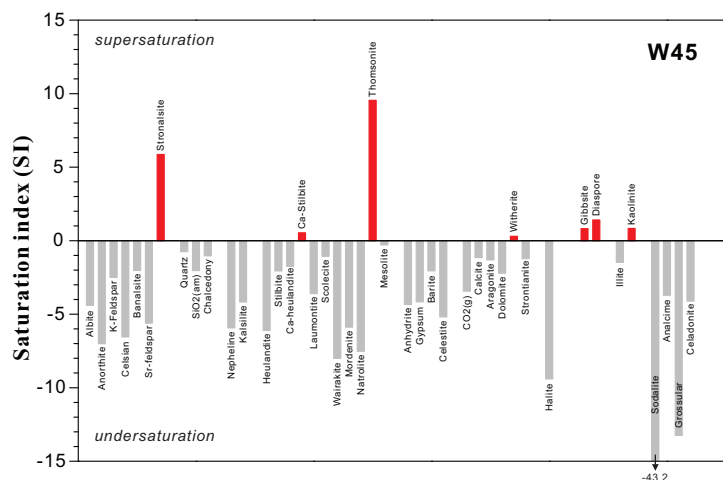


Fig. 5 (continued) Saturation index of different samples.

### 6.3 Mineral stability diagrams

Mineral stability diagrams in the system Ca-Na-Si-Al-O-H have been constructed at 1 bar and 25°C, which is regarded as equilibrium temperature of water. The topology and the field size of the diagrams don't change with pressure, but change remarkably with temperature. Stability fields of natrolite and thomsonite decrease gradually at elevated temperature (Fig. 6 and Fig. 7) and finally disappear at ca.150°C.

As shown in Fig. 6, all the sample points are plotted in the stability field of thomsonite, and very close to the boundary of diaspore stability. This modeled stability field is well consistent with the microscopic observations that thomsonite is present as a major phase coexisting with a very small amount of diaspore. As indicated by the modeled phase diagram as a function of varying activities of  $\text{Na}^+$ ,  $\text{Ca}^{2+}$  and  $\text{SiO}_2$  in the fluid, the texture of thomsonite can be reasonably interpreted as a reaction consequence of nepheline with decreasing activity of  $\text{Na}^+$ , but also probably with increasing activity of  $\text{Ca}^{2+}$ . For the decrease of the activity of  $\text{Na}^+$ , it could be a result of generation of natrolite which largely consumes  $\text{Na}^+$  in the fluid. It is well demonstrated from the occurrence of natrolite and thomsonite at different locations or at the same sites, which indicate that the activities of  $\text{Na}^+$  and  $\text{Ca}^{2+}$  in the fluids are close to the boundary condition between natrolite and thomsonite in the phase diagram (Fig. 6).

### 6.4 Partial pressure of CO<sub>2</sub>

CO<sub>2</sub> partial pressures of all water samples, which have been calculated according to alkalinity and pH data, are shown in Table 4 and Fig. 6. Values of logP<sub>CO2</sub> have a narrow range from -3.07 to -5.10 excluding sample W44 which has -8.93. All the samples are weakly oversaturated or undersaturated with respect to calcite at the field conditions.

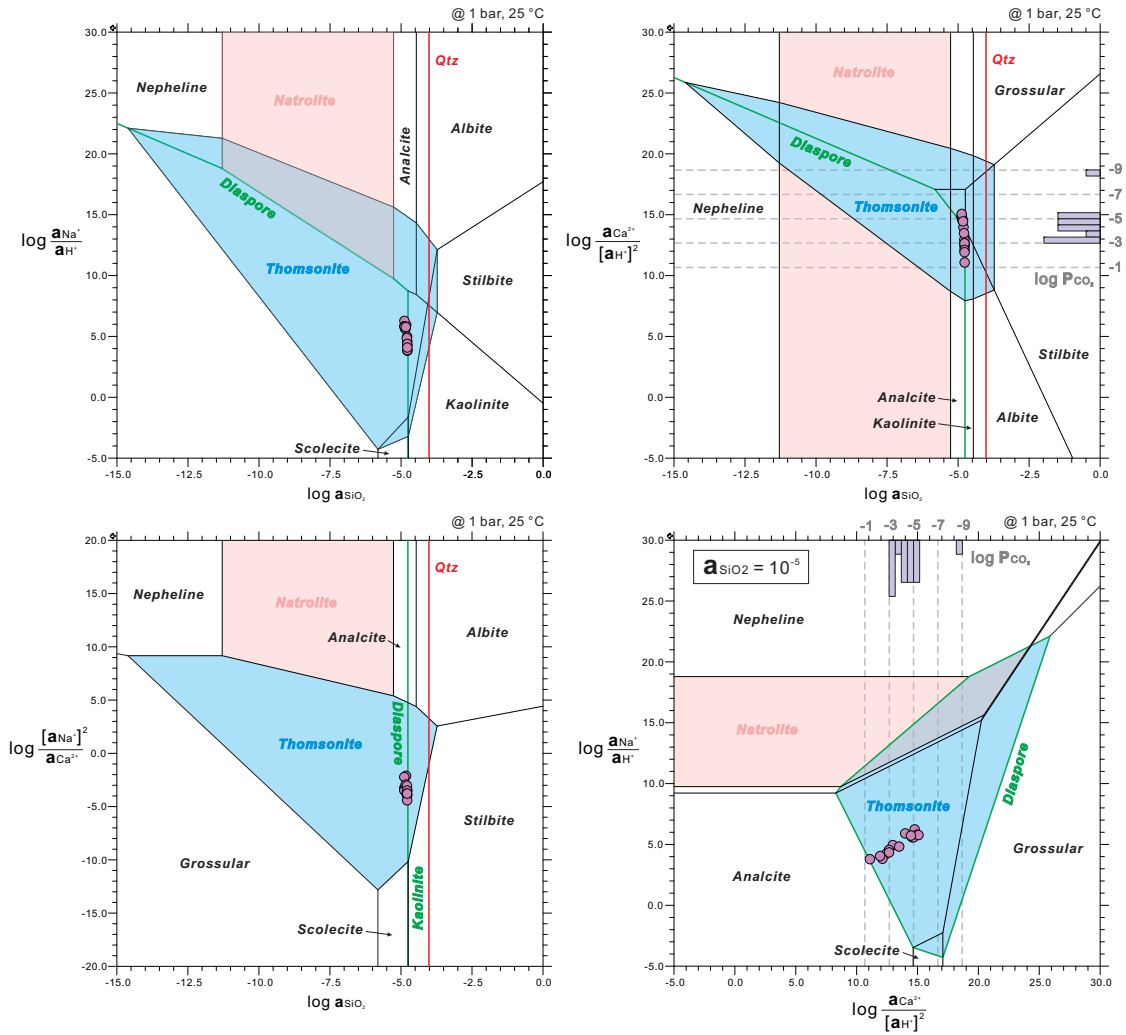


**Fig. 6 Activity-activity diagrams for mineral stability at 1 bar and 25 °C. See text for explanations.**

Corresponding partial pressure of CO<sub>2</sub> based on calcite dissolution reaction, ratios of Ca<sup>2+</sup> concentration and pH are also presented in Fig. 6. Sample points plotted in the activity-activity diagram fall into logP<sub>CO2</sub> range of -1 to -6.

Calcite and thomsonite are stable phases coexisting with each, as observed from the nepheline syenite samples. The relation of their coexisting is also demonstrated by the modeling result that they are corresponding to similar values of  $\log a_{\text{Ca}^{2+}/[\text{a}_{\text{H}^+}]^2}$  (mostly 10~15), which requires low activity of  $\text{CO}_2$  in fluid ( $\log P_{\text{CO}_2}$  range of -1 to -6, Fig. 6). The low activity of  $\text{CO}_2$  in fluid for the stabilization of zeolite has also been revealed by the study of Weisenberger and Bucher (2010).

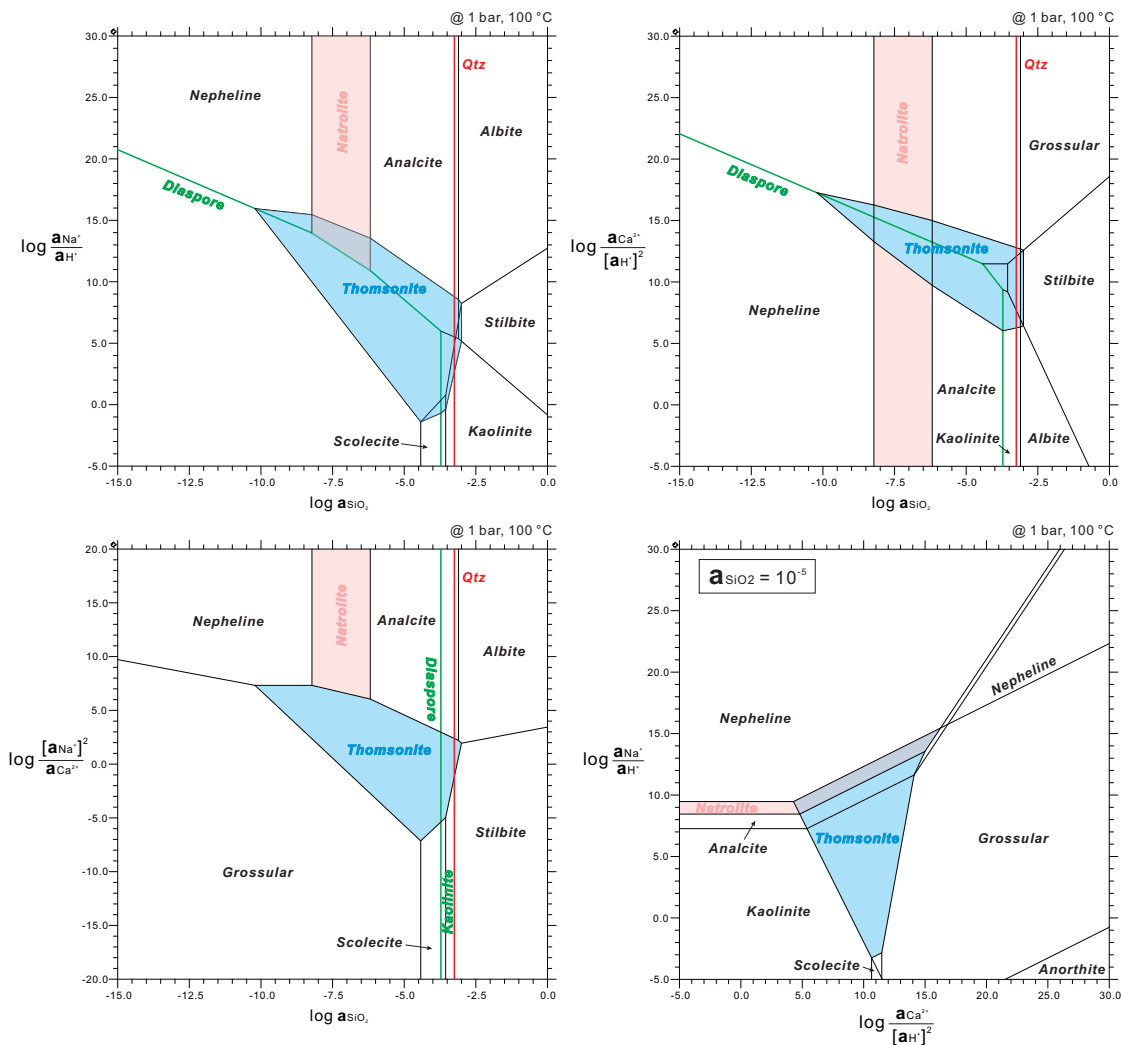


**Fig. 7** Activity-activity diagrams for mineral stability at 1 bar and 100 °C. See text for explanations.

Mineral/Component	Formula	$\Delta H_f$ [KJ/mol]	$\Delta G_f$ [KJ/mol]	Reference	Dissolution reaction	$\Delta H_r$ [KJ/mol]	Log K	Reference
Thomsonite	$Ca_2NaAl_3Si_6O_{20} \cdot 6H_2O$	-12509.689	-11553.866		$Thm + 20H^+ = 2Ca^{2+} + Na^+ + 5SiO_2 + 5Al^{3+} + 16H_2O$	-496.726	37.216	
Natrolite	$Na_2Al_2Si_3O_{10} \cdot 2H_2O$	-5720.7	-5318.7		$Nat + 8H^+ = 2Na^+ + 3SiO_2 + 2Al^{3+} + 6H_2O$	-199.037	18.063	
Sodalite	$Na_8Al_6Si_6O_{22} \cdot Cl_2$	-13457.866	-12703.74	Komada et al., 1995	$Sod + 24H^+ = 8Na^+ + 6SiO_2 + 6Al^{3+} + 12H_2O + 2Cl^-$	-757.128	74.525	
Banalite	$BaNa_2Al_3Si_4O_{16}$	-8237.034	-8072.604		$Ban + 16H^+ = Ba^{2+} + 2Na^+ + 4SiO_2 + 4Al^{3+} + 8H_2O$	-753.299	33.777	
Stronalisite	$SrNa_2Al_3Si_4O_{16}$	-8281.034	-8114.204		$Str + 16H^+ = Sr^{2+} + 2Na^+ + 4SiO_2 + 4Al^{3+} + 8H_2O$	-725.622	27.031	
Celsian	$BaAl_2Si_2O_8$	-4244.3	-4021.87	Chernyshova et al., 1991	$Celsian + 8H^+ = Ba^{2+} + 2SiO_2 + 2Al^{3+} + 4H_2O$	-279.315	22.646	
Sr-feldspar	$SrAl_2Si_2O_8$	-4248.	-4023.75	Chernyshova et al., 1991	$Sr-feldspar + 8H^+ = Sr^{2+} + 2SiO_2 + 2Al^{3+} + 4H_2O$	-291.938	22.857	
Ca-Stilbite	$CaAl_2Si_2O_8 \cdot 7H_2O$	-10889.88	-9997.917	Frey et al., 1991	$Ca-Stib + 8H^+ = Ca^{2+} + 7SiO_2 + 2Al^{3+} + 11H_2O$	-46.763	-4.987	Seelig and Bucher, 2010
Ca-Heulandite	$CaAl_2Si_2O_8 \cdot 6H_2O$	-10565.397	-9747.668	Frey et al., 1991	$Ca-Heu + 8H^+ = Ca^{2+} + 7SiO_2 + 2Al^{3+} + 10H_2O$	-85.416	-2.691	Seelig and Bucher, 2010
H <sup>+</sup>		0	0	Cox et al., 1989				
Si <sup>2+</sup>		-553.9	-563.867	Shock et al., 1997				
Ba <sup>2+</sup>		-537.577	-560.782	Shock et al., 1997				
Mg <sup>2+</sup>		-467.	-455.4	Cox et al., 1989				
Ca <sup>2+</sup>		-543.	-552.8	Cox et al., 1989				
Na <sup>+</sup>		-240.34	-261.953	Cox et al., 1989				
K <sup>+</sup>		-252.14	-282.51	Cox et al., 1989				
Al <sup>3+</sup>		-540.	-487.65	Seelig and Bucher, 2010				
Cl <sup>-</sup>		-167.08	-131.228	Cox et al., 1989				
SiO <sub>2</sub> aq		-881.359	-833.258	Berman, 1988				
H <sub>2</sub> O		-285.83	-237.14	Cox et al., 1989				

**Table 2 Thermodynamic data used to calculate  $\Delta H_r$  and logK for the minerals additionally inserted into the Inl.dat database.**

Samples	Phase	W31		W32		W33		W34		W35		W36		W37		W38		W39		W40		W41		W42		W43		W44		W45																																																																																																																																																															
		SI	SI	SI	SI	SI	SI	SI	SI	SI	SI	SI	SI	SI	SI	SI	SI	SI	SI	SI	SI	SI	SI	SI	SI	SI	SI	SI	SI	SI	SI	SI																																																																																																																																																													
Feldspar group	Albite	-3.68	-3.96	-4.42	-4.31	-4.41	-4.45	-4.06	-4.28	-3.85	-4.08	-4.44	-4.32	-4.28	-4.48	-4.48	-4.40	Silica minerals	Quartz	-0.79	-0.85	-0.86	-0.82	-0.83	-0.86	-0.81	-0.75	-0.76	-0.77	-0.77	-0.76	-0.76	-0.76	-0.75	-0.75	Nepheline group	Nepheline	-5.13	-5.29	-5.74	-5.71	-5.79	-5.78	-5.48	-5.81	-5.37	-5.60	-5.93	-5.84	-5.81	-6.01	-5.93	Zeolite group	Heulandite	-5.91	-2.21	-2.71	-2.64	-2.40	-2.44	-2.20	-2.13	-1.63	-1.65	-2.15	-1.75	-1.67	-1.59	-2.06	Other minerals	Strombolite	-5.14	-5.09	-4.97	-4.92	-5.09	-4.97	-4.99	-4.89	-4.89	-4.89	-4.89	-4.89	-4.89	-4.89	-4.89	-4.89	Sulphates	Anhydrite	-3.33	-3.65	-3.85	-3.88	-3.96	-3.61	-3.60	-4.18	-3.16	-3.16	-4.36	-3.77	-3.63	-3.65	-4.34	Carbonates	Calcite	0.10	0.21	0.16	0.02	0.16	0.24	0.12	-0.16	0.12	-0.36	-0.45	-0.47	-0.25	-0.38	-1.16	Halides	Halite	-8.10	-8.38	-8.90	-8.88	-9.08	-8.85	-8.66	-9.27	-8.73	-8.98	-9.26	-9.31	-9.24	-9.51	-9.40	Hydroxides	Gibbsite	-0.22	-0.64	-0.66	-0.46	-0.51	-0.66	-0.37	1.18	0.48	0.63	0.05	0.71	0.64	0.95	0.82	Clay minerals	Illite	-2.62	-3.30	-3.29	-3.02	-3.08	-3.34	-2.77	-0.92	-1.54	-1.40	-2.45	-1.37	-1.41	-1.09	-1.48	Fluoride	Fluorite	-5.77	-5.77	-5.77	-5.77	-5.77	-5.77	-5.77	-5.77	-5.77	-5.77	-5.77	-5.77	-5.77	-5.77	-5.77

Table 3 Saturation state of waters from nepheline syenite - carbonatite catchment.

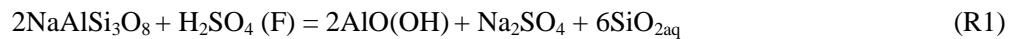


## 6.5 Strontium and barium

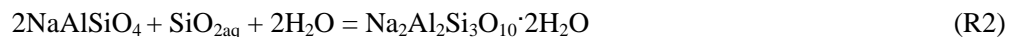
Stronalsite, banalsite and Sr-rich thomsonite are observed in the nepheline syenite, which suggest considerable abundance of Sr and Ba in the fluids. However, the strontium concentration in the fluid is relatively low ranging between 0.33 and 1.21 mg/L, and the Ba concentration is lower than detection limit, which infers that relatively low concentrations of Sr and Ba are capable to precipitate Sr-Ba tectosilicates from high-alkalinity fluids. The transition from nepheline to stronalsite in a fluid environment has been described by Liferovich et al. (2006), consuming Sr and Ba cations in fluids. It is similar the case in this study, in which Sr and Ba cations in fluids might have been derived by dissolution of Sr and Ba-rich primary minerals, such as nepheline, albite and calcite.

## 6.6 Reactions controlling the water component

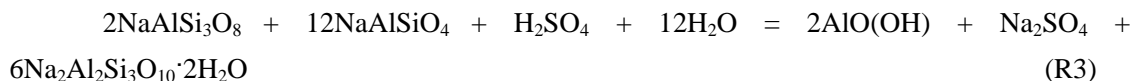
Albite dissolution have been observed in nepheline syenite (Fig. 2b), the corresponding reaction could be described by the following reaction:



The reaction consumes  $\text{H}_2\text{SO}_4$  component from fluid and release silica and thenardite component to the fluid. Simultaneously, diaspre precipitated in the in situ locality or other place. The released  $\text{SiO}_2$  will increase the silica activity of the fluid, which thus destabilized nepheline by reactions like these:



The above nepheline dissolution reaction is accompanied by precipitation of natrolite (R2). The process consumes the silica derived from R1. The combined reaction is:

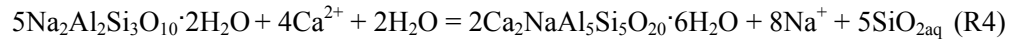


This could explain the co-occurrence of natrolite and diaspre which replace nepheline (Fig. 2d). The reaction would increase the Na activity of the fluid. This arbitrary reaction also would maintain constant silica activity, only if all the silica released by R1 is totally consumed by R2, which however can hardly be fulfilled in a real case.

Therefore, combing the reactions R1 and R2 and phase diagram in Fig. 6, silica and  $\text{Na}^+$  activities of fluid increase together as a result of R1, which further promote the stabilization of

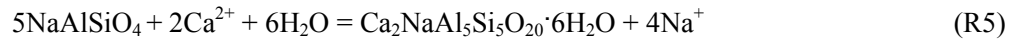
natrolite through the reaction R2. As a result of reaction R2 and precipitation of natrolite, silica activity would be compensated partly but still tends to increase. Thus the initial fluid of nepheline syenite catchment would have a  $\text{Na}_2\text{SO}_4$  -rich signature which is partly represented by water type E of sample W31 and W32 (Fig. 3c).

Large amount of Ca- $\text{HCO}_3$  fluid (Type A) from carbonatite catchment probably have infiltrated into nepheline syenite along faults or fractures and mixed with the initial fluid of nepheline syenite. The mixed fluid would increase Ca activity and decrease  $\log_{[a_{\text{Na}^+}]^2/a_{\text{Ca}^{2+}}}$  at constant  $\text{SiO}_2$  activity. As shown in Fig. 6c, fluid will cross the natrolite field and enter the thomsonite stability field. Thomsonite which overgrowth on natrolite (Fig. 2f) and co-precipitated with calcite (Fig. 2a and Fig. 2e) could be explained by this mixed fluid. The corresponding reaction is:



The reaction R4 would consume the  $\text{Ca}^{2+}$  and release  $\text{Na}^+$  with the precipitation of thomsonite. But the ratio of  $\log_{a_{\text{Na}^+}/[a_{\text{H}^+}]}$  and  $\log_{a_{\text{Ca}^{2+}}/[a_{\text{H}^+}]^2}$  in the fluid is gradually close to 0.5, which is obviously indicated by sample points plotted in Fig. 6d that forms a trend parallel to the wedge-like natrolite-thomsonite stability overprint field.

The direct alteration of nepheline to thomsonite (Fig. 2e) could be described by reaction:



The transportation of Ca- $\text{HCO}_3$  fluid along fractures in nepheline syenite will precipitate thomsonite on the fracture wall when contact with nepheline or natrolite (Fig. 2e), and precipitate calcite in the middle of fluid conduit through reaction:



The formation of calcite together with thomsonite indicates a relative low  $\text{CO}_2$  partial pressure (Fig. 6). The precipitation of calcite in this case emphasizes the importance of local disequilibrium in the water-rock system.

## 7. Conclusions

Based on the investigation of the water chemistry from alkaline rock in the Seiland igneous province of northern Norway, combined with the microscopic observation of secondary minerals in the rock samples and thermodynamic modeling for water and mineral assemblages,

several conclusions concerning the evolution of water chemistry can be drawn below:

- (1) Fluids from nepheline syenite are mostly dominated by  $\text{NaSO}_4$  component, while fluids from carbonatite catchment  $\text{Ca-HCO}_3$ . The variation among all fluids is resulted from mixing vector of  $\text{NaSO}_4$ -  $\text{Ca-HCO}_3$  to different extents.
- (2) Albite dissolution provide the high  $\text{NaSO}_4$  signature of the fluid in nepheline syenite, the released  $\text{SiO}_2$  simultaneously promote the precipitation of natrolite.
- (3) Infiltration of  $\text{Ca-HCO}_3$  fluid from carbonatite into the nepheline syenite along fractures has resulted in the generation of thomsonite by transformation from nepheline and natrolite, and precipitation of calcite in the middle of fluid conduit, which both indicate local disequilibrium between water and host rock.
- (4) Thomsonite tends to be stabilized at low  $\text{CO}_2$  partial pressure.

## References

- Appleyard, E.C., 1974. Syn-orogenic igneous alkaline rocks of eastern Ontario and northern Norway. *Lithos*, 7(3): 147-169.
- Appleyard, E.C., 1980. Mass balance computations in metasomatism: Metagabbro/nepheline syenite pegmatite interaction in northern Norway. *Contributions to Mineralogy and Petrology*, 73(2): 131-144.
- Berman, R., 1988. Internally-consistent thermodynamic data for minerals in the system  $\text{Na}_2\text{O-K}_2\text{O-CaO-MgO-FeO-Fe}_2\text{O}_3\text{-Al}_2\text{O}_3\text{-SiO}_2\text{-TiO}_2\text{-H}_2\text{O-CO}_2$ . *Journal of Petrology*, 29(2): 445.
- Bucher, K. and Stober, I., 2010. Fluids in the upper continental crust. *Geofluids*, 10(1-2): 241-253.
- Bucher, K., Stober, I. and Seelig, U., 2012. Water deep inside the mountains: Unique water samples from the Gotthard rail base tunnel, Switzerland. *Chemical Geology*, 334(0): 240-253.
- Bucher, K., Zhang, L. and Stober, I., 2009. A hot spring in granite of the Western Tianshan, China. *Applied Geochemistry*, 24(3): 402-410.
- Can, I., 2002. A new improved Na/K geothermometer by artificial neural networks. *Geothermics*, 31(6): 751-760.
- Chernyshova, I.V. et al., 1991. Thermodynamic properties of strontium and barium feldspars. *Thermochimica Acta*, 175(2): 119-127.
- Daly, J.S., Aitchison, S.J., Cliff, R.A., Gayer, R.A. and Rice, A.H.N., 1991. Geochronological Evidence from Discordant Plutons for a Late Proterozoic Orogen in the Caledonides of Finnmark, Northern Norway. *Journal of the Geological Society*, 148: 29-40.
- Deer, W.A., Howie, R.A., Zussman, J. and Wise, W.S., 2004. *Framework Silicates: Silica Minerals, Feldspathoids and the Zeolites*. Geological Society.
- Fournier, R. and Potter, R., 1982. Revised and expanded silica (quartz) geothermometer. *Bull., Geotherm. Resour. Counc.(Davis, Calif.);(United States)*, 11(10).
- Fournier, R.O., 1977. Chemical geothermometers and mixing models for geothermal systems. *Geothermics*, 5(1-4): 41-50.
- Fournier, R.O. and Truesdell, A.H., 1973. An empirical Na-K-Ca geothermometer for natural waters. *Geochimica et Cosmochimica Acta*, 37(5): 1255-1275.
- Frey, M., Capitani, C.D. and Liou, J.G., 1991. A new petrogenetic grid for low-grade metabasites. *Journal of Metamorphic Geology*, 9(4): 497-509.

- Gee, D., 1975. A tectonic model for the central part of the Scandinavian Caledonides. *American Journal of Science*, 275: 468–515.
- Geis, H.P., 1979. Nepheline syenite on Stjernøy, Northern Norway. *Economic Geology*, 74(5): 1286-1295.
- Giggenbach, W.F., 1981. Geothermal mineral equilibria. *Geochimica et Cosmochimica Acta*, 45(3): 393-410.
- Heier, K., 1961. Layered gabbro, hornblendite, carbonatite and nepheline syenite on Stjernøy, North Norway. *Norsk Geologisk Tidsskrift*, 41: 109-155.
- Heier, K., 1964. Geochemistry of the nepheline syenite on Stjernøy, North Norway. *Norsk Geologisk Tidsskrift*, 44: 205-216.
- Heier, K. and Taylor, S., 1962. A note on the U, Th and K contents in the nepheline syenite on Stjernøy, north Noeway. *Norsk Geologisk Tidsskrift*, 42: 287-292.
- Heier, K.S., 1966. Some Crystallo-chemical Relations of Nephelines and Feldspars on Stjernøy, North Norway. *J. Petrology*, 7(1): 95-113.
- Helgeson, H.C., Kirkham, D.H. and Flowers, G.C., 1981. Theoretical prediction of the thermodynamic behavior of aqueous electrolytes by high pressures and temperatures; IV, Calculation of activity coefficients, osmotic coefficients, and apparent molal and standard and relative partial molal properties to 600 degrees C and 5kb. *American Journal of Science*, 281(10): 1249-1516.
- Holdridge, D., 1962. A clay mineral from Stjernøy, Norway. *Clay Minerals*, 5(27): 26-30.
- Holland, T.J.B. and Powell, R., 2011. An improved and extended internally consistent thermodynamic dataset for phases of petrological interest, involving a new equation of state for solids. *Journal of Metamorphic Geology*, 29(3): 333-383.
- Johnson, J.W., Oelkers, E.H. and Helgeson, H.C., 1992. SUPCRT92: A software package for calculating the standard molal thermodynamic properties of minerals, gases, aqueous species, and reactions from 1 to 5000 bar and 0 to 1000°C. *Computers & Geosciences*, 18(7): 899-947.
- Karingithi, C.W., 2009. Chemical geothermometers for geothermal exploration. Short Course IV on Exploration for Geothermal Resources, UNU-GTP.
- Kirkland, C.L., Daly, J.S., Eide, E.A. and Whitehouse, M.J., 2006. The structure and timing of lateral escape during the Scandian Orogeny: A combined strain and geochronological investigation in Finnmark, Arctic Norwegian Caledonides. *Tectonophysics*, 425(1-4): 159-189.
- Kirkland, Christopher L., Stephen Daly, J. and Whitehouse, Martin J., 2007. Provenance and Terrane Evolution of the Kalak Nappe Complex, Norwegian Caledonides: Implications for Neoproterozoic Paleogeography and Tectonics. *The Journal of Geology*, 115(1): 21-41.
- Kjøsnes, K., 1980. Fertilization of layered mafic rocks in the Lillebukt alkaline complex, Stjernøy, Norway. *Lithos*, 13(2): 215-215.
- Komada, N. et al., 1995. Thermodynamic properties of sodalite at temperatures from 15 K to 1000 K. *The Journal of Chemical Thermodynamics*, 27(10): 1119-1132.
- Kousehlar, M., Weisenberger, T.B., Tutti, F. and Mirnejad, H., 2012. Fluid control on low-temperature mineral formation in volcanic rocks of Kahrizak, Iran. *Geofluids*: no-no.
- Krogh, E. and Elvevold, S., 1990. A Precambrian age for an early gabbro-monzonitic intrusive on the ksfjord peninsula, Seiland Igneous Province, northern Norway. *Norsk Geologisk Tidsskrift*, 70(4): 267-273.
- Lieberman, J. and Petrakakis, K., 1991. TWEEQU thermobarometry; analysis of uncertainties and applications to granulites from western Alaska and Austria. *The Canadian Mineralogist*, 29(4): 857-887.
- Liferovich, R.P., Mitchell, R.H., Zozulya, D.R. and Shpachenko, A.K., 2006. Paragenesis and composition of Banasite, Stronalsite, and their solid solution in nepheline syenite and ultramafic alkaline rocks. *Can Mineral*, 44(4): 929-942.
- Marks, M. and Markl, G., 2001. Fractionation and Assimilation Processes in the Alkaline Augite Syenite Unit of the Ilimaussaq Intrusion, South Greenland, as Deduced from Phase Equilibria. *J. Petrology*, 42(10): 1947-1969.
- Marks, M., Neukirchen, F., Vennemann, T. and Markl, G., 2009. Textural, chemical, and isotopic effects of late-magmatic carbonatitic fluids in the carbonatite-syenite Tamazeght complex, High Atlas Mountains, Morocco. *Mineralogy and Petrology*, 97(1): 23-42.
- Marks, M., Vennemann, T., Siebel, W. and Markl, G., 2003. Quantification of Magmatic and Hydrothermal Processes in a Peralkaline Syenite-Alkali Granite Complex Based on Textures, Phase Equilibria, and Stable and Radiogenic Isotopes. *Journal of Petrology*, 44(7): 1247-1280.

- Marks, M.A.W. et al., 2012. The volatile inventory (F, Cl, Br, S, C) of magmatic apatite: An integrated analytical approach. *Chemical Geology*, 291(0): 241-255.
- Natalie, J., 2010. Der karbonatit auf Stjernøy. Bachelor Thesis, University of Freiburg, Freiburg, 57 pp.
- Nordstrom, D.K., Ball, J.W., Donahoe, R.J. and Whittemore, D., 1989. Groundwater chemistry and water-rock interactions at Stripa. *Geochimica et Cosmochimica Acta*, 53(8): 1727-1740.
- Oosterom, M., 1963. The ultramafites and layered gabbro sequences in the granulite facies rocks on Stjernøy (Finnmark, Norway). *Leidse Geol Mededelingen*, 28: 177-296.
- Parkhurst, D.L. and Appelo, C., 1999. User's guide to PHREEQC (Version 2): A computer program for speciation, batch-reaction, one-dimensional transport, and inverse geochemical calculations.
- Pedersen, R., Dunning, G. and Robins, B., 1989. U-Pb ages of nepheline syenite pegmatites from the Seiland Magmatic Province, N. Norway. *The Caledonide Geology of Scandinavia*: 3-8.
- Powell, M., 1978. The crystallisation history of the Igdlarfjgssalik nepheline syenite intrusion, Greenland. *Lithos*, 11(2): 99-120.
- Roberts, D., 2003. The Scandinavian Caledonides: event chronology, palaeogeographic settings and likely modern analogues. *Tectonophysics*, 365(1-4): 283-299.
- Roberts, R.J., Corfu, F., Torsvik, T.H., Ashwal, L.D. and Ramsay, D.M., 2006. Short-lived mafic magmatism at 560-570 Ma in the northern Norwegian Caledonides: U-Pb zircon ages from the Seiland Igneous Province. *Geological Magazine*, 143(6): 887-903.
- Roberts, R.J., Corfu, F., Torsvik, T.H., Hetherington, C.J. and Ashwal, L.D., 2010. Age of alkaline rocks in the Seiland Igneous Province, Northern Norway. *Journal of the Geological Society*, 167(1): 71-81.
- Robins, B., 1984. Petrography and petrogenesis of nephelized metagabbros from Finnmark, Northern Norway. *Contributions to Mineralogy and Petrology*, 86(2): 170-177.
- Robins, B. and Gardner, P.M., 1975. The magmatic evolution of the Seiland province, and Caledonian plate boundaries in northern Norway. *Earth and Planetary Science Letters*, 26(2): 167-178.
- Robins, B. and Tysseland, M., 1980. Fenitization of mafic cumulates by the Pollen carbonatite, Finnmark, Norway. *Lithos*, 13(2): 220-220.
- Robins, B. and Tysseland, M., 1983. The geology, geochemistry and origin of ultrabasic fenites associated with the Pollen Carbonatite (Finnmark, Norway). *Chemical Geology*, 40(1-2): 65-95.
- Salter, D.L. and Appleyard, E.C., 1974. An occurrence of vein palygorskite from the nepheline syenite of Lillebukt, Stjernøy, northern Norway. *Norsk Geologisk Tidsskrift*, 54: 329-336.
- Schilling, J., Marks, M.A.W., Wenzel, T. and Markl, G., 2009. Reconstruction of magmatic to subsolidus processes in an apatitic system using eudialyte textures and composition: A case study from tamazeght, morocco. *Can Mineral*, 47(2): 351-365.
- Schilling, J. et al., 2011. The Magmatic to Hydrothermal Evolution of the Intrusive Mont Saint-Hilaire Complex: Insights into the Late-stage Evolution of Peralkaline Rocks. *Journal of Petrology*, 52(11): 2147-2185.
- Seelig, U. and Bucher, K., 2010. Halogens in water from the crystalline basement of the Gotthard rail base tunnel (central Alps). *Geochimica et Cosmochimica Acta*, 74(9): 2581-2595.
- Stober, I. and Bucher, K., 2005. The upper continental crust, an aquifer and its fluid: hydraulic and chemical data from 4&nbsp;km depth in fractured crystalline basement rocks at the KTB test site. *Geofluids*, 5(1): 8-19.
- Strand, T., 1980. The chemistry of the Lillebukt carbonatite, Stjernøy, Norway. *Lithos*, 13(2): 223-223.
- Sturt, B.A., Miller, J.A. and Fitch, F.J., 1967. The age of alkaline rocks from West Finnmark, northern Norway, and their bearing on the datings of the Caledonian orogeny. *Norsk Geologisk Tidsskrift*, 47: 255-273.
- Sturt, B.A., Pringle, I.R. and Ramsay, D.M., 1978. The Finnmarkian phase of the Caledonian Orogeny. *Journal of the Geological Society*, 135(6): 597-610.
- Weisenberger, T. and Bucher, K., 2010. Zeolites in fissures of granites and gneisses of the Central Alps. *Journal of Metamorphic Geology*, 28(8): 825-847.
- Weisenberger, T. and Bucher, K., 2011. Mass transfer and porosity evolution during low temperature water-rock interaction in gneisses of the simano nappe: Arvigo, Val Calanca, Swiss Alps. *Contributions to Mineralogy and Petrology*, 162(1): 61-81.
- Weisenberger, T. and Selbekk, R., 2009. Multi-stage zeolite facies mineralization in the Hvalfjörður area, Iceland. *International Journal of Earth Sciences*, 98(5): 985-999.
- Zhu, C. and Sverjensky, D.A., 1991. Partitioning of F-Cl-OH between minerals and hydrothermal fluids. *Geochimica Et Cosmochimica Acta*, 55(7): 1837-1858.

Zhu, C. and Sverjensky, D.A., 1992. F-Cl-OH partitioning between biotite and apatite. *Geochimica Et Cosmochimica Acta*, 56(9): 3435-3467.

**Part V Multiple metamorphism in the contact aureole of the Reinfjord ultramafic complex, Seiland Igneous Province, Northern Norway**

## 1. Abstract

The Reinford ultramafic complex is one of the largest layered peridotite and gabbro plutons in the Seiland Igneous Province. The ultramafic rocks have been emplaced in the lower part of the Sørøy Succession of Kalak nappe complex and developed a distinct contact aureole in the gneissic country rocks. Three main stages in a chronological order could be summarized from the P-T conditions and mineral stability fields: (1) contact metamorphism at 850-900°C and 7.5-9.5 kbar; (2) uplift cooling with pressure decrease by ~3 kbar and temperature decrease by ~100°C (ends at 800°C and 6.5 kbar); (3) thrust cooling until 650°C and 10kbar. The first high temperature contact metamorphism was resulted from the Proterozoic emplacement of volumes of ultramafic rocks. The following uplift cooling corresponded to the initial rifting and extension. Sequential thrust cooling was accompanied with Caledonian crustal thickening and compression.

## 2. Introduction

The Norwegian Caledonian orogenic belt is characterized by a series of thrust sheets that are grouped into the Uppermost Allochthon representing exotic Laurentian terranes, the Upper Allochthon representing the Iapetus oceanic lithosphere, and the Lower and Middle Allochthon representing the margin of Pre-Caledonian Baltica (Andresen, 1988; Ritzmann and Faleide, 2007; Roberts and Gee, 1985; Stephens and Gee, 1985), all of which thrust eastwards onto the Precambrian crystalline basement of the Baltic shield during the Silurian continental collision (ca. 431-428 Ma at Finnmark, Kirkland et al., 2006a; Kirkland et al., 2007) between Baltica and Laurentia following the early Palaeozoic closure of the Iapetus Ocean (Gee, 1975; Roberts, 2003).

The development of Norwegian Caledonian orogenic belt involves a series of sequential events: the formation of Iapetus ocean crust with associated initial rifting, the production of ophiolite, the subsequent consumption of ocean crust along a destructive plate margin, and a continent-continent collision with stacking of crusts, crustal thickening and lateral nappe displacements (e.g. Andersen et al., 1991; Bucher-Nurminen, 1991; Gee et al., 2012; Osmundsen and Andersen, 1994). The present knowledge of the metamorphism related to the above events is mostly based on the detailed investigation on eclogites (e.g. Markl and Bucher, 1997). However, metamorphism and metamorphic rocks related to the widespread rift-related magmatic products have been nearly neglected considering their geological importance, except for a few studies (e.g. Drüppel et al., 2013)

In this study, we present the multiple metamorphic events recorded by country rocks from



contact aureole of the Reinfjord ultramafic complex, Seiland Igneous Province, Northern Norway.

### 3. Geological background

The Seiland Igneous Province (SIP) now resides within and as a part of the highest nappe of the Kalak Nappe Complex (KNC) which belongs to the Middle Allochthon, occupying an area of nearly 5,000 km<sup>2</sup> on the islands of Seiland, Sørøy and Stjernøy, and on the Øksfjord Peninsula in the northern Finnmark, Norway (Fig. 1).

The Seiland igneous province has a long and complex history concerning magmatic evolution: voluminous ultramafic rocks at 829±18 Ma (Krogh and Elvevold, 1990), layered gabbroic plutons of 700±33 Ma, 604±44 Ma and 570 Ma (Daly et al., 1991; Roberts et al., 2006) and a final stage of calc-alkaline intrusions represented by alkaline pyroxenite, syenite, nepheline syenite and carbonatite at 574± 5 Ma (Roberts et al., 2010). All these various rocks are considered to represent a synorogenic (Caledonian orogenic belt) intrusive activity evolved from tholeiitic basalt, compositionally ranging from high-K calc-alkaline magmas, through alkaline olivine basalt and picrite and finally to highly differentiated alkaline magmas and carbonatite (Appleyard, 1974; Robins and Gardner, 1975; Sturt et al., 1967; Sturt et al., 1978).

The metasedimentary succession of the KNC which hosts the SIP deposited between ca. 840 and 910 Ma (long time prior to the opening of Iapetus Ocean) (Kirkland et al., 2007), and represents an exotic allochthonous mobile belt that was juxtaposed and sutured to Baltica at ca. 710 Ma (Fall et al., 2007; Kirkland et al., 2008a; Kirkland et al., 2006b; Kirkland et al., 2008b; Roberts et al., 2007). Based on U–Pb zircon dating of discordant plutonic rocks within the nappe, several tectonothermal events have been identified in the KNC (Akselsen, 1982; Daly et al., 1991; Kirkland et al., 2006a; Kirkland et al., 2006b; Kirkland et al., 2005; Kirkland et al., 2007; Sturt et al., 1978). However, the corresponding metamorphic events have not been widely investigated in this area. The present researches (Elvevold and Reginiussen, 1996; Elvevold et al., 1994) were performed on metapelitic xenolith in metagabbro of 929 ±18 Ma, for which three metamorphic stages could be identified: (1) Contact metamorphism: 930-960 °C / 5-6.5 kb; (2) Cooling: 700-750 °C / 5-7 kb; (3) Compression: 650-700 °C / 8-10 kb.

The Reinfjord ultramafic complex is one of the largest layered peridotite and gabbro plutons in the Seiland Igneous Province (Fig. 1). The Reinfjord ultramafic rocks have been emplaced near the margin of pyroxene gabbro (Fig. 2a) during an early phase of the Caledonian orogeny. The complex is cylindrically zoned and consists of a dunite core and a series of layered wehrlite (Fig. 2a-b). Pressure of 6-8 kbar (20-30 km depth) and the solidus temperature of

1300°C were estimated (Bennett, 1974). The gneissic country rocks belong to the lower part of the Sørøy Succession of Kalak nappe complex and developed a distinct contact aureole with melting phenomena (Bennett, 1974).

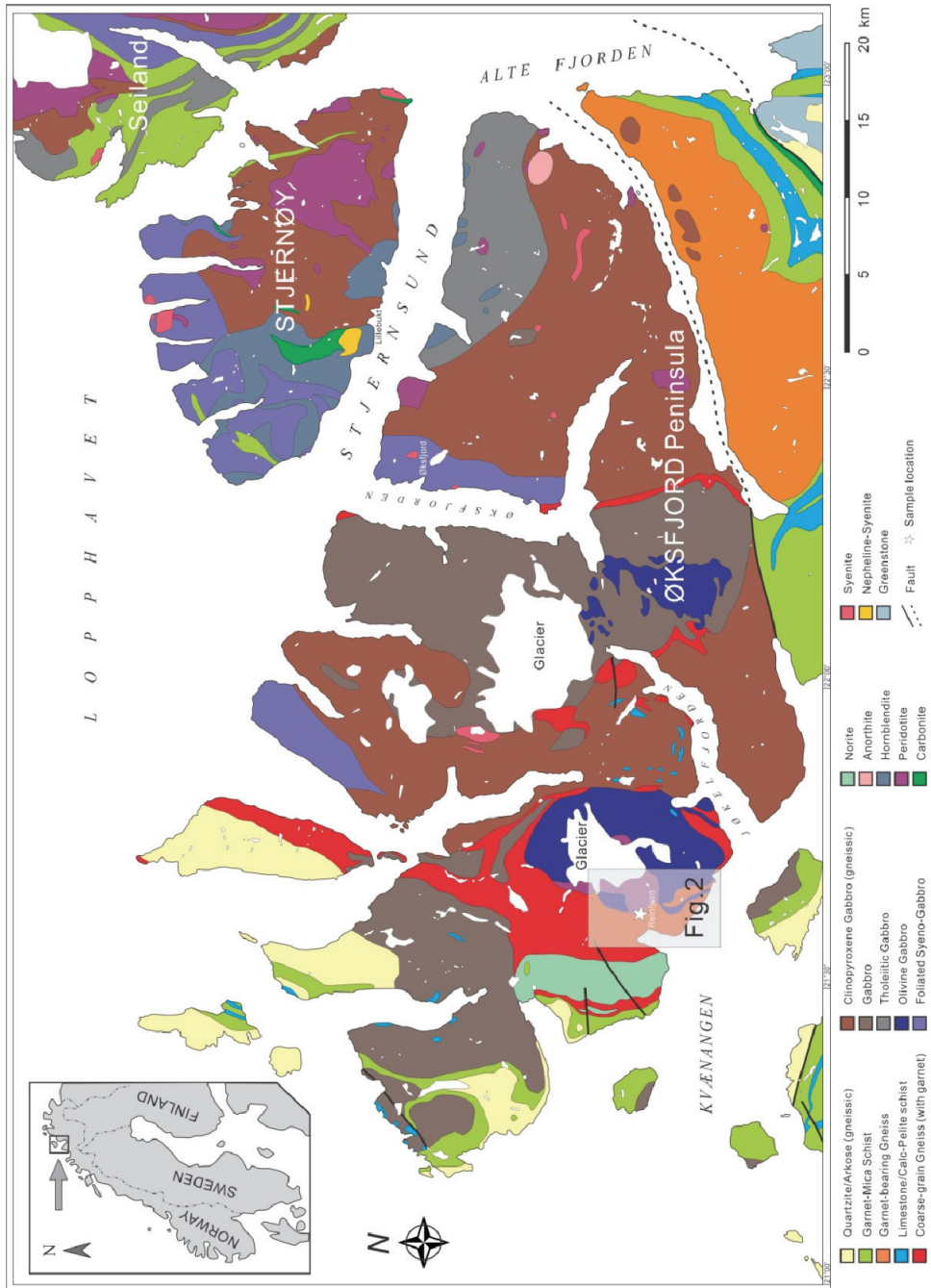


**Fig. 1 Geological sketch of the Seiland Igneous Province, Northern Norway modified after Roberts (1974).**

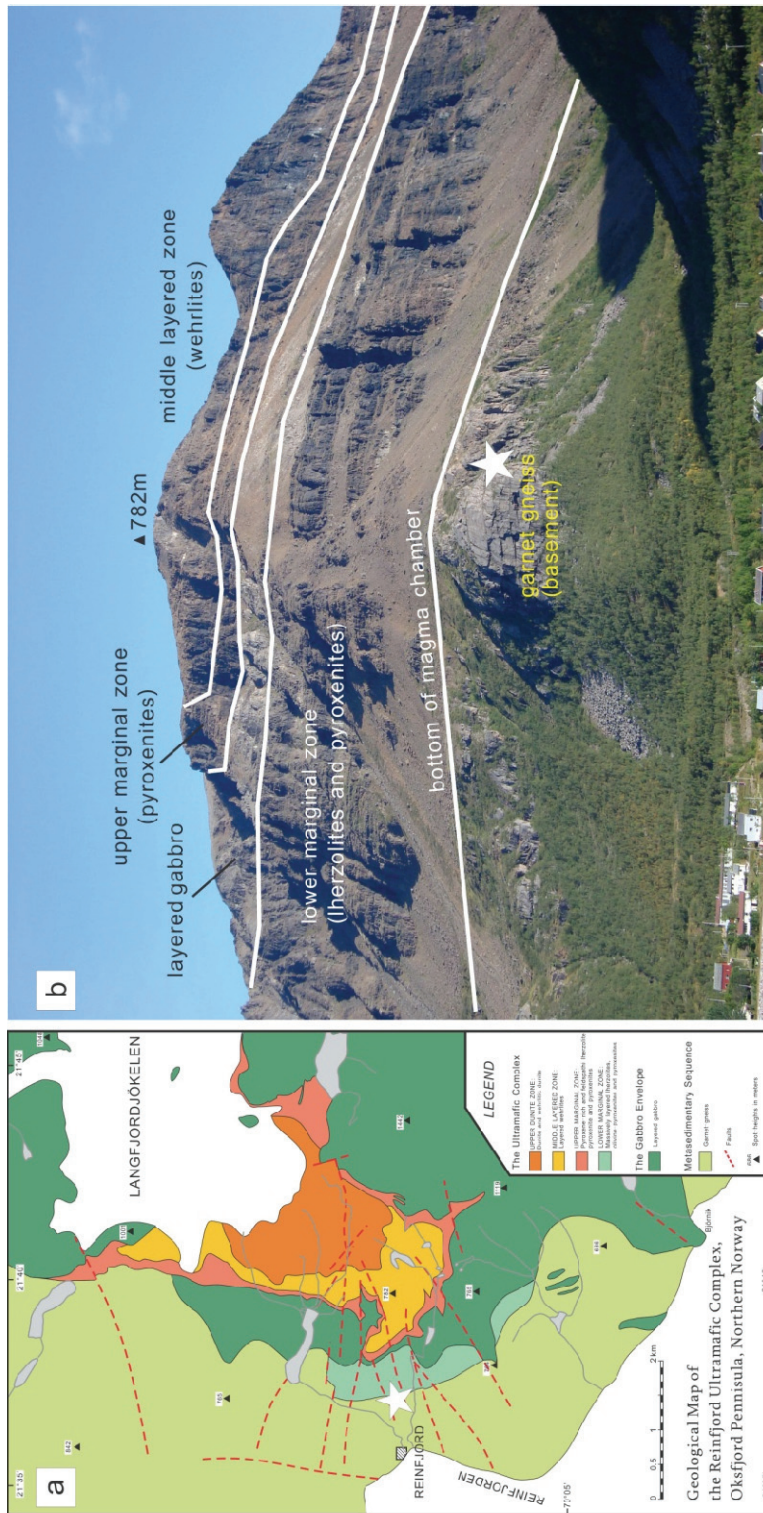


Fig. 2 (a) Detailed geological map of Rein fjord Ultramafic complex modified after Bennett (1974); (b) Photograph showing lithological units and sampling location.

## 4. Methods

### 4.1 Sampling

During the excursions in 2003 and 2009, eleven country rock samples around Reinfjord ultramafic complex were collected, and seven of them were investigated in this study. Six samples (1125, 1283, 1284, 1286, 1289, and 1290) were collected from the west margin of the complex, which is below the bottom of the magma chamber (Fig. 2b), while sample 1291 came from the Reinfjord quarry that located at northwest of the Reinfjord village.

### 4.2 Whole-rock analysis

The composition of the rock samples was analyzed at the Institute of Geosciences, University of Freiburg. A Philips 2404 X-ray fluorescence spectrometer was used with element specific acceleration voltage 30 kV and current 40 nA, with fused beads for major elements and powder pellets for minor elements, respectively. Loss on ignition (LOI) was determined to complete the XRF analyses, and total Fe is reported as  $\text{Fe}_2\text{O}_3\text{tot}$ . Bulk compositions are listed in Table 1.

### 4.3 Mineral analysis

Mineral analyses were performed by electron beam microanalysis using wavelength-dispersive spectrometry (WDS) of a digital CAMECA SX100 electron microprobe at the Institute of Geosciences, University of Freiburg. During analyses an accelerating voltage of 15 kV and a current of 20 nA were used. Beam diameter was 0.5  $\mu\text{m}$  (for feldspar, sometimes 5  $\mu\text{m}$ ). We used the stoichiometric method of Droop (1987) to estimate the ferrous and ferric iron contents in pyroxene, biotite and garnet. Representative analyses of minerals are represented in Tables 2-7 and Fig. 3.

### 4.4 Cathodoluminescence

Cathodoluminescence (CL) images were obtained by ELM-3R luminoscope at the Institute of Geosciences, University of Freiburg with an accelerating voltage of 12 kV and beam current of 0.8 mA. All the CL images were captured by Leica DC500 camera with exposure time of 60s.

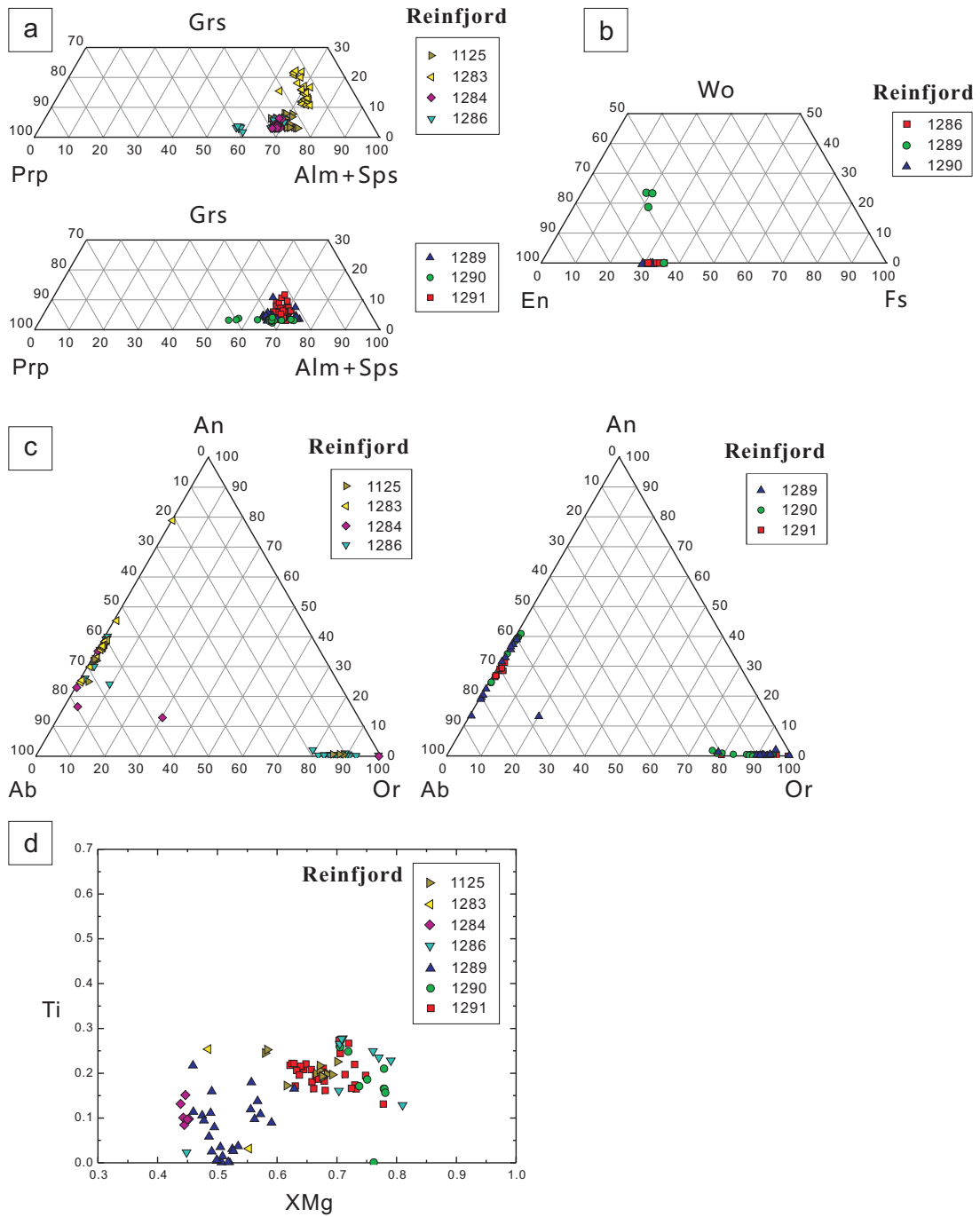


Fig. 3 Compositional plots for garnet (a), pyroxene (b), feldspar (c), and biotite (d).

Table 1 Main compositions of samples and the input forTheriak /Domio software

Sample	1125	1283	1284	1286	1289-A	1289-B	1290	1291
Oxide wt%					dark	light		
SiO <sub>2</sub>	58.60	65.31	58.94	58.11	56.15	71.01	61.81	61.60
TiO <sub>2</sub>	1.23	1.04	1.26	1.70	1.30	0.34	1.20	1.14
Al <sub>2</sub> O <sub>3</sub>	20.06	14.92	18.66	19.99	19.27	11.82	17.05	16.99
Fe <sub>2</sub> O <sub>3</sub> tot	7.23	7.07	9.10	8.50	7.24	9.29	9.93	7.56
MnO	0.09	0.13	0.21	0.04	0.10	0.31	0.21	0.13
MgO	2.35	2.08	2.56	2.86	2.37	1.68	2.52	2.29
CaO	2.26	3.04	2.62	0.99	1.23	2.29	1.17	2.73
Na <sub>2</sub> O	2.58	3.09	2.62	1.38	2.12	1.66	1.36	2.92
K <sub>2</sub> O	3.58	1.95	2.61	4.68	7.95	0.39	3.51	2.92
P <sub>2</sub> O <sub>5</sub>	0.12	0.08	0.16	0.12	0.15	0.10	0.10	0.19
LOI	0.23	0.52	1.10	0.00	0.96	0.00	0.00	0.19
Sum	98.33	99.23	99.84	98.37	98.84	98.89	98.86	98.66
Input for Theriak/Domino								
Si	56.291	62.899	56.804	56.245	53.788	70.404	60.359	59.290
Ti	0.889	0.753	0.913	1.238	0.937	0.254	0.881	0.825
Al	22.711	16.935	21.195	22.804	21.756	13.812	19.623	19.273
Fe	5.226	5.124	6.600	6.191	5.219	6.931	7.297	5.476
Mg	3.365	2.986	3.678	4.127	3.385	2.483	3.669	3.286
Ca	2.326	3.137	2.705	1.027	1.262	2.433	1.224	2.815
Na	4.805	5.770	4.896	2.590	3.938	3.191	2.575	5.449
K	4.387	2.396	3.209	5.779	9.715	0.493	4.373	3.585
O	163.939	168.037	164.262	164.701	158.777	175.721	167.578	165.235

Table 2 Representative microprobe analyses of garnet.

Sample Point	1125 grt 053	1125 grt 059	1283 grt 005	1283 grt 029	1284 grt 017	1284 grt 012	1286 grt 049	1286 grt 079	1289 grt 058	1289 grt 084	1290 grt 013	1290 grt 040	1291 grt 075	1291 grt 078
Wt%														
SiO <sub>2</sub>	39.12	38.75	37.75	38.16	38.76	39.22	38.97	39.01	37.99	38.74	39.39	37.03	37.63	38.3
TiO <sub>2</sub>	0.02	0.03	0.02	0.05	0	0.03	0.02	0.04	0	0.02	0.03	0	0.03	0.02
Al <sub>2</sub> O <sub>3</sub>	21.93	21.68	21.21	21.6	21.16	21.87	22.24	22.15	21.2	22.47	21.05	21.73	22.23	22.12
Cr <sub>2</sub> O <sub>3</sub>	0.04	0.04	0	0	0	0	0.07	0.02	0	0.02	0	0	0.01	0.01
FeOtotal	30.15	31.09	32.02	30.1	30.37	29.97	31.46	27.29	32.98	31.49	27.65	33.15	31.8	31.79
MnO	0.22	0.2	1.59	0.81	1.02	1.21	0.25	0.08	1.41	0.53	0.21	1.68	0.47	0.28
MgO	7.2	7.02	3.73	3.33	7.42	6.41	7.51	10.4	5.75	8.03	10.3	5.78	7.64	6.91
CaO	1.74	1.23	4.51	7.9	1.31	2.17	1.15	1.17	1.26	1.05	1.39	1.07	1.27	2.09
Na <sub>2</sub> O	0.01	0.04	0	0.02	0	0.04	0.01	0.01	0.03	0.05	0	0.03	0.03	0.01
K <sub>2</sub> O	0.01	0.02	0.01	0.02	0	0	0	0.04	0.01	0	0	0	0	0
Total	100.44	100.10	100.84	101.99	100.04	100.92	101.68	100.21	100.63	102.40	100.02	100.47	101.11	101.53
Cations per 12 oxygens														
Si	3.027	3.021	2.981	2.964	3.027	3.033	2.991	2.976	2.987	2.945	3.019	2.916	2.904	2.953
Ti	0.001	0.002	0.001	0.003	0.000	0.002	0.001	0.002	0.000	0.001	0.002	0.000	0.002	0.001
Al(IV)	0.000	0.000	0.019	0.036	0.000	0.000	0.009	0.024	0.013	0.055	0.000	0.084	0.096	0.047
Al(VI)	2.000	1.992	1.956	1.941	1.948	1.994	2.003	1.967	1.952	1.958	1.902	1.932	1.926	1.962
Cr	0.002	0.002	0.000	0.000	0.000	0.000	0.004	0.001	0.000	0.001	0.000	0.000	0.001	0.001
Fe <sup>3+</sup>	0.000	0.000	0.061	0.095	0.000	0.000	0.000	0.057	0.067	0.100	0.056	0.157	0.170	0.084
Fe <sup>2+</sup>	1.951	2.027	2.053	1.860	1.984	1.938	2.019	1.684	2.102	1.902	1.716	2.026	1.882	1.966
Mn	0.014	0.013	0.106	0.053	0.067	0.079	0.016	0.005	0.094	0.034	0.014	0.112	0.031	0.018
Mg	0.830	0.816	0.439	0.386	0.864	0.739	0.859	1.183	0.674	0.910	1.177	0.678	0.879	0.794
Ca	0.144	0.103	0.382	0.657	0.110	0.180	0.095	0.096	0.106	0.086	0.114	0.090	0.105	0.173
Na	0.002	0.006	0.000	0.003	0.000	0.006	0.001	0.001	0.005	0.007	0.000	0.005	0.004	0.001
K	0.001	0.002	0.001	0.002	0.000	0.000	0.000	0.004	0.001	0.000	0.000	0.000	0.000	0.000
Total	7.972	7.984	8.000	8.000	7.999	7.971	8.000	8.000	8.000	8.000	8.000	8.000	8.000	8.000
Endmembers														
Prp	28.25	27.57	14.73	13.04	28.56	25.17	28.75	39.86	22.65	31.04	38.96	23.34	30.34	26.91
Alm	66.36	68.51	68.89	62.92	65.58	66.01	67.55	56.75	70.63	64.87	56.81	69.70	64.97	66.62
Sps	0.49	0.45	3.57	1.80	2.23	2.70	0.54	0.17	3.16	1.16	0.45	3.85	1.06	0.62
Grs	4.91	3.47	12.80	22.23	3.62	6.12	3.16	3.22	3.57	2.92	3.78	3.11	3.63	5.85
XMg	0.30	0.29	0.17	0.16	0.30	0.28	0.30	0.40	0.24	0.31	0.40	0.24	0.30	0.28

Table 3 Representative microprobe analyses of pyroxene

Sample Point	1286 opx 094	1286 opx 099	1289 opx 008	1289 opx 050	1289 opx 051	1289 opx 052	1290 opx 024	1290 opx 025	1290 opx 030
Comment									
SiO <sub>2</sub>	51.06	49.85	52.49	55.04	52.86	54.23	50.87	51.35	50.3
TiO <sub>2</sub>	0.04	0.05	0.21	0.03	0.14	0.04	0.03	0	0.01
Al <sub>2</sub> O <sub>3</sub>	6.76	9.63	3.34	1.72	3.42	2.08	6.36	5.75	6.23
Cr <sub>2</sub> O <sub>3</sub>	0.01	0.03	0.03	0.1	0.12	0.16	0.01	0	0
FeOtotal	18.48	19.13	21.92	10.19	11.08	10.94	20.37	19.82	20.43
MnO	0	0.05	0.15	0.08	0.1	0.07	0.05	0.04	0.04
MgO	23.46	21.33	22.35	17.63	17.12	16.75	23.06	23.23	22.98
CaO	0.14	0.45	0.22	12.61	10.84	12.5	0.08	0.09	0.11
Na <sub>2</sub> O	0.04	0.02	0.04	0.19	0.22	0.31	0.01	0.03	0.01
K <sub>2</sub> O	0.06	0.17	0	0.06	0.94	0.06	0.01	0.01	0.01
Total	100.050	100.710	100.750	97.650	96.840	97.140	100.850	100.320	100.120
Cations per 6 oxygens									
Si	1.859	1.810	1.929	2.040	1.989	2.030	1.850	1.875	1.843
Ti	0.001	0.001	0.006	0.001	0.004	0.001	0.001	0.000	0.000
Al <sup>(IV)</sup>	0.141	0.190	0.071	0.000	0.011	0.000	0.150	0.125	0.157
Al <sup>(VI)</sup>	0.149	0.222	0.073	0.075	0.141	0.092	0.123	0.123	0.112
Cr	0.000	0.001	0.001	0.003	0.004	0.005	0.000	0.000	0.000
Fe <sup>3+</sup>	0.000	0.000	0.000	0.000	0.000	0.000	0.026	0.005	0.046
Fe <sup>2+</sup>	0.563	0.581	0.674	0.316	0.349	0.342	0.594	0.601	0.580
Mn	0.000	0.002	0.005	0.003	0.003	0.002	0.002	0.001	0.001
Mg	1.273	1.154	1.224	0.974	0.961	0.935	1.250	1.265	1.255
Ca	0.005	0.018	0.009	0.501	0.437	0.501	0.003	0.004	0.004
Na	0.003	0.001	0.003	0.014	0.016	0.022	0.001	0.002	0.001
K	0.003	0.008	0.000	0.003	0.045	0.003	0.000	0.000	0.000
Total	3.998	3.987	3.994	3.928	3.960	3.933	4.000	4.000	4.000
Endmembers									
Fs	30.6	33.5	35.5	18.7	21.6	20.6	32.2	32.2	31.6
Wo	0.0	0.0	0.0	23.5	18.7	23.3	0.0	0.0	0.0
En	69.4	66.5	64.5	57.8	59.6	56.1	67.8	67.8	68.4

Table 4 Representative microprobe analyses of feldspar.

Sample Point	1125 pl 062	1289 pl 010	1290 pl 004	1289 pl 007	1290 pl 026	1291 pl 010	1289 kfs 006	1289 kfs 016
Comment			Plagioclase				K-feldspar	
SiO <sub>2</sub>	60.75	58.54	57.6	68.32	60.54	59.56	63.97	64.22
TiO <sub>2</sub>	0.01	0.05	0	0.01	0.01	0	0	0
Al <sub>2</sub> O <sub>3</sub>	25.63	26.72	26.31	21.81	26.54	25.39	19.22	19.27
Cr <sub>2</sub> O <sub>3</sub>	0.01	0	0	0	0	0	0	0
FeOtotal	0.15	0.24	0.2	0	0.19	0.09	0.02	0.01
MnO	0	0.04	0	0.02	0	0	0.02	0
MgO	0	0	0	0	0.07	0	0	0.01
CaO	6.6	8.26	8.37	2.08	4.89	6.38	0.04	0.09
Na <sub>2</sub> O	7.51	7.07	6.94	10.06	8.24	8.1	0.75	1.38
K <sub>2</sub> O	0.14	0.16	0.18	0.09	0.11	0.16	14.87	13.98
Total	100.80	101.08	99.60	102.39	100.59	99.68	98.89	98.96
Cations per 8 oxygens								
Si	2.679	2.596	2.593	2.919	2.667	2.664	2.972	2.972
Ti	0.000	0.002	0.000	0.000	0.000	0.000	0.000	0.000
Al	1.332	1.396	1.396	1.098	1.378	1.338	1.052	1.051
Cr	0.000	0.000	0.000	0.000	0.000	0.000	0.000	0.000
Fe	0.006	0.009	0.008	0.000	0.007	0.003	0.001	0.000
Mn	0.000	0.002	0.000	0.001	0.000	0.000	0.001	0.000
Mg	0.000	0.000	0.000	0.000	0.005	0.000	0.000	0.001
Ca	0.312	0.392	0.404	0.095	0.231	0.306	0.002	0.004
Na	0.642	0.608	0.606	0.833	0.704	0.702	0.068	0.124
K	0.008	0.009	0.010	0.005	0.006	0.009	0.881	0.825
Total	4.979	5.013	5.017	4.951	4.998	5.023	4.976	4.977
Endmembers								
An	32.42	38.88	39.59	10.20	24.53	30.05	0.21	0.47
Ab	66.76	60.22	59.40	89.27	74.81	69.05	7.10	12.98
Or	0.82	0.90	1.01	0.53	0.66	0.90	92.69	86.55

Table 5 Representative microprobe analyses of biotite and muscovite

Sample Point	1125 bt 026	1283 bt 72	1284 bt 026	1286 bt 082	1289 bt 023	1290 bt 020	1291 bt 102	1284 kf 023	1284 kf 024	1284 kf 029
Comment				biotite				muscovite		
SiO <sub>2</sub>	38.11	34.63	35.55	38.33	37.79	39.24	37.59	47.44	47.17	47.73
TiO <sub>2</sub>	3.84	0.61	1.92	4.71	3.56	3.4	4.13	0	0	0.01
Al <sub>2</sub> O <sub>3</sub>	17.4	20.16	17.74	16.29	16.19	15.19	17	36.61	37.87	34.35
Cr <sub>2</sub> O <sub>3</sub>	0.07	0.1	0.02	0.02	0.11	0.02	0.13	0.01	0.03	0
FeO <sub>total</sub>	12.41	17.01	20.57	8.79	17.06	9.53	13.65	1.7	1.16	2.83
MnO	0.03	0.01	0.12	0	0.04	0	0	0	0	0.01
MgO	14.56	11.79	9.17	18.59	12.03	18.8	13.85	0.33	0.04	1.73
CaO	0.03	0.22	0.12	0.03	0.03	0	0.04	0	0.02	0.09
Na <sub>2</sub> O	0.05	0.04	0	0.04	0.04	0.01	0.04	0.45	0.46	0.36
K <sub>2</sub> O	9.85	8.66	8.94	9.64	9.64	9.82	9.02	10.36	10.01	10.44
F	0.96	0.26	0.19	0.91	0.35	1.62	0.98	0.08	0.05	0.05
Cl	0.01	0.02	0.44	0	0.03	0.01	0.01	0.01	0.02	0.04
-O=F+Cl	0.41	0.11	0.18	0.38	0.15	0.68	0.41	0.04	0.03	0.03
H <sub>2</sub> O <sub>calc</sub>	4.10	4.24	4.10	4.22	4.29	3.87	4.01	4.55	4.58	4.56
Total <sub>calc</sub>	100.04	97.36	98.07	100.28	100.63	99.19	99.05	101.42	101.32	102.08
	Cations per 11 oxygens							Cations per 11 oxygens		
Si	2.508	2.374	2.478	2.472	2.537	2.537	2.517	3.096	3.066	3.114
Ti	0.190	0.031	0.101	0.228	0.180	0.165	0.208	0.000	0.000	0.000
Al <sup>(IV)</sup>	1.350	1.626	1.457	1.238	1.281	1.158	1.342	0.904	0.934	0.886
Al <sup>(VI)</sup>	0.000	0.003	0.000	0.000	0.000	0.000	0.000	1.911	1.968	1.755
Cr	0.004	0.005	0.001	0.001	0.006	0.001	0.007	0.001	0.002	0.000
Fe <sup>3+</sup>	0.683	0.975	1.199	0.474	0.958	0.515	0.764	0.000	0.000	0.044
Fe <sup>2+</sup>	0.000	0.000	0.000	0.000	0.000	0.000	0.000	0.093	0.063	0.110
Mn	0.002	0.001	0.007	0.000	0.002	0.000	0.000	0.000	0.000	0.001
Mg	1.428	1.205	0.953	1.787	1.204	1.812	1.383	0.032	0.004	0.168
Ca	0.002	0.016	0.009	0.002	0.002	0.000	0.003	0.000	0.001	0.006
Na	0.006	0.005	0.000	0.005	0.005	0.001	0.005	0.057	0.058	0.046
K	0.827	0.757	0.795	0.793	0.826	0.810	0.771	0.862	0.830	0.869
Total	7.000	7.000	7.000	7.000	7.000	7.000	7.000	6.956	6.926	7.000
Volatiles										
F	0.200	0.056	0.042	0.186	0.074	0.331	0.208	0.017	0.010	0.010
Cl	0.001	0.002	0.052	0.000	0.003	0.001	0.001	0.001	0.002	0.004
OH	1.799	1.941	1.906	1.814	1.922	1.668	1.791	1.982	1.988	1.985
X <sub>Mg</sub>	0.677	0.553	0.443	0.790	0.557	0.779	0.644	0.257	0.058	0.521

Table 6 Representative microprobe analyses of hercynite and corundum.

Sample Point	1283 her 63	1283 her 64	1286 her 015	1286 hc 018	1290 her 001	1290 her 047	1283 crn 68	1283 crn 69	1290 crn 050
Comment			Hercynite				Corundum		
SiO <sub>2</sub>	0.03	0.03	0.00	0.00	0.04	0.04	0.01	0.02	0.04
TiO <sub>2</sub>	0.01	0.00	0.00	0.02	0.02	0.02	0.03	0.03	0.02
Al <sub>2</sub> O <sub>3</sub>	58.30	57.22	60.89	61.29	60.06	61.08	97.39	96.36	100.36
Cr <sub>2</sub> O <sub>3</sub>	0.08	0.08	0.12	0.18	0.11	0.27	0.01	0.06	0.00
FeO <sub>total</sub>	31.68	30.81	27.22	25.80	28.06	28.30	0.33	0.43	0.89
MnO	0.06	0.07	0.00	0.04	0.05	0.03	0.00	0.00	0.00
MgO	4.82	4.75	8.08	8.88	7.89	8.55	0.00	0.01	0.01
CaO	0.01	0.03	0.02	0.02	0.02	0.00	0.03	0.02	0.00
NiO	0.04	0.04	0.36	0.36	0.47	0.35	0.06	0.02	0.03
ZnO	5.80	6.00	4.18	3.85	3.73	2.30	0.04	0.03	0.02
V <sub>2</sub> O <sub>3</sub>	0.00	0.00	0.26	0.24	0.00	0.00	0.00	0.00	0.00
Total	100.83	99.03	101.13	100.68	100.45	100.94	97.90	96.98	101.37
	Cations per 4 oxygens						Cations per 3 oxygens		
Si	0.001	0.001	0.000	0.000	0.001	0.001	0.000	0.000	0.001
Ti	0.000	0.000	0.000	0.000	0.000	0.000	0.000	0.000	0.000
Al	1.929	1.928	1.952	1.960	1.942	1.951	1.993	1.991	1.986
Cr	0.002	0.002	0.003	0.004	0.002	0.006	0.000	0.001	0.000
Fe <sup>3+</sup>	0.067	0.068	0.039	0.030	0.053	0.040	0.005	0.006	0.012
Fe <sup>2+</sup>	0.677	0.668	0.580	0.555	0.591	0.602	0.000	0.000	0.000
Mn	0.001	0.002	0.000	0.001	0.001	0.001	0.000	0.000	0.000
Mg	0.202	0.202	0.328	0.359	0.323	0.346	0.000	0.000	0.000
Ca	0.000	0.001	0.001	0.001	0.001	0.000	0.001	0.000	0.000
Ni	0.001	0.001	0.008	0.008	0.010	0.008	0.001	0.000	0.000
Zn	0.120	0.127	0.084	0.077	0.076	0.046	0.001	0.000	0.000
V	0.000	0.000	0.006	0.005	0.000	0.000	0.000	0.000	0.000
Total	3.000	3.000	3.000	3.000	3.000	3.000	2.000	2.000	2.000



Table 7 Representative microprobe analyses of Fe-Ti oxides.

Sample Point	1125 ilm 024	1284 ilm 021	1286 ilm 021	1289 ilm 008	1290 ilm 078	1291 ilm 033	1125 rt 067	1284 rt 020	1289 rut 026	1290 rut 082
Comment	Ilmenite						Rutile			
SiO <sub>2</sub>	0.24	0.03	0.07	0.03	0.05	0.06	0.04	0.03	0.12	0.04
TiO <sub>2</sub>	50.67	52.95	51.00	52.13	51.54	52.55	98.76	98.02	99.95	97.75
Al <sub>2</sub> O <sub>3</sub>	0.08	0.00	0.07	0.00	0.00	0.00	0.00	0.00	0.00	0.00
Cr <sub>2</sub> O <sub>3</sub>	0.05	0.01	0.05	0.02	0.01	0.00	0.05	0.15	0.09	0.10
FeOtotal	45.45	43.24	46.29	46.06	45.23	44.42	0.21	0.60	0.51	0.42
MnO	1.07	2.40	0.15	1.73	0.16	0.77	0.00	0.00	0.02	0.00
MgO	0.39	0.05	0.53	0.09	1.23	0.69	0.00	0.00	0.00	0.00
CaO	0.05	0.00	0.01	0.01	0.00	0.00	0.02	0.01	0.03	0.01
NiO	0.02	0.00	0.04	0.00	0.05	0.00	0.05	0.00	0.05	0.00
ZnO	0.00	0.00	0.18	0.00	0.00	0.00	0.00	0.00	0.00	0.02
V <sub>2</sub> O <sub>3</sub>	0.00	0.00	2.43	0.00	0.00	2.61	0.00	0.00	0.00	0.00
Total	98.02	98.68	100.82	100.07	98.27	101.10	99.13	98.81	100.77	98.34
	Cations per 3 oxygens						Cations per 2 oxygens			
Si	0.006	0.001	0.002	0.001	0.001	0.001	0.001	0.000	0.002	0.001
Ti	0.977	1.013	0.955	0.988	0.986	0.979	0.996	0.991	0.991	0.993
Al	0.002	0.000	0.002	0.000	0.000	0.000	0.000	0.000	0.000	0.000
Cr	0.001	0.000	0.001	0.000	0.000	0.000	0.001	0.002	0.001	0.001
Fe <sup>3+</sup>	0.031	0.000	0.034	0.022	0.026	0.000	0.002	0.007	0.006	0.005
Fe <sup>2+</sup>	0.943	0.919	0.930	0.948	0.936	0.920	0.000	0.000	0.000	0.000
Mn	0.023	0.052	0.003	0.037	0.003	0.016	0.000	0.000	0.000	0.000
Mg	0.015	0.002	0.020	0.003	0.047	0.025	0.000	0.000	0.000	0.000
Ca	0.001	0.000	0.000	0.000	0.000	0.000	0.000	0.000	0.000	0.000
Ni	0.000	0.000	0.001	0.000	0.001	0.000	0.001	0.000	0.001	0.000
Zn	0.000	0.000	0.003	0.000	0.000	0.000	0.000	0.000	0.000	0.000
V	0.000	0.000	0.049	0.000	0.000	0.052	0.000	0.000	0.000	0.000
Total	2.000	1.987	2.000	2.000	2.000	1.994	1.000	1.000	1.000	1.000

## 4.5 Phase diagram modeling

Bulk composition used in phase diagram modeling are normalized as atom proportion and listed in Table 1. For sample 1289, XRF analyses were performed on dark and light layer respectively, which could easily be separated. Other bulk compositions are derived from homogenous sample that are considered as effective bulk composition required for modeling. The  $\text{TiO}_2\text{-Na}_2\text{O-CaO-K}_2\text{O-FeO-MgO-Al}_2\text{O}_3\text{-SiO}_2\text{-H}_2\text{O}$  (TiNCKFMASH) component system was considered for all the samples. Mn was omitted because the trace amounts in bulk rock XRF results and its exclusive presence in garnet. The water activity was kept to one for all modeling.

Mineral assemblage stability diagrams were calculated using Theriak-Domino software (de Capitani and Brown, 1987; de Capitani and Petrakakis, 2010) with the readable translation of the THERMOCALC database (Holland and Powell, 1998). Mineral solution models used are listed in following: garnet, biotite, spinel, ilmenite and melt (White et al., 2007); cordierite and epidote (Holland and Powell, 1998); clinopyroxene (Holland and Powell, 1996); orthopyroxene (White et al., 2002); amphibole (Diener et al., 2007); feldspar (Holland and Powell, 2003); chloritoid (White et al., 2000); chlorite (Holland et al., 1998); white mica (Coggon and Holland, 2002); sapphirine (Kelsey et al., 2004).

## 5 Petrography and mineral chemistry

All samples investigated show distinctive gneiss foliation with parallel alternating dark and light layers on outcrop and microprobe scales. Four groups of samples could be divided according to the textural details, and will be described separately below.

### 5.1 Textures under CL

Cathodoluminescence (CL) images are employed to reveal the textures of minerals, especially for K-feldspar, plagioclase and quartz which are usually related with melt phase.

Quartz shows typical deep blue to black color (e.g. Fig. 4b). K-feldspars are characterized of bright blue core and gray rim (Fig. 4j, Fig. 5k and Fig. 6m), which have different Ab components. This is possibly due to the sequential crystallization from melt. For instance, the large K-feldspar core (Ab=10) of sample 1289 crystallized earlier from melt, while the relict melt crystallized as K-feldspar rim (Ab=7) and interstitial mineral intergrowth of Plagioclase (An = 10) + Qtz during cooling (Fig. 6m). Similarly, there are two distinctive types of plagioclase in sample 1289. The coarse-grained plagioclases (An=40) show light green color (Fig. 6k), and the other

(An=10) which intergrowth with quartz show brown color (Fig. 6m).

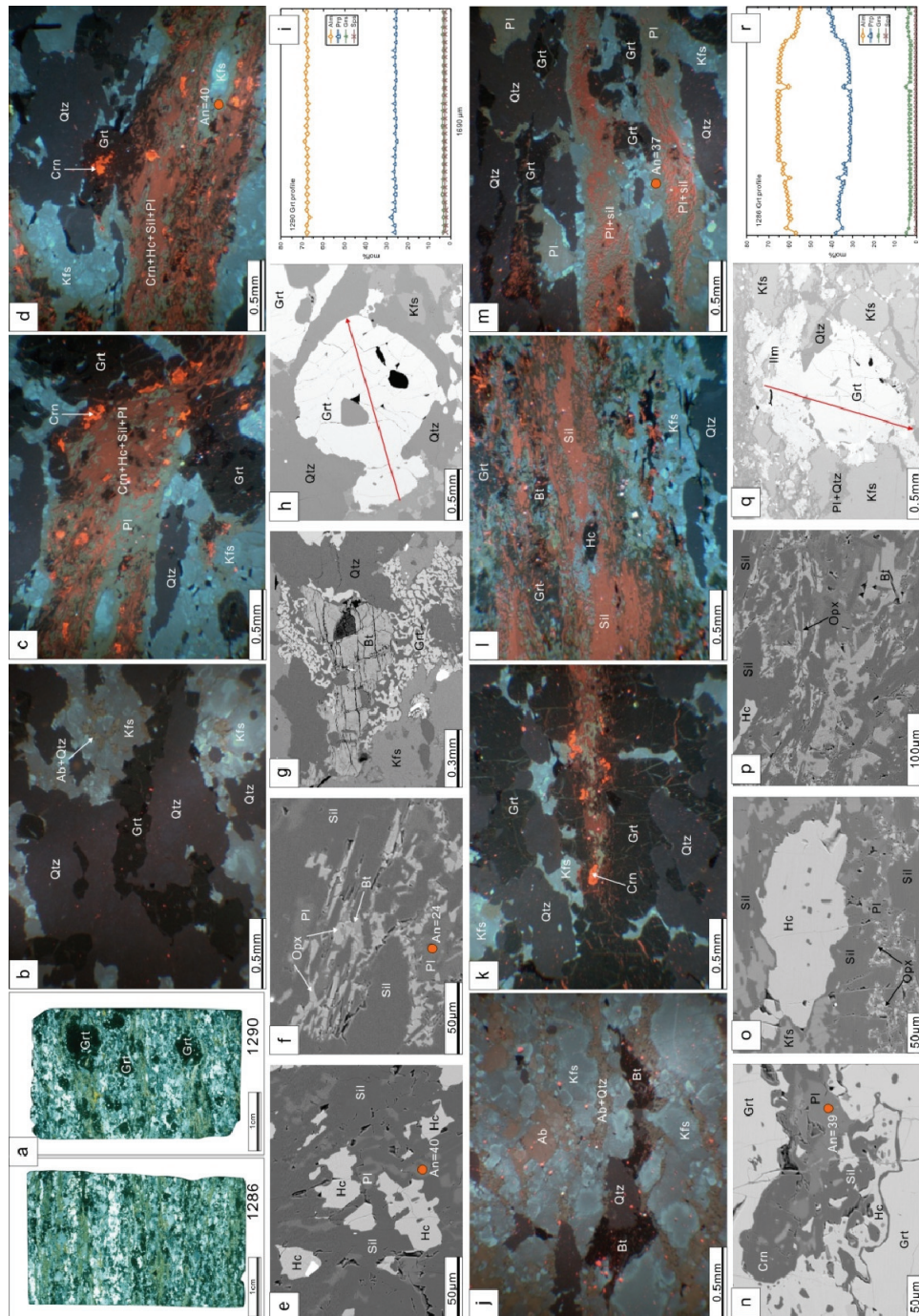


**Fig. 4** Cathodoluminescence images and BSE images show textures of sample 1286 and 1290. (b-i): CL and BSE images of sample 1290; (j-r): CL and BSE images of sample 1286. See text for explanations.

Corundum and sillimanite have remarkable bright origin color under CL (e.g. Fig. 4k, Fig. 7d). Fe-rich minerals such as garnet, biotite, Fe-Ti oxides are black under CL.

## 5.2 Sample 1286 and 1290

Sample 1286 and 1290 have similar textural signatures and mineral compositions. Alternating felspathic-rich layers and brown layers (Fig. 4a) could be observed under thin sections. The felspathic-rich layers are mostly consist of quartz, K-feldspar and garnet with interstitial albite + quartz aggregate (Fig.4b and Fig. 4j). The brown layers are sillimanite-rich layer with inclusions of hercynite and garnet (Fig.4i). Small orthopyroxene (En=64-70) and biotite (Ti=0.1-0.3 apfu with  $X_{Mg}=0.7-0.8$ ) grains (Fig. 4f and Fig. 4o) at the periphery of sillimanite could be indentified in these brown layers. The sillimanite-rich layers are usually intergrowth with plagioclase (An=37) and surrounded by K-feldspar (Fig. 4m), which possibly indicate the crystallization of former melt.

Garnets with different textural distribution modes could be distinguished: garnet porphyroblast (0.5-1cm diameter) which is crosscutting layers (Fig. 4a), and small garnet (< 10 mm diameter) co-existing with hercynite and sillimanite distributing along brown layers (Fig. 4o). As shown in Fig. 3a, sample 1296 and sample 1290 both have two garnet groups: garnet porphyroblasts have an average composition of  $Alm_{67}Prp_{28}Grs_3$ , while the small garnets have an average composition of  $Alm_{57}Prp_{40}Grs_5$ .

The variations of garnet are also illustrated by Fig. 8 with isopleths. From the high temperature garnet (green hexagon) to the low temperature garnet (blue hexagon), the amount of garnet increased slightly at the expense of corundum + hercynite  $\pm$  sillimanite, with the increasing Alm and decreasing Prp components until entering the cordierite stability field. Hereafter, Garnet porphyroblasts experienced the thrust cooling stage (see section 8.3), and grown rapidly with constant composition, as indicated by the slopes of isopleths of garnet mole and components. This process is the main growing stage of the large garnet porphyroblasts which have corresponding flat profiles. For instance, large garnet porphyroblasts in the felspathic layers show distinct flat profiles with minor variation at rims where overgrowth could be observed (Fig. 4h, Fig. 4i, Fig. 4q and Fig. 4r). In addition, garnet overgrowth with composition of  $Alm_{57}Prp_{38}Grs_4$  (Fig. 4q and Fig. 4r) indicates local reactions with the crystallizing melt after the generation of large garnet porphyroblast, therefore don't conflict with the above garnet evolution history.

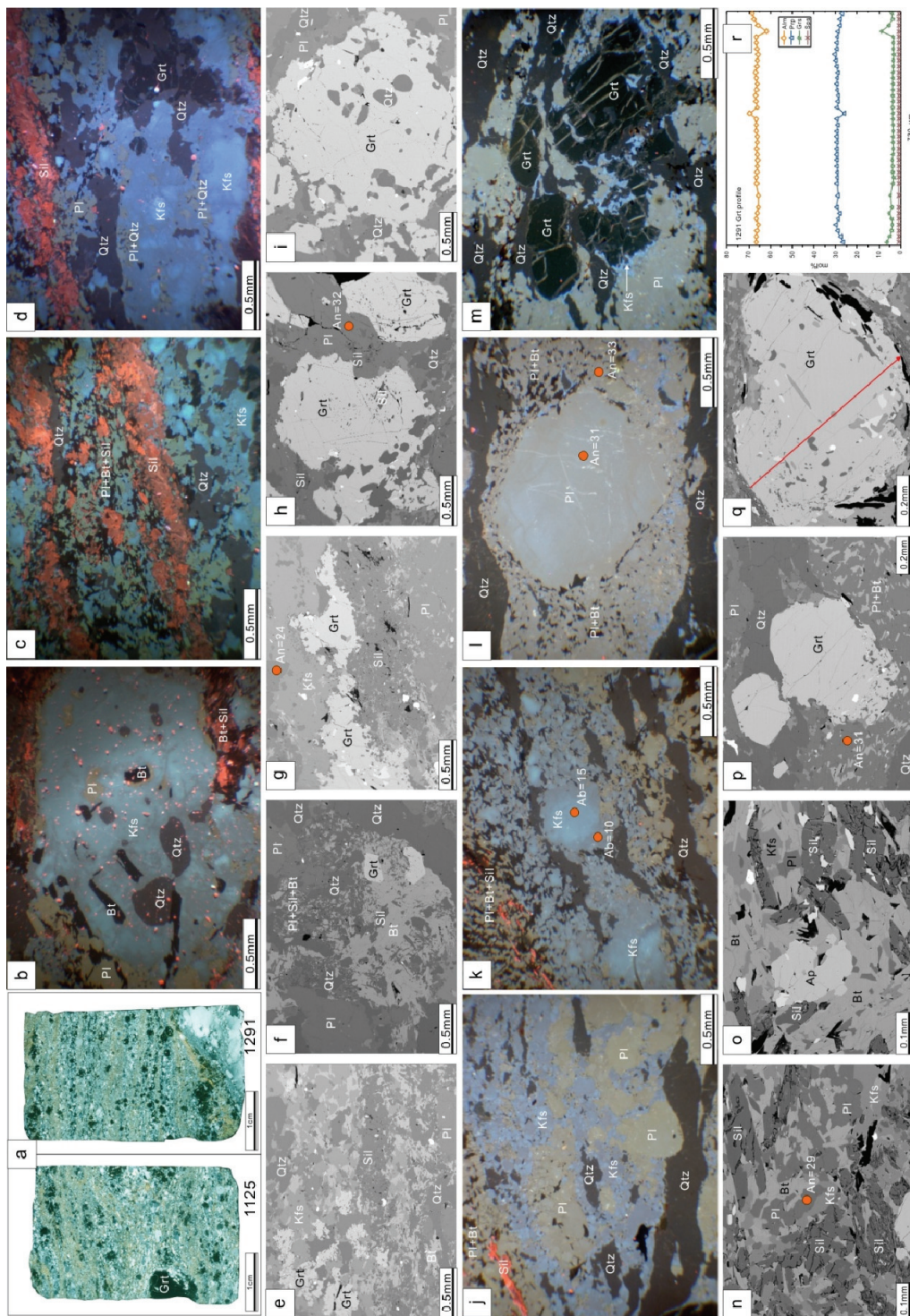


**Fig. 5** Cathodoluminescence images and BSE images show textures of sample 1125 and 1291. (b-i): CL and BSE images of sample 1125; (j-r): CL and BSE images of sample 1291. See text for explanations.

### 5.3 Sample 1125 and 1291

Alternating felspathic-rich layers and brown layers are remarkable in Sample 1125 and 1291 (Fig. 5a). Notably, the detailed mineral assemblages are different in these two samples.

In sample 1125, the mineral assemblage of felspathic-rich layers consists elongated quartz, K-feldspar and garnet with interstitial plagioclase (An=32) + quartz aggregate (Fig. 5c-d). Minor large K-feldspar grains with inclusions of biotite, plagioclase, and quartz, could also be observed (Fig. 5b). The brown layer is composed of plagioclase (An=24) + biotite (Ti=0.17- 0.25 apfu with  $X_{Mg}=0.58-0.7$ ) + sillimanite aggregate and minor small garnet grains (Fig. 5c, Fig. 5e-f).

In contrast, for sample 1291, the felspathic-rich layers is composed of elongated quartz, rounded plagioclase (An=31) and garnet with interstitial K-feldspar (Ab=10-15) aggregate (Fig. 5j-m). The brown layers are sillimanite-rich layers intergrowth with plagioclase (An=29) and K-feldspar (Fig. 5n-o).

Small idioblastic garnets are concentrated in felspathic-rich layers; minor large porphyroblasts are included in wide felspathic-rich layers which are further surrounded by brown layers (Fig. 5a). The garnet compositions of sample 1125 and sample 1291 have been presented in Fig. 3a. Both samples have the similar narrow compositional range with limited composition variations from  $Alm_{68}Prp_{27}Grs_5$  to  $Alm_{67}Prp_{25}Grs_8$ , which indicates the slight increase of grossular component. Consequently, an increase of pressure could be derived from the garnet isopleths in Fig. 9. Garnet was growing with constant Alm and Prp component and increasing Grs component during the pressure increase. The steep slopes of parallel Alm and Prp isopleths also support the compositional variation of garnet.

### 5.4 Sample 1284 and 1289

The alternating felspathic-rich layers and brown layers are much wider in sample 1284 and 1289 (Fig. 6a). Felspathic-rich layers in sample 1294 are composed of idioblastic garnet and quartz (Fig. 6b and Fig. 6e), but that of sample 1289 consist additional plagioclase (Fig. 6j and Fig. 6n).

The brown layers of sample 1284 and 1289 are remarkably different with that of other samples by the mineral assemblage of biotite + garnet + plagioclase (An=40) (Fig. 6h).

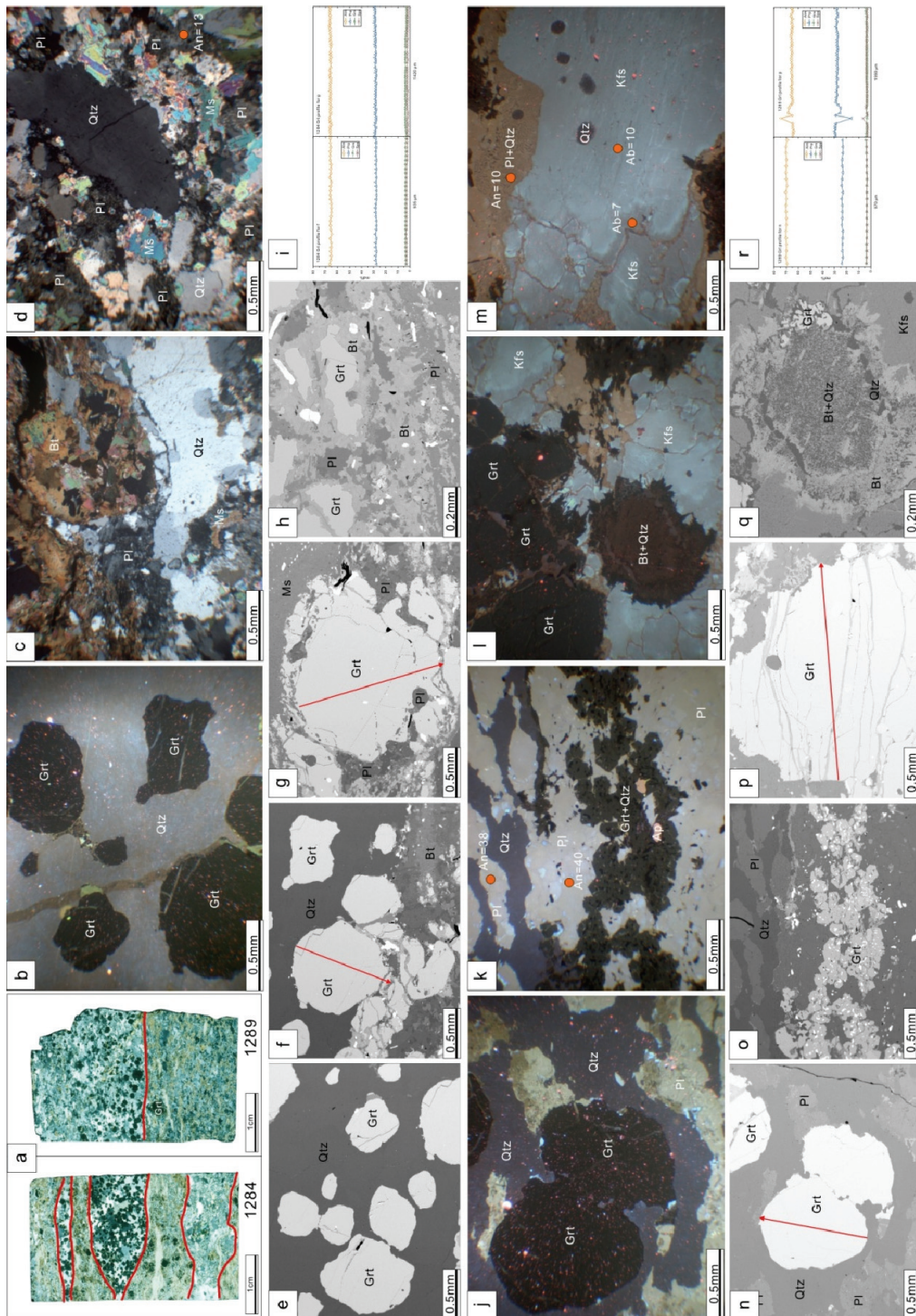


Fig. 6 Cathodoluminescence images and BSE images show textures of sample 1284 and 1289. (b-i): CL and BSE images of sample 1284; (j-r): CL and BSE images of sample 1289. See text for explanations.

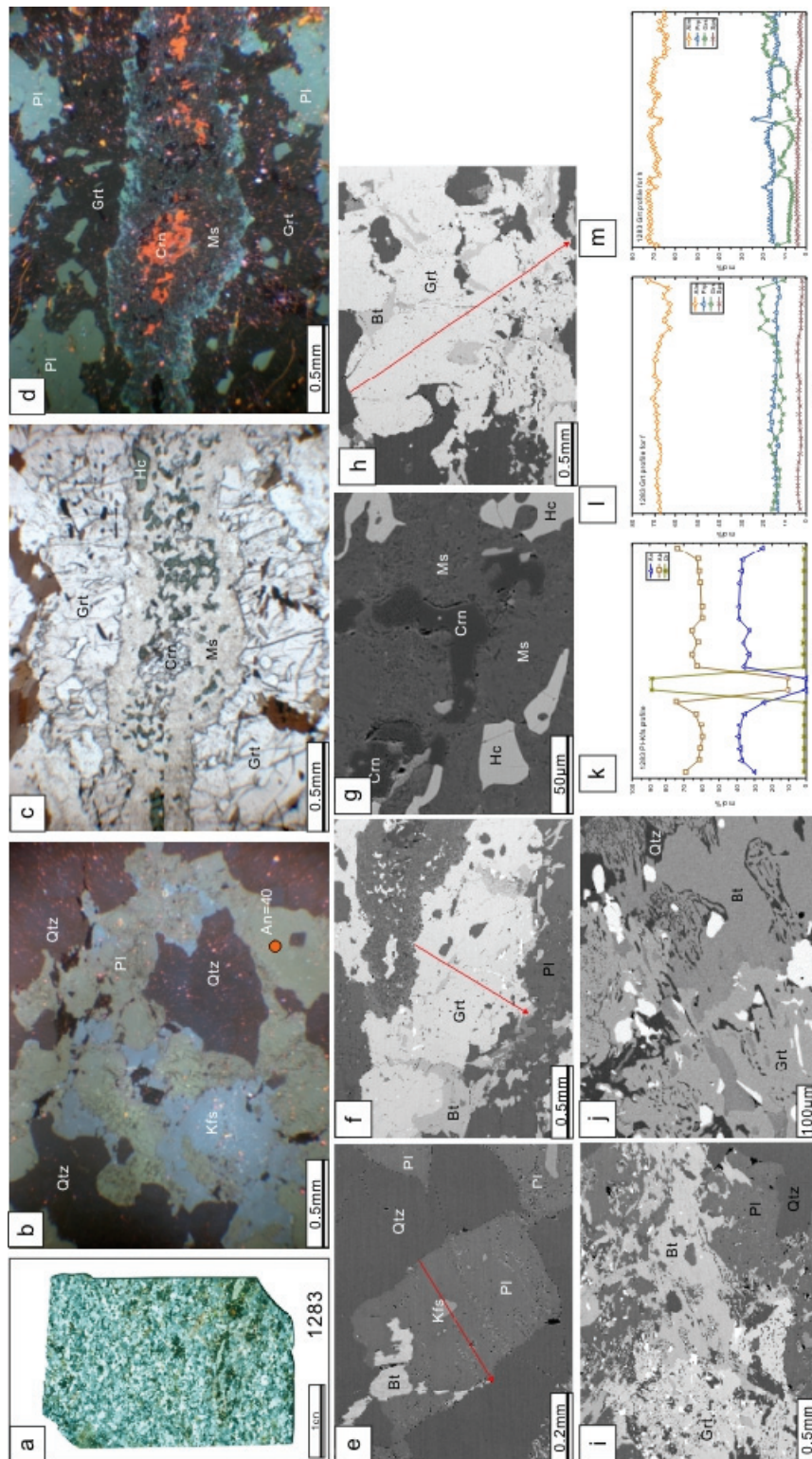


Fig. 7 Cathodoluminescence images and BSE images show textures of sample 1283. See text for explanations.



Muscovite-rich areas could be observed in sample 1284 (Fig. 6d). Notably, rounded biotite + quartz aggregates within K-feldspar matrix of sample 1289 are possibly the indication of previous cordierite. These phenomena are perhaps derived from the late hydrated retrogression. Interstitial plagioclase (An=10) + quartz intergrowth could be observed between the large K-feldspar (Ab=7-10) grains (Fig. 6m).

Garnets in sample 1284 have flat profiles with average compositions of  $\text{Alm}_{68}\text{Prp}_{28}\text{Grs}_4$  (Fig. 6i). For sample 1289, garnet in felspathic-rich layer has flat profile with average composition of  $\text{Alm}_{70}\text{Prp}_{23}\text{Grs}_3$  (Fig. 6i), but garnet in brown layer has flat profile with average composition of  $\text{Alm}_{64}\text{Prp}_{28}\text{Grs}_3$ .

As shown in Fig.3a, garnets from sample 1284 have a narrow range compared with that of sample 1289. The slight variation between  $\text{Alm}_{68}\text{Prp}_{27}\text{Grs}_5$  to  $\text{Alm}_{67}\text{Prp}_{25}\text{Grs}_8$  of garnet in 1284 indicates an increase of pressure in Fig.10. This compositional variation could be predicted by the weakly intersecting of Alm and Prp isopleths. Correspondingly, phase diagrams constructed on light part of sample 1289 show similar formation condition for garnet with that of sample 1284.

## 5.5 Sample 1283

Sample 1283 are relatively homogenous without significant layer structures (Fig. 7a). Felspathic-rich parts are mostly consist of quartz, plagioclase (An=40), K-feldspar (Fig. 7b). Large plagioclase grain shows a slight increase of Ab component (from 60 to 70) when contacts with K-feldspar inclusion and matrix quartz (Fig. 7e and Fig. 7k).

In the relative brown parts, the similar topology of garnet + ilmenite intergrowth and biotite + quartz intergrowth (Fig. 7i-j) possibly indicates that garnet + ilmenite were produced by biotite breakdown.

Large elongated garnet porphyroblasts which have white hollows could be observed under thin sections (Fig. 7a and Fig. 7c). The white hollows are fulfilled by corundum + hercynite which are surrounded by muscovite matrix (Fig. 7c-d and Fig. 7g). The surrounding garnet has a general flat profile with average composition of  $\text{Prp}_{15}\text{Alm}_{68}\text{Grs}_{15}\text{Sps}_3$  (Fig. 7i and Fig. 7m). The slight variation is due to the combination of several individual grains whose boundaries could be identified by the traces of tiny inclusions (Fig. 7f and Fig. 7h).

## 6. P-T conditions estimated by phase diagrams

### 6.1 Sample 1286 and 1290

Fig. 8 shows the resulting equilibrium phase diagrams calculated for sample 1286 (left) and sample 1290 (right).

#### 6.1.1 Sample 1286

For sample 1286, the stability field corresponding to core of garnet porphyroblast (green field) is composed of biotite, corundum, hercynite, ilmenite, cordierite, garnet and melt. The field ranges from 830-900°C with pressures between 7 kbar to 8.5 kbar. The temperature interval is constrained by the appearance of sillimanite, hercynite and corundum at lower temperature, and the disappearance of corundum and garnet at higher temperature. The co-occurrence of Sil + Hc + Crn is consistent with the calculated stability field (Fig. 4i and 4n). The absence of cordierite is probably due to the fully consumption by following garnet formation reaction, which formed garnet films around the Sil + Hc + Crn assemblage (Fig. 4n). The Opx + melt (Pl) assemblage (Fig. 4o and Fig. 4p) could not be illustrated in the phase diagram, and that is perhaps due to the local biotite melting at high temperature ( $\approx 900^\circ\text{C}$ ).

The following stability field (blue field) of second garnet generation is composed of the assemblage of biotite, ilmenite, sillimanite, garnet and melt at 740-830°C and 6.5-9.5 kbar. This field is constrained by disappearance of quartz and plagioclase at lower temperature, and the appearance of corundum at higher temperature. The pressures of this stability field are delimited by the appearance of cordierite at lower pressure, and the transformation of sillimanite to kyanite at higher pressure.

#### 6.1.2 Sample 1290

For sample 1290, the high temperature mineral assemblage is composed of corundum, ilmenite, garnet and melt. This assemblage is only stable in a small field at 880-920°C and pressure above 8.5kbar, which is mostly identical to that of corundum. The temperature interval is constrained by the appearance of corundum at lower temperature, and the disappearance of garnet at higher temperature. This calculated assemblage is well illustrated in Fig. 4c and Fig. 4d. The absence of hercynite could be explained by the over estimation of oxygen fugacity used in modeling.

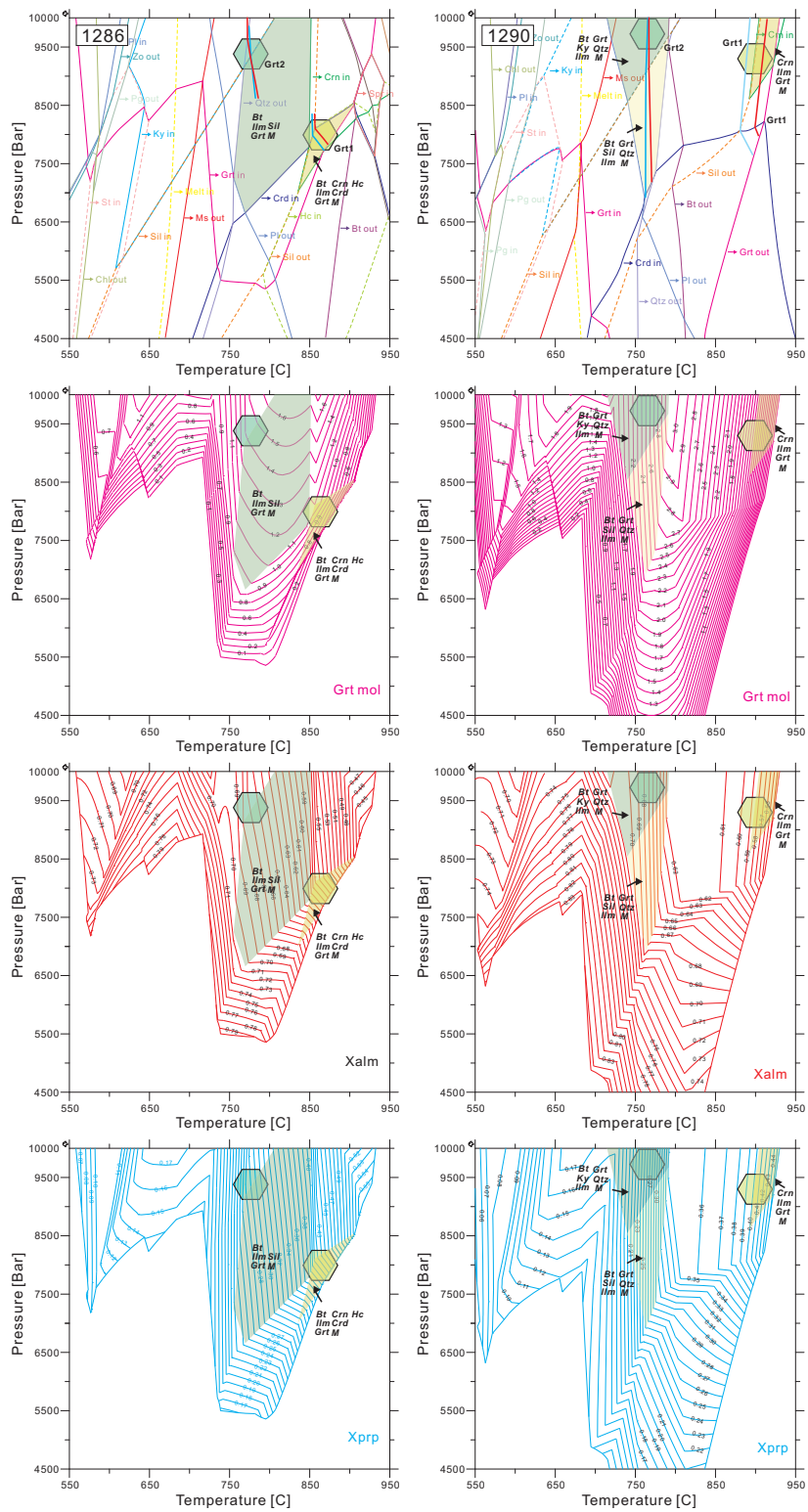


**Fig. 8** Phase diagrams constructed for sample 1286 and sample 1290. See text for explanations.

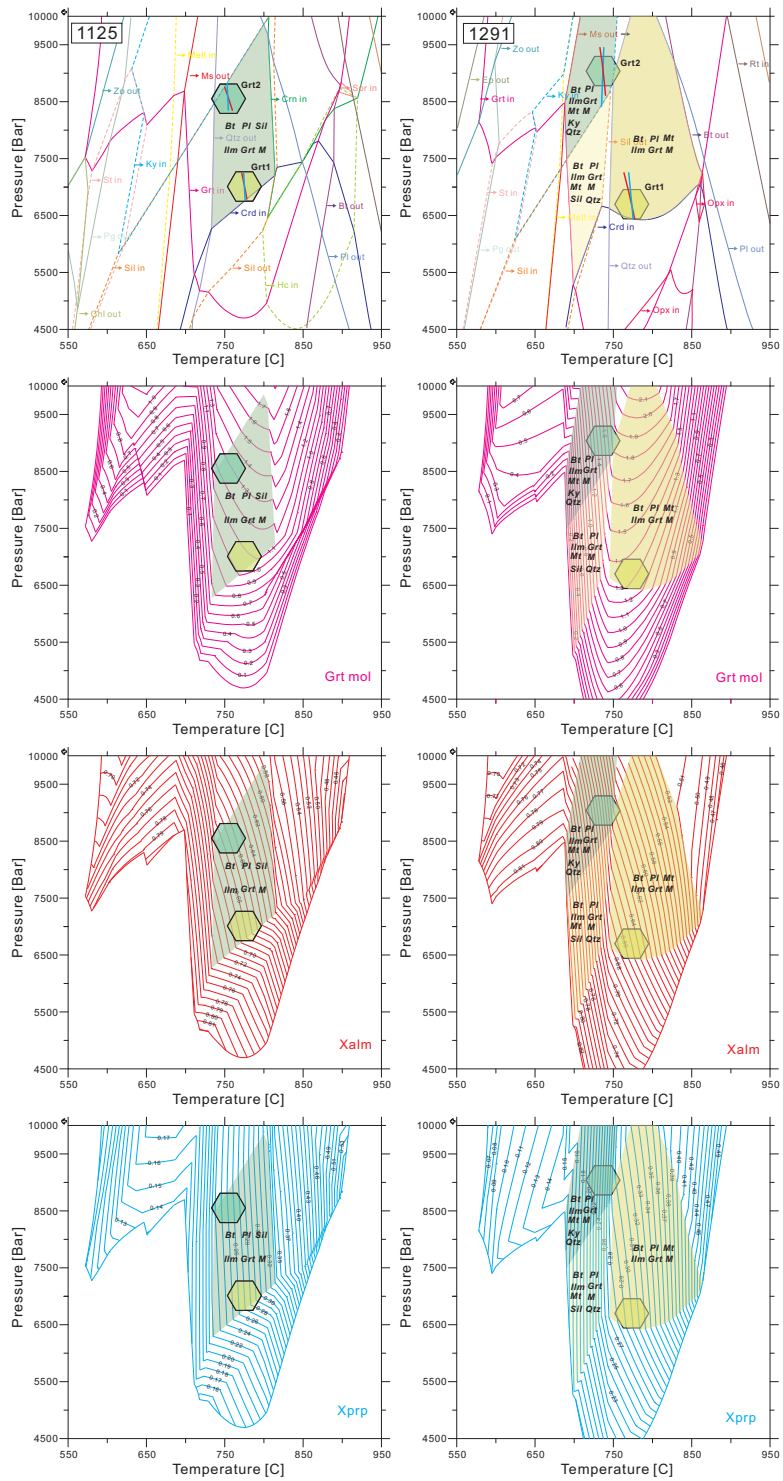


Fig. 9 Phase diagrams constructed for sample 1125 and sample 1291. See text for explanations.

Stability field constrained by composition of second garnet generation is composed of biotite, garnet, kyanite, quartz, ilmenite and melt. Considering the flat garnet profile and absence of kyanite under this section, the stability field suitable for this generation of garnet should be at lower pressure, the yellow field (Fig. 8) which contains sillimanite and other minerals.

## 6.2 Sample 1125 and 1291

Fig. 9 shows the resulting equilibrium phase diagrams calculated for sample 1125 (left) and sample 1291 (right).

### 6.2.1 Sample 1125

The observed textures, which mostly related to melt phase, are almost homogeneous distributed in sample 1125. In addition, the compositions of garnet don't have significant variation. Correspondingly, the only stability field has wide range of 730-800°C with pressures between 6.5 kbar to 9.5 kbar. The assemblage consist biotite, plagioclase, sillimanite, ilmenite, garnet and melt (Fig.5c and Fig. 5d). The temperature interval is constrained by the disappearance of quartz at lower temperature, and the appearance of corundum at higher temperature. The pressures of this stability field are delimited by the appearance of cordierite at lower pressure, and the transformation of sillimanite to kyanite at higher pressure. Rounded quartz inclusions (Fig. 5b and Fig. 5i) are the relict of former melt-producing reaction, in contrast, the new formed irregular quartz (Fig. 5d) are crystallized from the melt during cooling.

### 6.2.2 Sample 1291

For sample 1291, the high temperature mineral assemblage is composed of biotite, plagioclase, magnetite, ilmenite, garnet and melt. This assemblage is stable in a wide field at 750-850°C and pressure above 6.5kbar. The temperature interval is constrained by the disappearance of quartz at lower temperature, and the disappearance of biotite at higher temperature. The pressure of this stability field is limited by the appearance of cordierite at lower pressure.

Stability field constrained by composition of second garnet generation is composed biotite, garnet, kyanite, quartz, ilmenite and melt. Similarly to sample 1290, the flat garnet profile and absence of kyanite, the stability field suitable for this generation of garnet should be at lower pressure, the yellow field (Fig. 8) which contains sillimanite and other minerals. The temperature interval is constrained by the appearance of garnet at lower temperature, and the disappearance of sillimanite at higher temperature. This calculated assemblage is consistent with that observed in

Fig. 5n and Fig. 5o.

## 6.3 Sample 1284 and 1289

Fig. 10 shows the resulting equilibrium phase diagrams calculated for sample 1284 (left) and sample 1289 (middle and right).

### 6.3.1 Sample 1284

Two stability fields could be identified in the phase diagrams. The stability field at lower pressure (5.5-7.5kbar) is composed of ilmenite, garnet, biotite, plagioclase, quartz, sillimanite and melt. The field at higher pressure (above 7.5kbar) contains kyanite instead of sillimanite. Both fields have the same temperature range of 700-740°C, which is constrained by melt-producing at lower temperature, and the disappearance of quartz at higher temperature. The pressures are delimited by appearance of cordierite at lower pressure and kyanite at higher pressure. Muscovite (Fig. 6c and Fig. 6d) observed in the sample possibly indicates lower temperature assemblage which across the Ms-out line during cooling.

### 6.3.2 Sample 1289

Phase diagrams are constructed on the light part (leucosome) and dark part (mesosome) of sample 1289.

For the light part, stability field at 720-750°C with assemblage of biotite, ilmenite, plagioclase, garnet, quartz and melt could be proofed by the mineral observation in leucosome (Fig. 6j and Fig. 6k). Notably, the biotite and quartz aggregates (Fig. 6q) are considered as the alteration product of former cordierite. Therefore, a previous stability field which has pressure lower than 5kbar was possibly crossed before.

Two stability fields with muscovite have been shown on the phase diagram of dark part. All of these two fields (at temperature lower than 650°C) are beyond the left sides of melt-producing reaction and the disappearance of muscovite. The pervasive muscovite also supports this calculated stability fields.



## 6.4 Sample 1283

Fig. 11 shows the resulting equilibrium phase diagrams calculated for sample 1283.

The available stability field derived from garnet composition is composed of quartz, ilmenite, magnetite, muscovite, garnet, biotite, plagioclase and melt. The conditions corresponding to the garnet composition are 650-700 °C with pressure above 9kbar. The observed mineral assemblage (Fig. 7i and Fig. 7j) is consistent with this estimation.

In contrast, stability field for corundum + hercynite (Fig. 7c and Fig. 7d) could not be illustrated in the calculated phase diagram, and this is possibly due to the local disequilibrium or the unfaithful bulk composition used. Compared with sample 1286 and 1290 which have the similar texture of garnet enclosing corundum and hercynite, temperature between 850°C to 900 °C was achieved before.

## 7. Metamorphic evolution

### 7.1 Peak metamorphic condition

Peak mineral assemblage of corundum + hercynite ± sillimanite has been observed in sample 1286, 1290 and 1283. But the P-T estimates for this peak assemblage have only been obtained in sample 1290 and 1286. The stability fields have a narrow temperature range between 850°C to 900°C and a relative wide pressure range from 7.5 kbar to 9.5 kbar (Fig. 12). this estimated P-T range is consistent with that of Reinfjord ultramafic complex with pressure of 6-8 kbar (20-30 km depth) and the solidus temperature of 1300°C (Bennett, 1974). The emplacement of the hot ultramafic rock caused high temperature metamorphism in the country rocks rapidly so that no information of primary rock and minerals could survive.

### 7.2 Uplift cooling

The decrease of temperature and pressure from sample 1290 to sample 1286 possibly indicate an uplift event with cooling after the peak metamorphism. This is also supported by the occurrence of cordierite (sample 1289, see text above) which mostly exists below pressure of 7kbar. The process is accompanied with the disappearance of corundum and hercynite which are usually replaced by garnet (e.g. Fig. 4k and Fig. 4n) and cordierite (Ms-rich matrix of Fig. 7d). The lowest pressure has been estimated as 6.5kbar for sample 1291. The stability field is distributed just above the cordierite field.



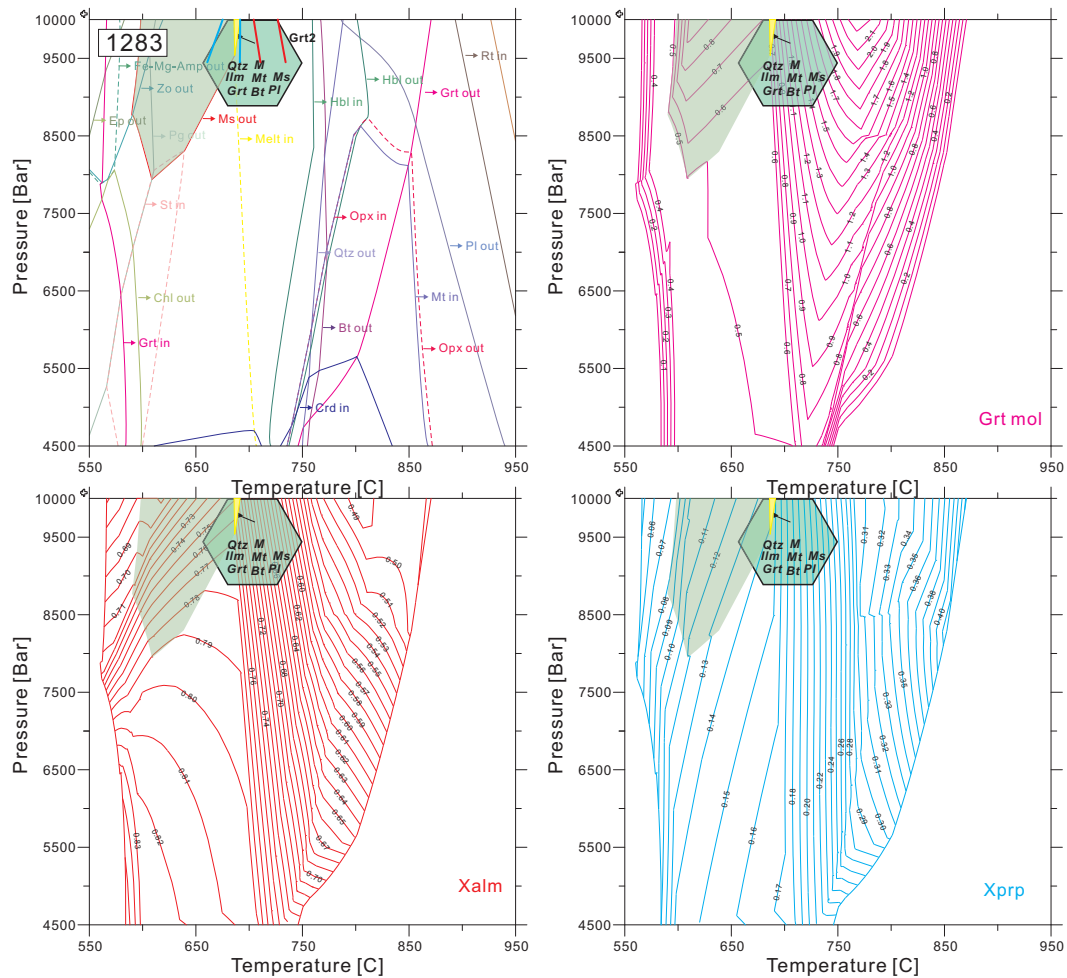


Fig. 11 Phase diagrams constructed for sample 1283. See text for explanations.

The compositional isopleths of garnet during this process generally have relatively steep slopes in the P-T space (Fig. 8); therefore garnet profiles related with this process are flat-shaped. This is consistent with the middle compositional profile of large garnet porphyroblast that surrounding the peak assemblage (Fig. 4i, Fig. 4r, Fig. 7f and Fig. 7i).

### 7.3 Thrust cooling

A pressure increase has been illustrated clearly by utilizing stability fields from sample 1291, 1125 and 1284. This process is accompanied with new garnet generation that overgrowth on the porphyroblast (e.g. Fig.4q, Fig. 5p-q and Fig.7h) and individual small crystals crystallized

from melt (Fig. 4h, Fig. 6e and Fig. 6n). Garnet profiles related with this process have an increase of Xgrs and Xalm for the overgrowth rims (Fig.5r and Fig.7i). The compositional isopleths (Xalm and Xprp) of garnet during this process also have relatively steep slopes in the P-T space (Fig. 9 and Fig. 10). The sequential amounts increase of quartz, sillimanite could be deduced from the increase direction of pressure. The upper limit of pressure is constrained by the transformation of sillimanite to kyanite, at pressures above 7.5 kbar for 750°C, and 9.5 kbar for 700°C.

The stability field of 1283 and the stability fields at lower temperatures from 1284, 1286, 1290 and 1291 define a pressure range of 8-10 kbar at 650-700°C. The P-T range is consistent with that derived other samples.

## 8. Implications for tectonic evolution

As shown in Fig. 12, there stages could be summarized from the P-T conditions and mineral stability fields: (1) contact metamorphism at 850-900°C and 7.5-9.5 kbar; (2) uplift cooling with pressure decrease of 3 kbar and temperature decrease of 100°C (ends at 800°C and 6.5 kbar); (3) thrust cooling until 650°C and 10kbar.

Similarly, researches performed on metapelitic xenolith in metagabbro of 929 ±18 Ma have demonstrated three metamorphic stages: (1) Contact metamorphism: 930-960 °C / 5-6.5 kb; (2) Cooling: 700-750 °C / 5-7 kb; (3) Compression: 650-700 °C / 8-10 kb (Elvevold and Reginiussen, 1996; Elvevold et al., 1994).

Although the absolute values of temperature and pressure are different, country rocks from these two areas perhaps experienced the same tectonothermal history. The first high temperature contact metamorphism was deduced by the emplacement of volumes of ultramafic rocks in the Seiland igneous province at 829±18 Ma (Krogh and Elvevold, 1990). The following uplift cooling corresponded to the initial rifting and extension, which could be represented by the calc-alkaline intrusions including alkaline pyroxenite, syenite, nepheline syenite and carbonatite at 574± 5 Ma (Roberts et al., 2010). Sequential thrust cooling was accompanied with crustal thickening and compression during the formation of Caledonian orogeny belt, which involving eastwards thrust of the Seiland igneous province onto the Precambrian crystalline basement of the Baltic shield during the Silurian continental collision (ca. 431-428 Ma at Finnmark, Kirkland et al., 2006a; Kirkland et al., 2007) between Baltica and Laurentia following the early Palaeozoic closure of the Iapetus Ocean (Gee, 1975; Roberts, 2003).

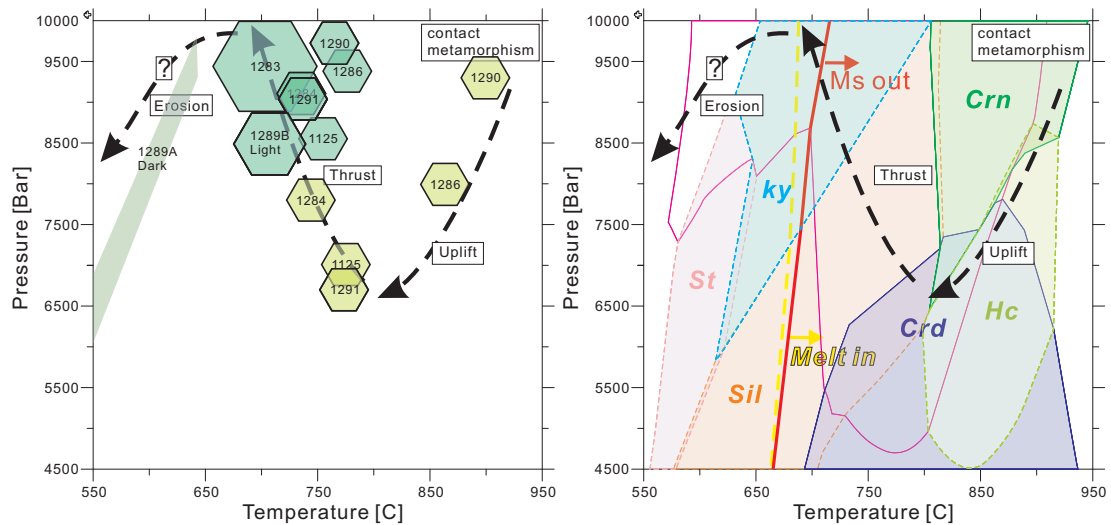


**Fig. 12 Utilized metamorphic conditions and established P-T path on the mineral stability fields from sample 1125. See text for explanations.**

## 9. Conclusions

Three main stages in a chronological order could be summarized from the P-T conditions and mineral stability fields: (1) contact metamorphism at 850-900°C and 7.5-9.5 kbar; (2) uplift cooling with pressure decrease by ~3 kbar and temperature decrease by ~100°C (ends at 800°C and 6.5 kbar); (3) thrust cooling until 650°C and 10kbar. The first high temperature contact metamorphism was deduced by the emplacement of volumes of ultramafic rocks. The following uplift cooling corresponded to the initial rifting and extension. Sequential thrust cooling was accompanied with crustal thickening and compression.

## References

- Akselsen, J., 1982. Precambrian and Caledonian Tectonometamorphic Evolution of Northeastern Seiland, Finnmark, North Norway. *Norges Geologiske Undersøkelse Bulletin*(66): 45-61.
- Andersen, T.B., Jamtveit, B., Dewey, J.F. and Swensson, E., 1991. Subduction and exhumation of continental crust: major mechanisms during continent-continent collision and orogenic extensional collapse, a model based on the south Norwegian Caledonides. *Terra Nova*, 3(3): 303-310.
- Andresen, A., 1988. Caledonian terranes of Northern Norway and their characteristics. *Trabajos de geología*, 17: 103-117.
- Appleyard, E.C., 1974. Syn-orogenic igneous alkaline rocks of eastern Ontario and northern Norway. *Lithos*, 7(3): 147-169.

- Bennett, M.C., 1974. The emplacement of a high temperature peridotite in the Seiland Province of the Norwegian Caledonides. *Journal of the Geological Society*, 130(3): 205-226.
- Bucher-Nurminen, K., 1991. Mantle fragments in the Scandinavian caledonides. *Tectonophysics*, 190(2-4): 173-192.
- Coggon, R. and Holland, T., 2002. Mixing properties of phengitic micas and revised garnet-phengite thermobarometers. *Journal of Metamorphic Geology*, 20(7): 683-696.
- Daly, J.S., Aitchison, S.J., Cliff, R.A., Gayer, R.A. and Rice, A.H.N., 1991. Geochronological Evidence from Discordant Plutons for a Late Proterozoic Orogen in the Caledonides of Finnmark, Northern Norway. *Journal of the Geological Society*, 148: 29-40.
- de Capitani, C. and Brown, T., 1987. The computation of chemical equilibrium in complex systems containing non-ideal solutions. *Geochimica Et Cosmochimica Acta*, 51(10): 2639-2652.
- de Capitani, C. and Petrakakis, K., 2010. The computation of equilibrium assemblage diagrams with Theriak/Domino software. *American Mineralogist*, 95(7): 1006-1016.
- Diener, J.F.A., Powell, R., White, R.W. and Holland, T.J.B., 2007. A new thermodynamic model for clino- and orthoamphiboles in the system Na<sub>2</sub>O–CaO–FeO–MgO–Al<sub>2</sub>O<sub>3</sub>–SiO<sub>2</sub>–H<sub>2</sub>O–O. *Journal of Metamorphic Geology*, 25(6): 631-656.
- Droop, G., 1987. A general equation for estimating Fe<sup>3+</sup> concentrations in ferromagnesian silicates and oxides from microprobe analyses, using stoichiometric criteria. *Mineralogical Magazine*, 51(361): 431-435.
- Drüppel, K., Elsäßer, L., Brandt, S. and Gerdes, A., 2013. Sveconorwegian Mid-crustal Ultrahigh-temperature Metamorphism in Rogaland, Norway: U–Pb LA-ICP-MS Geochronology and Pseudosections of Sapphirine Granulites and Associated Paragneisses. *Journal of Petrology*, 54(2): 305-350.
- Elvevold, S. and Reginiussen, H., 1996. Reaction textures in contact-metamorphosed xenoliths; implications for the tectonothermal evolution of the Seiland igneous province, Norwegian Caledonides. *European Journal of Mineralogy*, 8(4): 777-789.
- Elvevold, S., Reginiussen, H., Krogh, E.J. and Bjorklund, F., 1994. Reworking of Deep-Seated Gabbros and Associated Contact Metamorphosed Paragneisses in the South-Eastern Part of the Seiland Igneous Province, Northern Norway. *Journal of Metamorphic Geology*, 12(4): 539-556.
- Fall, A., Bodnar, R.J., Szabó, C. and Pál-Molnár, E., 2007. Fluid evolution in the nepheline syenites of the Ditrau Alkaline Massif, Transylvania, Romania. *Lithos*, 95(3-4): 331-345.
- Gee, D., 1975. A tectonic model for the central part of the Scandinavian Caledonides. *American Journal of Science*, 275: 468–515.
- Gee, D.G., Janák, M., Majka, J., Robinson, P. and van Roermund, H., 2012. Subduction along and within the Baltoscandian margin during closing of the Iapetus Ocean and Baltica-Laurentia collision. *Lithosphere*.
- Holland, T., Baker, J. and Powell, R., 1998. Mixing properties and activity-composition and relationships of chlorites in the system MgO–FeO–Al<sub>2</sub>O<sub>3</sub>–SiO<sub>2</sub>–H<sub>2</sub>O. *Eur J Mineral*, 10(3): 395-406.
- Holland, T. and Powell, R., 1996. Thermodynamics of order-disorder in minerals: II, Symmetric formalism applied to solid solutions. *American Mineralogist*, 81(11-12): 1425-1437.
- Holland, T. and Powell, R., 2003. Activity–composition relations for phases in petrological calculations: an asymmetric multicomponent formulation. *Contributions to Mineralogy and Petrology*, 145(4): 492-501.
- Holland, T.J.B. and Powell, R., 1998. An internally consistent thermodynamic data set for phases of petrological interest. *Journal of Metamorphic Geology*, 16(3): 309-343.
- Kelsey, D.E., White, R.W., Holland, T.J.B. and Powell, R., 2004. Calculated phase equilibria in K<sub>2</sub>O–FeO–MgO–Al<sub>2</sub>O<sub>3</sub>–SiO<sub>2</sub>–H<sub>2</sub>O for sapphirine-quartz-bearing mineral assemblages. *Journal of Metamorphic Geology*, 22(6): 559-578.
- Kirkland, C.L., Daly, J.S., Chew, D.M. and Page, L.M., 2008a. The Finnmarkian Orogeny revisited: An isotopic investigation in eastern Finnmark, Arctic Norway. *Tectonophysics*, 460(1-4): 158-177.
- Kirkland, C.L., Daly, J.S., Eide, E.A. and Whitehouse, M.J., 2006a. The structure and timing of lateral escape during the Scandian Orogeny: A combined strain and geochronological investigation in Finnmark, Arctic Norwegian Caledonides. *Tectonophysics*, 425(1-4): 159-189.
- Kirkland, C.L., Daly, J.S. and Whitehouse, M., 2006b. Granitic magmatism of Grenvillian and late Neoproterozoic age in Finnmark, Arctic Norway - Constraining pre-Scandian deformation in the Kalak Nappe Complex. *Precambrian Research*, 145(1-2): 24-52.

- Kirkland, C.L., Daly, J.S. and Whitehouse, M.J., 2005. Early Silurian magmatism and the Scandian evolution of the Kalak Nappe Complex, Finnmark, Arctic Norway. *Journal of the Geological Society*, 162(6): 985-1003.
- Kirkland, C.L., Daly, J.S. and Whitehouse, M.J., 2008b. Basement-cover relationships of the Kalak Nappe Complex, Arctic Norwegian Caledonides and constraints on Neoproterozoic terrane assembly in the North Atlantic region. *Precambrian Research*, 160(3-4): 245-276.
- Kirkland, Christopher L., Stephen Daly, J. and Whitehouse, Martin J., 2007. Provenance and Terrane Evolution of the Kalak Nappe Complex, Norwegian Caledonides: Implications for Neoproterozoic Paleogeography and Tectonics. *The Journal of Geology*, 115(1): 21-41.
- Krogh, E. and Elvevold, S., 1990. A Precambrian age for an early gabbro-monzonitic intrusive on the ksfjord peninsula, Seiland Igneous Province, northern Norway. *Norsk Geologisk Tidsskrift*, 70(4): 267-273.
- Markl, G. and Bucher, K., 1997. Proterozoic eclogites from the Lofoten islands, northern Norway. *Lithos*, 42(1-2): 15-35.
- Osmundsen, P.T. and Andersen, T.B., 1994. Caledonian Compressional and Late-Orogenic Extensional Deformation in the Staveneset Area, Sunnfjord, Western Norway. *Journal of Structural Geology*, 16(10): 1385-1401.
- Ritzmann, O. and Faleide, J.I., 2007. Caledonian basement of the western Barents Sea. *Tectonics*, 26(5): TC5014.
- Roberts, D., 1974. Geologisk kart over Norge, berggrunskart. Hammerfest 1:250000. Norges geologiske undersøkelse.
- Roberts, D., 2003. The Scandinavian Caledonides: event chronology, palaeogeographic settings and likely modern analogues. *Tectonophysics*, 365(1-4): 283-299.
- Roberts, D. and Gee, D.G., 1985. An introduction to the structure of the Scandinavian Caledonides. In Gee, D.G. & Sturt, B.A. (eds.) *The Caledonide orogen - Scandinavia and related areas*: 55-68.
- Roberts, D., Nordgulen, Ø. and Melezhik, V., 2007. The Uppermost Allochthon in the Scandinavian Caledonides: From a Laurentian ancestry through Taconian orogeny to Scandian crustal growth on Baltica. *Geological Society of America Memoirs*, 200: 357-377.
- Roberts, R.J., Corfu, F., Torsvik, T.H., Ashwal, L.D. and Ramsay, D.M., 2006. Short-lived mafic magmatism at 560-570 Ma in the northern Norwegian Caledonides: U-Pb zircon ages from the Seiland Igneous Province. *Geological Magazine*, 143(6): 887-903.
- Roberts, R.J., Corfu, F., Torsvik, T.H., Hetherington, C.J. and Ashwal, L.D., 2010. Age of alkaline rocks in the Seiland Igneous Province, Northern Norway. *Journal of the Geological Society*, 167(1): 71-81.
- Robins, B. and Gardner, P.M., 1975. The magmatic evolution of the Seiland province, and Caledonian plate boundaries in northern Norway. *Earth and Planetary Science Letters*, 26(2): 167-178.
- Stephens, M.B. and Gee, D.G., 1985. A tectonic model for the evolution of the eugeoclinal terranes in central Scandinavian Caledonides. In Gee, D.G. & Sturt, B.A. (eds.) *The Caledonide orogen - Scandinavia and related areas*: 953-978.
- Sturt, B.A., Miller, J.A. and Fitch, F.J., 1967. The age of alkaline rocks from West Finnmark, northern Norway, and their bearing on the datings of the Caledonian orogeny. *Norsk Geologisk Tidsskrift*, 47: 255-273.
- Sturt, B.A., Pringle, I.R. and Ramsay, D.M., 1978. The Finnmarkian phase of the Caledonian Orogeny. *Journal of the Geological Society*, 135(6): 597-610.
- White, R.W., Powell, R. and Clarke, G.L., 2002. The interpretation of reaction textures in Fe-rich metapelitic granulites of the Musgrave Block, central Australia: constraints from mineral equilibria calculations in the system  $K_2O-FeO-MgO-Al_2O_3-SiO_2-H_2O-TiO_2-Fe_2O_3$ . *Journal of Metamorphic Geology*, 20(1): 41-55.
- White, R.W., Powell, R. and Holland, T.J.B., 2007. Progress relating to calculation of partial melting equilibria for metapelites. *Journal of Metamorphic Geology*, 25(5): 511-527.
- White, R.W., Powell, R., Holland, T.J.B. and Worley, B.A., 2000. The effect of  $TiO_2$  and  $Fe_2O_3$  on metapelitic assemblages at greenschist and amphibolite facies conditions: mineral equilibria calculations in the system  $K_2O-FeO-MgO-Al_2O_3-SiO_2-H_2O-TiO_2-Fe_2O_3$ . *Journal of Metamorphic Geology*, 18(5): 497-511.

**Part VI Regional metamorphism in the  
paragneisses of Seiland Igneous Province,  
Northern Norway**

## 1. Abstract

Two main stages in a chronological order could be summarized from the P-T conditions and mineral stability fields of paragneisses from Øksfjord peninsula: (1) contact metamorphism at ca. 800°C and 5.5-6.5 kbar; (2) thrust cooling until 700°C and 9.5 kbar. The first high temperature contact metamorphism was deduced by the emplacement of volumes of ultramafic rocks. Sequential thrust cooling was accompanied with crustal thickening and compression.

## 2. Introduction

The Norwegian Caledonian orogenic belt is characterized by a series of thrust sheets that are grouped into the Uppermost Allochthon representing exotic Laurentian terranes, the Upper Allochthon representing the Iapetus oceanic lithosphere, and the Lower and Middle Allochthon representing the margin of Pre-Caledonian Baltica (Andresen, 1988; Ritzmann and Faleide, 2007; Roberts and Gee, 1985; Stephens and Gee, 1985), all of which thrust eastwards onto the Precambrian crystalline basement of the Baltic shield during the Silurian continental collision (ca. 431-428 Ma at Finnmark, Kirkland et al., 2006a; Kirkland et al., 2007) between Baltica and Laurentia following the early Palaeozoic closure of the Iapetus Ocean (Gee, 1975; Roberts, 2003).

The development of Norwegian Caledonian orogenic belt involves a series of sequential events: the formation of Iapetus ocean crust with associated initial rifting, the production of ophiolite, the subsequent consumption of ocean crust along a destructive plate margin, and a continent-continent collision with stacking of crusts, crustal thickening and lateral nappe displacements (e.g. Andersen et al., 1991; Bucher-Nurminen, 1991; Gee et al., 2012; Osmundsen and Andersen, 1994). The present knowledge of the metamorphism related to the above events is mostly based on the detailed investigation on eclogites (e.g. Markl and Bucher, 1997). However, metamorphism and metamorphic rocks related to the widespread rift-related magmatic products have been nearly neglected considering their geological importance, except for a few studies (e.g. Drüppel et al., 2013)

In this study, we present the regional metamorphic events recorded by paragneisses from five locations of Øksfjord peninsula, Seiland Igneous Province, Northern Norway.

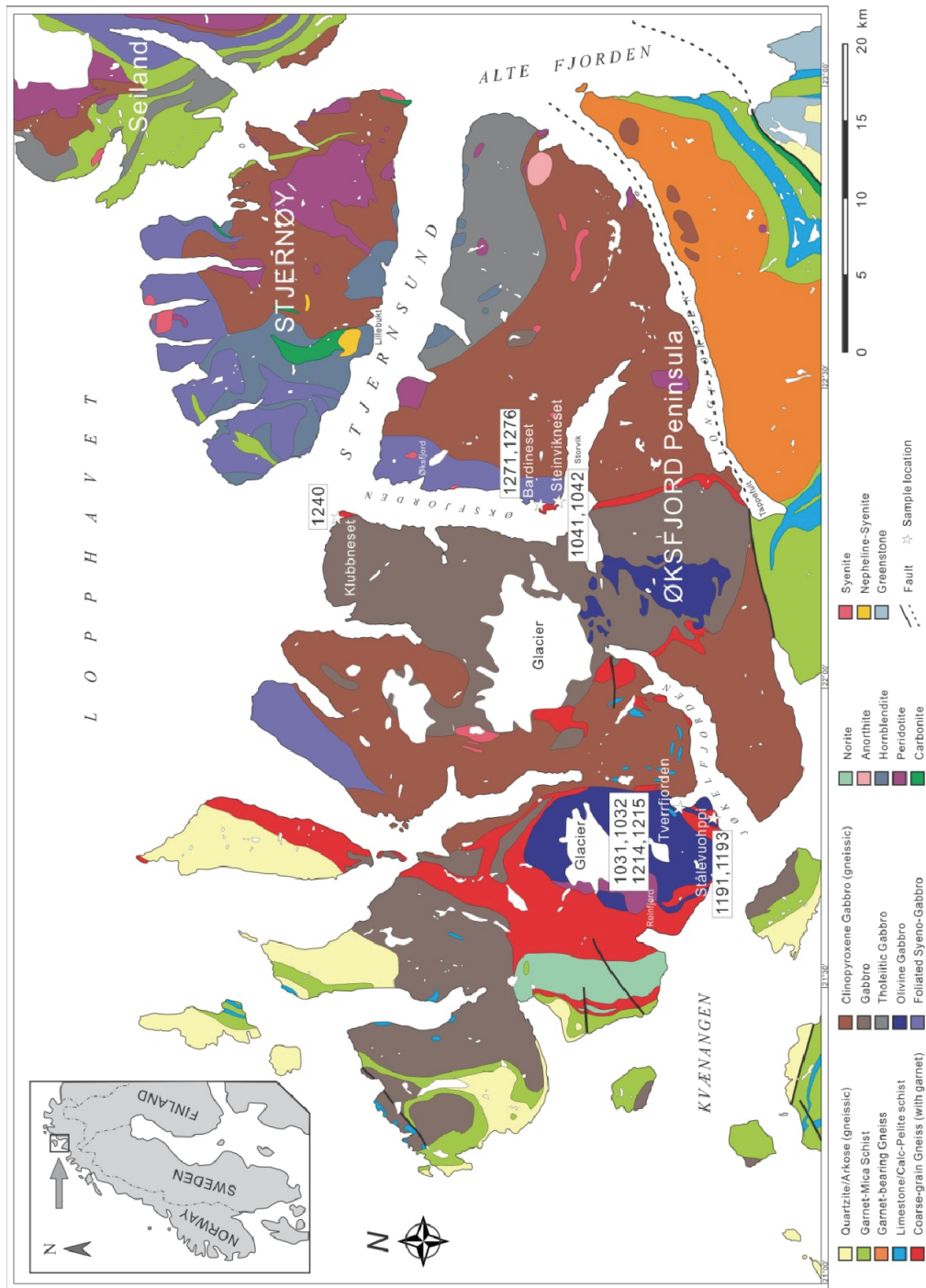


Fig. 1 Geological sketch of the Seiland Igneous Province, Northern Norway modified after Roberts (1974). White stars represent the sampling locations.



## 3. Geological background and sampling

### 3.1 Geological background

The Seiland Igneous Province (SIP) now resides within and as a part of the highest nappe of the Kalak Nappe Complex (KNC) which belongs to the Middle Allochthon, occupying an area of nearly 5,000 km<sup>2</sup> on the islands of Seiland, Sørøy and Stjernøy, and on the Øksfjord Peninsula in the northern Finnmark, Norway (Fig. 1).

The Seiland igneous province has a long and complex history concerning magmatic evolution: voluminous ultramafic rocks at 829±18 Ma (Krogh and Elvevold, 1990), layered gabbroic plutons of 700±33 Ma, 604±44 Ma and 570 Ma (Daly et al., 1991; Roberts et al., 2006) and a final stage of calc-alkaline intrusions represented by alkaline pyroxenite, syenite, nepheline syenite and carbonatite at 574± 5 Ma (Roberts et al., 2010). All these various rocks are considered to represent a synorogenic (Caledonian orogenic belt) intrusive activity evolved from tholeiitic basalt, compositionally ranging from high-K calc-alkaline magmas, through alkaline olivine basalt and picrite and finally to highly differentiated alkaline magmas and carbonatite (Appleyard, 1974; Robins and Gardner, 1975; Sturt et al., 1967; Sturt et al., 1978).

The metasedimentary succession of the KNC which hosts the SIP deposited between ca. 840 and 910 Ma (long time prior to the opening of Iapetus Ocean) (Kirkland et al., 2007), and represents an exotic allochthonous mobile belt that was juxtaposed and sutured to Baltica at ca. 710 Ma (Fall et al., 2007; Kirkland et al., 2008a; Kirkland et al., 2006b; Kirkland et al., 2008b; Roberts et al., 2007). Based on U–Pb zircon dating of discordant plutonic rocks within the nappe, several tectonothermal events have been identified in the KNC (Akselsen, 1982; Daly et al., 1991; Kirkland et al., 2006a; Kirkland et al., 2006b; Kirkland et al., 2005; Kirkland et al., 2007; Sturt et al., 1978). However, the corresponding metamorphic events have not been widely investigated in this area. The present researches (Elvevold and Reginiussen, 1996; Elvevold et al., 1994) were performed on metapelitic xenolith in metagabbro of 929 ±18 Ma, for which three metamorphic stages could be identified: (1) Contact metamorphism: 930-960 °C / 5-6.5 kb; (2) Cooling: 700-750 °C / 5-7 kb; (3) Compression: 650-700 °C / 8-10 kb.

### 3.2 Sampling

During the excursions in 2003 and 2009, several tens of paragneisses from various locations of Øksfjord peninsula were collected, and eleven of them from five locations (Tverrfjorden, Stålevuohppi, Steinvikneset, Bardineset, and Klubbneset) were investigated in this

study. Four samples (1031, 1032, 1214 and 1215) were collected from Tverrfjorden, and two samples (1191 and 1193) were collected from Stålevuohppi, these two regions are distributed along the Jøkelfjorden bay (Fig. 1). In addition, two samples (1041 and 1042) were collected from Steinvikneset, two samples (1271 and 1276) were collected from Bardineset, one sample (1240) was collected from Klubbneset, and these three regions locate along the Øksfjorden bay (Fig. 1).

## 4. Methods

### 4.1 Whole-rock analysis

The composition of the rock samples was analyzed at the Institute of Geosciences, University of Freiburg. A Philips 2404 X-ray fluorescence spectrometer was used with element specific acceleration voltage 30 kV and current 40 nA, with fused beads for major elements and powder pellets for minor elements, respectively. Loss on ignition (LOI) was determined to complete the XRF analyses, and total Fe is reported as  $\text{Fe}_2\text{O}_3\text{tot}$ . Bulk compositions are listed in Table 1.

### 4.2 Mineral analysis

Mineral analyses were performed by electron beam microanalysis using wavelength-dispersive spectrometry (WDS) of a digital CAMECA SX100 electron microprobe at the Institute of Geosciences, University of Freiburg. During analyses an accelerating voltage of 15 kV and a current of 20 nA were used. Beam diameter was 0.5  $\mu\text{m}$  (for feldspar, sometimes 5  $\mu\text{m}$ ). We used the stoichiometric method of Droop (1987) to estimate the ferrous and ferric iron contents in pyroxene, biotite and garnet. Representative analyses of minerals are represented in table 2-7 and Fig. 2.

### 4.3 Cathodoluminescence

Cathodoluminescence (CL) images were obtained by ELM-3R luminoscope at the Institute of Geosciences, University of Freiburg with an accelerating voltage of 12 kV and beam current of 0.8 mA. All the CL images were captured by Leica DC500 camera with exposure time of 60s.

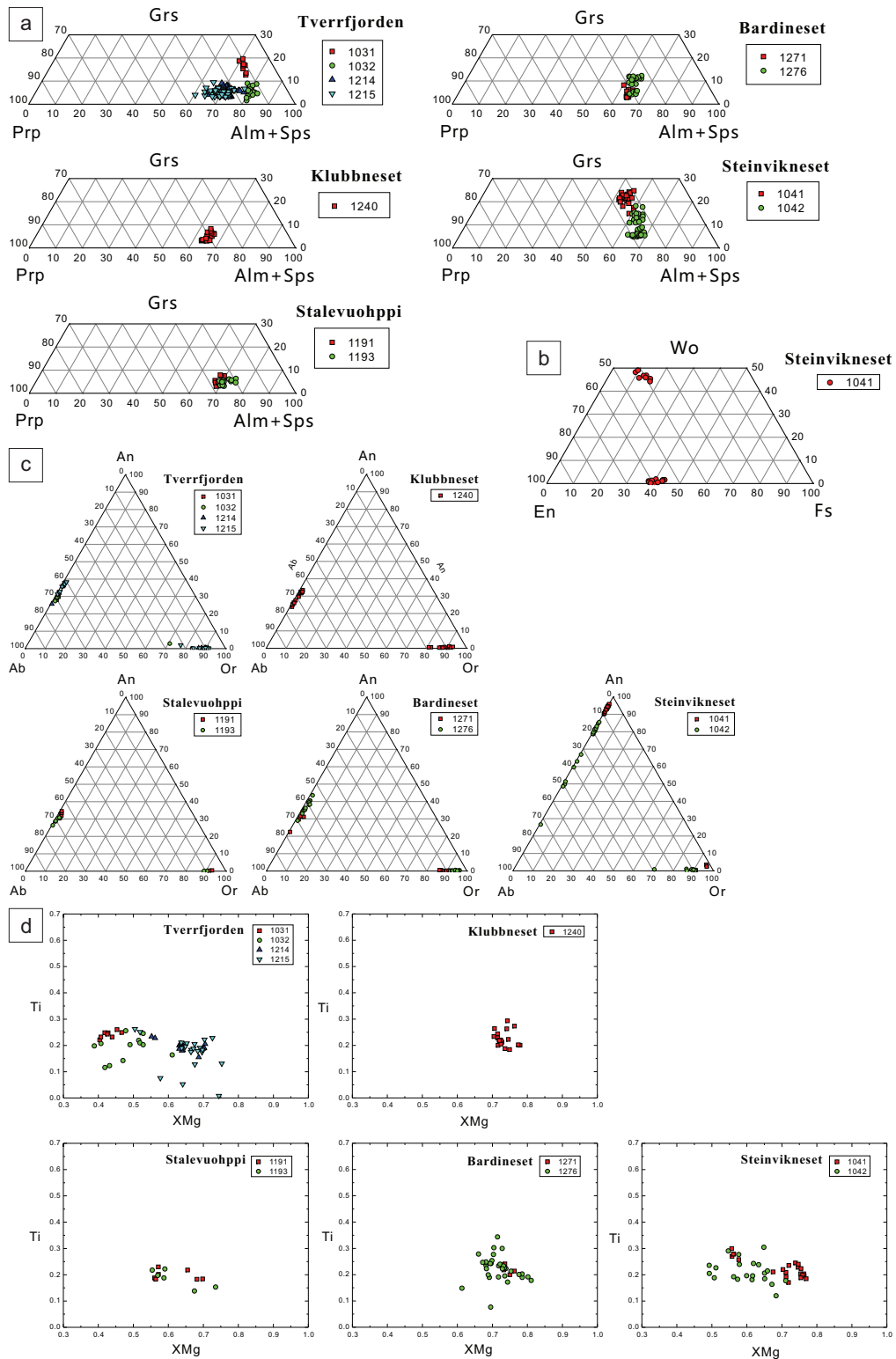


Fig. 2 Compositional plots for garnet (a), pyroxene (b), feldspar (c), and biotite (d).

Table 1 Main compositions of samples and the input for Theriak /Domio software

Area Sample Oxide wt%	Tverrfjorden				Stålevothppi		Steinvikneset		Bardneset		Klubbnaset 1240	
	1031	1032	1214	1215	1191-A dark	1191-B light	1193	1041-A light	1041-B dark	1042		1271
SiO <sub>2</sub>	61.35	71.72	61.48	77.01	65.54	71.04	59.29	87.73	58.04	79.73	59.79	50.35
TiO <sub>2</sub>	1.17	0.6	1.11	0.47	1.17	0.59	1.14	0.18	2.13	0.53	1.29	2.19
Al <sub>2</sub> O <sub>3</sub>	16.27	13.42	17.82	11.75	16.38	12.15	17.88	5.54	12.75	9.64	18.39	20.79
Fe <sub>2</sub> O <sub>3</sub> tot	8.74	2.69	8.3	2.9	5.33	9.89	9.51	0.34	11.18	2.11	9.78	13.9
MnO	0.17	0.05	0.17	0.05	0.08	0.22	0.2	0.0	0.18	0.04	0.15	0.28
MgO	1.42	0.71	2.19	0.77	1.86	1.99	2.42	0.29	5.95	0.51	2.83	4.38
CaO	3.69	2.01	2.27	2.04	3.55	2.01	1.49	0.26	7.65	2.69	1.27	4.09
Na <sub>2</sub> O	3.35	2.82	2.16	2.11	3.61	1.66	2.01	0.27	0.31	0.65	1.59	2.9
K <sub>2</sub> O	1.92	3.72	3.29	2.21	1.5	0.59	5.57	3.9	0.8	2.19	3.97	1.29
P <sub>2</sub> O <sub>5</sub>	0.48	0.08	0.21	0.08	0.16	0.17	0.13	0.02	0.28	0.04	0.12	0.08
LOI	0.0	0.55	0.0	0.09	0.26	0.0	0.0	0.17	0.0	0.17	0.0	0.0
Sum	98.56	98.37	99.0	99.48	99.44	100.31	99.64	98.7	99.27	98.3	99.18	100.25
Input for Domio software												
Si	59.56	69.34	59.32	74.31	62.29	69.42	56.69	86.98	57.03	79.12	57.76	47.89
Ti	0.85	0.44	0.81	0.34	0.84	0.43	0.82	0.13	1.57	0.4	0.94	1.57
Al	18.62	15.29	20.26	13.36	18.35	13.99	20.15	6.47	14.77	11.27	20.94	23.3
Fe	6.39	1.96	6.03	2.11	3.81	7.27	6.84	0.25	8.27	1.58	7.11	9.95
Mg	2.06	1.02	3.15	1.11	2.64	2.9	3.45	0.43	8.72	0.75	4.08	6.21
Ca	3.84	2.08	2.35	2.11	3.61	2.1	1.53	0.28	8.05	2.86	1.31	4.17
Na	6.31	5.29	4.04	3.95	6.65	3.15	3.73	0.52	0.59	1.25	2.98	5.35
K	2.38	4.59	4.05	2.72	1.82	0.74	6.79	4.93	1.0	2.77	4.89	1.57
O	165.39	172.48	166.21	177.99	168.06	174.91	162.33	187.63	165.19	183.14	165.23	157.65



Table 3 Representative microprobe analyses of pyroxene

Sample Point	1041 cpx 058	1041 cpx 073	1041 cpx 080	1041 cpx 084	1041 cpx 092	1041 opx 059	1041 opx 067	1041 opx 077	1041 opx 082	1041 opx 091
	Clinopyroxene					Orthopyroxene				
SiO <sub>2</sub>	52.31	52.47	53.4	52.16	52.46	51.67	52.67	53.02	51.13	52.09
TiO <sub>2</sub>	0.09	0.2	0.13	0.1	0.21	0.07	0.03	0.07	0.01	0.05
Al <sub>2</sub> O <sub>3</sub>	1.38	1.35	1.72	1.15	1.53	1.06	1.37	0.89	0.96	0.87
Cr <sub>2</sub> O <sub>3</sub>	0.06	0.05	0.02	0.03	0.07	0.06	0.04	0.05	0	0.03
FeOtotal	7.39	9.54	7.75	9.16	9.92	26.05	24.87	24.96	26.73	25.5
MnO	0.13	0.27	0.17	0.26	0.27	0.44	0.34	0.49	0.62	0.5
MgO	14.41	13.3	14.3	13.6	13.07	20.15	20.56	21.12	18.94	20.02
CaO	23.28	22.97	23.11	22.54	22.25	0.44	0.35	0.52	0.52	0.47
Na <sub>2</sub> O	0.31	0.23	0.34	0.27	0.18	0.03	0.03	0.05	0.04	0.01
K <sub>2</sub> O	0	0	0.01	0	0	0	0	0	0	0
Total	99.360	100.380	100.950	99.270	99.960	99.970	100.260	101.170	98.950	99.540
Cations per 6 oxygens										
Si	1.949	1.955	1.961	1.960	1.967	1.954	1.975	1.971	1.966	1.979
Ti	0.003	0.006	0.004	0.003	0.006	0.002	0.001	0.002	0.000	0.001
Al <sup>(IV)</sup>	0.051	0.045	0.039	0.040	0.033	0.046	0.025	0.029	0.034	0.021
Al <sup>(VI)</sup>	0.009	0.015	0.036	0.011	0.034	0.002	0.036	0.010	0.010	0.018
Cr	0.002	0.001	0.001	0.001	0.002	0.002	0.001	0.001	0.000	0.001
Fe <sup>3+</sup>	0.057	0.034	0.020	0.042	0.000	0.040	0.000	0.017	0.026	0.000
Fe <sup>2+</sup>	0.173	0.263	0.218	0.246	0.311	0.784	0.780	0.759	0.833	0.810
Mn	0.004	0.009	0.005	0.008	0.009	0.014	0.011	0.015	0.020	0.016
Mg	0.800	0.739	0.783	0.762	0.730	1.136	1.149	1.171	1.086	1.134
Ca	0.929	0.917	0.909	0.908	0.894	0.018	0.014	0.021	0.021	0.019
Na	0.022	0.017	0.024	0.020	0.013	0.002	0.002	0.004	0.003	0.001
K	0.000	0.000	0.000	0.000	0.000	0.000	0.000	0.000	0.000	0.000
Total	4.000	4.000	4.000	4.000	3.999	4.000	3.994	4.000	4.000	4.000
Endmembers										
Fs	9.2	14.0	11.8	13.0	16.7	40.0	40.4	38.8	42.7	41.4
Wo	48.2	46.8	45.7	46.6	44.2	1.9	0.0	1.3	1.6	0.5
En	42.6	39.3	42.5	40.3	39.2	58.0	59.6	59.9	55.7	58.0

Table 4 Representative microprobe analyses of feldspar.

Sample Point	1031 pl 001	1032 pl 005	1214 pl 015	1215 pl 004	1041 pl 025	1042 pl 103 plagioclase	1191 pl 001	1193 pl 015	1240 pl 062	1271 pl 003	1276 pl 039	1214 kf 016	1215 kfs 005	1191 kfs 004 K-feldspar	1193 kf 013	1271 kf 39
SiO <sub>2</sub>	61.28	61.9	62.01	58.26	44.87	47.97	60	60.92	62.09	59.44	57.71	63.81	64.72	64.03	64.39	64.15
TiO <sub>2</sub>	0	0	0.01	0	0	0.02	0	0	0	0	0	0	0	0	0	0
Al <sub>2</sub> O <sub>3</sub>	24.76	24.79	24.74	26.39	35.76	33.71	24.94	25.13	24.38	25.49	26.51	19.13	19.55	19.22	18.72	19.01
Cr <sub>2</sub> O <sub>3</sub>	0	0.01	0	0.03	0.02	0	0.03	0	0.02	0	0	0.01	0.01	0.03	0	0.01
FeOtotal	0.01	0.06	0.01	0.11	0	0	0	0.04	0.01	0.08	0.08	0.04	0	0	0.06	0.06
MnO	0	0.04	0	0.01	0	0	0	0.01	0.02	0.03	0.02	0.01	0	0	0	0.03
MgO	0.01	0	0	0	0	0	0	0.01	0	0	0	0.01	0	0.02	0	0
CaO	6.3	6.19	5.56	7.78	19.16	16.64	6.47	6.44	5.34	6.37	8.38	0.07	0.39	0.09	0.04	0.05
Na <sub>2</sub> O	8.2	8.27	8.85	6.83	0.68	2.12	7.36	7.88	8.73	7.41	6.94	1.28	2.32	0.69	1	1.07
K <sub>2</sub> O	0.23	0.23	0.09	0.25	0.01	0.03	0.35	0.37	0.11	0.52	0.28	14.54	12.62	14.71	14.72	14.54
Total	100.79	101.49	101.26	99.56	100.61	100.49	99.15	100.75	100.74	99.27	99.92	98.90	99.61	98.79	98.93	98.92
Cations per 8 oxygens																
Si	2.705	2.713	2.720	2.613	2.060	2.187	2.690	2.692	2.735	2.667	2.590	2.966	2.963	2.974	2.989	2.977
Ti	0.000	0.000	0.000	0.000	0.000	0.001	0.000	0.000	0.000	0.000	0.000	0.000	0.000	0.000	0.000	0.000
Al	1.288	1.281	1.279	1.395	1.935	1.811	1.318	1.309	1.266	1.348	1.402	1.048	1.055	1.052	1.024	1.040
Cr	0.000	0.000	0.000	0.001	0.001	0.000	0.001	0.000	0.001	0.000	0.000	0.000	0.000	0.001	0.000	0.000
Fe	0.000	0.002	0.000	0.000	0.004	0.000	0.000	0.000	0.001	0.000	0.003	0.002	0.000	0.000	0.002	0.002
Mn	0.000	0.001	0.000	0.000	0.000	0.000	0.000	0.000	0.001	0.001	0.001	0.000	0.000	0.000	0.000	0.001
Mg	0.001	0.000	0.000	0.000	0.000	0.000	0.000	0.000	0.001	0.000	0.000	0.001	0.000	0.001	0.000	0.000
Ca	0.298	0.291	0.261	0.374	0.942	0.813	0.311	0.305	0.252	0.306	0.403	0.003	0.019	0.004	0.002	0.002
Na	0.702	0.703	0.753	0.594	0.061	0.187	0.640	0.675	0.746	0.645	0.604	0.115	0.206	0.062	0.090	0.096
K	0.013	0.013	0.005	0.014	0.001	0.002	0.020	0.021	0.006	0.030	0.016	0.862	0.737	0.872	0.872	0.861
Total	5.008	5.004	5.019	4.992	5.003	5.001	4.980	5.002	5.008	4.997	5.019	4.998	4.981	4.966	4.980	4.981
Endmembers																
An	29.42	28.89	25.64	38.07	93.91	81.12	32.02	30.46	25.11	31.23	39.39	0.36	1.99	0.48	0.21	0.26
Ab	69.30	69.84	73.86	60.48	6.03	18.70	65.92	67.45	74.28	65.74	59.04	11.76	21.40	6.62	9.34	10.03
Or	1.28	1.28	0.49	1.46	0.06	0.17	2.06	2.08	0.62	3.04	1.57	87.89	76.61	92.90	90.45	89.71

Table 5 Representative microprobe analyses of biotite and muscovite

Sample	1031	1032	1041	1042	1191	1193	1214	1215	1240	1271	1276
Point	bt 005	bt 008	bt 008	bt 008	bt 001	bt 018	bt 017	bt 088	bt 023	bt 41	bt 001
Wt%											
SiO <sub>2</sub>	35.09	36.31	38.78	36.55	38.04	36.9	36.74	39.19	38.37	38.48	38.08
TiO <sub>2</sub>	4.21	2.37	4.64	3.99	3.68	4.28	4.66	0.17	5.31	4.87	4.73
Al <sub>2</sub> O <sub>3</sub>	17.14	17.87	16.02	18.54	17.35	17.71	17.45	18.47	15.3	15.5	15.96
Cr <sub>2</sub> O <sub>3</sub>	0	0.07	0.07	0.06	0.13	0.08	0.08	0	0.09	0.12	0.06
FeO <sub>total</sub>	21.81	20.93	10.08	17.44	12.47	16.15	16.88	10.91	11.44	10.62	12.57
MnO	0.03	0.08	0	0	0	0.01	0	0	0.03	0	0.04
MgO	8.28	8.93	16.6	9.5	14.99	11.25	11.68	17.84	15.43	16.57	15.1
CaO	0.01	0.18	0.05	0.02	0.07	0.03	0.01	0.06	0.02	0.01	0.05
Na <sub>2</sub> O	0.04	0.13	0.11	0.03	0.14	0.04	0.06	0.07	0.06	0.03	0.04
K <sub>2</sub> O	8.68	8.48	9.57	9.62	8.91	9.47	9.74	9.66	9.89	9.65	9.63
F	0.21	0.35	1.08	0.18	1.27	0.95	1.06	1.63	1.71	1.35	1.55
Cl	0.02	0.01	0.14	0.03	0.04	0.02	0.01	0.01	0	0.02	0.03
-O=F+Cl	0.09	0.15	0.49	0.08	0.54	0.40	0.45	0.69	0.72	0.57	0.66
H <sub>2</sub> O <sub>calc</sub>	4.19	4.17	4.03	4.30	3.92	3.98	3.99	3.91	3.72	3.92	3.80
Total <sub>calc</sub>	99.39	99.37	99.46	99.97	99.16	99.49	100.84	99.59	98.94	99.19	99.40
Cations per 11 oxygens											
Si	2.451	2.508	2.540	2.495	2.516	2.495	2.450	2.509	2.538	2.530	2.515
Ti	0.221	0.123	0.229	0.205	0.183	0.218	0.234	0.008	0.264	0.241	0.235
Al <sup>(IV)</sup>	1.411	1.455	1.237	1.492	1.352	1.411	1.372	1.394	1.193	1.201	1.243
Al <sup>(VI)</sup>	0.000	0.000	0.000	0.000	0.000	0.000	0.000	0.000	0.000	0.000	0.000
Cr	0.000	0.004	0.004	0.003	0.007	0.004	0.004	0.000	0.005	0.006	0.003
Fe <sup>3+</sup>	1.274	1.209	0.552	0.996	0.690	0.913	0.941	0.584	0.633	0.584	0.694
Fe <sup>2+</sup>	0.000	0.000	0.000	0.000	0.000	0.000	0.000	0.000	0.000	0.000	0.000
Mn	0.002	0.005	0.000	0.000	0.000	0.001	0.000	0.000	0.002	0.000	0.002
Mg	0.862	0.919	1.621	0.967	1.478	1.134	1.161	1.703	1.522	1.624	1.487
Ca	0.001	0.013	0.004	0.001	0.005	0.002	0.001	0.004	0.001	0.001	0.004
Na	0.005	0.017	0.014	0.004	0.018	0.005	0.008	0.009	0.008	0.004	0.005
K	0.773	0.747	0.800	0.838	0.752	0.817	0.829	0.789	0.835	0.809	0.812
Total	7.000	7.000	7.000	7.000	7.000	7.000	7.000	7.000	7.000	7.000	7.000
Volatiles											
F	0.046	0.076	0.224	0.039	0.266	0.203	0.224	0.330	0.358	0.281	0.324
Cl	0.002	0.001	0.016	0.003	0.004	0.002	0.001	0.001	0.000	0.002	0.003
OH	1.951	1.922	1.761	1.958	1.730	1.795	1.775	1.669	1.642	1.717	1.673
X <sub>Mg</sub>	0.404	0.432	0.746	0.493	0.682	0.554	0.552	0.745	0.706	0.736	0.682

Table 6 Representative microprobe analyses of hercynite and corundum.

Sample	1042	1042	1214	1214	1214	1214	1214	1214	1214
Point	hc 144	hc 148	Hc 027	Hc 028	Hc 030	Hc 031	Hc 032	Co 024	Co 025
Comment			Hercynite				Corundum		
SiO <sub>2</sub>	0.02	0.01	0.03	0.03	0.04	0.00	0.03	0.03	0.03
TiO <sub>2</sub>	0.00	0.03	0.00	0.01	0.02	0.00	0.00	0.00	0.00
Al <sub>2</sub> O <sub>3</sub>	61.12	61.07	60.16	59.93	60.76	59.69	60.11	100.43	100.55
Cr <sub>2</sub> O <sub>3</sub>	0.28	0.28	0.13	0.17	0.22	0.10	0.29	0.06	0.04
FeO <sub>total</sub>	21.54	21.57	19.81	19.53	24.97	19.84	20.07	0.49	0.62
MnO	0.06	0.05	0.09	0.04	0.07	0.08	0.02	0.00	0.01
MgO	7.34	7.44	5.43	5.45	6.57	5.51	5.33	0.00	0.00
CaO	0.01	0.01	0.01	0.00	0.01	0.00	0.01	0.04	0.02
NiO	0.26	0.29	0.22	0.32	0.29	0.38	0.31	0.00	0.00
ZnO	10.25	9.85	15.75	15.62	9.44	15.53	15.50	0.02	0.00
V <sub>2</sub> O <sub>3</sub>	0.00	0.00	0.00	0.00	0.00	0.00	0.00	0.00	0.00
Total	100.88	100.60	101.63	101.10	102.39	101.13	101.67	101.07	101.27
Cations per 4 oxygens								Cations per 3 oxygens	
Si	0.001	0.000	0.001	0.001	0.001	0.000	0.001	0.001	0.001
Ti	0.000	0.001	0.000	0.000	0.000	0.000	0.000	0.000	0.000
Al	1.981	1.983	1.977	1.979	1.957	1.971	1.976	1.991	1.990
Cr	0.006	0.006	0.003	0.004	0.005	0.002	0.006	0.001	0.001
Fe <sup>3+</sup>	0.011	0.010	0.018	0.015	0.035	0.027	0.016	0.007	0.009
Fe <sup>2+</sup>	0.484	0.487	0.444	0.442	0.535	0.438	0.452	0.000	0.000
Mn	0.001	0.001	0.002	0.001	0.002	0.002	0.000	0.000	0.000
Mg	0.301	0.306	0.226	0.228	0.268	0.230	0.222	0.000	0.000
Ca	0.000	0.000	0.000	0.000	0.000	0.000	0.000	0.001	0.000
Ni	0.006	0.006	0.005	0.007	0.006	0.009	0.007	0.000	0.000
Zn	0.208	0.200	0.324	0.323	0.190	0.321	0.319	0.000	0.000
V	0.000	0.000	0.000	0.000	0.000	0.000	0.000	0.000	0.000
Total	3.000	3.000	3.000	3.000	3.000	3.000	3.000	2.000	2.000

Table 7 Representative microprobe analyses of ilmenite.

Sample	1031	1041	1042	1125	1191	1193	1214	1215	1276
Point	ilm 022	ilm 075	ilm 019	ilm 024	ilm 009	ilm 016	ilm 049	ilm 073	ilm 020
Wt%									
SiO <sub>2</sub>	0.02	0.02	0.00	0.24	0.02	0.04	0.01	0.02	0.16
TiO <sub>2</sub>	52.91	51.27	52.25	50.67	52.16	52.78	52.68	52.51	51.55
Al <sub>2</sub> O <sub>3</sub>	0.00	0.00	0.00	0.08	0.00	0.00	0.00	0.00	0.00
Cr <sub>2</sub> O <sub>3</sub>	0.00	0.01	0.03	0.05	0.00	0.02	0.09	0.04	0.04
Fe <sub>total</sub>	45.23	45.76	45.13	45.45	44.86	44.16	46.08	45.81	45.01
MnO	0.34	0.56	0.20	1.07	0.27	0.19	0.10	0.19	0.80
MgO	0.06	0.05	0.65	0.39	0.41	0.90	1.41	1.34	0.05
CaO	0.02	0.06	0.03	0.05	0.04	0.06	0.00	0.04	0.00
NiO	0.03	0.06	0.00	0.02	0.00	0.02	0.00	0.02	0.02
ZnO	0.14	0.00	0.10	0.00	0.15	0.33	0.00	0.17	0.33
V <sub>2</sub> O <sub>3</sub>	0.00	0.00	0.00	0.00	0.00	0.00	0.00	0.00	2.58
Total	98.75	97.79	98.39	98.02	97.91	98.50	100.37	100.14	100.54
Cations per 3 oxygens									
Si	0.001	0.001	0.000	0.006	0.001	0.001	0.000	0.000	0.004
Ti	1.012	0.995	1.002	0.977	1.006	1.007	0.985	0.985	0.972
Al	0.000	0.000	0.000	0.002	0.000	0.000	0.000	0.000	0.000
Cr	0.000	0.000	0.001	0.001	0.000	0.000	0.002	0.001	0.001
Fe <sup>3+</sup>	0.000	0.009	0.000	0.031	0.000	0.000	0.027	0.028	0.000
Fe <sup>2+</sup>	0.962	0.978	0.963	0.943	0.962	0.937	0.931	0.927	0.944
Mn	0.007	0.012	0.004	0.023	0.006	0.004	0.002	0.004	0.017
Mg	0.002	0.002	0.025	0.015	0.016	0.034	0.052	0.050	0.002
Ca	0.001	0.002	0.001	0.001	0.001	0.002	0.000	0.001	0.000
Ni	0.001	0.001	0.000	0.000	0.000	0.000	0.000	0.000	0.000
Zn	0.003	0.000	0.002	0.000	0.003	0.006	0.000	0.003	0.006
V	0.000	0.000	0.000	0.000	0.000	0.000	0.000	0.000	0.052
Total	1.988	2.000	1.997	2.000	1.994	1.992	2.000	2.000	1.998



## 4.4 Phase diagram modeling

Bulk composition used in phase diagram modeling are normalized as atom proportion and listed in Table 1. For sample 1041 and 1091, XRF analyses were performed on dark and light layer respectively, which could easily be separated. Other bulk compositions are derived from homogenous sample that are considered as effective bulk composition required for modeling. The  $\text{TiO}_2\text{-Na}_2\text{O-CaO-K}_2\text{O-FeO-MgO-Al}_2\text{O}_3\text{-SiO}_2\text{-H}_2\text{O}$  (TiNCKFMASH) component system was considered for all the samples. Mn was omitted because the trace amounts in bulk rock XRF results and its exclusive presence in garnet. The water activity was kept to one for all modeling.

Mineral assemblage stability diagrams were calculated using Theriak-Domino software (de Capitani and Brown, 1987; de Capitani and Petrakakis, 2010) with the readable translation of the THERMOCALC database (Holland and Powell, 1998). Mineral solution models used are listed in following: garnet, biotite, spinel, ilmenite and melt (White et al., 2007); cordierite and epidote (Holland and Powell, 1998); clinopyroxene (Holland and Powell, 1996); orthopyroxene (White et al., 2002); amphibole (Diener et al., 2007); feldspar (Holland and Powell, 2003); chloritoid (White et al., 2000); chlorite (Holland et al., 1998); white mica (Coggon and Holland, 2002); sapphirine (Kelsey et al., 2004).

## 5 Petrography and mineral chemistry

All samples investigated show distinctive gneiss foliation with parallel alternating dark and light layers on outcrop and microprobe scales. Samples will be described according to the sampling areas below.

### 5.1 Textures under CL

Cathodoluminescence (CL) images are employed to reveal the textures of minerals, especially for K-feldspar, plagioclase and quartz which are usually related with melt phase.

Quartz shows typical deep blue to black color (e.g. Fig. 3k). K-feldspars are characterized of bright blue core and gray rim (e.g. Fig. 4j, Fig. 6m), which have different Ab components. The coarse-grained plagioclases ( $\text{An}=30$ ) show light green color (Fig. 3d). Corundum and sillimanite have remarkable bright origin color under CL (e.g. Fig. 4d). Fe-rich minerals such as garnet, biotite, Fe-Ti oxides are black under CL.

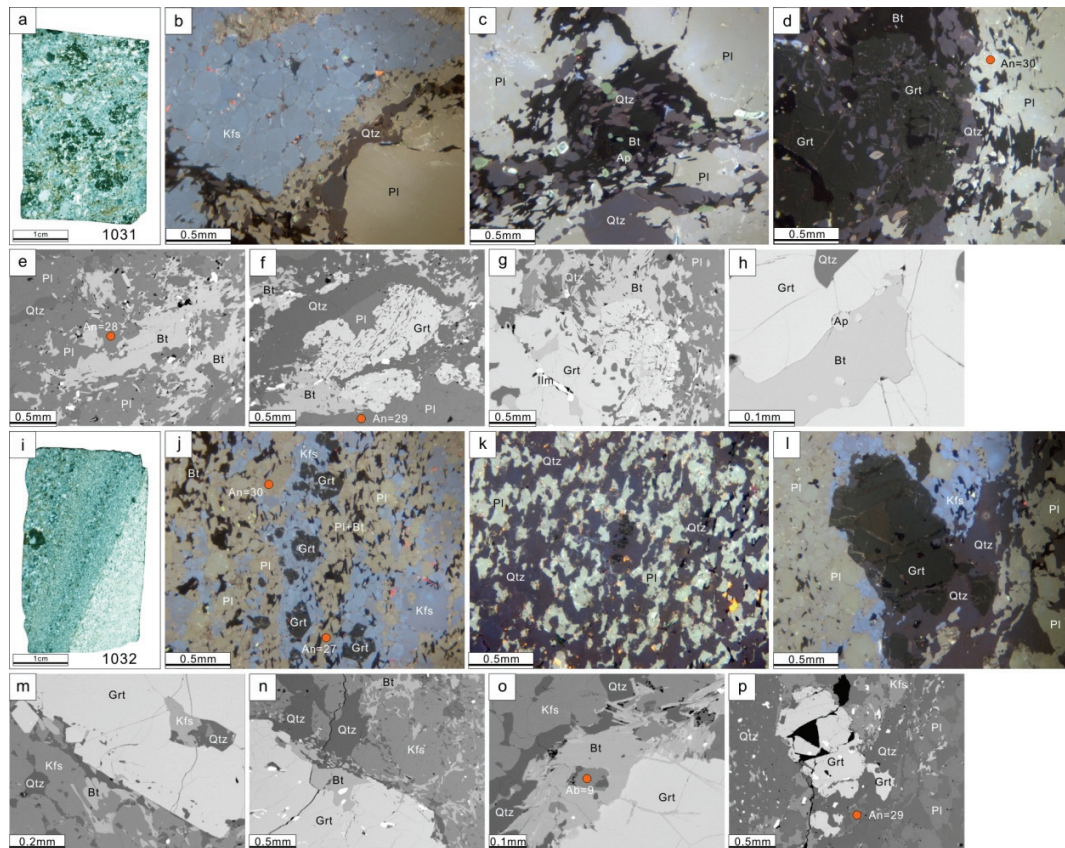


**Fig. 3** Cathodoluminescence images and BSE images show textures of sample 1031 and 1032. (a-h): CL and BSE images of sample 1031; (i-p): CL and BSE images of sample 1032. See text for explanations.

## 5.2 Samples from Tverrfjorden

### 5.2.1 Sample 1031

Sample 1034 is characterized by large garnet porphyroblast under thin section (Fig. 3a). There is no obvious alternating layer structure for this sample. Large garnet porphyroblast are enriched of biotite, quartz and ilmenite inclusions (Fig. 3g-h). The garnet overgrowth and small garnets in the matrix are filled by tiny quartz inclusions (Fig. 3f-g). Plagioclase, K-feldspar, quartz, and biotite constitute the rock matrix. Apatite grains (Fig. 3c) are observed both in the matrix and as inclusion.

From the core of large porphyroblast to the overgrowth rim, garnet compositions of sample 1031 vary from  $\text{Alm}_{77}\text{Prp}_{13}\text{Grs}_{10}$  to  $\text{Alm}_{70}\text{Prp}_{11}\text{Grs}_{19}$  (Fig.2a).

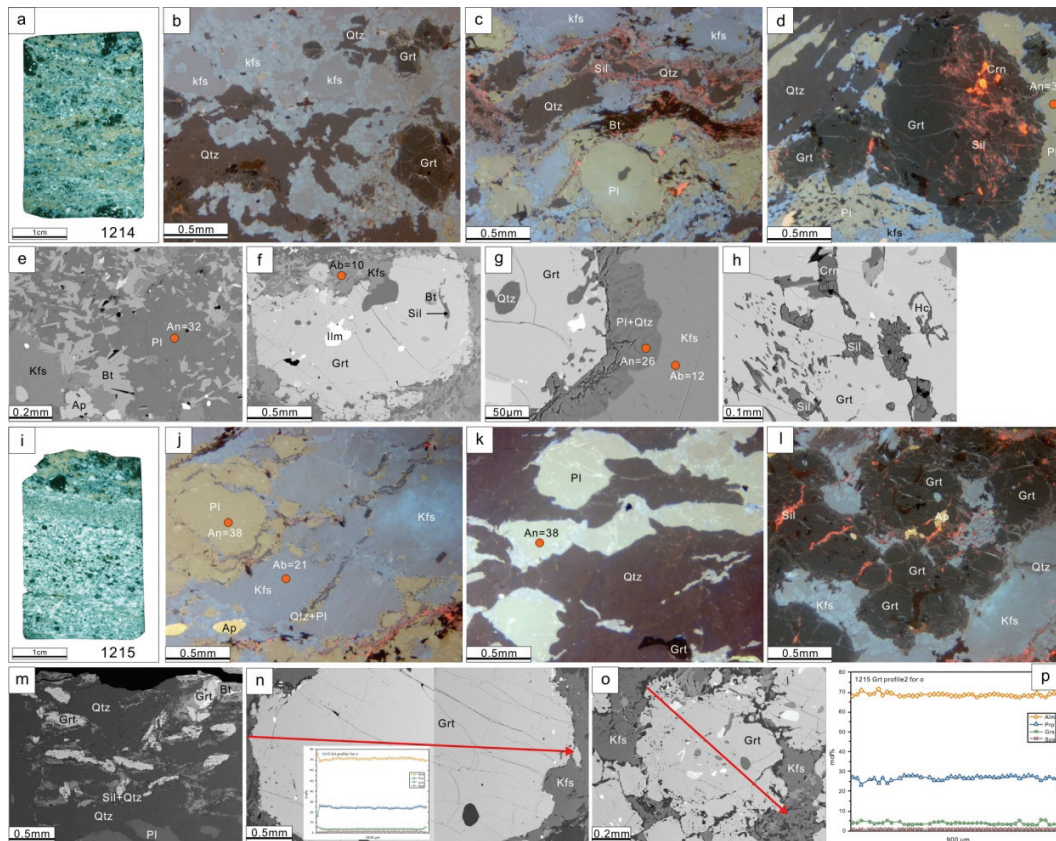


**Fig. 4** Cathodoluminescence images and BSE images show textures of sample 1214 and 1215. (a-h): CL and BSE images of sample 1214; (i-p): CL and BSE images of sample 1215. See text for explanations.

### 5.2.2 Sample 1032

Sample 1032 shows remarkable gneiss structure with alternating light and dark layers (cross polarized, Fig. 3i). The light layers are composed of plagioclase, biotite, K-feldspar and small garnet (diameter less than 0.2 mm) (Fig. 3j). Dark layers have the same mineral assemblage but with higher quartz contents (Fig. 3k). The small garnets are usually surrounded by K-feldspar (Fig. 3j and Fig. 3i). One large garnet porphyroblast have been observed in sample 1032 (Fig. 3i, Fig. 3m-o). The large garnet porphyroblast have been replaced by biotite at margin (Fig. 3n-o).

Two groups of garnet could be identified by their textural and compositional features: the rare large garnet porphyroblasts (Fig. 3m) with  $\text{Alm}_{80}\text{Prp}_{17}\text{Grs}_2$ ; pervasive idioblastic garnets (Fig. 3j) with average composition of  $\text{Alm}_{80}\text{Prp}_{14}\text{Grs}_6$ .

### **5.2.3 Sample 1214**

Sample 1214 represents alternating light and brown layers (Fig. 4a). The light layers are composed of plagioclase (An=32), quartz, K-feldspar and garnet (Fig. 4b-c and Fig. 4e). Corundum, hercynite and sillimanite inclusions have been observed in one garnet porphyroblast (Fig. 4d and Fig. 4h). This special garnet has composition of  $\text{Alm}_{73}\text{Prp}_{22}\text{Grs}_4$ . Ilmenite, biotite, quartz and sillimanite are present as inclusions in various garnet grains (Fig. 4f). Garnet overgrowth which related with melt phase (Pl + Qtz intergrowth, Fig. 4g) have composition of  $\text{Alm}_{65}\text{Prp}_{30}\text{Grs}_4$ .

### **5.2.4 Sample 1215**

Two parts could be observed under thin section of sample 1215: upper brown coarse-grained part with large garnet porphyroblasts; lower light part with small garnet. The former part is composed of sillimanite, K-feldspar (Ab=12) and garnet (Fig. 7i). Sillimanite aggregate are usually distributed in the grain boundaries of garnet (Fig. 4i). Garnet porphyroblasts have thin overgrowth rims, which are enriched by quartz inclusions (Fig. 4o).

For the fine-grained part, plagioclase (An=38) and K-feldspar (Ab=21) are the main mineral constituents, with intergranular Pl + Qtz + Sil intergrowth (Fig. 4j-k and Fig. 4m).

## **5.3 Samples from Stålevuohppi**

### **5.3.1 Sample 1191**

The gneiss structure is distinct in sample 1191 (Fig. 5a). The brown layer is composed of large plagioclase and small plagioclase and biotite grains (Fig. 5b). In contrast, the light garnet-rich layer is composed of plagioclase, quartz, K-feldspar and garnet (Fig. 5c and Fig. 5g). Garnets usually have overgrowth rims when contacts with the brown biotite-rich layer (Fig. 5e-f).

### **5.3.2 Sample 1193**

Sample 1193 has similar textural signature like sample 1191. Quartz, K-feldspar, plagioclase and garnet constitute the light garnet-rich layer (Fig. 5i-m). The brown layer is composed of large K-feldspar and small plagioclase and biotite grains (Fig. 5k and Fig. 5n). There are also garnet overgrowth rims when contacts with the brown biotite-rich layer (Fig. 5q-r).

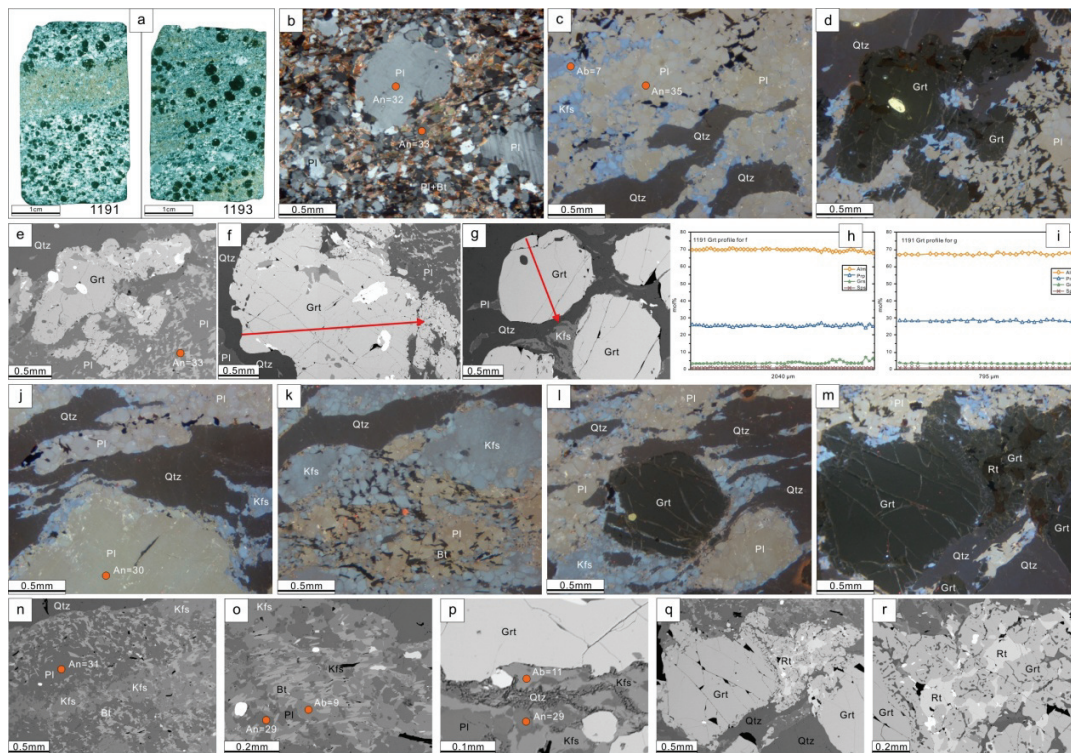


**Fig. 5** Cathodoluminescence images and BSE images show textures of sample 1191 and 1193. (b-i): CL and BSE images of sample 1191; (j-r): CL and BSE images of sample 1193. See text for explanations.

## 5.4 Samples from Steinvikneset

### 5.4.1 Sample 1041

There are significant alternating layers in sample 1041 (Fig. 6a). The light layer is composed of K-feldspar (Ab=7-9) and quartz (Fig. 6d). The brown layers have complex mineral constituents. Small garnets, biotite and plagioclase are present near the boundary (Fig. 6b-c and Fig. 6e). Orthopyroxene, clinopyroxene and large plagioclase constitute the main assemblage in the internal of the brown layer (Fig. f). At local locations, garnet and amphibole are observed rimming other minerals (Fig. 6g-h).

### 5.4.2 Sample 1042

Sillimanite, K-feldspar and quartz have been observed in large garnet porphyroblast (Fig. 6j and Fig. 6n-o). The rock matrix is composed of garnet, plagioclase, K-feldspar and sillimanite

(Fig. 6k-m). The intergranular locations between minerals are fulfilled by Qtz + Kfs intergrowth (Fig. 6p-r), which is possibly the former melt phase.

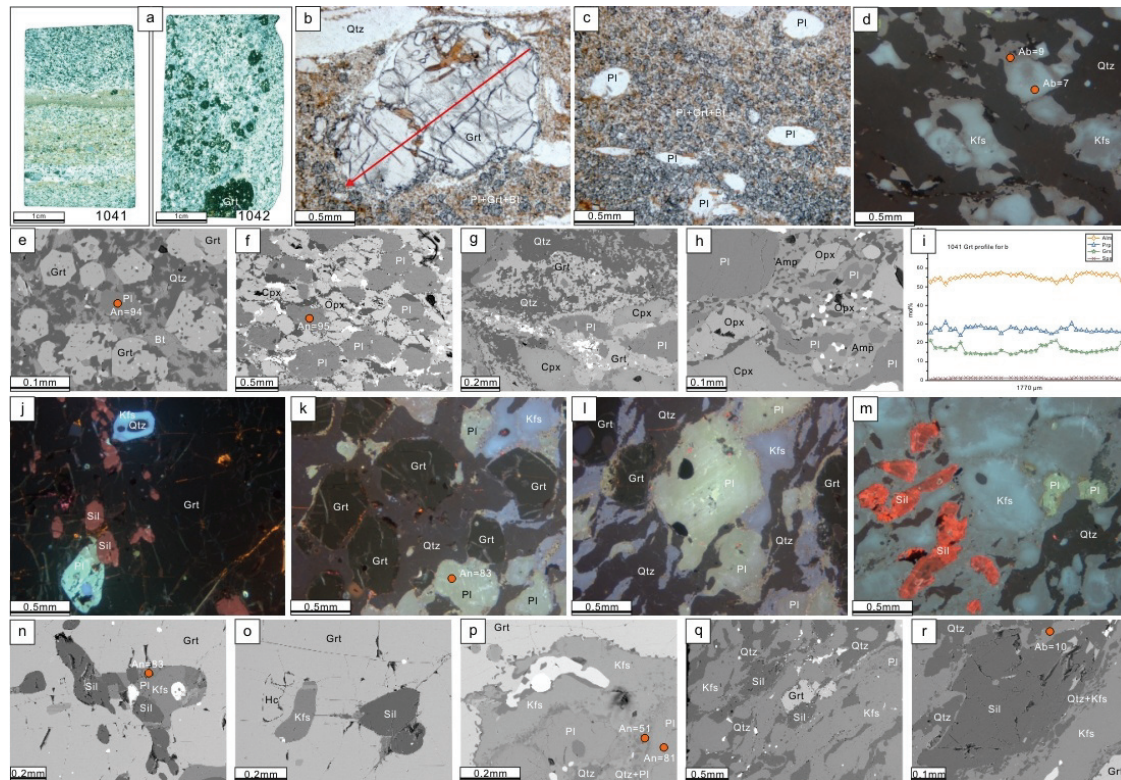


**Fig. 6** Cathodoluminescence images and BSE images show textures of sample 1041 and 1042. (b-i): CL and BSE images of sample 1041; (j-r): CL and BSE images of sample 1042. See text for explanations.

## 5.5 Samples from Bardineset

### 5.5.1 Sample 1271

Two parts could be observed under thin section of sample 1271: upper fine-grained part; lower coarse-grained part with large garnet porphyroblasts. The former part is composed of sillimanite, quartz, plagioclase (An=31), K-feldspar (Ab=12) and garnet (Fig. 7g-h). Thin kyanite rim on sillimanite (Fig. 7m) could be observed. For the coarse-grained part, garnet porphyroblast has inclusions of biotite, rutile, and quartz (Fig. 7j), which demonstrate the biotite breakdown. Sillimanite, which replacing garnet, could also be observed (Fig. 7k). there is also tiny garnet

overgrowth (Fig. 7i).

Garnet in sample 1271 has a relative homogeneous composition with average of  $\text{Alm}_{63}\text{Prp}_{33}\text{Grs}_4$  (Fig. 2a). Large garnet porphyroblast has a flat profile with Alm decreasing and Prp increasing signatures in the inner core (Fig. 7p).

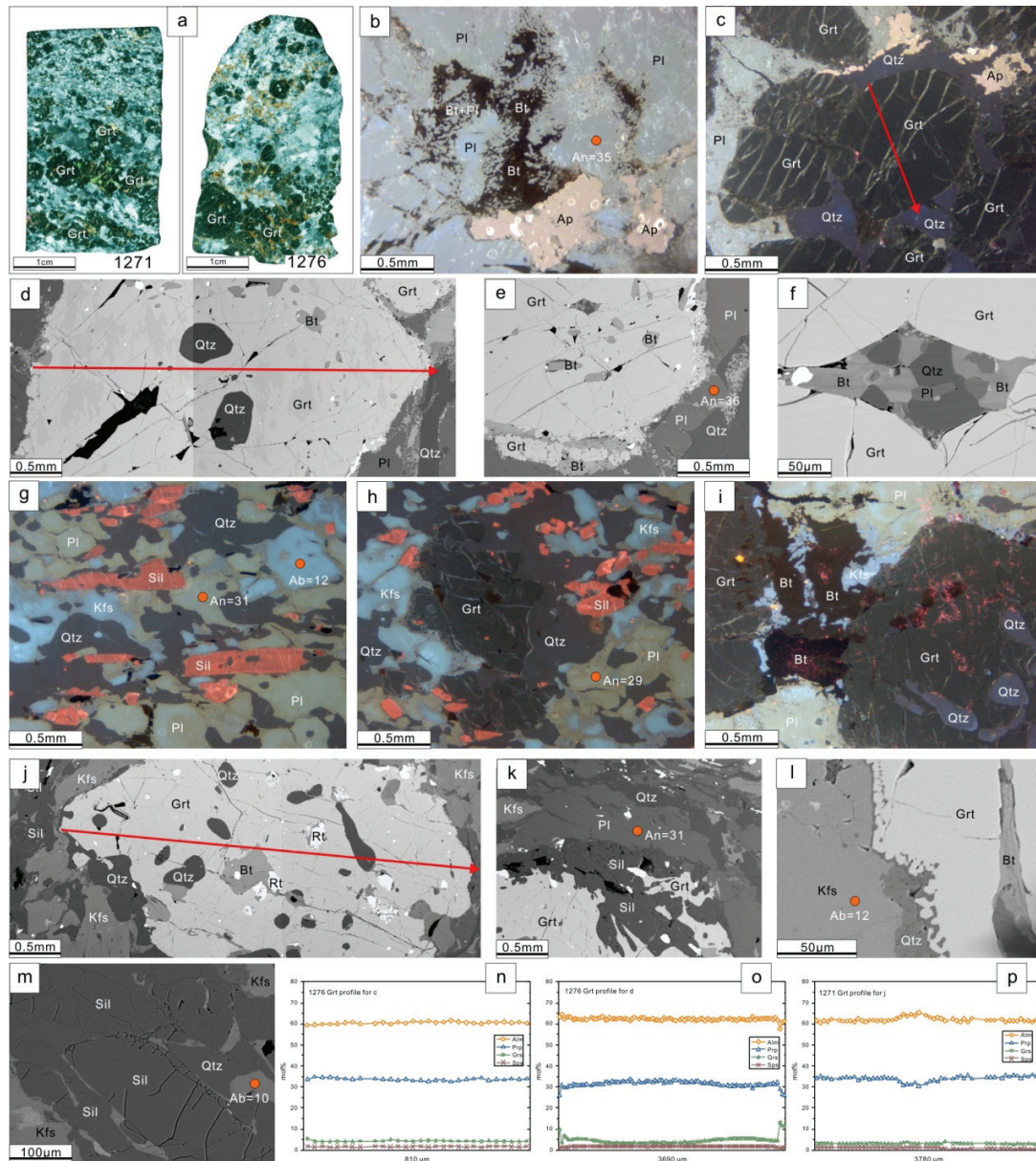


**Fig. 7** Cathodoluminescence images and BSE images show textures of sample 1271 and 1276. (b-f and n-o): CL and BSE images of sample 1276; (j-m and p): CL and BSE images of sample 1271. See text for explanations.

### 5.5.2 Sample 1276

There is no distinct gneiss structure in sample 1276. The light parts of sample 1276 are composed of plagioclase, biotite, quartz and apatite (Fig. 7b).

Large garnet porphyroblasts of sample 1276 usually have thin overgrowth rims (Fig. 7e). Correspondingly, two compositional groups could be observed in Fig. 2a: overgrowth rims with high Grs component have average composition of  $\text{Alm}_{63}\text{Prp}_{26}\text{Grs}_{10}$ , and large garnet porphyroblasts with low Grs component have average composition of  $\text{Alm}_{65}\text{Prp}_{35}\text{Grs}_5$ . The core of garnet porphyroblast is enriched in biotite, plagioclase, and quartz inclusions (Fig. 73-f), which possibly indicates the formation of garnet from biotite breakdown.

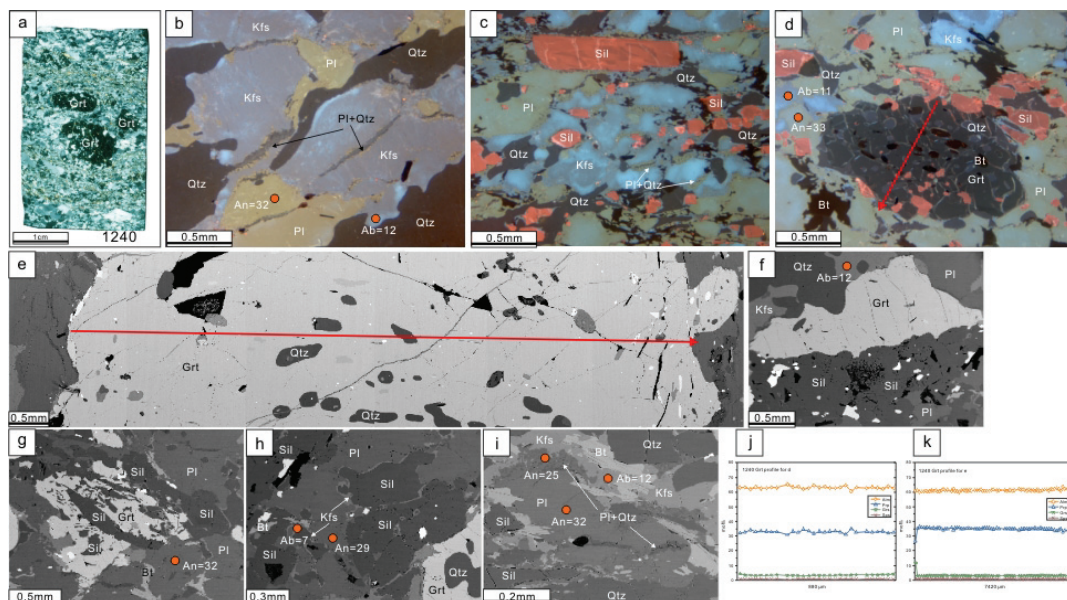


**Fig. 8** Cathodoluminescence images and BSE images show textures of sample 1240. See text for explanations.

### 5.6 Sample 1240 from Klubbneset

Three large garnet porphyroblast are observed in sample 1240 (Fig. 8a). Quartz inclusions are concentrated in garnet core (Fig. 8e). Felspathic-rich part is composed of plagioclase (An=32), K-feldspar, quartz and Pl + Qtz intergrowth (Fig. 8a). In contrast, the brown layer is composed of sillimanite, K-feldspar, plagioclase, quartz and garnet (Fig. 8c-d).



As shown in Fig. 2a, garnets from sample 1240 have a narrow range with variation between  $\text{Alm}_{65}\text{Prp}_{30}\text{Grs}_5$  to  $\text{Alm}_{64}\text{Prp}_{26}\text{Grs}_9$ . Combining with the flat profiles, this composition information perhaps indicates the garnet growth with nearly constant component. The parallel isopleths of Alm and Prp component, with weakly intersection, is consistent with the compositional variation.

## 6. P-T conditions estimated by phase diagrams

### 6.1 Samples from Tverrfjorden

Fig. 9 shows the resulting equilibrium phase diagrams calculated for sample 1031 (left and middle) and sample 1032 (right). Fig. 10 shows the resulting equilibrium phase diagrams calculated for sample 1214 (left and middle) and sample 1215 (right).

#### 6.1.1 Sample 1031

Three P-T conditions corresponding to the compositional ranges of garnet (Fig. 2a) have been marked on Fig. 9. Garnet with lowest Grs component has lowest pressure condition, and that with higher Grs component has higher pressure. Thus from the large garnet porphyroblasts (Grt1) to the garnet overgrowth (Grt2), a remarkable pressure increase could be illustrated in Fig. 9. All the conditions marked are fall into the stability field of biotite + plagioclase + ilmenite + garnet + quartz + magnetite + melt (blue field in Fig. 9). The temperature interval is constrained by the appearance of melt at lower temperature (700°C), and the disappearance of quartz at higher temperature (740°C). The absence of cordierite is probably due to the fully consumption by following garnet formation reaction. As shown by the isopleths, during pressure increasing (from 5.5 kbar to 10 kbar), the amount of garnet will increase weakly with nearly constant Alm and Prp component but significant increase of Grs component.

#### 6.1.2 Sample 1032

As shown in Fig. 9, the calculated stability field of garnet is significant small compared with that of other samples. However, the compositions of idioblastic garnets are well consistent with the field (700-750°C, above 7 kbar). The stable assemblage of this field is biotite + plagioclase + quartz + ilmenite + garnet + melt, which are also present in Fig.3j and Fig.3k.

The reason, why the composition of rare garnet porphyroblast couldn't be show in the calculated diagram, is that the used bulk composition was not equilibrated with the porphyroblast which formed earlier.

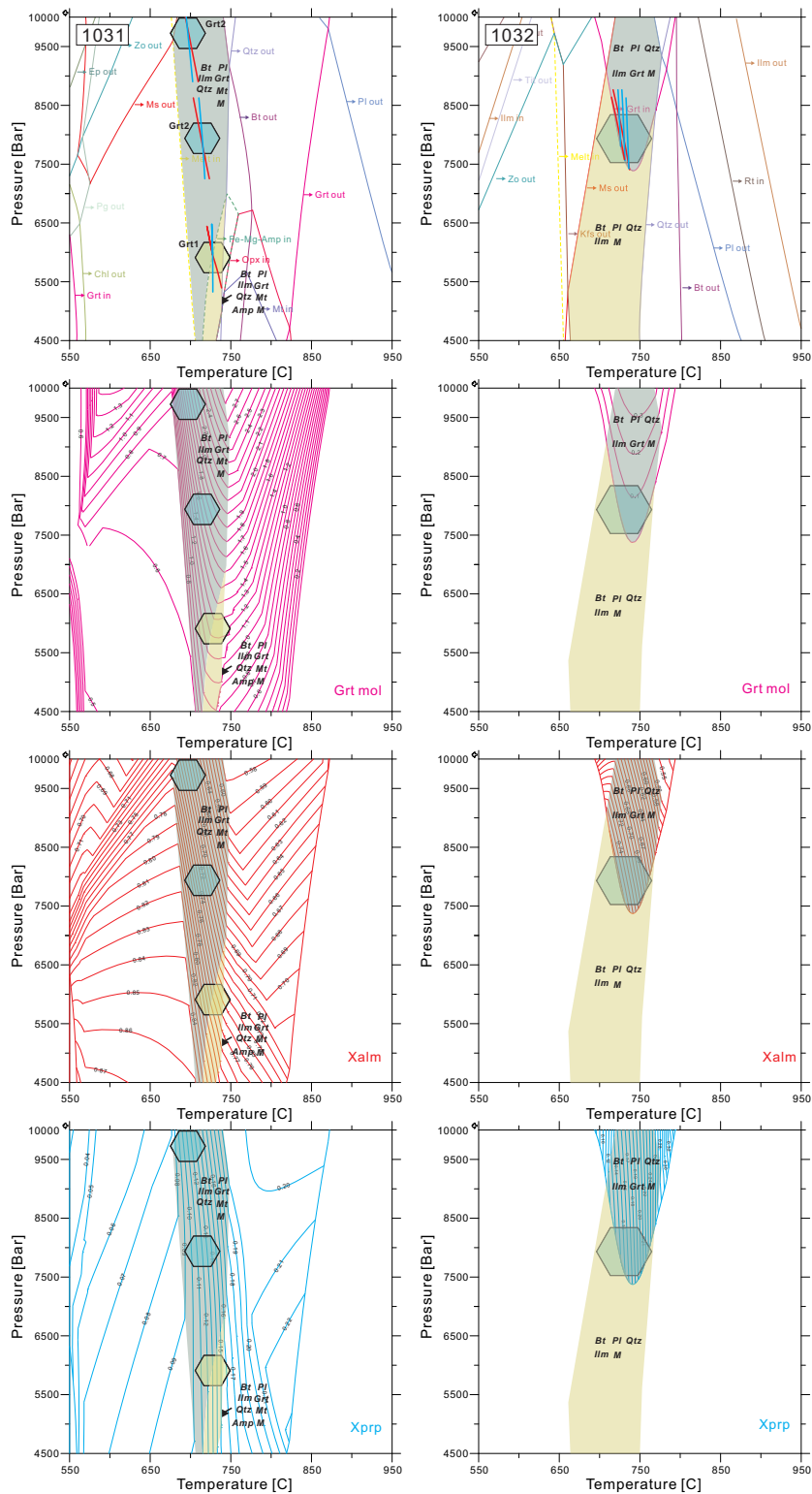


Fig. 9 Phase diagrams constructed for sample 1031 and 1032. See text for explanations.

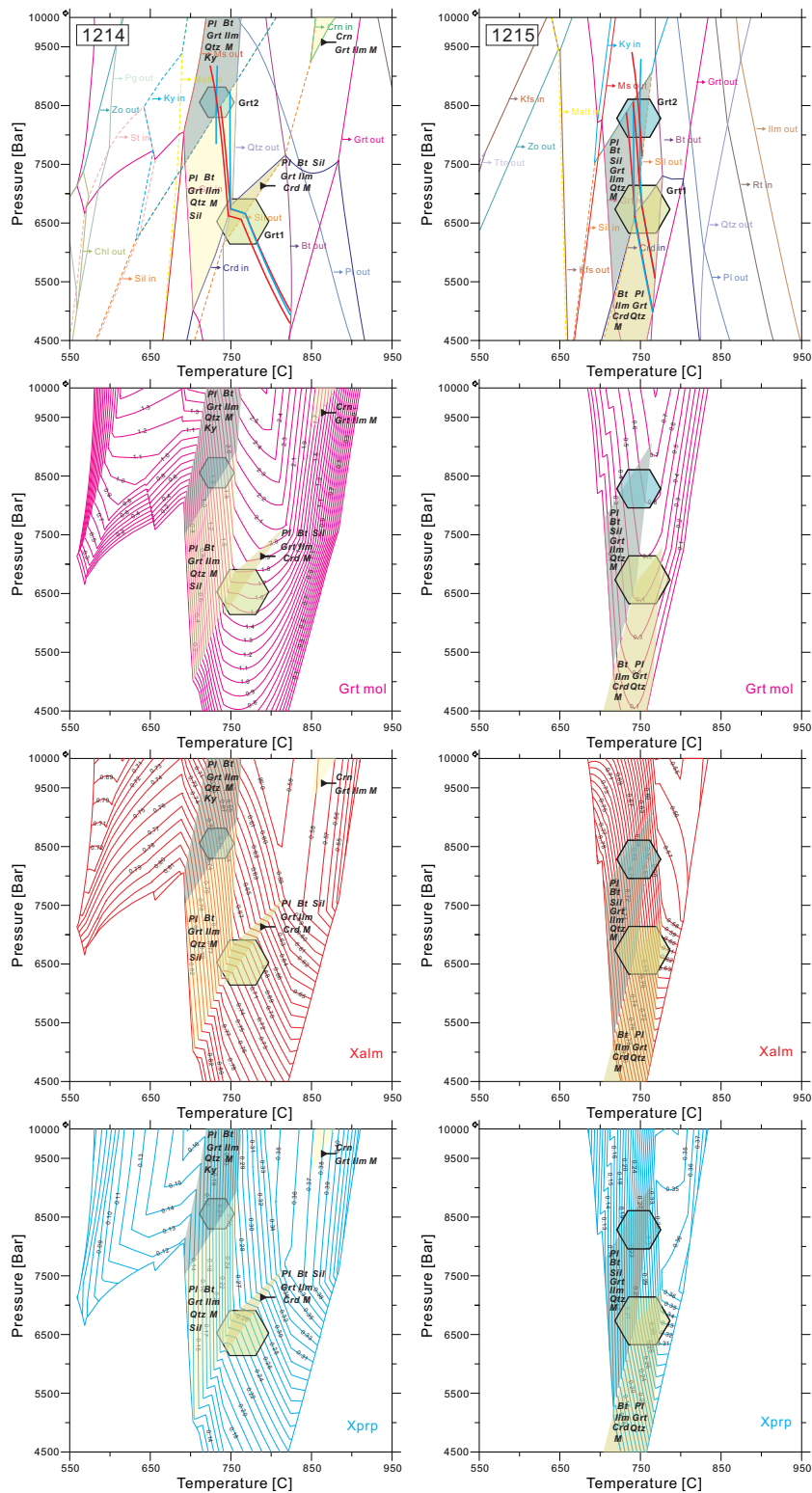


Fig. 10 Phase diagrams constructed for sample 1214 and 1215. See text for explanations.

### **6.1.3 Sample 1214**

Stability field corresponding to garnets which have corundum, hercynite and sillimanite inclusions (Fig. 4d) locates in the cordierite field at 750-800°C and 6-7.5 kbar. The assemblage of this field is composed of plagioclase, biotite, garnet, ilmenite, cordierite and melt. The pressures are constrained by the disappearance of cordierite at lower pressure, and the disappearance of sillimanite at lower pressure. Since corundum is only stable at 850°C and 9.5 kbar in Fig. 10, a former HP-HT assemblage of corundum + garnet + ilmenite + melt is suggested to be present. The garnets which have lots of biotite, K-feldspar and quartz inclusions (Fig. 4f) have the similar conditions like that with Crn + Hc + Sil inclusions.

For garnet overgrowth, the corresponding stability field locates on the transition line of sillimanite to kyanite (Fig. 10). Considering the absence of kyanite and the pervasive sillimanite, the plausible stability field is at lower pressure with assemblage of Pl + Bt + Grt + Ilm + Qtz + Sil + Melt. Minerals illustrated in Fig. 4c coincide with this conclusion.

### **6.1.4 Sample 1215**

Similar to sample 1214, two stability fields are derived from the two generations of garnet in Fig. 10. Garnets with biotite, rutile, K-feldspar and quartz inclusions (Fig. 4o) indicate stability field (below 6.5 kbar) which consists assemblage of Bt + Pl + Ilm + Grt + Crd + Qtz + Melt. The garnet overgrowth represents a stability field at higher pressure (6.5-8.5 kbar) which is composed of Bt + Pl + Sil + Ilm + Grt + Qtz + Melt. Both fields have narrow temperature range of 700-750°C. The transition of these two fields is represented by the production of sillimanite and garnet at the expense of cordierite.

## **6.2 Samples from Stålevuohppi**

Fig. 11 shows the resulting equilibrium phase diagrams calculated for sample 1191 (left and middle) and sample 1193 (right).

### **6.2.1 Sample 1191**

The modeling on the dark part of sample 1191 represents two formation conditions for the observed garnet generations (Fig. 11). The first generation of garnet formed at lower pressure (7.5 kbar), and the second generation at higher pressure (9.5 kbar). According to the absence of sillimanite and kyanite, the likely stability field consist assemblage of biotite, plagioclase, ilmenite, magnetite, garnet, quartz and melt (Fig. 11). The assemblage is constant with that

observed in Fig. 5i. The lower temperature side is defined by the disappearance of kyanite and sillimanite at 700 °C, and the higher temperature side is defined by the appearance of amphibole at 730 °C.

The modeling result of light part from sample 1191 shows similar formation condition of garnet like that of the dark part. As shown in Fig. 11, the stable mineral assemblage is composed of biotite, plagioclase, kyanite, ilmenite, garnet, quartz and melt.

### **6.2.2 Sample 1193**

Stability field for garnet compositions of sample 1193 is located at the boundaries adjacent to the corundum stability field (Fig. 11). Considering the absence of sillimanite and corundum and the mineral assemblage observed, the plausible stability field is located at the right side of Sil-out line (Fig. 11). The stable assemblage is composed of Bt + Pl + Mt + Ilm + Grt + M at 770-860°C and 5.5-9 kbar. The temperature interval is constrained by the disappearance of sillimanite at lower temperature, and the appearance of hercynite at higher temperature. The lower pressure is delimited by the appearance of cordierite, and the upper by the appearance of corundum.

## **6.3 Samples from Steinvikneset**

Fig. 12 shows the resulting equilibrium phase diagrams calculated for sample 1041 (left and middle) and sample 1042 (right).

### **6.3.1 Sample 1041**

Coinciding with the complex minerals observed under thin section, the phase diagram of sample 1041 also shows relative complex mineral stability fields.

As shown in Fig. 12, two generations of garnet represents two distinct stability fields in the phase diagrams of the dark part of sample 1041. Large garnet porphyroblasts indicate a stability assemblage of Pl + Ilm + Cpx + Opx + Qtz + Melt (800-870°C and 5.5 kbar), which is consistent with the observation (Fig. 6f-g). In contrast, small garnets, which rimmed plagioclase, pyroxene and amphibole (Fig. 6g-h), indicate a stability assemblage of Pl + Ilm + Cpx + Amp + Qtz + Bt + Melt (740-780°C and 8.5 kbar).

For the modeling of light part shown in Fig. 12, the K-feldspar-rich and plagioclase-poor feature (Fig. 6d) indicate a stability condition at low pressure (700 °C and <6.5 kbar).

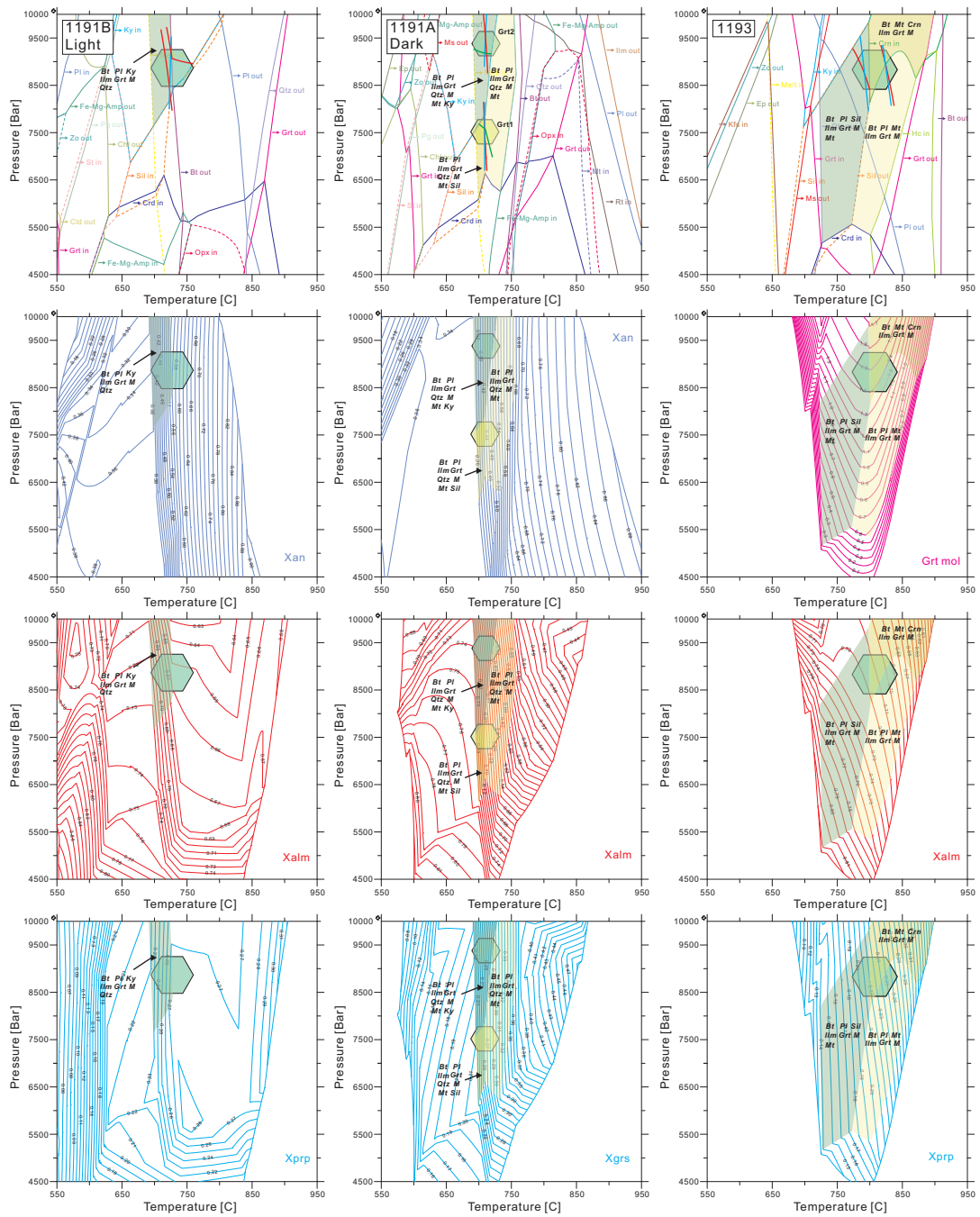


Fig. 11 Phase diagrams constructed for sample 1191 (light and dark layers) and sample 1193. See text for explanations.

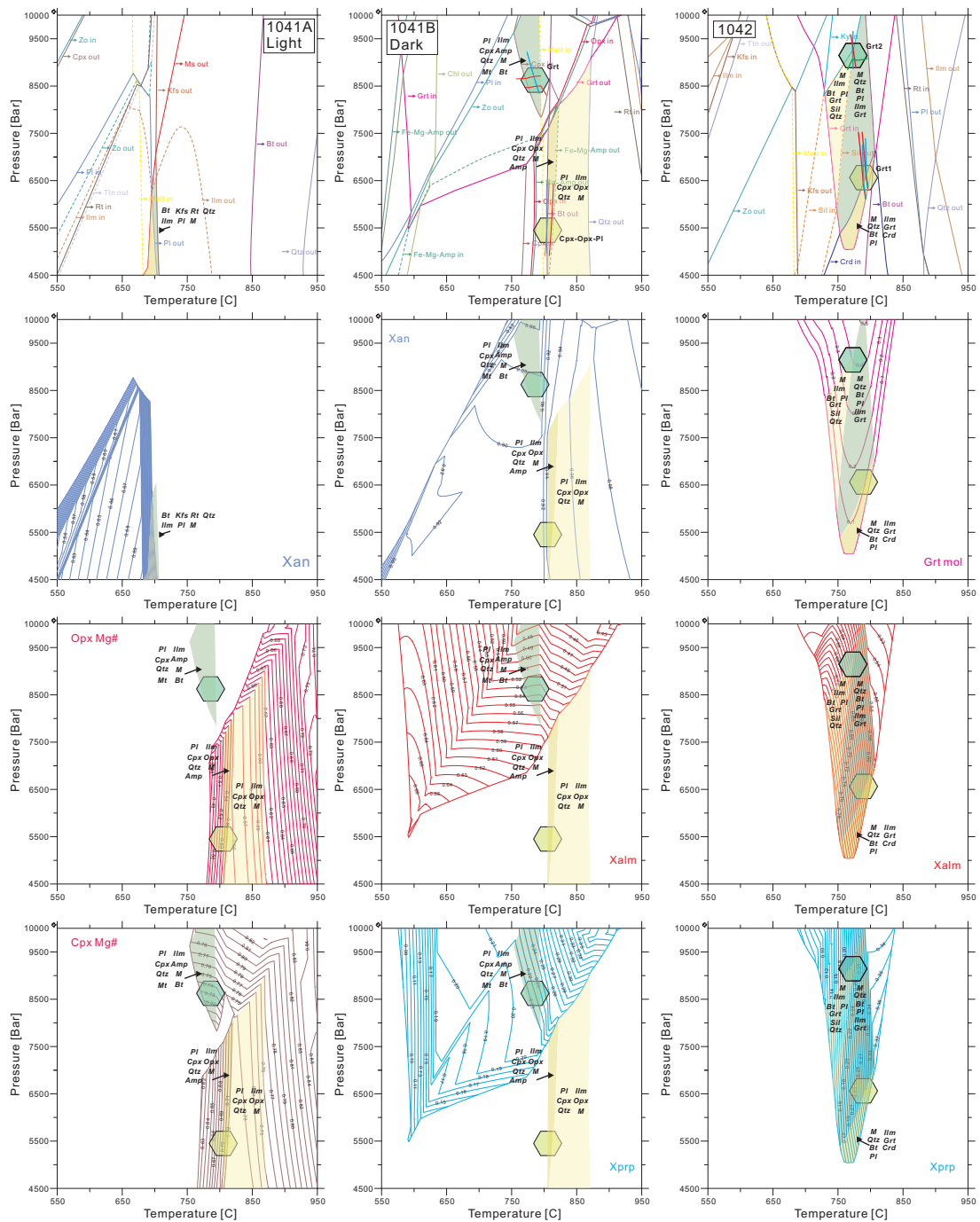


Fig. 12 Phase diagrams constructed for sample 1041 (light and dark layers) and sample 1042. See text for explanations.

### **6.3.2 Sample 1042**

Two formation conditions for garnets of sample 1042 have been illustrated in Fig. 12. Large garnet porphyroblasts formed at low pressure of 6.5 kbar, while the overgrowth has pressure condition of 9 kbar. Because sillimanite are observed in matrix and as inclusions in garnet, the real stability field should locate at left side of the Sil-out line (Fig. 12). Therefore, the stability field has an assemblage of Bt + Pl + Ilm + Grt + Sil + Qtz + Melt at 720-750 °C and 5.5-9.5 kbar.

## **6.4 Samples from Bardineset**

Fig. 13 shows the resulting equilibrium phase diagrams calculated for sample 1271 (left) and sample 1276 (right).

### **6.4.1 Sample 1271**

The stability field corresponding to the homogeneous garnet composition is composed of biotite, garnet, sillimanite, ilmenite, magnetite and melt. The wide field has temperature ranges from 750°C to 850°C and pressure ranges between 7 kbar and 9 kbar. The temperature interval is constrained by the disappearance of quartz at lower temperature, and the appearance of corundum at higher temperature. The pressures of this stability field are delimited by the appearance of cordierite at lower pressure, and the transformation of sillimanite to kyanite at higher pressure. Notably, the thin kyanite rims around the matrix sillimanite (Fig. 7m) suggest a higher pressure condition above the upper boundary of the calculated field.

The pervasive rutile, quartz, and biotite inclusions in large garnet porphyroblasts (Fig. 7j) indicate that garnet formed at the expense of biotite breakdown. In addition, sillimanite replacing garnet (Fig. 7k) demonstrate that the sillimanite-out line have been crossed before reaching the above stability field. Thus, the large garnet porphyroblast should have formed at condition between the Sil-out and Bt-out lines in Fig.13 at lower pressure, which locates in the cordierite stability field. The survival Alm decreasing and Prp increasing signatures in the inner core of large garnet porphyroblast (Fig. 7p) are well consistent with this conclusion based on the Alm and Prp isopleths in the cordierite field.



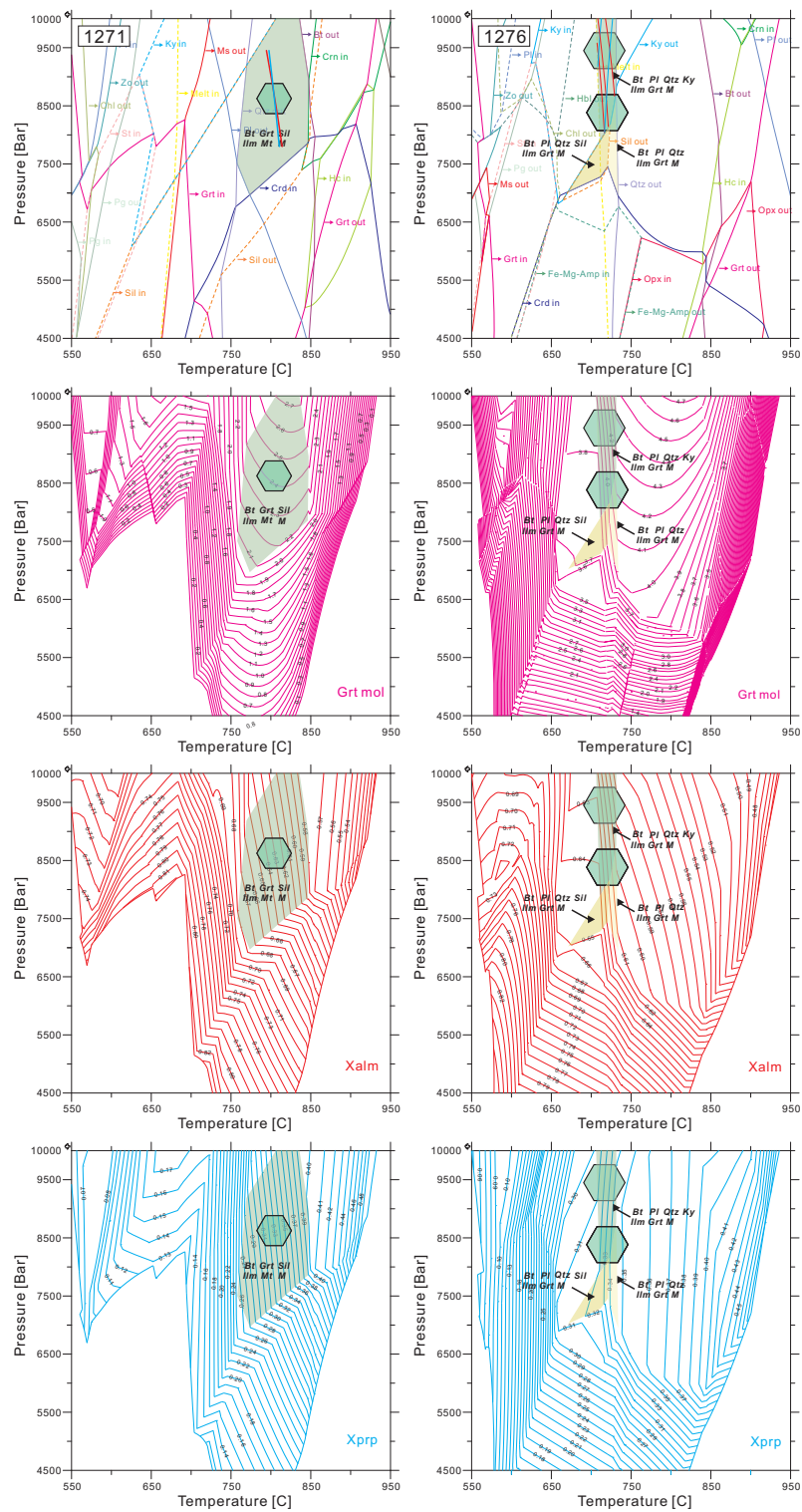


Fig. 13 Phase diagrams constructed for sample 1271 and sample 1276. See text for explanations.

### **6.4.2 Sample 1276**

The formation conditions for the average compositions of two garnet groups all locate above the stability line of kyanite. Considering the wide variation of Grs component from 4 to 12 and the relative constant Alm and Prp components, the stability fields for garnet could extend towards lower pressure. Combining with the absence of sillimanite and kyanite, the plausible stability field is the yellow area (Fig. 13) which consist assemblage of biotite, plagioclase, quartz, ilmenite, garnet and melt. This narrow field (720-730°C, 7-8 kbar) is constrained by the disappearance of sillimanite at lower temperature, and the disappearance of quartz at higher temperature.

The inclusions of biotite + quartz + plagioclase assemblage (Fig. 7d-f), which suggesting partial melting of biotite, and the absence of original quartz indicate that peak metamorphic temperature is at the right side of Qtz-out line in Fig. 12. Thus a former hotter (>730°C) assemblage with biotite + plagioclase + quartz + ilmenite+ garnet + melt was deduced to be present.

## **6.5 Sample 1240 from Klubbneset**

Fig. 14 shows the resulting equilibrium phase diagrams calculated for sample 1240.

For sample 1240, the narrow stability field corresponding to inter core of garnet porphyroblast (green field) is composed of cordierite, biotite, ilmenite, garnet and melt. The field ranges from 830-850°C with pressures between 6.3 kbar to 7 kbar. The temperature interval is constrained by the disappearance of plagioclase at lower temperature, and the disappearance of biotite at higher temperature. The absence of cordierite is probably due to the fully consumption by following garnet formation reaction.

The formation condition corresponding to garnet composition of upper limited is located on the field boundary of two fields which are separated by the transformation of sillimanite to kyanite at higher pressure. Considering the absence of kyanite in the thin section, the yellow field with assemblage of biotite, plagioclase, sillimanite, ilmenite, garnet and melt at 740-820°C and 7-9 kbar is the plausible one. This assemblage is consistent with that observed. This field is constrained by disappearance of quartz at lower temperature, as well as the disappearance of plagioclase at higher temperature. The pressures of this stability field are delimited by the appearance of cordierite at lower pressure, and the transformation of sillimanite to kyanite at higher pressure.

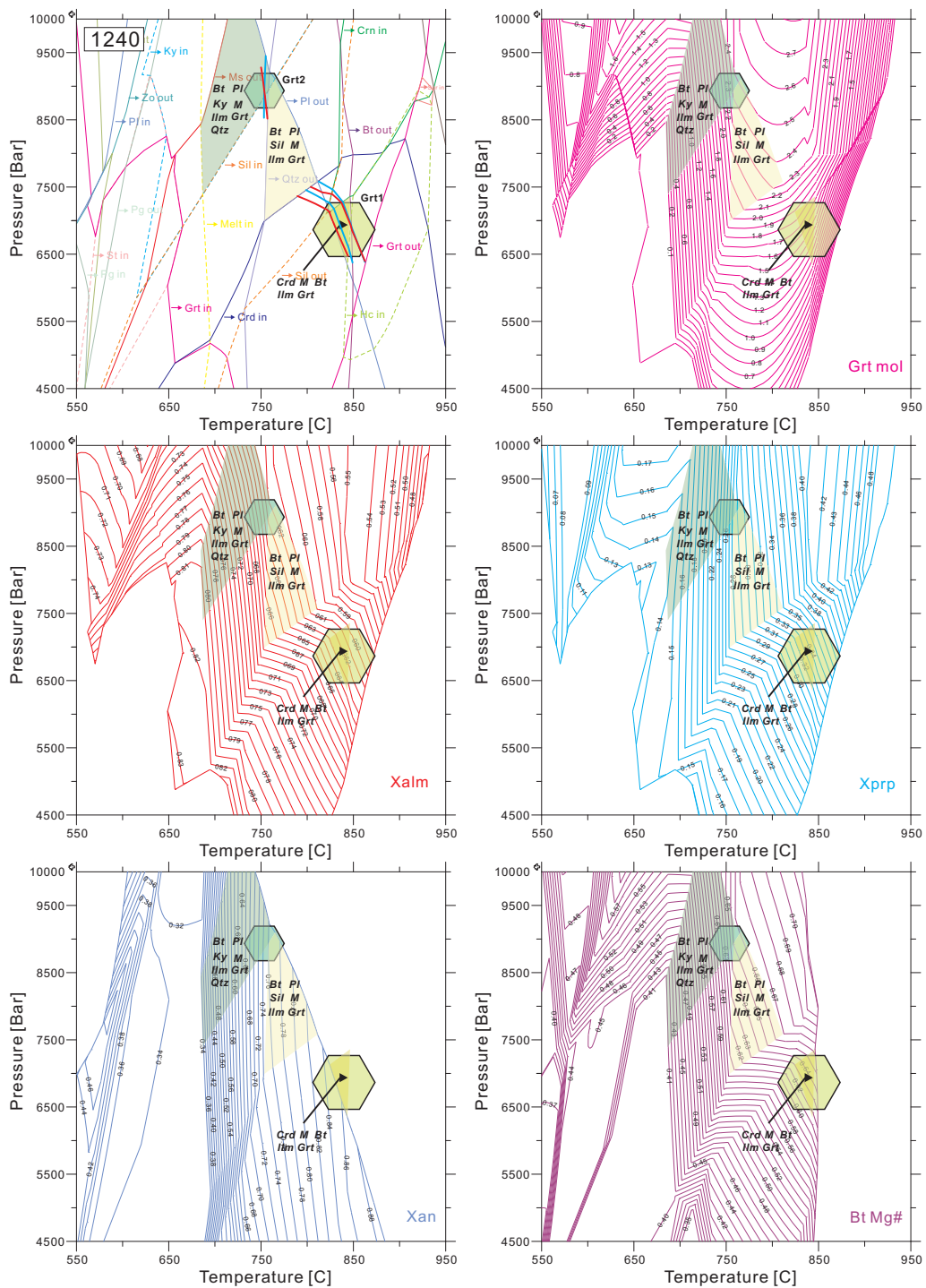


Fig. 14 Phase diagrams constructed for sample 1240. See text for explanations.

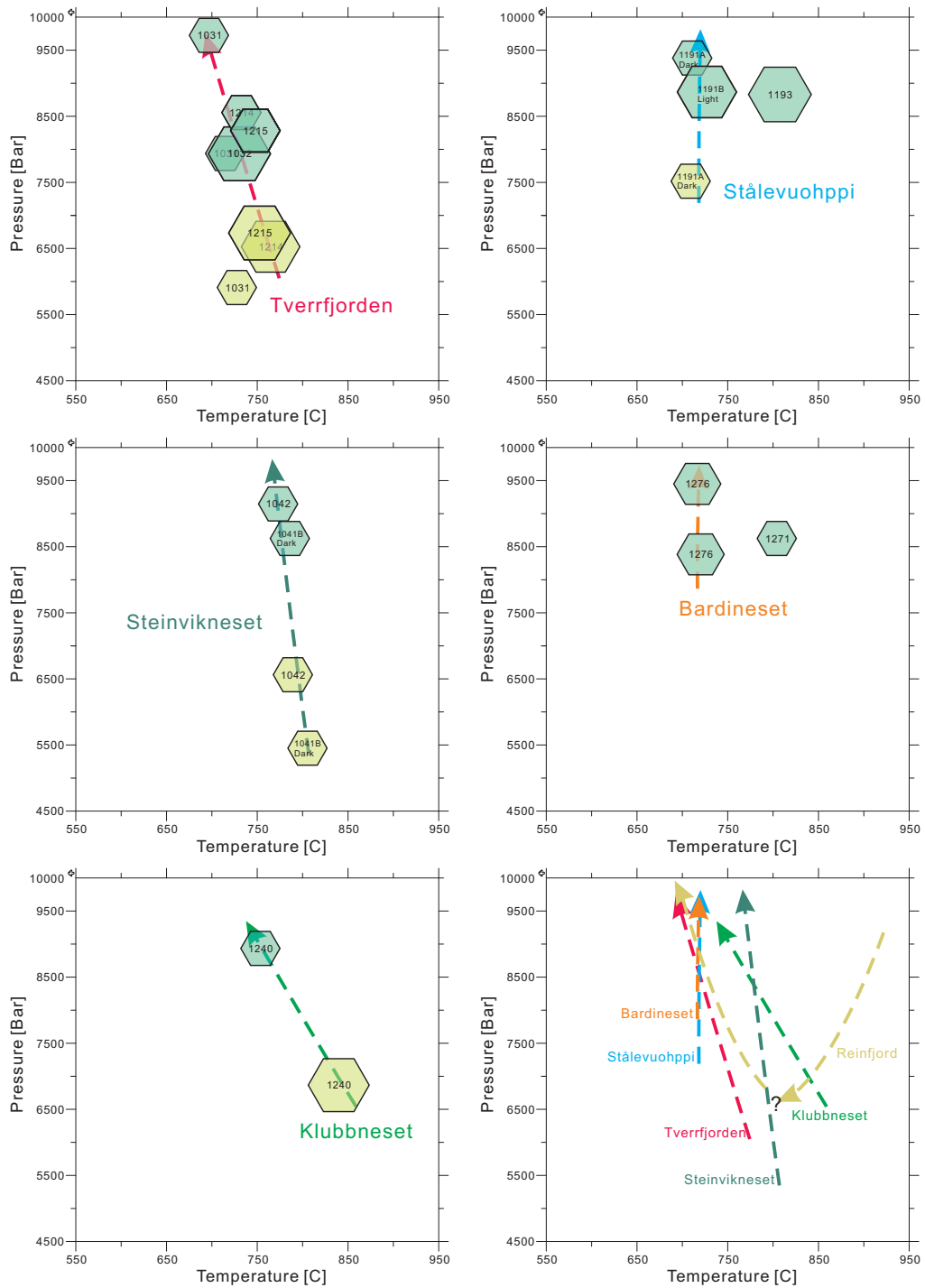


Fig. 15 Utilized metamorphic conditions for samples from the same area. See text for explanations.

## 7. Metamorphic evolution

### 7.1 Peak metamorphic condition

A former peak mineral assemblage of corundum + hercynite + sillimanite has been observed directly in sample 1214 (Fig.4d), which has corundum stability field (at 850°C and 9.5 kbar) in the calculated phase diagram (Fig. 10). This high temperature mineral assemblage has also been observed in the country rocks of adjacent Reinfjord ultramafic complex, which developed a contact aureole. Similarly, the corundum + hercynite +sillimanite of sample 1214 are possibly derived from the emplacement of olivine gabbro.

In contrast, other samples record a general thermal event at about 800°C and 5.5-6.5 kbar (Fig. 15). The representative mineral assemblage of this stage is Pl +Bt +Sil +Grt +M ± Crd. Garnet compositions of this event are recorded in the large porphyroblasts which formed by biotite partial melting.

### 7.2 Thrust cooling

A pressure increase (from 5.5 kbar to 9.5 kbar) has been illustrated clearly by utilizing stability fields from all samples from various areas (Fig. 15). This process is accompanied with new garnet generation that overgrowth on the porphyroblast (e.g. Fig.3g, Fig. 4o and Fig.7e) and individual small crystals crystallized from melt (Fig. 3j). The compositional isopleths ( $X_{Alm}$  and  $X_{Prp}$ ) of garnet during this process also have relatively steep slopes in the P-T space (Fig. 9-14). The upper limit of pressure is constrained by the transformation of sillimanite to kyanite (Fig. 7m), at pressures above 9.5 kbar for 700°C.

## 8. Implications for tectonic evolution

As shown in Fig. 15, two stages could be summarized from the P-T conditions and mineral stability fields: (1) contact or regional metamorphism at ca. 800°C and 5.5-6.5 kbar; (2) thrust cooling until 700°C and 9.5 kbar.

Sm-Nd isochron age of  $531 \pm 10$  Ma from a coarse-grained garnet-rich granulite (monzonite) have been achieved at Klubbneset area (from where sample 1240 was collected ), and this age was further interpreted as that of high-grade metamorphism (Mørk and Stabel, 1990). Metagabbro along the Øksfjorden bay, which host the paragneisses, has an intrusion age of  $829 \pm 18$  Ma dating by Rb-Sr whole rock method (Krogh and Elvevold, 1990). Researches performed

on metapelitic xenolith in the metagabbro have demonstrated three metamorphic stages: (1) Contact metamorphism: 930-960 °C / 5-6.5 kb; (2) Cooling: 700-750 °C / 5-7 kb; (3) Compression: 650-700 °C / 8-10 kb (Elvevold and Reginiussen, 1996; Elvevold et al., 1994). A similar three stages have also been demonstrated in the Reinfjord area: (1) contact metamorphism at 850-900°C and 7.5-9.5 kbar; (2) uplift cooling with pressure decrease by ~3 kbar and temperature decrease by ~100°C (ends at 800°C and 6.5 kbar); (3) thrust cooling until 650°C and 10kbar. In addition, recent work on migmatitic gneisses from Øksfjorden bay gives partial melting condition of 760-820 °C and 7.5-9.5 kb (Menegon et al., 2011). Although the absolute values of temperature and pressure from literature and this paper are different, country rocks from these five areas perhaps experienced the same tectonothermal history. The first high temperature contact metamorphism was deduced by the emplacement of volumes of ultramafic rocks in the Seiland igneous province at 829±18 Ma (Krogh and Elvevold, 1990). Sequential thrust cooling was accompanied with crustal thickening and compression during the formation of Caledonian orogeny belt, which involving eastwards thrust of the Seiland igneous province onto the Precambrian crystalline basement of the Baltic shield during the Silurian continental collision (ca. 431-428 Ma at Finnmark, Kirkland et al., 2006a; Kirkland et al., 2007) between Baltica and Laurentia following the early Palaeozoic closure of the Iapetus Ocean (Gee, 1975; Roberts, 2003).

## 9. Conclusions

Two main stages in a chronological order could be summarized from the P-T conditions and mineral stability fields of paragneisses from Øksfjord peninsula: (1) contact metamorphism at ca. 800°C and 5.5-6.5 kbar; (2) thrust cooling until 700°C and 9.5 kbar. The first high temperature contact metamorphism was deduced by the emplacement of volumes of ultramafic rocks. Sequential thrust cooling was accompanied with crustal thickening and compression.

## References

- Akselsen, J., 1982. Precambrian and Caledonian Tectonometamorphic Evolution of Northeastern Seiland, Finnmark, North Norway. *Norges Geologiske Undersøkelse Bulletin*(66): 45-61.
- Andersen, T.B., Jamtveit, B., Dewey, J.F. and Swensson, E., 1991. Subduction and exhumation of continental crust: major mechanisms during continent-continent collision and orogenic extensional collapse, a model based on the south Norwegian Caledonides. *Terra Nova*, 3(3): 303-310.
- Andresen, A., 1988. Caledonian terranes of Northern Norway and their characteristics. *Trabajos de geología*, 17: 103-117.
- Appleyard, E.C., 1974. Syn-orogenic igneous alkaline rocks of eastern Ontario and northern Norway. *Lithos*, 7(3): 147-169.
- Bucher-Nurminen, K., 1991. Mantle fragments in the Scandinavian caledonides. *Tectonophysics*, 190(2-4): 173-192.
- Coggon, R. and Holland, T., 2002. Mixing properties of phengitic micas and revised garnet-phengite

- thermobarometers. *Journal of Metamorphic Geology*, 20(7): 683-696.
- Daly, J.S., Aitchison, S.J., Cliff, R.A., Gayer, R.A. and Rice, A.H.N., 1991. Geochronological Evidence from Discordant Plutons for a Late Proterozoic Orogen in the Caledonides of Finnmark, Northern Norway. *Journal of the Geological Society*, 148: 29-40.
- de Capitani, C. and Brown, T., 1987. The computation of chemical equilibrium in complex systems containing non-ideal solutions. *Geochimica Et Cosmochimica Acta*, 51(10): 2639-2652.
- de Capitani, C. and Petrakakis, K., 2010. The computation of equilibrium assemblage diagrams with Theriak/Domino software. *American Mineralogist*, 95(7): 1006-1016.
- Diener, J.F.A., Powell, R., White, R.W. and Holland, T.J.B., 2007. A new thermodynamic model for clino- and orthoamphiboles in the system Na<sub>2</sub>O–CaO–FeO–MgO–Al<sub>2</sub>O<sub>3</sub>–SiO<sub>2</sub>–H<sub>2</sub>O–O. *Journal of Metamorphic Geology*, 25(6): 631-656.
- Droop, G., 1987. A general equation for estimating Fe<sup>3+</sup> concentrations in ferromagnesian silicates and oxides from microprobe analyses, using stoichiometric criteria. *Mineralogical Magazine*, 51(361): 431-435.
- Drüppel, K., Elsäßer, L., Brandt, S. and Gerdes, A., 2013. Sveconorwegian Mid-crustal Ultrahigh-temperature Metamorphism in Rogaland, Norway: U–Pb LA-ICP-MS Geochronology and Pseudosections of Sapphirine Granulites and Associated Paragneisses. *Journal of Petrology*, 54(2): 305-350.
- Elvevold, S. and Reginiussen, H., 1996. Reaction textures in contact-metamorphosed xenoliths; implications for the tectonothermal evolution of the Seiland igneous province, Norwegian Caledonides. *European Journal of Mineralogy*, 8(4): 777-789.
- Elvevold, S., Reginiussen, H., Krogh, E.J. and Bjorklund, F., 1994. Reworking of Deep-Seated Gabbros and Associated Contact Metamorphosed Paragneisses in the South-Eastern Part of the Seiland Igneous Province, Northern Norway. *Journal of Metamorphic Geology*, 12(4): 539-556.
- Fall, A., Bodnar, R.J., Szabó, C. and Pál-Molnár, E., 2007. Fluid evolution in the nepheline syenites of the Ditrau Alkaline Massif, Transylvania, Romania. *Lithos*, 95(3-4): 331-345.
- Gee, D., 1975. A tectonic model for the central part of the Scandinavian Caledonides. *American Journal of Science*, 275: 468–515.
- Gee, D.G., Janák, M., Majka, J., Robinson, P. and van Roermund, H., 2012. Subduction along and within the Baltoscandian margin during closing of the Iapetus Ocean and Baltica-Laurentia collision. *Lithosphere*.
- Holland, T., Baker, J. and Powell, R., 1998. Mixing properties and activity-composition and relationships of chlorites in the system MgO–FeO–Al<sub>2</sub>O<sub>3</sub>–SiO<sub>2</sub>–H<sub>2</sub>O. *Eur J Mineral*, 10(3): 395-406.
- Holland, T. and Powell, R., 1996. Thermodynamics of order-disorder in minerals: II, Symmetric formalism applied to solid solutions. *American Mineralogist*, 81(11-12): 1425-1437.
- Holland, T. and Powell, R., 2003. Activity–composition relations for phases in petrological calculations: an asymmetric multicomponent formulation. *Contributions to Mineralogy and Petrology*, 145(4): 492-501.
- Holland, T.J.B. and Powell, R., 1998. An internally consistent thermodynamic data set for phases of petrological interest. *Journal of Metamorphic Geology*, 16(3): 309-343.
- Kelsey, D.E., White, R.W., Holland, T.J.B. and Powell, R., 2004. Calculated phase equilibria in K<sub>2</sub>O–FeO–MgO–Al<sub>2</sub>O<sub>3</sub>–SiO<sub>2</sub>–H<sub>2</sub>O for sapphirine-quartz-bearing mineral assemblages. *Journal of Metamorphic Geology*, 22(6): 559-578.
- Kirkland, C.L., Daly, J.S., Chew, D.M. and Page, L.M., 2008a. The Finnmarkian Orogeny revisited: An isotopic investigation in eastern Finnmark, Arctic Norway. *Tectonophysics*, 460(1-4): 158-177.
- Kirkland, C.L., Daly, J.S., Eide, E.A. and Whitehouse, M.J., 2006a. The structure and timing of lateral escape during the Scandian Orogeny: A combined strain and geochronological investigation in Finnmark, Arctic Norwegian Caledonides. *Tectonophysics*, 425(1-4): 159-189.
- Kirkland, C.L., Daly, J.S. and Whitehouse, M., 2006b. Granitic magmatism of Grenvillian and late Neoproterozoic age in Finnmark, Arctic Norway - Constraining pre-Scandian deformation in the Kalak Nappe Complex. *Precambrian Research*, 145(1-2): 24-52.
- Kirkland, C.L., Daly, J.S. and Whitehouse, M.J., 2005. Early Silurian magmatism and the Scandian evolution of the Kalak Nappe Complex, Finnmark, Arctic Norway. *Journal of the Geological Society*, 162(6): 985-1003.
- Kirkland, C.L., Daly, J.S. and Whitehouse, M.J., 2008b. Basement-cover relationships of the Kalak Nappe Complex, Arctic Norwegian Caledonides and constraints on Neoproterozoic terrane assembly in

- the North Atlantic region. *Precambrian Research*, 160(3-4): 245-276.
- Kirkland, Christopher L., Stephen Daly, J. and Whitehouse, Martin J., 2007. Provenance and Terrane Evolution of the Kalak Nappe Complex, Norwegian Caledonides: Implications for Neoproterozoic Paleogeography and Tectonics. *The Journal of Geology*, 115(1): 21-41.
- Krogh, E. and Elvevold, S., 1990. A Precambrian age for an early gabbro-monzonitic intrusive on the Øksfjord peninsula, Seiland Igneous Province, northern Norway. *Norsk Geologisk Tidsskrift*, 70(4): 267-273.
- Markl, G. and Bucher, K., 1997. Proterozoic eclogites from the Lofoten islands, northern Norway. *Lithos*, 42(1-2): 15-35.
- Menegon, L., Nasipuri, P., Stünitz, H., Behrens, H. and Ravna, E., 2011. Dry and strong quartz during deformation of the lower crust in the presence of melt. *Journal of Geophysical Research*, 116(B10): B10410.
- Mørk, M.B.E. and Stabel, A., 1990. Cambrian Sm-Nd dates for an ultramafic intrusion and for high-grade metamorphism on the Oksfjord peninsula, Finmark, North Norway. *Norsk Geologisk Tidsskrift*, 70: 275-291.
- Osmundsen, P.T. and Andersen, T.B., 1994. Caledonian Compressional and Late-Orogenic Extensional Deformation in the Staveneset Area, Sunnfjord, Western Norway. *Journal of Structural Geology*, 16(10): 1385-1401.
- Ritzmann, O. and Faleide, J.I., 2007. Caledonian basement of the western Barents Sea. *Tectonics*, 26(5): TC5014.
- Roberts, D., 1974. Geologisk kart over Norge, berggrunskart. Hammerfest 1:250000. Norges geologiske undersøkelse.
- Roberts, D., 2003. The Scandinavian Caledonides: event chronology, palaeogeographic settings and likely modern analogues. *Tectonophysics*, 365(1-4): 283-299.
- Roberts, D. and Gee, D.G., 1985. An introduction to the structure of the Scandinavian Caledonides. In Gee, D.G. & Sturt, B.A. (eds.) *The Caledonide orogen - Scandinavia and related areas*: 55-68.
- Roberts, D., Nordgulen, Ø. and Melezhik, V., 2007. The Uppermost Allochthon in the Scandinavian Caledonides: From a Laurentian ancestry through Taconian orogeny to Scandian crustal growth on Baltica. *Geological Society of America Memoirs*, 200: 357-377.
- Roberts, R.J., Corfu, F., Torsvik, T.H., Ashwal, L.D. and Ramsay, D.M., 2006. Short-lived mafic magmatism at 560-570 Ma in the northern Norwegian Caledonides: U-Pb zircon ages from the Seiland Igneous Province. *Geological Magazine*, 143(6): 887-903.
- Roberts, R.J., Corfu, F., Torsvik, T.H., Hetherington, C.J. and Ashwal, L.D., 2010. Age of alkaline rocks in the Seiland Igneous Province, Northern Norway. *Journal of the Geological Society*, 167(1): 71-81.
- Robins, B. and Gardner, P.M., 1975. The magmatic evolution of the Seiland province, and Caledonian plate boundaries in northern Norway. *Earth and Planetary Science Letters*, 26(2): 167-178.
- Stephens, M.B. and Gee, D.G., 1985. A tectonic model for the evolution of the eugeoclinal terranes in central Scandinavian Caledonides. In Gee, D.G. & Sturt, B.A. (eds.) *The Caledonide orogen - Scandinavia and related areas*: 953-978.
- Sturt, B.A., Miller, J.A. and Fitch, F.J., 1967. The age of alkaline rocks from West Finnmark, northern Norway, and their bearing on the datings of the Caledonian orogeny. *Norsk Geologisk Tidsskrift*, 47: 255-273.
- Sturt, B.A., Pringle, I.R. and Ramsay, D.M., 1978. The Finnmarkian phase of the Caledonian Orogeny. *Journal of the Geological Society*, 135(6): 597-610.
- White, R.W., Powell, R. and Clarke, G.L., 2002. The interpretation of reaction textures in Fe-rich metapelitic granulites of the Musgrave Block, central Australia: constraints from mineral equilibria calculations in the system  $K_2O-FeO-MgO-Al_2O_3-SiO_2-H_2O-TiO_2-Fe_2O_3$ . *Journal of Metamorphic Geology*, 20(1): 41-55.
- White, R.W., Powell, R. and Holland, T.J.B., 2007. Progress relating to calculation of partial melting equilibria for metapelites. *Journal of Metamorphic Geology*, 25(5): 511-527.
- White, R.W., Powell, R., Holland, T.J.B. and Worley, B.A., 2000. The effect of  $TiO_2$  and  $Fe_2O_3$  on metapelitic assemblages at greenschist and amphibolite facies conditions: mineral equilibria calculations in the system  $K_2O-FeO-MgO-Al_2O_3-SiO_2-H_2O-TiO_2-Fe_2O_3$ . *Journal of Metamorphic Geology*, 18(5): 497-511.